Photoexcited state dynamics in carotenoids



Dilhan Manawadu

Thesis submitted for the degree of Doctor of Philosophy

Linacre College, University of Oxford

Hilary 2023

Declaration of Authorship

The work presented in this thesis is my own, except where otherwise stated. No part of this thesis has been submitted for any other degree at this or any other university.

Dilhan Manawadu

August, 2023

Abstract

Carotenoids are an important class of biomolecules found in nature with exquisite photophysical properties. The quasi-one-dimensional nature of carotenoids enhances the roles of the electron-electron interactions and electron-nuclear coupling in their π-conjugated systems. This gives rise to a fascinating excited state structure with a nonemissive 'dark' excited state, labelled $S_1/2\,^1A_g^-$, of energy below the photoexcited 'bright' state, labelled $S_2/1\,^1B_u^+$. This energetic reversal gives rise to the nonemissive properties of carotenoids, their photoprotection properties in light harvesting complexes, and the ability to undergo singlet fission.

Singlet fission (SF) is a process by which a singlet excitation dissociates to form two spin-uncorrelated triplet excitations. In carotenoids, the first step of SF is thought to be internal conversion of the photoexcited $1\,^1B_u^+$ state to a correlated triplet-pair state. The low-lying excited states of polyenes are studied using the density matrix renormalisation group (DMRG) method to solve the Pariser−Parr−Pople-Peierls (PPPP) model of π-conjugated systems. The triplet-pair nature of $2\,^1A_g^-$, $1\,^1B_u^-$, and $3\,^1A_g^-$ states are established *via* calculation of excitation energies, bond dimerisations, and exciton wavefunctions. Importantly, the $1\,^1B_u^-$ state is identified as a potential intermediate state for the internal conversion process in carotenoids.

Following the static DMRG calculations, the internal conversion process is probed dynamically using the adaptive time-dependent density matrix renormalisation group method with Ehrenfest dynamics describing the nuclear motion (tDMRG-Ehrenfest). Using the UV-Peierls (UVP) Hamiltonian, two sets of parameters are used to account for the theoretical and experimental uncertainty surrounding the ordering of excited state energies around the Franck-Condon point. Using these two sets of parameters, two internal conversion pathways are investigated, using two different carotenoids as model systems. For both pathways, for both molecules, ultrafast internal conversion of the $1\,^1B_u^+$ state to a triplet-pair state is observed within ~ 5 fs. For all simulations, a triplet-pair yield of $\sim 65\%$ is attained within ~ 50 fs. These results present the first instance of a dynamical simulation of the internal conversion process in carotenoids.

The calculation of theoretical transient spectra using Lanczos-DMRG is incorporated to the dynamical simulation scheme to relate to the available spectroscopic data. The dominant spectral features exhibit a blue shift as the nuclei relax, confirming the $1\,^1B_u^+ \rightarrow 2\,^1A_g^-$ internal conversion. Following the calculation of exciton wavefunction of the state dipole connected to the $2\,^1A_g^-$ state, these dominant transitions are assigned to the charge-transfer character of the $2\,^1A_g^-$ state.

The electron transfer process surrounding the internal conversion is scrutinised using a two-level toy model. Using the Landau-Zener theory of electronic transition, it is shown that the electronic transition during the internal conversion evolves from a non-adiabatic transition to a primarily adiabatic transition as the magnitude of the symmetry breaking increases. It is shown that for parameters relevant to carotenoids, the internal conversion process lies in the adiabatic limit.

Acknowledgements

I am deeply grateful to those who have supported and inspired me throughout the journey of writing this thesis. This serves as a recognition of those who played a significant role in making this work possible.

I wish to express my heartfelt gratitude to my supervisor, Professor William Barford, for offering me a place in his research group and accompanying me throughout my DPhil journey. The unwavering support, mentorship, and encouragement I received has been invaluable in shaping my growth as a researcher and helping me bring this thesis to completion. I am especially grateful for his patience and understanding as I navigated my way through this journey. I also wish to extend my sincerest thanks to our collaborator, Dr Jenny Clark, for elevating our research and making it more relevant and meaningful. I am sincerely grateful to Oxford Advanced Research Computing facility for their invaluable support in my research, providing both computing time and helpful troubleshooting, which have greatly contributed to the progress of my work.

I express my sincere appreciation to Professor David Logan for granting me a place in the TMCS programme at Oxford. His faith in my abilities has been a source of inspiration and I am truly appreciative of the opportunity he offered me. I am immensely grateful to Linacre College for their generous funding through the Carolyn and Franco Gianturco scholarship and their unwavering support during the pandemic. My sincerest thanks go to Mrs. Leema Chapman for her continuous support during my first year at Oxford.

During my time at the TMCS, I was fortunate to meet some great friends. I extend my heartfelt thanks to members of the fifth cohort, including Matt, Harry, Rhos, Tristan, Issy, Jack, Mike, Ava, Derek, and Shree for their warm welcome and friendship. I would also like to thank past and present members of the Barford group. In particular, I would like to express my gratitude to Darren Valentine for the guidance he provided during my early months at the Barford group. The code he developed forms the foundation of my work. I am thankful to Max Marcus for his help with DFT calculations and for sharing his knowledge of quantum chemistry teaching, and to Timothy Georges for his thorough proofreading of this thesis.

The Linacre community has given me a safe and welcoming home for the past

four years and I am grateful for the cherished friendships I have formed here. A big shout-out to Ani for always being my go-to friend, and Varnika for the delicious mango chocolate sweets, among other things. To OCT household 2 of 20/21, thank you for keeping my spirits high even during the pandemic, and for tolerating the Levon Polkka. Thomas, thank you for the thought-provoking conversations and, of course, for all the cricket memes. Thank you Zuzana for the fantastic company over the years, especially during the pandemic over delicious food.

My journey from Galle in Sri Lanka to Oxford was built on the strong foundation of constant guidance and inspiration from those close to my heart back home. To my father, you were the motivation for me to pursue science. Thank you for nurturing the skeptic in me. To my mother, thank you for the sacrifices you made for me growing up, and igniting my passion for chemistry. To my sister, who has been by my side always for the best part of my life. To my grandmother, thank you for your love and care, and looking after me throughout my formative years. To Vihanga's mother and father, thank you for your kind care and support, and making Sri Lanka feel a little less far away than it actually is. To Raji aiya and Jayani akka, thank you for the love and support and raising my wonderful niece and nephew, Liyara and Esath. A video call from them has been the highlight of most of my weeks in the UK. To Vihanga, thank you for the loving relationship we share together. Time indeed flies when you are with someone who you love. I have had the best time of my life sharing our journey from the undergraduate classes in Colombo to proper adult life in Cambridge, and I cannot wait to see what the future holds for us.

While I was pursuing my DPhil in Oxford, my fellow citizens in Sri Lanka faced some difficult times. The country, which was reeling from the impact of the Easter bombings, was further devastated by the pandemic. Everything escalated in the March of 2022. The economy collapsed, and many people struggled to make ends meet. The horrific stories of people dying while queuing for fuel still resonate in my mind. My compatriots did not deserve this. Sri Lanka is a beautiful country with beautiful people. This thesis is dedicated to the people of Sri Lanka. Thank you for funding the education I received. I wish that Sri Lanka will emerge from these difficulties, stronger and more united than ever.

Abbreviations

ADC	Algebraic Diagrammatic Construction
BO	Born-Oppenheimer
BOW	Bond Order Wave
CASSCF	Complete Active Space Self Consistent Field
CDW	Charge Density Wave
COM	Centre Of Mass
CI	Configuration Interaction
CT	Charge Transfer
DFT	Density Functional Theory
DPH	Diphenylhexatriene
DMRG	Density Matrix Renormalisation Group
FSSH	Fewest Switches Surface Hopping
HOMO	Highest Occupied Molecular Orbital
LGS	Low Gap Semiconductor
LUMO	Lowest Unoccupied Molecular Orbital
MCSCF	Multi Configuration Self Consistent Field
MMVB	Molecular Mechanics-Valence Bond
MPS	Matrix Product State
NEVPT	n-Electron Valence Perturbation Theory
NRG	Numerical Renormalisation Group
PCE	Power Conversion Efficiency
PES	Potential Energy Surface
PPP	Parsier-Pople-Parr model
PPPP	Parsier-Pople-Parr-Peierls Model
PV	Photovoltaic
SCF	Self Consistent Field
SF	Singlet Fission
SDW	Spin Density Wave
TD-DFT	Time Dependent Density Functional Theory
tDMRG	Adaptive Time Dependent Density Matrix Renormalisation Group

SVD	Singular Value Decomposition
TDSCF	Time Dependent Self Consistent Field
TDSE	Time Dependent Schrödinger Equation
TEBD	Time Evolved Block Decimation
UVP	UV-Peierls Hamiltonian

Publications

The work presented in this thesis forms the basis of the following publications:

- **Chapters 3 and 6:** Manawadu, D.; Valentine, D. J.; Barford, W. Dynamical Simulations of Carotenoid Photoexcited States Using Density Matrix Renormalization Group Techniques. *J. Phys. Chem. A* **2023**, *127*, 3714–3727
- **Chapter 4:** Valentine, D. J.; Manawadu, D.; Barford, W. Higher energy triplet-pair states in polyenes and their role in intramolecular singlet fission. *Phys. Rev. B* **2020**, *102*, 125107
- **Chapter 5:** Manawadu, D.; Valentine, D. J.; Marcus, M.; Barford, W. Singlet Triplet-Pair Production and Possible Singlet-Fission in Carotenoids. *J. Phys. Chem. Lett.* **2022**, *13*, 1344–1349
- **Chapter 5:** Manawadu, D.; Georges, T. N.; Barford, W. Photoexcited State Dynamics and Singlet Fission in Carotenoids. *J. Phys. Chem. A* **2023**, *127*, 1342–1352

Contents

Declaration of Authorship i
Abstract ii
Acknowledgements iv
Abbreviations vi
Contents x

1 Introduction **1**
1.1 Solar Cells and the Detailed-Balance Limit 2
1.2 Singlet Fission Photovoltaic Devices 3
1.3 Mechanism of Singlet Fission in Carotenoids 5
1.4 Polyene Excited States and Internal Conversion 6
1.5 Studies of Polyene Internal Conversion 11
1.6 Aims of this Thesis 15

2 Theoretical Background **18**
2.1 The Many Body Hamiltonian 18
2.2 The Born-Oppenheimer Hamiltonian 20
2.2.1 Second Quantisation 23
2.2.2 Effective π-Electron Born-Oppenheimer Hamiltonian 24
2.3 Electron-Nuclear Interactions 27
2.3.1 Electron-Nuclear Coupling 27
2.3.2 Nuclear Potential Energy 29
2.3.3 The Peierls model 30
2.4 π-Electron Theories of Conjugated Polymers 31
2.4.1 Hückel Model 31
2.4.2 Pariser-Parr-Pople Model 32
2.4.3 UV Model 34
2.5 Symmetries 34
2.5.1 Spatial Symmetries 35
2.5.2 Electron-Hole Symmetry 36
2.6 Eigenstates of the Dynamical Hamiltonian 37
2.7 Non-adiabatic Dynamics 39

2.7.1 Standard Born-Oppenheimer Molecular Dynamics 40
2.7.2 Ehrenfest Method 41
2.7.3 Surface Hopping 44
2.7.4 TEBD-Ehrenfest 47

3 Computational Methods **52**
3.1 Density Matrix Renormalisation Group (DMRG) 52
3.1.1 Numerical Renormalisation Group (NRG) 53
3.1.2 Static DMRG algorithm 54
3.1.3 Adaptive Time-Dependent DMRG (tDMRG) 63
3.1.4 Lanczos-DMRG 66
3.1.5 DMRG and Entanglement Entropy 71
3.1.6 DMRG and Matrix Product States (MPS) 72
3.2 Ehrenfest Dynamics 75
3.2.1 Hellmann-Feynman technique 75
3.2.2 Initial conditions 77
3.2.3 tDMRG-Ehrenfest Algorithm 77
3.3 Parametrising $\hat{H}_\epsilon$ 78

4 Carotenoid Excited States **80**
4.1 Theoretical Studies of Polyene Excited States 80
4.2 Polyene Excited States 83
4.2.1 Undimerised Polyenes with Noninteracting Electrons 83
4.2.2 Broken Symmetries 87
4.2.3 Dimerised Chains with Noninteracting Electrons - Peierls Distortion and Solitons 88
4.2.4 Interacting Electrons 94
4.3 Triplet-Pair States in Polyenes 103
4.3.1 Excitation Energies 103
4.3.2 Soliton Structures 105
4.3.3 Exciton Wavefunctions 106
4.4 Conclusions 108

5 Singlet Triplet-Pair Production via Internal Conversion **109**
5.1 Parametrisation of the UV-Peierls Hamiltonian 110
5.1.1 Internal Conversion via the $1\,^1B_u^-$ State 110
5.1.2 Direct $1\,^1B_u^+ \rightarrow 2\,^1A_g^-$ Internal Conversion 112
5.2 Internal Conversion via the $1\,^1B_u^-$ State 115
5.2.1 Numerical Results for Zeaxanthin 115
5.2.2 Numerical Results for Neurosporene 120

5.3 Direct $1\,^1B_u^+ \rightarrow 2\,^1A_g^-$ Internal Conversion . . . 124
5.4 Transient Spectra Calculations . . . 128
5.5 Conclusions . . . 132

Appendices **134**
5.A Symmetry Breaking Hamiltonians . . . 134
5.A.1 Zeaxanthin . . . 134
5.A.2 Neurosporene . . . 135
5.B Accuracy and Convergence Analysis . . . 136
5.B.1 Truncation Error and Entanglement Entropy . . . 136
5.B.2 Trotter Error . . . 137
5.C Comparison with Static DMRG Calculations Based on the Hellmann-Feynman Theorem . . . 138
5.D Accuracy of Lanczos-DMRG Calculations . . . 139

6 Approximate Two Level Dynamics **141**
6.1 Two-Level Quantum System . . . 141
6.2 Landau-Zener Theory of Electronic Transitions . . . 143
6.3 Landau-Zener-Like Transition . . . 148
6.4 Conclusions . . . 152

7 Conclusions and Future Work **153**
7.1 Conclusions . . . 153
7.2 Future Work . . . 155

Bibliography **158**

Chapter 1

Introduction

Carotenoids are one of the most abundant classes of pigments found in nature, with over 1100 distinct structures reported.[5] They are derived from tetraterpenes, and contains eight isoprene units and therefore 40 carbon atoms. Carotenoids can be classified into two classes, xanthophylls (which contain oxygen) and carotenes (which are hydrocarbons). Carotenoids are produced naturally by all photosynthetic organisms (including plants and algae), and some non-photosynthetic organisms.[6] In physiological systems, they have varied functions including enhancing vision by quenching singlet oxygen and other radicals,[7] serving as an antioxidant by scavenging cation radicals,[8] enhancing immune functions,[9] and acting as anti-cancer agents.[10]

As shown in Fig. 1.1, carotenoids possess a conjugated polyene backbone usually

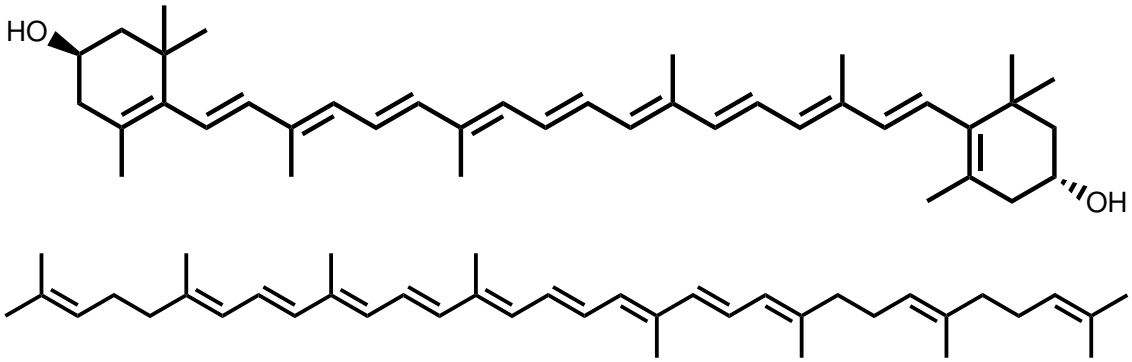

Figure 1.1: Structural formula of zeaxanthin, a xanthophyll (top) and neurosporene, a carotene (bottom). All carotenoids contain 40 carbon atoms, but the number of carbon atoms in the π-conjugated polyene backbone can vary.

of lengths between 18 to 26 carbon atoms (or 9 to 13 C-C double bonds), which gives rise to their bright yellow, orange, and red colours due to the strong absorption of visible light in the blue-green region.[11] This region is not accessible to chlorophylls, and therefore carotenoids found in photosynthetic systems can enhance their light harvesting properties and protect the light harvesting (chlorophyll) complexes from excess light.[12–14] Due to these crucial functions in photosynthetic systems, the study of carotenoid photoexcited state properties has gained considerable attention.

The study of the photophysics of carotenoids is also motivated by their potential to be utilised as efficient singlet fission (SF) materials in photovoltaic (PV) devices. Singlet fission is a photophysical process by which a singlet photoexcited state (labelled S_n) dissociates into two spin uncorrelated triplets (labelled T_1).[15] The coupling of SF materials to low-gap-semiconductors (LGS) is known to increase the efficiency of photovoltaic (PV) devices, and therefore is a major interest in the search for efficient renewable energy sources. To explain how carotenoids can increase the power conversion efficiency (PCE) of solar cells, thermodynamic loss mechanisms which limit the maximum PCE must be understood. In Section 1.1, we describe the detailed-balance limit, which sets an upper bound on the efficiency of single absorber PV devices, and in Section 1.2, we describe how incorporating SF materials to single absorber cells can help overcome this limit. The proposed mechanistic model of SF in carotenoids is described in Section 1.3.

1.1 Solar Cells and the Detailed-Balance Limit

The efficiency of PV devices is determined by the thermodynamics of converting solar energy to useful forms of work. This efficiency is constrained by a detailed balanced limit.[16,17] Consider a conventional single absorber silicon solar cell with an energy band gap $E_g \approx 1.1$ eV. There are four loss mechanisms that limit the

efficiency of this solar cell.[18,19]

1. Incomplete absorption: Photons with energy less than E_g are not absorbed.

2. Thermalisation: For photons with energy in excess of E_g, only the energy that corresponds to the silicon band-gap (E_g) is absorbed. The rest is lost as thermal energy.

3. Thermodynamic loss: Due to fundamental thermodynamic losses based on Carnot's theorem, the open circuit voltage of a PV device is always less than E_g.[20]

4. Radiative recombination: A small fraction of the excited states (S_2) decay radiatively to the ground state (S_0) through spontaneous emission.

A detailed-balance limit imposes a theoretical upper bound to the power conversion efficiency (PCE) of a silicon solar cell of 29%,[21] and the greatest PCE achieved in an experimental setting is 26.7%.[22] By optimising the bandgap $E_g = 1.4$ eV for the solar spectrum, the maximum achievable PCE for a single-junction solar cell is 33%.[20]

In single absorber PV devices, thermalisation is the dominant efficiency loss mechanism.[23] Multi-junction PV device architectures[20] and carrier multiplication processes, where a single photon generates multiple charge carriers, are suggested to overcome thermalisation losses. In organic semiconductors, SF promises to be a premier carrier multiplication process which can offset the thermalisation losses and overcome the theoretical upper bound set by the detailed-balance limit.

1.2 Singlet Fission Photovoltaic Devices

SF materials produce two triplet excitations per absorbed photon. For efficient SF materials, the energy of the triplets, E_{T_1}, is roughly half the energy of the

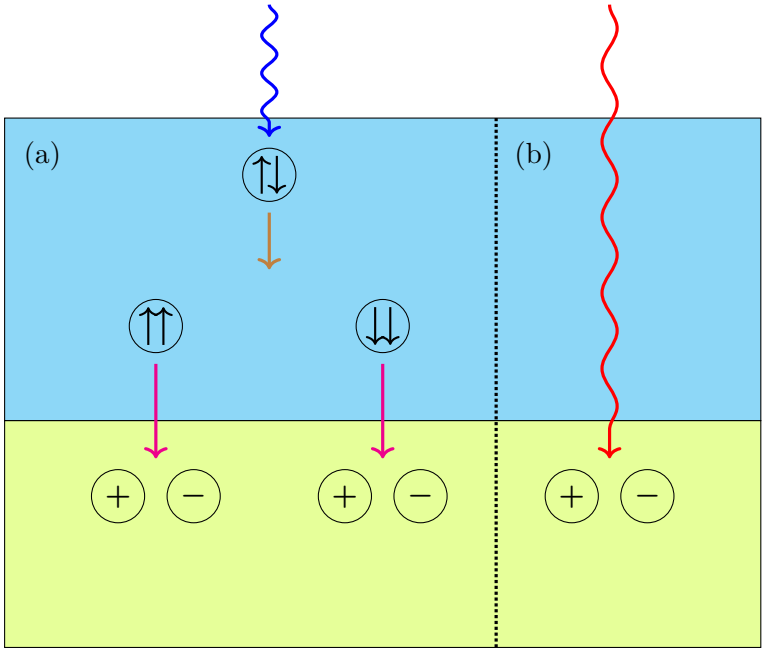

Figure 1.2: Schematic diagram illustrating a composite singlet fission PV device made by coupling a SF material (cyan) with bandgap $\approx 2E_g$ to a single absorber semiconductor (lime) with bandgap $\approx E_g$. (a) High energy photons (blue), with $h\nu > 2E_g$ are absorbed by the SF layer, forming the initial singlet photoexcited state S_n. S_n evolves into two triplets via SF (brown arrow). These triplets can each generate an electron hole pair in the semiconductor (magenta arrows). (b) Low energy photons with $E_g < h\nu < 2E_g$ pass through the (transparent) SF layer and are absorbed by the semiconductor, generating a single electron hole pair per photon absorbed.

photoexcited state, E_{S_n}. Therefore, compared to a single absorber PV device with the same bandgap, SF materials alone will produce twice the current at half its open circuit voltage, and no gain in PCE is achieved.[23]

To make progress, SF materials are combined with low-gap-semiconductor (LGS) materials.[24] These have bandgaps at half the value of the bandgap of the SF materials coupled to them, i.e., $E_g \approx E_{S_n}/2 \approx E_{T_1}$. The high energy photons reaching the PV device are absorbed by the SF materials, which produces two triplet excitations per incident photon. Photons with energy below the SF material bandgap pass through the SF material and are absorbed by the LGS, producing a single charge carrier. The open circuit potential of the device is determined by the LGS material, and the SF material acts to minimise the thermalisation losses. This process is illustrated in Fig. 1.2. For silicon solar cells with $E_g = 1.1$ eV, coupling to a single SF material

improves the theoretical upper bound of PCE from 29% to 35%.[23] Calculations show that using two SF materials with different bandgaps connected serially, a composite tandem PV device with a PCE of 45.7% can be achieved.[19]

1.3 Mechanism of Singlet Fission in Carotenoids

Understanding the mechanism of carotenoid singlet fission is important to unravelling the complex light-matter interactions of light harvesting complexes, as well as for production of PV devices with high efficiencies. Evidence for carotenoids undergoing SF was first reported in 1980.[25] SF is expected to proceed via the two-step Merrifield kinetic model,[26]

$$1\,{}^1B_u^+ \rightleftharpoons\ {}^1(TT) \rightleftharpoons T_1 + T_1. \tag{1.1}$$

In carotenoids, the first step of singlet fission is understood to be the internal conversion from the photoexcited $1\,{}^1B_u^+$ state to a correlated singlet triplet-pair state, ${}^1(TT)$. This is a spin-allowed process, and proceeds on ultrafast timescales ($\sim$ 100 fs). The role of triplet-pair states in SF has been extensively reviewed.[27,28] ${}^1(TT)$ is a dark state which is not optically accessible from the ground state, but it serves as an important intermediate for the SF mechanism as the rate of SF is determined by the coupling between the ${}^1(TT)$ and $1\,{}^1B_u^+$ states. ${}^1(TT)$ retains the spin information of the initial photoexcitation, which is subsequently lost when the two uncorrelated triplets are formed following the second step of the SF process.

The primary focus of this thesis is to understand the internal conversion process, the first step of the above mechanism, in the context of carotenoids. As the polyene backbone of carotenoids give rise to their photophysical features, experimental and theoretical studies explain the carotenoid excited states and internal conversion by investigating the excited state properties of polyenes. We review these studies in

Sections 1.4 and 1.5. The second step of the SF process, i.e., how the triplet-pair state generated via internal conversion loses its spin coherence to generate uncorrelated triplets, is a major research interest in carotenoid photophysics in itself. A critical research problem is whether this second step in carotenoids is intra- or intermolecular. In our recent work on this problem, we showed that carotenoids in distorted ground state geometries can undergo intermolecular exothermic SF.[4]

Fast intermolecular singlet fission has been observed in carotenoid aggregates.[29–31] In these aggregates, it is proposed that intermolecular singlet fission can proceed directly via the $1\,^1B_u^+$ state, without undergoing internal conversion to an intermediate $^1(TT)$ state.[31] Refs [15] and [32] provide extensive reviews of singlet fission in organic materials, while ref [33] reviews singlet fission from a theoretical standpoint.

1.4 Polyene Excited States and Internal Conversion

The quasi-one-dimensional nature of polyenes enhances the electron-electron interactions and electron-nuclear coupling, and is the cause for their complex excited state structure. Interaction of light excites polyenes from the ground state to a strongly dipole allowed 'bright' state, which is denoted by the symmetry label $1\,^1B_u^+$. The labelling of polyene excited states using their symmetries is described in Section 2.5.1.

One of the striking features of the complex excited state structure of polyenes is the presence of symmetry forbidden 'dark' states with energies comparable to the bright state, and therefore could be involved in the photophysical processes. In 1972, in the first important breakthrough in the study of polyene photoexcited states it was demonstrated via experiments of Hudson and Kohler[34] and theoretical analysis of Schulten and Karplus[35] that there exists a dark excited state, labelled $2\,^1A_g^-$, below

the photoexcited $1\,^1B_u^+$ state. Calculations of Schulten and Karplus predicted that for polyenes with conjugation length $n \geq 2$, the $2\,^1A_g^-$ state is below the $1\,^1B_u^+$ state. Hudson and Kohler confirmed the observation of Schulten and Karplus for $n = 4$, by investigating absorption and emission properties of α,ω-diphenyloctatetraene. Subsequent experiments using transient absorption spectroscopy have led to direct observation of the $2\,^1A_g^-$ state in other polyenes.[36–39] This discovery led to denoting the $1\,^1B_u^+$ state as S_2, the lowest energy dark excited state $2\,^1A_g^-$ as S_1, and the ground state as S_0 or $1\,^1A_g^-$ in carotenoid photophysics literature.

A second breakthrough in the study of polyene photophysics came in 1987, when it was shown via a theoretical study that for polyenes with $n > 8$, the energy of the $1\,^1B_u^-$ state falls within the $S_2 - S_1$ gap.[40] In 2002, Cerullo and co-workers presented the first direct experimental evidence for the signatures of intermediate states following photoexcitation via pump-probe time resolved spectroscopy.[41] Upon photoexcitation to the S_2 state, these states can serve as intermediary states on the internal conversion pathway.

The first evidence for the role of intermediate states in the internal conversion process was presented by Frank *et al.*, where it was shown via calculations on a series of spheroidene analogues that the internal conversion rates do not follow the energy gap law.[42] The energy gap law states that for nonradiative transitions, the rate of transmission decays exponentially with the energy gap of the initial and the final states.[43] Their work showed that while the $S_2 - S_1$ gap increases as a function of conjugation length from $n = 7$ to $n = 13$, the rate of internal conversion reaches a minimum at $n = 9$. This observation was soon confirmed experimentally by a study of a series of carotenoids with conjugation lengths ranging from $n = 5$ to $n = 13$ using femtosecond fluorescence up-conversion.[44] Transient absorption measurements performed by Cerullo and co-workers revealed that for longer carotenoids with $n > 8$,

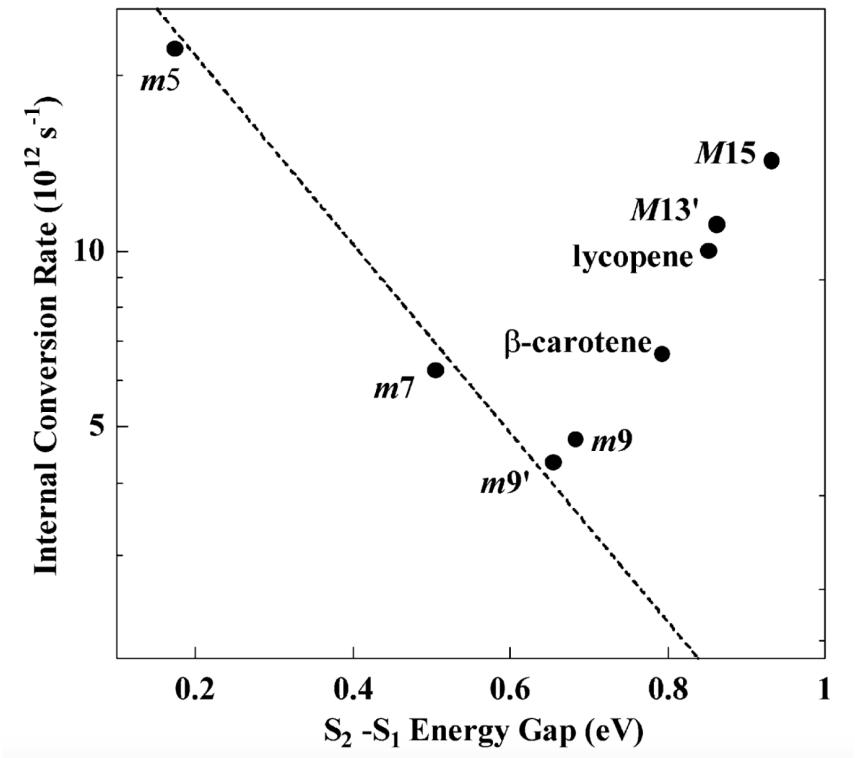

Figure 1.3: Internal conversion rates from the S_2 state as a function of the $S_2 - S_1$ energy gap. The dashed line shows the best fit for the energy gap law for the short carotenoids $m5$ ($n = 5$), $m7$ ($n = 9$) and $m9'$ ($n = 9$). Longer carotenoids β-carotene (effective $n = 9$), lycopene ($n = 11$), $M13'$ ($n = 13$), and $M15$ ($n = 15$) do not follow the energy gap law. Reproduced with permission from Kosumi, D.; Yanagi, K.; Fujii, R.; Hashimoto, H., et al. Conjugation length dependence of relaxation kinetics in β-carotene homologs probed by femtosecond Kerr-gate fluorescence spectroscopy. *Chem. Phys. Lett.* **2006**, *425*, 66–70.

the S_2 state can evolve dynamically to an intermediate dark state, which explains the non-monotonic behaviour of the rate of internal conversion as a function of n.[41,45] Kosumi *et al.* resolved the decay kinetics of the S_2 state using femtosecond Kerr-gate fluorescence spectroscopy and confirmed that the $S_2 \rightarrow S_1$ internal conversion process violated the energy gap law for carotenoids with $n > 8$.[46]

Several theoretical and experimental studies have attempted to characterise the nature and the symmetries of these intermediary dark states. Early calculations of Tavan and Schulten,[40] as well as recent theoretical calculations[47,48] suggest that the $1\,^1B_u^-$ state lies below the S_2 state for $n > 4$. Koyama, Kobayashi, and their co-workers performed extensive transient absorption experiments on a series of all-*trans* carotenoids with $n = 9 - 13$.[49] They found that the internal conversion of

neurosporene ($n = 9$) and spheroidene ($n = 10$) indicate a pathway mediated by the $1\,^1B_u^-$ state. For longer carotenoids lycopene ($n = 11$), anhydrorhodovibrin ($n = 12$), and spirilloxanthin ($n = 13$), they found that the high lying $3\,^1A_g^-$ state can also be involved, giving rise to complex internal conversion pathways.[50–53] Intermediate dark states that can be populated via internal conversion from the S_2 state is reviewed in ref [54].

While the anomalous non-monotonic behaviour of the $S_2 \rightarrow S_1$ internal conversion rate constant with n can be explained by invoking intermediary dark states, certain transient absorption features related to the ultrafast dynamical processes in the timescales of internal conversion cannot be satisfactorily described as absorptions from the $1\,^1B_u^-$ state.[55] Additionally, non-linear time-resolved experiments cast doubt over the need to involve an intermediary state to explain the internal conversion process. For instance, four-wave mixing spectroscopy experiments on excited state dynamics of β-carotene, a carotenoid with 9 effective carbon-carbon double bonds, revealed that the mechanism can be explained without involving intermediate states.[56] Transient grating experiments performed on lycopene ($n = 11$) and astaxanthin (effective $n = 9$) further support this direct internal conversion mechanism.[57] Very recent *ab initio* calculations of polyene excited states argue that for carotenoids with effective $n \leq 13$, the photoexcited state $1\,^1B_u^+$ is the lowest lying excited state at the Franck-Condon point.[58,59] As the $2\,^1A_g^-$ state couples to the nuclei more strongly than the $1\,^1B_u^+$ state, nuclear reorganisation following photoexcitation can facilitate a direct internal conversion process, without needing to invoke the intermediate dark states. The two proposed internal conversion mechanisms are illustrated in Fig. 1.4.

In conclusion, disputes over the relative ordering of the singlet excited states and the role of intermediary states in internal conversion has transformed internal

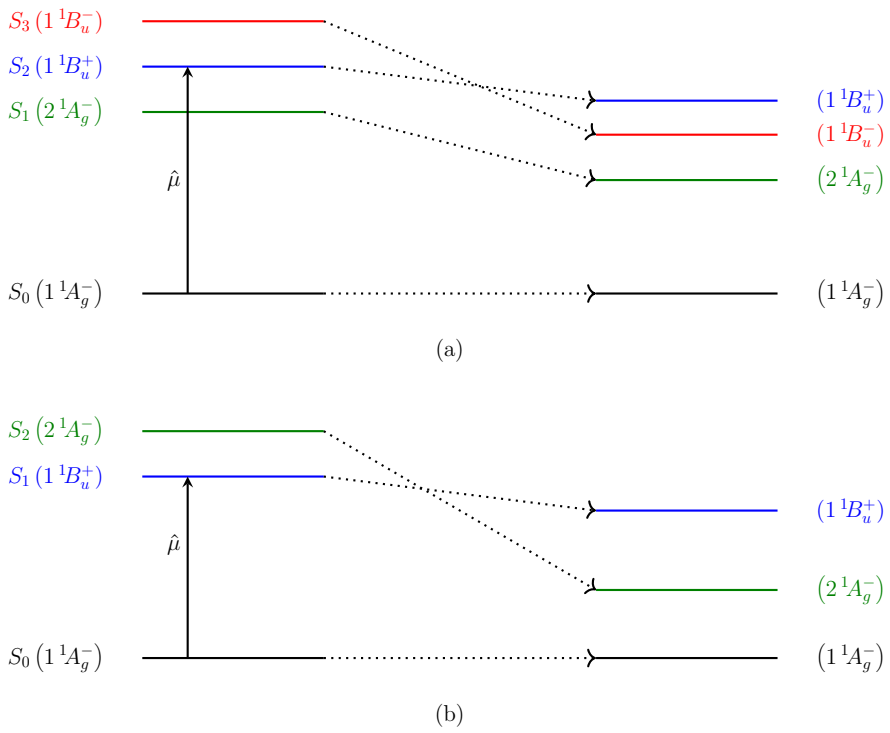

Figure 1.4: Two proposed mechanisms of internal conversion in polyenes. (a) Internal conversion via the intermediary $1\,^1B_u^-$ state. The initial photoexcited $1\,^1B_u^+$ state (blue) is above the $2\,^1A_g^-$ state (green), and below $1\,^1B_u^-$ state (red), at the Franck-Condon point. As the nuclei relaxes, the energy of the $1\,^1B_u^-$ state falls below the energy of the $1\,^1B_u^+$ state as $1\,^1B_u^-$ state couples to the nuclei stronger than the $1\,^1B_u^+$ state. This allows internal conversion to the $1\,^1B_u^-$ state. Subsequent internal conversion from the $1\,^1B_u^-$ state results in the occupation of the $2\,^1A_g^-$ state. (b) Direct internal conversion. The initial photoexcited $1\,^1B_u^+$ state (blue) is below the $2\,^1A_g^-$ state (green) at Franck-Condon point. $2\,^1A_g^-$ state couples more strongly to the nuclei compared to the $1\,^1B_u^+$ state, and as a consequence the energies of the two states cross along the nuclei relaxation pathway. This allows direct internal conversion of the photoexcited $1\,^1B_u^+$ state to the $2\,^1A_g^-$ state.

conversion of the photoexcited state of carotenoids to an important research problem in polyene photophysics. In Section 1.5, we present some of the experimental studies of the internal conversion processes in polyenes and carotenoids.

1.5 Studies of Polyene Internal Conversion

As described in Section 1.2, controlling the energy of the S_1 state is important for the production of efficient SF materials. The energies of polyene excited states mainly depend on the length of the hydrocarbon chain. Via time-resolved and steady-state fluorescence studies, Bachilo *et al.* studied the variation of the S_1 and S_2 state energies of short polyenes up to $n = 7$ and showed the energies of both states can be fitted to an equation of the form

$$E_i \approx E_i^0 + \frac{\alpha}{\sqrt{n + \Delta n}}, \tag{1.2}$$

where E_i is the energy of the state S_i, and $E_i^0, \alpha, \Delta n$ are fitting parameters.[60] For longer carotenoids with $n = 9 - 13$, carotenoid excited state energies are inversely proportional to the conjugation length n.[61] As n increases, the excitation energy of the covalent state, S_1, falls faster than the excitation of the ionic state, S_2, and therefore the $E_2 - E_1$ energy gap increases with n.[62] A schematic diagram illustrating the variation of the energies of the S_1 and S_2 states with the conjugation length n is shown in Fig. 1.5.

The initial photoexcitation is described by the S_2 state. For polyenes with $n < 9$, $S_2 \rightarrow S_1$ internal conversion follows the energy gap law, and therefore as a consequence the lifetime of the S_2 state increases with increasing n. It follows that for sufficiently long polyenes that undergo direct $S_2 \rightarrow S_1$ internal conversion, $S_2 \rightarrow S_0$ fluorescence emission is observed.[60] Meanwhile, the energy gap between S_0

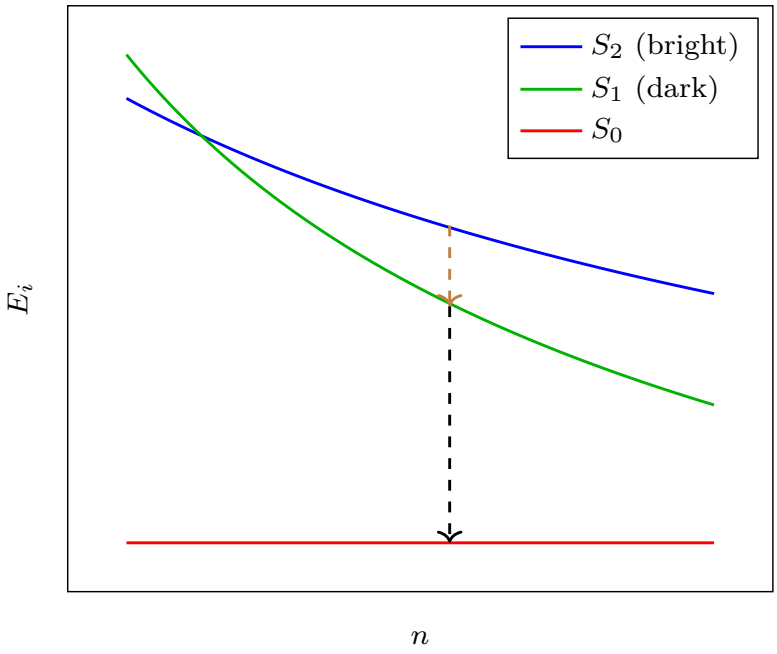

Figure 1.5: Schematic diagram of the variation of ground state and the first two excited state energies of polyenes as a function of conjugation length n. $S_2 \rightarrow S_1$ (direct) internal conversion is denoted by the brown dashed arrow. As n increases, the energy gap between S_2 and S_1 states increase, and therefore the S_2 lifetime increases. As a consequence, polyenes with $n > 3$ can exhibit fluorescence from the S_2 state.[60] As n increases, $E_1 - E_0$ decreases and therefore the $S_2 \rightarrow S_1$ internal conversion rate (shown by the black dashed arrow) increases, and therefore the S_1 lifetime decreases.[60,63]

and S_1, $E_1 - E_0$, decreases with increasing n. From the energy gap law it follows that the rate of internal conversion to the ground state, i.e., $S_1 \rightarrow S_0$, increases with n. Thus, the lifetime of the S_1 state decreases as a function of n. This trend has been observed for short polyenes,[60] carotenoid derivatives with $n = 7 - 10$,[63] and xanthophyll carotenoids with $n = 11 - 13$.[64]

Fluorescence of organic molecules generally follow Kasha's rule, which states that as a consequence of the fast internal conversion and vibrionic relaxation from higher lying excited states, fluorescence is observed only from the the lowest lying singlet excited state, i.e., S_1.[65] However, as seen above, polyenes with sufficiently long conjugation can show emission from the S_2 state, violating Kasha's rule.[60,66] Anti-Kasha fluorescence has been observed for carotenoids of varying conjugation lengths.[42,67–70] Using an all-*trans* polyene with $n = 9$ (shown in Fig. 1.6) and $n = 11$, Catalán and co-workers devised Kasha-type systems where fluorescence

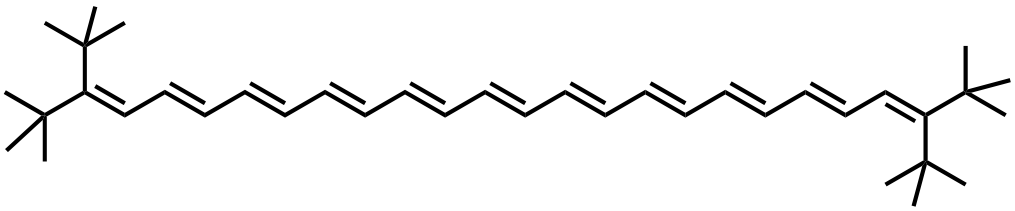

Figure 1.6: Structural formula of ttbP9,[71] a polyene with a conjugation length of $n = 9$ and four *tert*-butyl end groups. Presence of methyl groups at the terminal atoms is known to reduce the energy of the bright state.[73] Fluorescence signals characteristic of the $2\,^1A_g^-$ state of long linear polyenes is not detected in ttbP9. This is attributed to $1\,^1B_u^+$ state being the lowest singlet excited state of ttbP9.

from the $2\,^1A_g^-$ state is not observed.[71,72] They concluded that the first singlet state in these molecular systems is the $1\,^1B_u^+$ state.

Carotenoid photophysics in solution is affected by the interactions between the carotenoids and solvent molecules. Solvent effects are specifically pronounced in carotenoids with conjugated carbonyl groups.[61] Frank and co-workers demonstrated that the lifetime of the S_1 state of peridinin diminishes greatly in strongly polar solvents.[74] They explained the solvent dependence via the presence of a low-lying charge-transfer (CT) state which lies above the S_1 state in nonpolar solvents. This state is stabilised by polar solvents, and for sufficiently polar solvents it lies below the S_1 state and quenches fluorescence from the S_1 state. This change of energy level ordering is illustrated in Fig. 1.7. Via a comparative study, the same authors showed that this reduction of the S_1 lifetime is observed only for carotenoids containing carbonyl functional groups.[75] Similar reduction of S_1 lifetimes were found for carotenoid aldehyde derivatives,[76,77] and recently for shorter carotenoids comprised of lactone rings with $n = 7 - 8$ conjugated double bonds.[78]

The energy of the optically active S_2 state of carotenoids in solution depends on the refractive index of the solvent, which in turn depends on the polarisability of the solvent. As the solvent polarisability increases, the excitation energy of the S_2 state is red shifted.[79] Excitation energy of the dark S_1 state is largely unaffected by solvent polarisability,[79] and therefore the $E_2 - E_1$ energy gap decreases as solvent

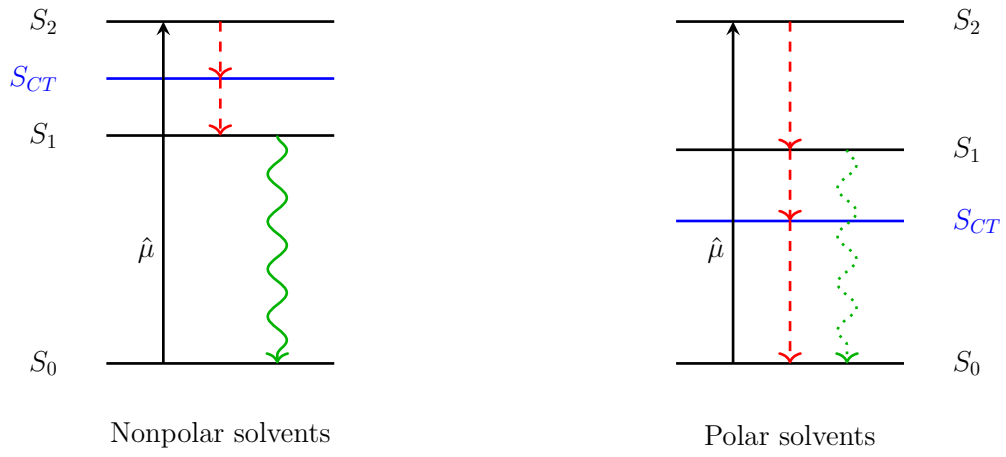

Figure 1.7: Energy level diagram of relative ordering of low-lying excited states in nonpolar and polar solvents.[74] The CT state (S_{CT}, shown in blue) is above the S_1 state in nonpolar solvents, and cannot quench fluorescence (illustrated by the green arrows) from the S_1 state. CT states are stabilised by solvent polarity, and therefore in polar solvents S_{CT} can fall below the S_1 state. In such solvents, S_{CT} can quench fluorescence from the S_1 state via rapid internal conversion, and reduce S_1 lifetimes significantly. The dotted red arrows show the internal conversion pathways.

polarisability increases. It is therefore expected that the rate of $S_2 \rightarrow S_1$ will increase with the solvent polarisability, and Andersson *et al.* demonstrated this phenomenum for all *trans* carotenes with $n = 7 - 8$.[68]

The study of carotenoid systems in the gas phase, devoid of solvent interactions, has been attempted. Gavin *et al.* reported the first study of all-*trans* octatetraene in gas phase, and showed that the fluorescence emission in gas phase occurs from the $1\,^1B_u^+$ state, as opposed to from the $2\,^1A_g^-$ state in solution.[80] Gas phase studies of $1\,^1B_u^+ \leftarrow 1\,^1A_g^-$ transition of all-*trans* octatetraene were reported via coupling of jet cooling to fluorescence spectroscopy,[81] and to direct ultraviolet absorption spectroscopy.[82] Gas phase fluorescence characteristics of short polyenes with $n = 4 - 5$ has demonstrated anti-Kasha behaviour.[83]

The study of polyene photophysics is also inspired by the need to understand photoexcitation processes of retinal. Retinal is a small polyene ($n = 6$) found in the photoreceptor cells of the retina. Its structural formula is shown in Fig. 1.8. Photoisomerisation of 11-*cis* retinal to all-*trans* retinal forms the foundation of vision

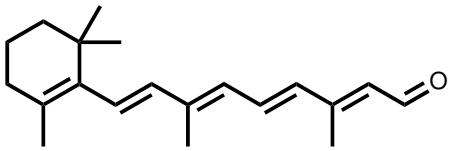

Figure 1.8: Structural formula of retinal, a short polyene found in photoreceptor cells of the retina.

in retinal cells.[84] Early studies of retinal measured the photoisomerisation quantum yields of retinal isomers and related short polyenes.[85–88] Photoisomerisation of retinal in photoreceptor cells creates a Schiff base linkage. Becker and Freedman studied the photoisomerisation process of the Schiff base and the protonated Schiff base of the 11-*cis* retinal.[89] They found that as solvent polarity increases, the $1\,^1B_u^+$ state mixes with the $2\,^1A_g^-$ state, and in the protonated form the lowest lying excited state is of B_u character. Ultrafast $S_2 \rightarrow S_1$ internal conversion has been observed in all-*trans* retinal in protonated Schiff base form.[90] By modifying the backbone substituents of retinal protonated Schiff bases, Bassolino *et al.* managed to achieve drastic improvements of excited state lifetimes and photoisomerisation quantum yields.[91]

1.6 Aims of this Thesis

Understanding the dynamical processes of the photoexcited states of carotenoids is important for the development of efficient photovoltaic devices, as well as for elucidating the light harvesting mechanisms of photosynthetic systems. Internal conversion of the photoexcited state to a triplet-pair state is the first step, and a key step, of the dynamical relaxation process. However, there is still considerable debate surrounding the mechanism of this internal conversion process. In this work, we aim to develop a dynamical simulation scheme to accurately describe the photoexcited state internal conversion process of carotenoids.

The dynamical simulation scheme is built up from several theoretical techniques,

which are described in detail in Chapter 2. Starting from the Born-Oppenheimer Hamiltonian, we derive several effective π-electron models utilised to describe excited states of polyenes. We describe the eigenstates of the model Hamiltonians used in this work and the symmetries that are relevant for the description of those eigenstates. This chapter also introduces some of the non-adiabatic dynamics methods relevant to the work presented in this thesis.

The numerical simulations performed in this thesis are based on density matrix renormalisation group (DMRG) techniques. DMRG is a highly efficient numerical algorithm to describe one-dimensional quantum systems, such as the π-conjugated electrons of carotenoids. Chapter 3 introduces several variants of DMRG which are employed in subsequent chapters to analyse the carotenoid excited states. Chapter 3 will also introduce the Ehrenfest dynamical scheme, the numerical technique used to model nuclear dynamics for the results presented in this thesis.

We examine the excited states of carotenoids in Chapter 4. After a short review of the theoretical techniques employed for modelling polyene (carotenoid) excited states, we describe the symmetries that define these excited states. The nature of the carotenoid excited states are described in the manifold of fundamental excitations of π-conjugate systems, i.e., solitons, spinons, magnons, and excitons. The second part of this chapter reviews a published article on the nature of the polyene triplet-pair states.

Chapter 5 presents the results of our dynamical simulations. After describing the parametrisation of the model Hamiltonians, we model the dynamical relaxation of two carotenoids using two parameter regimes that correspond to two different internal conversion pathways. We present our results for the theoretical transient spectra calculations, and use it to describe the microscopic mechanism of direct internal conversion.

The carotenoid internal conversion process can be understood as an approximate two-level system. Within this framework, we look at the internal conversion process as a Landau-Zener type transition in Chapter 6.

The thesis concludes with a summary of results, and an outlook at the future research avenues in Chapter 7.

Chapter 2

Theoretical Background

This chapter aims to provide a brief overview of the theoretical techniques used to investigate the internal conversion process in carotenoids. The many body Hamiltonian which governs the physics of carotenoid systems is too complex to be solved in its full form, and certain approximations are required. A common approximation scheme is to use effective π-electron models to describe the photophysics of polyene systems. This chapter introduces the effective π-electron models used in this thesis, starting with the Born-Oppenheimer approximation and then introducing the electron-nuclear interactions explicitly. The eigenstates and the symmetries of the model Hamiltonians are introduced. Accurate description of transitions between excited electronic states in polyenes requires methods that go beyond the adiabatic approximation, and the chapter concludes with a discussion of some of the non-adiabatic techniques relevant to this work.

2.1 The Many Body Hamiltonian

The many body Hamiltonian of a system with interacting electrons and nuclei is given by

$$\hat{H} = \hat{H}_{n-n}(\{\mathbf{R}\}) + \hat{H}_{e-e}(\{\mathbf{r}\}) + \hat{H}_{e-n}(\{\mathbf{r}\},\{\mathbf{R}\}), \tag{2.1}$$

where $\{\mathbf{R}\}$ is the set of nuclear coordinates and $\{\mathbf{r}\}$ is the set of electronic coordinates. The nuclear-nuclear interaction term,

$$\hat{H}_{n-n}(\{\mathbf{R}\}) = \sum_{\alpha} \frac{P_{\alpha}^2}{2M_{\alpha}} + \frac{1}{2} \sum_{\alpha \neq \beta} \frac{Z_{\alpha} Z_{\beta} \mathrm{e}^2}{4\pi\epsilon_0 |\mathbf{R}_{\alpha} - \mathbf{R}_{\beta}|}, \tag{2.2}$$

describes the kinetic energy of the nuclei and the Coulomb repulsions between the nuclei. P_{α}, M_{α}, Z_{α}, and $\mathbf{R}_{\alpha}$ denote the momentum, mass, charge, and the coordinate of the αth atom. e is the electronic charge, and ϵ_0 is the permittivity of free space. The electron-electron interactions are described by

$$\hat{H}_{e-e}(\{\mathbf{e}\}) = \sum_{i} \frac{p_i^2}{2m} + \frac{1}{2} \sum_{i \neq j} \frac{\mathrm{e}^2}{4\pi\epsilon_0 |\mathbf{r}_i - \mathbf{r}_j|}, \tag{2.3}$$

where p_i and $\mathbf{r}_i$ are the momentum and the coordinate of the ith electron respectively. m is the mass of an electron. The Coulomb interactions between the electrons and the nuclei are described by

$$\hat{H}_{e-n}(\{\mathbf{r}\}, \{\mathbf{R}\}) = -\sum_{\alpha, i} \frac{Z_{\alpha} \mathrm{e}^2}{4\pi\epsilon_0 |\mathbf{R}_{\alpha} - \mathbf{r}_i|}. \tag{2.4}$$

The full many body Hamiltonian can be analytically solved only for Hydrogenic systems. For all other systems, various approximation techniques are employed to solve the Hamiltonian. An important approximation is the Born-Oppenheimer approximation, which is described in Section 2.2. Another approximation scheme is to separate low energy degrees of freedom from high energy degrees of freedom, and describe the low energy degrees of freedom via semi-empirical parameters. This leads to the construction of effective π-electron Hamiltonians, which are routinely utilised to describe low energy excited states of polyenes. These models are described in Section 2.4.

2.2 The Born-Oppenheimer Hamiltonian

Since the mass of the nuclei are much larger than the mass of the electrons, the nuclei are expected to move slower than the electrons. This separates the dynamics of the system to two scales. The nuclear dynamics are 'slow' compared to the 'fast' electron dynamics. As the electrons move fast, the nuclei are 'frozen' with respect to the instantaneous changes of the electrons. Therefore, the electronic wavefunction, ψ_i, depends parametrically on the nuclear coordinates, i.e., $\psi_i = \psi_i(\{\mathbf{r}\};\{\mathbf{R}\})$, and is called the adiabatic electronic wavefunction. $\psi_i(\{\mathbf{r}\};\{\mathbf{R}\})$ satisfies the time independent Schrödinger equation for the Born-Oppenheimer Hamiltonian, i.e.,

$$\hat{H}_{BO}(\{\mathbf{r}\};\{\mathbf{R}\})\psi_i(\{\mathbf{r}\};\{\mathbf{R}\}) = E_i(\{\mathbf{R}\})\psi_i(\{\mathbf{r}\};\{\mathbf{R}\}), \tag{2.5}$$

where

$$\hat{H}_{BO}(\{\mathbf{r}\};\{\mathbf{R}\}) = \hat{H}_{e-e}(\{\mathbf{r}\}) + \hat{H}_{e-n}(\{\mathbf{r}\},\{\mathbf{R}\}) + \frac{1}{2}\sum_{\alpha\neq\beta}\frac{Z_\alpha Z_\beta \mathrm{e}^2}{4\pi\epsilon_0|\mathbf{R}_\alpha - \mathbf{R}_\beta|}, \tag{2.6}$$

and $E_i(\{\mathbf{R}\})$ is the potential energy surface of the electron i.

With

$$\frac{P_\alpha^2}{2M_\alpha} = -\frac{\hbar^2}{2M_\alpha}\nabla_\alpha^2, \tag{2.7}$$

the full Schrödinger equation is given by

$$\hat{H}\Psi(\{\mathbf{r}\},\{\mathbf{R}\}) = \left[\hat{H}_{BO} - \frac{\hbar^2}{2}\sum_\alpha \frac{1}{M_\alpha}\nabla_\alpha^2\right]\Psi(\{\mathbf{r}\},\{\mathbf{R}\}) = E\Psi(\{\mathbf{r}\},\{\mathbf{R}\}). \tag{2.8}$$

Solutions of Eq. (2.5) form a complete orthonormal basis. Therefore we can write

$$\Psi(\{\mathbf{r}\},\{\mathbf{R}\}) = \sum_i \phi_i(\{\mathbf{R}\})\psi_i(\{\mathbf{r}\};\{\mathbf{R}\}), \tag{2.9}$$

where the coefficients $\phi_i(\{\mathbf{R}\})$ depend only on the nuclear coordinates. By substituting Eq. (2.9) to Eq. (2.8), left multiplying by $\psi_j^*(\{\mathbf{r}\};\{\mathbf{R}\})$, and integrating over the electronic coordinates $\{\mathbf{r}\}$, we arrive at

$$E_j(\{\mathbf{R}\})\phi_j(\{\mathbf{R}\}) - \frac{\hbar^2}{2}\int d\mathbf{r}\ \left\{\psi_j^*(\{\mathbf{r}\};\{\mathbf{R}\})\sum_\alpha \frac{1}{M_\alpha}\nabla_\alpha^2\left[\sum_i \phi_i(\{\mathbf{R}\})\psi_i(\{\mathbf{r}\};\{\mathbf{R}\})\right]\right\}$$
$$= E\phi_j(\{\mathbf{R}\}). \tag{2.10}$$

Defining the first order derivative couplings as

$$\mathbf{d}_{i,j}^\alpha(\{\mathbf{R}\}) = \int d\mathbf{r}\ \left\{\psi_j^*(\{\mathbf{r}\};\{\mathbf{R}\})\left[\nabla_\alpha\psi_i(\{\mathbf{r}\};\{\mathbf{R}\})\right]\right\}, \tag{2.11}$$

and the second order derivative couplings as

$$D_{i,j}^\alpha(\{\mathbf{R}\}) = -\int d\mathbf{r}\ \left\{\psi_j^*(\{\mathbf{r}\};\{\mathbf{R}\})\left[\nabla_\alpha^2\psi_i(\{\mathbf{r}\};\{\mathbf{R}\})\right]\right\}, \tag{2.12}$$

Eq. (2.10) can be written as

$$E_j(\{\mathbf{R}\})\phi_j(\{\mathbf{R}\}) - \frac{\hbar^2}{2}\sum_\alpha \frac{1}{M_\alpha}\left\{\sum_i\left[-D_{i,j}^\alpha(\{\mathbf{R}\})\phi_i(\{\mathbf{R}\}) + \mathbf{d}_{i,j}^\alpha(\{\mathbf{R}\})\cdot\nabla_\alpha\phi_i(\{\mathbf{R}\})\right]\right\}$$
$$+\sum_\alpha \frac{P_\alpha^2}{2M_\alpha}\phi_j(\{\mathbf{R}\}) = E\phi_j(\{\mathbf{R}\}). \tag{2.13}$$

If the electronic wavefunctions vary sufficiently slowly such that $\mathbf{d}_{i,j}^\alpha(\{\mathbf{R}\}) = 0$ and $D_{i,j}^\alpha(\{\mathbf{R}\}) = 0$ for $i \neq j$, we can write Eq. (2.13) as

$$E_j(\{\mathbf{R}\})\phi_j(\{\mathbf{R}\}) - \frac{\hbar^2}{2}\sum_\alpha \frac{1}{M_\alpha}\left[-D_{j,j}^\alpha(\{\mathbf{R}\})\phi_j(\{\mathbf{R}\}) + \mathbf{d}_{j,j}^\alpha(\{\mathbf{R}\})\cdot\nabla_\alpha\phi_j(\{\mathbf{R}\})\right]$$
$$+\sum_\alpha \frac{P_\alpha^2}{2M_\alpha}\phi_j(\{\mathbf{R}\}) = E\phi_j(\{\mathbf{R}\}). \tag{2.14}$$

Since $\{\psi_i(\{\mathbf{r}\};\{\mathbf{R}\})\}$ is an orthonormal set, it follows that $\mathbf{d}_{i,j}^\alpha(\{\mathbf{R}\})$ is anti-Hermitian

and therefore $\mathbf{d}^{\alpha}_{j,j}(\{\mathbf{R}\}) = 0$. With this simplification, we arrive at

$$\left\{ E_j(\{\mathbf{R}\}) + \sum_{\alpha} \left[\frac{\hbar^2}{2M_\alpha} D^{\alpha}_{j,j}(\{\mathbf{R}\}) + \frac{P^2_\alpha}{2M_\alpha} \right] \right\} \phi_j(\{\mathbf{R}\}) = E\phi_j(\{\mathbf{R}\}). \tag{2.15}$$

From Eq. (2.15), we see that $\phi_i(\{\mathbf{R}\})$ satisfies the nuclear Schrödinger equation, and therefore these are the nuclear wavefunctions.

If the electronic wavefunctions are sufficiently separated in energy, only one adiabatic electronic state is required in the expansion Eq. (2.9). This is the adiabatic approximation, and the resultant full wavefunction is a product of the electronic and nuclear wavefunctions,

$$\Psi(\{\mathbf{r}\}, \{\mathbf{R}\}) = \phi_i(\{\mathbf{R}\})\psi_i(\{\mathbf{r}\}; \{\mathbf{R}\}). \tag{2.16}$$

Finally, the Born-Oppenheimer approximation is to assume that the second order derivative couplings $D^{\alpha}_{j,j}(\{\mathbf{R}\}) = 0$. With this simplification, the nuclear wavefunction $\phi_i(\{\mathbf{R}\})$ satisfies

$$\left(E_j(\{\mathbf{R}\}) + \sum_{\alpha} \frac{P^2_\alpha}{2M_\alpha} \right) \phi_j(\{\mathbf{R}\}) = E\phi_j(\{\mathbf{R}\}). \tag{2.17}$$

$E_i(\{\mathbf{R}\})$ is the effective potential experienced by the nuclei, and is known as the adiabatic potential energy surface. The Born-Oppenheimer approximation is widely used in quantum chemistry to study electronic systems. However, around degeneracies of the electronic wavefunctions, the omitted non-adiabatic couplings become important. These are called non-adiabatic processes, and are important in photophysical processes like internal conversion. Non-adiabatic dynamics methods are discussed in Section 2.7.

2.2.1 Second Quantisation

Second quantisation is a convenient formalism to represent fermionic operators.[92] Let $\psi_i(\mathbf{r})$ be a single-particle wavefunction (orbital) of particle i. In Dirac notation, $\psi_i(\mathbf{r})$ is the projection of the single-particle state $|i\rangle$ on to the coordinate representation $|\mathbf{r}\rangle$, i.e.,

$$\psi_i(\mathbf{r}) = \langle \mathbf{r}|i\rangle \,. \tag{2.18}$$

The fermionic creation operator is defined as

$$|i\rangle = \hat{c}_i^\dagger \,|0\rangle \,, \tag{2.19}$$

where $|0\rangle$ is the vacuum state. $\hat{c}_i = (\hat{c}_i^\dagger)^\dagger$ destroys a fermion (electron) in state $|i\rangle$. The fermionic operators satisfy anti-commutation relationships, $\{\hat{c}_i, \hat{c}_j^\dagger\} = \delta_{ij}$, $\{\hat{c}_i, \hat{c}_j\} = 0$, and $\{\hat{c}_i^\dagger, \hat{c}_j^\dagger\} = 0$. In this formalism, the Born-Oppenheimer Hamiltonian can be written as

$$\begin{aligned}\hat{H}_{BO} =& \sum_{ij\sigma} \tilde{t}_{ij} \left(\hat{c}_{i\sigma}^\dagger \hat{c}_{j\sigma} + \hat{c}_{j\sigma}^\dagger \hat{c}_{i\sigma}\right) + \frac{1}{2} \sum_{ijkl\sigma\sigma'} \tilde{V}_{ijkl} \hat{c}_{i\sigma}^\dagger \hat{c}_{j\sigma'}^\dagger \hat{c}_{l\sigma'} \hat{c}_{k\sigma} \\ &+ \frac{1}{2} \sum_{\alpha\neq\beta} \frac{Z_\alpha Z_\beta \mathrm{e}^2}{4\pi\epsilon_0 |\mathbf{R}_\alpha - \mathbf{R}_\beta|},\end{aligned} \tag{2.20}$$

where

$$\tilde{t}_{ij} = \int d^3\mathbf{r}\ \psi_i^*(\mathbf{r}) \left[\frac{\mathbf{p}^2}{2m} - \sum_\alpha \frac{Z_\alpha \mathrm{e}^2}{4\pi\epsilon_0 |\mathbf{R}_\alpha - \mathbf{r}|}\right] \psi_j(\mathbf{r}) \tag{2.21}$$

is the one-electron integral and

$$\tilde{V}_{ijkl} = \int\int d^3\mathbf{r}\ d^3\mathbf{r}'\ \psi_i^*(\mathbf{r}) \psi_j^*(\mathbf{r}') \frac{\mathrm{e}^2}{4\pi\epsilon_0 |\mathbf{r} - \mathbf{r}'|} \psi_k(\mathbf{r}) \psi_l(\mathbf{r}') \tag{2.22}$$

is the two-electron integral. The first term of Eq. (2.20) corresponds to a transfer of an electron with spin σ from the orbital ψ_i to the orbital ψ_j when $i \neq j$, and the on-site energy when $i = j$. The second term of Eq. (2.20) represents the electron-electron interactions (cf. Eq. (2.3)).

Eq. (2.20) describes all electronic degrees of freedom of a given molecular system. For linear polyene systems we are mostly interested in low-energy excitations, and it is useful to truncate the basis to only include these low-energy excitations. This leads to the construction of effective π-electron Hamiltonians.

2.2.2 Effective π-Electron Born-Oppenheimer Hamiltonian

The carbon atoms of a linear polyene system are usually sp^2 hybridised. The sp^2 orbitals form σ bonds along the carbon backbone of the polymer, whereas the unhybridised p_z orbitals along the carbon chain combine to form the delocalised π-orbital system. In the absence of bond twisting, the σ and π bonds belong to different irreducible representations in their symmetry representations, and therefore the two types of excitations are decoupled. σ bonds, owing to their greater overlap, usually have high $\sigma \rightarrow \sigma^*$ excitation energies (~ 10 eV).[93] $\pi \rightarrow \pi^*$ excitations are of much lower excitation energy ($\sim 2 - 3$ eV). This natural separation of electronic degrees of freedom is visible in *ab initio* band structure calculations, as shown in Fig. 2.1.

With the separation σ and π orbitals, we can further simplify the Born-Oppenheimer Hamiltonian in Eq. (2.20) to form effective π-electron Hamiltonians. These models treat the π-electronic degrees of freedom explicitly, and the effects of the σ and core electrons are incorporated parametrically (implicitly) into the effective π-electron models. While in principle these parameters can be determined by *ab initio* calculations of the full electronic Hamiltonian, in practice they are evaluated semiempirically, often by mapping the parameter space to absorption spectra.[95] In Section 5.1,

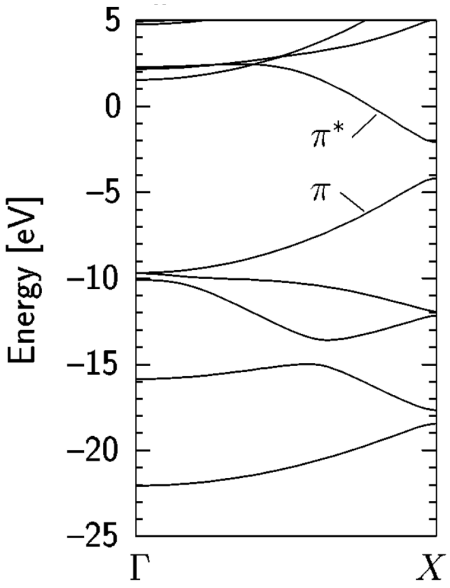

Figure 2.1: Electron-hole excitation band structure of trans-polyacetylene determined via *ab initio* calculations. Γ and X corresponds to the centre and edge of the Brillouin zone, respectively. At the χ point of the Brillouin zone, trans-polyacetylene has a band gap of 2.1 eV corresponding to a π(valence band) $\rightarrow \pi^*$(conduction band) transition. The four bands below the valence band are formed from the carbon sp^2 orbitals and hydrogen $1s$ orbitals. Reproduced with permission from Rohlfing, M.; Louie, S. G. Optical excitations in conjugated polymers. *Phys. Rev. Lett.* **1999**, *82*, 1959–1962.

we describe a semiempirical parameterisation of the effective π-electron model we use for our dynamical simulations.

In π-electron systems, the σ and the core electrons act to screen the Coulomb interactions between the remaining degrees of freedom. This screening can be modelled as a change of dielectric constant, and a reduction of effective nuclear charge. We describe the screened interaction between the nuclei and the electrons by the pseudopotential $V_p(\mathbf{r};\{\mathbf{R}\})$. Using this pseudopotential, the one-electron integral can be written as

$$\tilde{t}_{ij} = \int d^3\mathbf{r}\ \psi_i^*(\mathbf{r}) \left[\frac{\mathbf{p}^2}{2m} + V_p(\mathbf{r};\{\mathbf{R}\})\right] \psi_j(\mathbf{r}). \tag{2.23}$$

Similarly, the electron-electron interactions are modelled by the effective potential

$V_{e-e}^{\text{eff}}(\mathbf{r}-\mathbf{r}')$, using which the two-electron integral can be written as

$$\tilde{V}_{ijkl} = \int\int d^3\mathbf{r}\; d^3\mathbf{r}'\; \psi_i^*(\mathbf{r})\psi_j^*(\mathbf{r}')V_{e-e}^{\text{eff}}(\mathbf{r}-\mathbf{r}')\psi_k(\mathbf{r})\psi_l(\mathbf{r}') \tag{2.24}$$

By setting $i = j = k = l$ in Eq. (2.24), we derive an expression for the Coulomb interaction of two electrons in the same orbital,

$$U_i = \tilde{V}_{iiii} = \int\int d^3\mathbf{r}\; d^3\mathbf{r}'\; \psi_i^*(\mathbf{r})\psi_i^*(\mathbf{r}')V_{e-e}^{\text{eff}}(\mathbf{r}-\mathbf{r}')\psi_i(\mathbf{r})\psi_i(\mathbf{r}'). \tag{2.25}$$

By setting $i = k$ and $j = l$ in Eq. (2.24), we derive an expression for the Coulomb interaction of two electrons in different orbitals,

$$V_{ij} = \tilde{V}_{ijij} = \int\int d^3\mathbf{r}\; d^3\mathbf{r}'\; \psi_i^*(\mathbf{r})\psi_j^*(\mathbf{r}')V_{e-e}^{\text{eff}}(\mathbf{r}-\mathbf{r}')\psi_i(\mathbf{r})\psi_j(\mathbf{r}'). \tag{2.26}$$

The terms U_i and V_{ij} make the largest contribution for the two-electron integrals. We can also define the exchange interaction as

$$K_{ij} = \tilde{V}_{ijji} = \int\int d^3\mathbf{r}\; d^3\mathbf{r}'\; \psi_i^*(\mathbf{r})\psi_j^*(\mathbf{r}')V_{e-e}^{\text{eff}}(\mathbf{r}-\mathbf{r}')\psi_j(\mathbf{r})\psi_i(\mathbf{r}'), \tag{2.27}$$

which is proportional to the orbital overlap, $\psi_i^*(\mathbf{r})\psi_j(\mathbf{r}')$, and is usually neglected along with the density-dependent hopping terms $\tilde{V}_{iii,i+1}$ and bond-charge repulsion terms $\tilde{V}_{i,i+1,i+1,i}$ for models parametrised to fit to experiment.

We further simplify the effective π-electron models by assuming the one-electron integrals given by Eq. (2.23) are non-zero only when the electrons occupy the same or neighbouring orbitals. With this assumption, we define the on-site potential energy of orbital $\psi_i(\mathbf{r})$ as

$$\epsilon_i = \tilde{t}_{ii} = \int d^3\mathbf{r}\; \psi_i^*(\mathbf{r}) \left[\frac{\mathbf{p}^2}{2m} + V_p(\mathbf{r};\{\mathbf{R}\})\right] \psi_i(\mathbf{r}), \tag{2.28}$$

and nearest-neighbour hopping (or transfer) interaction as

$$t_i = -\tilde{t}_{i,i+1} = -\int d^3\mathbf{r}\ \psi_i^*(\mathbf{r}) \left[\frac{\mathbf{p}^2}{2m} + V_p(\mathbf{r};\{\mathbf{R}\})\right] \psi_{i+1}(\mathbf{r}). \tag{2.29}$$

With these approximations, the Born-Oppenheimer Hamiltonian of Eq. (2.20) reduces to

$$\begin{aligned}\hat{H}_{BO} =& \sum_i \epsilon_i \hat{N}_i - \sum_{i\sigma} t_i \left(\hat{c}^\dagger_{i+1,\sigma}\hat{c}_{i,\sigma} + \hat{c}^\dagger_{i,\sigma}\hat{c}_{i+1,\sigma}\right) \\ &+ U\sum_i \hat{N}_{i,\uparrow}\hat{N}_{i,\downarrow} + \frac{1}{2}\sum_{i\neq j} V_{ij}\hat{N}_i\hat{N}_j + V_{n-n},\end{aligned} \tag{2.30}$$

where $\hat{N}_{i,\sigma} = \hat{c}^\dagger_{i,\sigma}\hat{c}_{i,\sigma}$ is the number operator which counts the number of electrons with spin σ on site i, $\hat{N}_i = \sum_\sigma \hat{N}_{i,\sigma}$, $U = U_i$ for all sites i, and V_{n-n} is the effective potential for the screened nuclear-nuclear interaction. Eq. (2.30) is a highly simplified form of a second quantised Hamiltonian.

We see from Eq. (2.23) that electron-nuclear coupling is implicitly included in the effective Born-Oppenheimer Hamiltonian. In Section 2.3, we describe how we can go beyond the effective π-Electron Born-Oppenheimer Hamiltonian by explicitly including electron-nuclear coupling in the effective π-electron Hamiltonians.

2.3 Electron-Nuclear Interactions

2.3.1 Electron-Nuclear Coupling

We derive the electron-nuclear coupling interaction by writing the effective pseudopotential $V_p(\mathbf{r};\{\mathbf{R}\})$ in a Taylor series expansion around a reference geometry $\{\mathbf{R}^0\}$,

$$V_p(\mathbf{r};\{\mathbf{R}\}) = V_p(\mathbf{r};\{\mathbf{R}^0\}) + \sum_l \frac{\partial V_p(\mathbf{r};\{\mathbf{R}^0\})}{\partial \mathbf{R}_l}.\mathbf{u}_l + \ldots, \tag{2.31}$$

where $\mathbf{u}_l = \mathbf{R}_l - \mathbf{R}_l^0$ is the displacement of the lth nucleus from its reference geometry. Comparing Eqs. (2.28) and (2.29) with Eq. (2.31), we can write

$$\epsilon_i^0 = \int d^3\mathbf{r}\ \psi_i^*(\mathbf{r}) \left[\frac{\mathbf{p}^2}{2m} + V_p(\mathbf{r}; \{\mathbf{R}^0\}) \right] \psi_i(\mathbf{r}), \tag{2.32}$$

and

$$t_i^0 = -\int d^3\mathbf{r}\ \psi_i^*(\mathbf{r}) \left[\frac{\mathbf{p}^2}{2m} + V_p(\mathbf{r}; \{\mathbf{R}^0\}) \right] \psi_{i+1}(\mathbf{r}). \tag{2.33}$$

Further, by comparing Eq. (2.23) with Eq. (2.31), we can define an electron-nuclear coupling parameter

$$\alpha_{mnl} = \int d^3\mathbf{r}\ \psi_m^*(\mathbf{r}) \left[\frac{\partial V_p(\mathbf{r}; \{\mathbf{R}^0\})}{\partial \mathbf{R}_l} \right] \psi_n(\mathbf{r}). \tag{2.34}$$

We then define the non-zero electron-nuclear coupling parameters,

$$\alpha \equiv \alpha_{l,l+1,l+1} \equiv \alpha_{l+1,l,l+1} \equiv -\alpha_{l,l+1,l} \equiv -\alpha_{l+1,l,l} \tag{2.35}$$

and

$$\beta \equiv \alpha_{l,l,l+1} \equiv -\alpha_{l,l,l-1}. \tag{2.36}$$

Using Eqs. (2.28) $-$ (2.36), we can show that

$$\epsilon_i = \epsilon_i^0 + \beta.\left(\mathbf{u}_{i+1} - \mathbf{u}_{i-1}\right), \tag{2.37}$$

and

$$t_i = t_i^0 - \alpha.\left(\mathbf{u}_{i+1} - \mathbf{u}_i\right). \tag{2.38}$$

By comparing Eqs. (2.30), (2.37), and (2.38), we can define an explicit expression for the electron-nuclear interaction as

$$\hat{H}_{e-n} = \sum_{i\sigma} \left\{ \alpha . \left(\mathbf{u}_{i+1} - \mathbf{u}_i \right) \left(\hat{c}^{\dagger}_{i+1,\sigma} \hat{c}_{i,\sigma} + \hat{c}^{\dagger}_{i,\sigma} \hat{c}_{i+1,\sigma} \right) + \beta . \left(\mathbf{u}_{i+1} - \mathbf{u}_{i-1} \right) \hat{N}_{i,\sigma} \right\} . \quad (2.39)$$

The first term of Eq. (2.39) corresponds to the change of electronic kinetic energy caused by changes in bond lengths from their reference geometries. The second term corresponds to the change in electronic potential energy due to changes in the bond lengths.

2.3.2 Nuclear Potential Energy

The nuclear-nuclear interactions are described by

$$\hat{H}_{n-n} = \sum_{\alpha} \frac{P_{\alpha}^2}{2M_{\alpha}} + V_{n-n} \left(\{ \mathbf{u}_n \} \right) , \quad (2.40)$$

where $V_{n-n} \left(\{ \mathbf{u}_n \} \right)$ models the effective nuclear potential as a result of electronic screening. For polyene systems, the effective nuclear potential is determined by the nuclear charges of the σ bonds, and can be described by a series of harmonic oscillators as

$$V_{n-n} \left(\{ \mathbf{u}_n \} \right) = \frac{K}{2} \sum_{i} \left(\mathbf{u}_{i+1} - \mathbf{u}_i \right)^2 , \quad (2.41)$$

where K is the nuclear spring constant.

2.3.3 The Peierls model

In the absence of nuclear dynamics the effects of electron-nuclear interactions in polyenes are described by the Peierls model, defined by

$$\hat{H}_{\text{Peierls}} = \hat{H}_{\text{kinetic}} + \hat{H}_{\text{elastic}}, \tag{2.42}$$

where the electronic kinetic energy is given by

$$\hat{H}_{\text{kinetic}} = -2\sum_i t_i \hat{T}_i, \tag{2.43}$$

and the elastic energy of the σ electrons is given by

$$\hat{H}_{\text{elastic}} = \frac{1}{4\pi t_0 \lambda}\sum_i \Delta_i^2. \tag{2.44}$$

t_0 is the average of the nearest neighbour hopping interaction, and

$$\hat{T}_i = \frac{1}{2}\sum_\sigma \left(\hat{c}^\dagger_{i+1,\sigma}\hat{c}_{i,\sigma} + \hat{c}^\dagger_{i,\sigma}\hat{c}_{i+1,\sigma}\right) \tag{2.45}$$

is the bond order operator for the ith bond. The bond dimerisation parameter Δ_i is defined by

$$\Delta_i = -2\alpha(u_{i+1} - u_i), \tag{2.46}$$

and the bond hybridisation integrals t_i are related to Δ_i by

$$t_i = t_0 + \frac{\Delta_i}{2}. \tag{2.47}$$

As the length of bond i decreases, Δ_i and t_i increases. Physically, this corresponds to an increase in the magnitude of the bond hybridisation integrals as the nuclei

separation decreases. By substituting Eq. (2.47) and Eq. (2.46) into Eq. (2.43), we arrive at

$$\hat{H}_{\text{kinetic}} = -2\sum_{i} t_0 \hat{T}_i + 2\sum_{i\sigma} \alpha \left(u_{i+1} - u_i\right) \hat{T}_i. \tag{2.48}$$

The second term of Eq. (2.48) couples the bond order to the nuclei, and corresponds to Eq. (2.39) with $\beta = 0$. Similarly, by comparing Eq (2.44) with Eq. (2.41), we can define the dimensionless electron-nuclear coupling parameter λ as

$$\lambda = \frac{2\alpha^2}{\pi K t_0}. \tag{2.49}$$

2.4 π-Electron Theories of Conjugated Polymers

In this section, we describe some of the effective π-electron Hamiltonian models used to describe polyene systems.

2.4.1 Hückel Model

Hückel model is one of the simplest models used to describe π-electron systems.[96] The model assumes that the nuclei are fixed and neglects the electron-electron interactions. With these assumptions, and setting the constant $V_{n-n} = 0$, the Hückel Hamiltonian is derived from Eq. (2.30),

$$\hat{H}_{\text{Hückel}} = \sum_{i} \epsilon_i \hat{N}_i - \sum_{i\sigma} t_i \left(\hat{c}^{\dagger}_{i+1,\sigma}\hat{c}_{i,\sigma} + \hat{c}^{\dagger}_{i,\sigma}\hat{c}_{i+1,\sigma}\right) \tag{2.50}$$

For linear polyene systems, we can define $t_i = t(1 + \delta_i)$, where δ_i is the distortion of the ith bond from the average bond length.

The Hückel Hamiltonian is routinely used to describe qualitative properties of fused ring systems. However, for accurate description of linear polyene systems like carotenoids the electron-electron interactions cannot be neglected, and π-electron

models which explicitly include electron-electron interactions are required.

2.4.2 Pariser-Parr-Pople Model

Pariser-Parr-Pople (PPP) Hamiltonian[97–100] defined by

$$\hat{H}_{\mathrm{PPP}} = -\sum_{i\sigma} t_0 \left(\hat{c}^{\dagger}_{i+1,\sigma}\hat{c}_{i,\sigma} + \hat{c}^{\dagger}_{i,\sigma}\hat{c}_{i+1,\sigma}\right) + U\sum_{i}\left(\hat{N}_{i\uparrow} - \frac{1}{2}\right)\left(\hat{N}_{i\downarrow} - \frac{1}{2}\right) + \frac{1}{2}\sum_{i\neq j} V_{ij}\Big(\hat{N}_i - 1\Big)\Big(\hat{N}_j - 1\Big), \tag{2.51}$$

is an effective π-electron model with fixed nuclei and interacting electrons. The last term of Eq. (2.51) can be expanded as,

$$\frac{1}{2}\sum_{i\neq j} V_{ij}\Big(\hat{N}_i - 1\Big)\Big(\hat{N}_j - 1\Big) = \frac{1}{2}\sum_{i\neq j} V_{ij}\hat{N}_i\hat{N}_j - \sum_{i\neq j} V_{ij}\hat{N}_i + \frac{1}{2}\sum_{i\neq j} V_{ij}. \tag{2.52}$$

The first term of the expansion is the electron-electron interaction term of Eq. (2.30). The second term describes the resultant effect of the nuclei charges $j \neq i$ on the potential energy experienced by electrons on site i. The third term describes an effective potential that depends solely on the other nuclei, and is equivalent to V_{n-n}. In other words, the PPP model can be parametrised to include the effects on electron-nuclear and nuclear-nuclear interactions due to the nuclear charges.

The electron-electron interaction parameter, V_{ij}, can be modelled using the semi-empirical Ohno potential,

$$V_{ij} = \frac{U}{\sqrt{1 + (U\epsilon_r r_{ij}/14.397)^2}}, \tag{2.53}$$

where ϵ_r is the relative permittivity, and r_{ij} is the distance between the sites i and j. By supplementing the PPP Hamiltonian with the Peierls model introduced in Section 2.3.3 and Coulomb interactions, we arrive at the Pariser-Parr-Pople-Peierls

(PPPP) Hamiltonian,

$$\hat{H}_{\text{PPPP}} = \hat{H}_{\text{PPP}} + \hat{H}_{\text{el-ph}} + \hat{H}_{\text{elastic}}, \tag{2.54}$$

where $\hat{H}_{\text{el-ph}}$ describes the electron-nuclear coupling,

$$\hat{H}_{\text{el-ph}} = 2\alpha \sum_i (u_{i+1} - u_i)\, \hat{T}_i - 2\alpha W \sum_i (u_{i+1} - u_i)\Big(\hat{N}_{i+1} - 1\Big)\Big(\hat{N}_i - 1\Big), \tag{2.55}$$

and $\hat{H}_{\text{elastic}}$ is defined in Eq. (2.44). The first term of Eq. (2.55) is the electron-nuclear coupling due to the change in the electronic kinetic energy, and is the same as the first term of Eq. (2.39). The second term of Eq. (2.55) corresponds to the changes in the Coulomb interactions due to the change in the bond lengths. As the density-density correlator, $(\hat{N}_i - 1)(\hat{N}_j - 1)$, decays rapidly with the distance, only the nearest neighbour Coulomb interactions are considered. To first order,

$$W = -\frac{1}{2\alpha}\left(\frac{\partial V_{ij}}{\partial r_{ij}}\right)_{r_{ij}=r_0} = \frac{U\gamma r_0}{2\alpha(1+\gamma r_0^2)^{3/2}}, \tag{2.56}$$

where $\gamma = (U\epsilon_r/14.397)^2$ and r_0 is the undistorted average bond length. We can rewrite this term as

$$\begin{aligned} &-2\alpha W \sum_i (u_{i+1} - u_i)\Big(\hat{N}_{i+1} - 1\Big)\Big(\hat{N}_i - 1\Big) \\ &\quad = -2\alpha W \sum_i (u_{i+1} - u_i)\, \hat{N}_{i+1}\hat{N}_i + 2\alpha W \sum_i (u_{i+1} - u_{i-1})\, \hat{N}_i + \text{constant} \end{aligned} \tag{2.57}$$

Comparing Eq. (2.57) and (2.39), we can assign $W = \frac{\beta}{2\alpha}$.

The PPP Hamiltonian has been widely used to study the electronic properties of conjugated polyenes.[101–107] Chapter 4 of this thesis describes a study of the polyene excited states using the PPPP model.

2.4.3 UV Model

By omitting the long-range electron-electron interactions of the PPP model, we obtain the UV Hamiltonian as

$$\hat{H}_{\mathrm{UV}} = -\sum_{i\sigma} t_0 \left(\hat{c}^{\dagger}_{i+1,\sigma}\hat{c}_{i,\sigma} + \hat{c}^{\dagger}_{i,\sigma}\hat{c}_{i+1,\sigma}\right) + U\sum_{i}\left(\hat{N}_{i\uparrow} - \frac{1}{2}\right)\left(\hat{N}_{i\downarrow} - \frac{1}{2}\right) + \frac{V}{2}\sum_{i}\left(\hat{N}_i - 1\right)\left(\hat{N}_{i+1} - 1\right). \tag{2.58}$$

The UV Hamiltonian only contains on-site and nearest neighbour interactions. As described in Section 3.1.3, the UV Hamiltonian can therefore be efficiently utilised to study time-dependent systems. By supplementing the UV Hamiltonian with the Peierls model, we derive the UV-Peierls (UVP) Hamiltonian,

$$\hat{H}_{\mathrm{UVP}} = \hat{H}_{\mathrm{UV}} + 2\alpha\sum_{i\sigma}\left(u_{i+1} - u_i\right)\left(\hat{c}^{\dagger}_{i+1,\sigma}\hat{c}_{i,\sigma} + \hat{c}^{\dagger}_{i,\sigma}\hat{c}_{i+1,\sigma}\right) + \frac{K}{2}\sum_{i}\left(u_{i+1} - u_i\right)^2, \tag{2.59}$$

where the dependency of nearest neighbour Coulomb interaction on nuclear coordinates have been neglected by setting $W = 0$ in Eq. (2.55). In Chapter 5, we use the UVP model to study the internal conversion process in carotenoids.

2.5 Symmetries

The eigenstates of the effective π-electron models described in Section 2.4 can be distinguished by different symmetries. While these symmetries are only approximate descriptions of the ground and excited states of molecular systems, they are useful to characterise the state of these dynamic systems. In polyenes, the ground and the excited states can be characterised by both spatial symmetries and discrete electron-hole symmetry.

2.5.1 Spatial Symmetries

Ideal polyene systems with even chain lengths possess two-fold rotation (C_2) and reflection (σ_h) symmetries, and therefore belong to the C_{2h} point group. The character table of C_{2h} point group is shown in Table 2.1.

C_{2h}	E	C_2	i	σ_h
A_g	1	1	1	1
B_g	1	-1	1	-1
A_u	1	1	-1	-1
B_u	1	-1	-1	1

Table 2.1: Character table of the C_{2h} point group. E, C_2, i, and σ_h are identity, two-fold rotation, inversion, and reflection symmetry operations respectively.

We are interested in the p_z orbitals of polyenes, which are distinguished by being anti-symmetric with respect to reflection around the plane of symmetry, σ_h. As the character of the σ_h operation for both A_u and B_g irreducible representations is -1, it follows that the molecular orbitals composed of these p_z orbitals are of either A_u or B_g symmetry. The multiplication rules for the irreducible representations are

$$A_u \otimes A_u = B_g \otimes B_g = A_g \otimes A_g = B_u \otimes B_u = A_g, \tag{2.60}$$

and

$$A_u \otimes B_g = B_g \otimes A_u = B_u. \tag{2.61}$$

As polyenes contain an even number of electrons, it follows that the excited states of neutral polyenes are of either A_g or B_u symmetry.

2.5.2 Electron-Hole Symmetry

Within the single-site basis of the π-electron models, i.e., $\{|0\rangle_i, |\uparrow\rangle_i, |\downarrow\rangle_i, |\uparrow\downarrow\rangle_i\}$, the electron-hole operator, $\hat{J}$, is defined by

$$\begin{aligned}
\hat{J}\,|0\rangle_i &= |\uparrow\downarrow\rangle_i\,, \\
\hat{J}\,|\uparrow\rangle_i &= (-1)^{i+1}\,|\uparrow\rangle_i\,, \\
\hat{J}\,|\downarrow\rangle_i &= (-1)^{i}\,|\downarrow\rangle_i\,, \\
\hat{J}\,|\uparrow\downarrow\rangle_i &= |0\rangle_i\,,
\end{aligned} \tag{2.62}$$

and it transforms as,

$$\begin{aligned}
\hat{J}\hat{c}^{\dagger}_{i,\sigma} &= (-1)^{i}\hat{c}_{i,\bar{\sigma}}\hat{J} \\
\hat{J}\hat{c}_{i,\sigma} &= (-1)^{i}\hat{c}^{\dagger}_{i,\bar{\sigma}}\hat{J}.
\end{aligned} \tag{2.63}$$

In this thesis, we follow the electron-hole sign convention of ref. [2], which is commonly used by the experimental community but is the opposite definition to refs. [104] and [93]. It can easily be shown using Eq. (2.63) that

$$\hat{J}\hat{T}_i = \hat{T}_i\hat{J}, \tag{2.64}$$

and

$$\hat{J}\left(\hat{N}_{i,\uparrow}-\frac{1}{2}\right)\left(\hat{N}_{i,\downarrow}-\frac{1}{2}\right) = -\left(\hat{N}_{i,\downarrow}-\frac{1}{2}\right)\hat{J}\left(\hat{N}_{i,\downarrow}-\frac{1}{2}\right) = \left(\hat{N}_{i,\uparrow}-\frac{1}{2}\right)\left(\hat{N}_{i,\downarrow}-\frac{1}{2}\right)\hat{J}. \tag{2.65}$$

Therefore, the π-electron models described in Section 2.4 are invariant under an electron-hole transformation, i.e., $[\hat{H}, \hat{J}] = 0$. This implies that the eigenstates of $\hat{H}$

can be *symmetrised* to have definite +/− electron-hole eigenvalues. It can also be shown that for such Hamiltonians, the expectation value of the number operator,

$$\left\langle \hat{N} - 1 \right\rangle = 1. \tag{2.66}$$

Further, the singlet eigenstates that are negative under an electron-hole transformation have an even electron-hole parity, and are therefore labelled $^1A_g^-$, and singlet eigenstates that are positive under an electron-hole transformation have an odd electron-hole parity, and are labelled $^1B_u^+$. A proof of these two properties can be found in Appendix B and Section 3.7.1 of ref. [93], respectively.

2.6 Eigenstates of the Dynamical Hamiltonian

In this section we introduce the Hamiltonians used in our dynamics model and define their eigenstates used for the dynamical simulations of photoexcited states of carotenoids presented in this thesis. In order to facilitate internal conversion from the photoexcited $1\,^1B_u^+$ state to the triplet-pair states (which are of negative electron-hole character), an interaction term which breaks the electron-hole symmetry is required. We define the symmetry breaking term

$$\hat{H}_\epsilon = \sum_{i=1}^{N} \epsilon_i (\hat{N}_i - 1), \tag{2.67}$$

where ϵ_i is the on-site potential energy parameter on the ith C-atom. The inclusion of H_ϵ is justified as carotenoids with both electron donating and withdrawing substituent groups (shown in Fig. 1.1), which act as electron donors and acceptors to the π-system, are known to undergo singlet fission.[11]

Since we are only interested in the singlet excitations, we project out the high

spin contributions to the Hilbert space by supplementing the Hamiltonian with

$$\hat{H}_\lambda = \lambda \hat{S}^2, \tag{2.68}$$

where $\hat{S}$ is the total spin operator, and $\lambda > 0$.

For our dynamical simulations, we define the full Born-Oppenheimer Hamiltonian as

$$\hat{H} = \hat{H}_{\mathrm{UVP}} + \hat{H}_\lambda + \hat{H}_\epsilon. \tag{2.69}$$

As a result of the inclusion of the broken symmetry term, eigenstates of $\hat{H}$ will not have definite C_2 or electron-hole symmetries. They are labelled adiabatic (singlet) eigenstates, and are defined by

$$\hat{H} \left| S_i \right\rangle = E_i \left| S_i \right\rangle . \tag{2.70}$$

We define a diabatic (singlet) basis spanned by the eigenstates of $(\hat{H}_{\mathrm{UVP}} + \hat{H}_\lambda)$ as

$$\left(\hat{H}_{\mathrm{UVP}} + \hat{H}_\lambda\right) \left| \phi_j \right\rangle = E_{\phi_j} \left| \phi_j \right\rangle . \tag{2.71}$$

The diabatic eigenstates for idealised carotenoids have definite C_2 and electron-hole symmetries.

We can calculate the probability that the system described by $\Psi(t)$ occupies the adiabatic state S_i by

$$P(\Psi(t); S_i) = |\left\langle S_i | \Psi(t) \right\rangle|^2 \tag{2.72}$$

and the probability that it occupies the diabatic state ϕ_j by

$$P(\Psi(t); \phi_j) = |\left\langle \phi_j | \Psi(t) \right\rangle|^2. \tag{2.73}$$

Finally, the probability that the adiabat S_i occupies the diabat ϕ_j is

$$P(S_i;\phi_j) = |\,\langle\phi_j|S_i\rangle\,|^2. \tag{2.74}$$

Eigenstates of $\hat{H} = (\hat{H}_{\mathrm{UVP}} + \hat{H}_{\lambda})$ with a positive particle-hole symmetry are termed 'ionic', as the expectation value of the ionicity operator, $\hat{I} = \sum_i \left(\hat{N}_i - 1\right)^2$, is larger for these states than for eigenstates with a negative particle-hole symmetry, termed 'covalent'. This property of a larger ionicity for ionic states can be used to distinguish them from covalent states, and is used to identify the $1\,^1B_u^+$ state in the results presented in Chapter 5.

2.7 Non-adiabatic Dynamics

Conventional molecular dynamics is routinely utilised to simulate numerical dynamics of a diverse range of chemical processes, including gas phase molecular collisions,[108] reactions in liquids,[109] and biomolecular dynamics.[110–112] At the heart of the molecular dynamics method is the adiabatic approximation (Eq. (2.16)), the assumption that electronic degrees of freedom instantaneously adjust to the nuclear motion such that the electrons move on a single adiabatic surface. Dynamical processes involving electronic transitions violate the adiabatic approximation, and as a consequence molecular dynamics is inadequate for the description of dynamical processes involving electronic transitions, and non-adiabatic methods are required. In this section, we introduce the standard Born-Oppenheimer molecular dynamics scheme built upon the adiabatic approximation, and the non-adiabatic Ehrenfest dynamics method which is used for the dynamical simulations described in this thesis. Two other non-adiabatic methods, surface hopping and the recently developed TEBD-Ehrenfest method, are briefly described.

2.7.1 Standard Born-Oppenheimer Molecular Dynamics

Analogous to the time-independent Born-Oppenheimer wavefunction of Eq. (2.16), the time-dependent Born-Oppenheimer wavefunction $\Psi(\{\mathbf{r}\},\{\mathbf{R}\},t)$ can be written as a product of a 'slow' time-dependent nuclear wavefunction $\phi_j(\{\mathbf{R}\},t)$ and a time-independent 'fast' electronic wavefunction $\psi_j(\{\mathbf{r}\};\{\mathbf{R}\})$,

$$\Psi(\{\mathbf{r}\},\{\mathbf{R}\},t) = \phi_j(\{\mathbf{R}\},t)\psi_j(\{\mathbf{r}\};\{\mathbf{R}\}). \tag{2.75}$$

$\phi_j(\{\mathbf{R}\},t)$ satisfies the time-dependent Schrödinger equation,

$$i\hbar\frac{\partial}{\partial t}\phi_j(\{\mathbf{R}\},t) = \left(E_j(\{\mathbf{R}\}) - \frac{\hbar^2}{2}\sum_\alpha \frac{1}{M_\alpha}\nabla_\alpha^2\right)\phi_j(\{\mathbf{R}\},t). \tag{2.76}$$

Conventional molecular dynamics is built upon a second assumption; the nuclear motion is fully determined by Newtonian equations of motion. Following ref [113], it can be shown that by expressing $\phi_j(\{\mathbf{R}\},t)$ as

$$\phi_j(\{\mathbf{R}\},t) = A(\{\mathbf{R}\},t)\exp\left\{\frac{i}{\hbar}S(\{\mathbf{R}\},t)\right\}, \tag{2.77}$$

where $A(\{\mathbf{R}\},t)$ and $S(\{\mathbf{R}\},t)$ are real-valued functions, at the classical limit defined by $\hbar \to 0$, Newton's equations of motion,

$$\dot{P}_\alpha = M_\alpha\ddot{R}_\alpha = -\nabla_\alpha E_j(\{\mathbf{R}\}), \tag{2.78}$$

are retrieved, where

$$S(\{\mathbf{R}\}) \equiv S(t) = -\int_0^t dt'\ E(t'), \tag{2.79}$$

is the sum of classical kinetic and potential energies, and A^2 is the probability density.

Standard molecular dynamics treats the electronic (quantum) and nuclear (classical) degrees of freedom in a self consistent way. The potential energy surface $E_j(\{\mathbf{R}\})$ depends on the classical nuclear coordinates, while the forces and momenta of the classical nuclei are determined by the quantum mechanical energy gradient $\nabla_\alpha E_j(\{\mathbf{R}\})$.

2.7.2 Ehrenfest Method

The electronic wavefunction in conventional molecular dynamics is confined to a single potential energy surface. Ehrenfest dynamics is a non-adiabatic method where the 'slow' nuclear degrees of freedom evolve on an effective potential energy surface defined by the weighted average of contributing adiabatic surfaces.[113] We begin with the time-dependent self consistent field (TDSCF) wavefunction,

$$\Psi(\{\mathbf{r}\},\{\mathbf{R}\},t) = \psi(\{\mathbf{r}\},t)\phi(\{\mathbf{R}\},t)\exp\left\{\frac{i}{\hbar}\int_0^t dt'\ E_r(t')\right\}, \tag{2.80}$$

where $\psi(\{\mathbf{r}\},t)$ and $\phi(\{\mathbf{R}\},t)$ are the (normalised) electronic and nuclear wavefunctions, respectively, and E_r is a phase factor. Comparing Eq. (2.80) with Eq. (2.75), we see that the electronic wavefunction $\psi(\{\mathbf{r}\},t)$ is now not limited to a single adiabatic basis function. $\Psi(\{\mathbf{r}\},\{\mathbf{R}\})$ satisfies the full time-dependent Schrödinger equation,

$$\hat{H}\Psi(\{\mathbf{r}\},\{\mathbf{R}\},t) = \left[\hat{H}_{BO} - \frac{\hbar^2}{2}\sum_\alpha \frac{1}{M_\alpha}\nabla_\alpha^2\right]\Psi(\{\mathbf{r}\},\{\mathbf{R}\},t) = i\hbar\frac{\partial}{\partial t}\Psi(\{\mathbf{r}\},\{\mathbf{R}\},t). \tag{2.81}$$

We can separate the kinetic and potential energy terms of $\hat{H}_{BO}$ as

$$\hat{H}_{BO}(\{\mathbf{r}\},\{\mathbf{R}\}) = -\frac{\hbar^2}{2m}\sum_{\beta}\nabla_{\beta}^2 + V_{rR}(\{\mathbf{r}\},\{\mathbf{R}\}), \tag{2.82}$$

where ∇_{β}^2 only depends on the electronic coordinates ($\{\mathbf{r}\}$). The TDSE for the electronic wavefunction is obtained by substituting Eq. (2.80) in Eq. (2.81), left multiplying by $\phi^*(\{\mathbf{R}\},t)$, and integrating over $\{\mathbf{R}\}$,

$$\begin{aligned} i\hbar\frac{\partial}{\partial t}\psi(\{\mathbf{r}\},t) &= -\frac{\hbar^2}{2m}\sum_{\beta}\nabla_{\beta}^2\psi(\{\mathbf{r}\},t) \\ &+ \left\{\int d\{\mathbf{R}\}\ \phi^*(\{\mathbf{R}\},t)\left[-\frac{\hbar^2}{2}\sum_{\alpha}\frac{1}{M_{\alpha}}\nabla_{\alpha}^2 + V_{rR}(\{\mathbf{r}\},\{\mathbf{R}\})\right]\phi(\{\mathbf{R}\},t)\right\}\psi(\{\mathbf{r}\},t) \\ &+ E_r(t)\psi(\{\mathbf{r}\},t) - i\hbar\left[\int d\{\mathbf{R}\}\ \phi^*(\{\mathbf{R}\},t)\frac{\partial}{\partial t}\phi(\{\mathbf{R}\},t)\right]\psi(\{\mathbf{r}\},t). \end{aligned} \tag{2.83}$$

A similar TDSE for the nuclear wavefunction is obtained by substituting Eq. (2.80) in Eq. (2.81), left multiplying by $\psi^*(\{\mathbf{r}\},t)$, and integrating over $\{\mathbf{r}\}$,

$$\begin{aligned} i\hbar\frac{\partial}{\partial t}\phi(\{\mathbf{R}\},t) &= -\frac{\hbar^2}{2}\sum_{\alpha}\frac{1}{M_{\alpha}}\nabla_{\alpha}^2\phi(\{\mathbf{R}\},t) \\ &+ \left\{\int d\{\mathbf{r}\}\ \psi^*(\{\mathbf{r}\},t)\left[-\frac{\hbar^2}{2m}\sum_{\beta}\nabla_{\beta}^2 + V_{rR}(\{\mathbf{r}\},\{\mathbf{R}\})\right]\psi(\{\mathbf{r}\},t)\right\}\phi(\{\mathbf{R}\},t) \\ &+ E_r(t)\phi(\{\mathbf{R}\},t) - i\hbar\left[\int d\{\mathbf{r}\}\ \psi^*(\{\mathbf{r}\},t)\frac{\partial}{\partial t}\psi(\{\mathbf{r}\},t)\right]\phi(\{\mathbf{R}\},t). \end{aligned} \tag{2.84}$$

The phase factor E_r can be defined arbitrarily, subject to satisfying Eqs. (2.83) and (2.84). Following the convention of ref [113],

$$E_r(t) = i\hbar\int d\{\mathbf{r}\}\ \psi^*(\{\mathbf{r}\},t)\frac{\partial}{\partial t}\psi(\{\mathbf{r}\},t), \tag{2.85}$$

reduces Eq. (2.83) to an effective TDSE for the electronic wavefunction,

$$i\hbar\frac{\partial}{\partial t}\psi(\{\mathbf{r}\},t) = -\frac{\hbar^2}{2m}\sum_{\beta}\nabla_{\beta}^2\psi(\{\mathbf{r}\},t) + \left\{\int d\{\mathbf{R}\}\ \phi^*(\{\mathbf{R}\},t)V_{rR}(\{\mathbf{r}\},\{\mathbf{R}\})\phi(\{\mathbf{R}\},t)\right\}\psi(\{\mathbf{r}\},t). \quad (2.86)$$

Likewise Eq. (2.84) reduces to an effective TDSE for the nuclear wavefunction,

$$i\hbar\frac{\partial}{\partial t}\phi(\{\mathbf{R}\},t) = -\frac{\hbar^2}{2}\sum_{\alpha}\frac{1}{M_\alpha}\nabla_{\alpha}^2\phi(\{\mathbf{R}\},t) + \left\{\int d\{\mathbf{r}\}\ \psi^*(\{\mathbf{r}\},t)\hat{H}_{BO}(\{\mathbf{r}\},\{\mathbf{R}\})\psi(\{\mathbf{r}\},t)\right\}\phi(\{\mathbf{R}\},t). \quad (2.87)$$

Eqs. (2.86) and (2.87) form the basis of the TDSCF method.[114] The electrons move in an average potential energy surface created by the nuclear degrees of freedom, and similarly the nuclear motion is determined by an effective mean field created by the electrons. The Ehrenfest approximation is to take the classical limit of the TDSCF method for nuclear motion. Similar to Section 2.7.1, by writing $\phi_j(\{\mathbf{R}\},t)$ as

$$\phi_j(\{\mathbf{R}\},t) = A(\{\mathbf{R}\},t)\exp\left\{\frac{i}{\hbar}S(\{\mathbf{R}\},t)\right\}, \quad (2.88)$$

we can derive the Ehrenfest equations of motion

$$\frac{dP_\alpha}{dt} = -\nabla_\alpha\left[\int d\{\mathbf{r}\}\ \psi^*(\{\mathbf{r}\},t)\hat{H}_{BO}(\{\mathbf{r}\},\{\mathbf{R}\})\psi(\{\mathbf{r}\},t)\right] = -\nabla_\alpha\left\langle\hat{H}_{BO}\right\rangle. \quad (2.89)$$

The classical limit of Eq. (2.86) is obtained by replacing the nuclear wavefunction by a Dirac delta function at the classical coordinates $\{\mathbf{R}\}$,

$$i\hbar\frac{\partial}{\partial t}\psi(\{\mathbf{r}\},\{\mathbf{R}\},t) = \hat{H}_{BO}(\{\mathbf{r}\},\{\mathbf{R}\})\psi(\{\mathbf{r}\},\{\mathbf{R}\},t). \quad (2.90)$$

The Ehrenfest method allows for feedback between the nuclear and electronic degrees of freedom in both directions, and therefore is a self-consistent method. It is routinely used to model non-adiabatic dynamics.[115–119] Implementation of Ehrenfest dynamics for the polyene systems considered in this thesis is explained in Section 3.2.

2.7.3 Surface Hopping

While Ehrenfest dynamics produce accurate results if the coupled adiabatic states are similar in character, its mean-field nature implies that it fails to properly describe dynamics if the wavepacket bifurcates onto adiabatic surfaces with very different character.[113] Tully's surface hopping technique was developed to overcome the erroneous mean-field approximation of the Ehrenfest method.[120]

Surface hopping is a multi-configuration method, where the product wavefunction of Eq. (2.75) is replaced by

$$\Psi(\{\mathbf{r}\},\{\mathbf{R}\},t) = \sum_i \phi_i(\{\mathbf{R}\},t)\psi_i(\{\mathbf{r}\};\{\mathbf{R}\}), \tag{2.91}$$

where we have used the Born-Oppenheimer (or adiabatic) basis for the electronic wavefunctions. Substituting Eq. (2.91) into the full TDSE, left multiplying by $\psi_j(\{\mathbf{r}\};\{\mathbf{R}\})$, and integrating over $\{\mathbf{r}\}$ gives an effective TDSE for the nuclear wavefunction,

$$\begin{aligned} i\hbar\frac{\partial}{\partial t}\phi_j(\{\mathbf{R}\},t) = &-\frac{\hbar^2}{2}\sum_\alpha \frac{1}{M_\alpha}\nabla_\alpha^2\phi_j(\{\mathbf{R}\},t) + E_j(\{\mathbf{R}\})\phi_j(\{\mathbf{R}\},t) \\ &+ \frac{\hbar^2}{2}\sum_{\alpha,i}\frac{1}{M_\alpha}D^\alpha_{j,i}(\{\mathbf{R}\})\phi_i(\{\mathbf{R}\},t) \\ &- \hbar^2\sum_{\alpha,i\neq j}\frac{1}{M_\alpha}\mathbf{d}^\alpha_{j,i}(\{\mathbf{R}\})\cdot\nabla_\alpha\phi_i(\{\mathbf{R}\},t), \end{aligned} \tag{2.92}$$

where $\mathbf{d}^{\alpha}_{j,i}(\{\mathbf{R}\})$ and $D^{\alpha}_{j,i}(\{\mathbf{R}\})$ are the non-adiabatic coupling terms defined by Eqs. (2.11) and (2.12) respectively. Comparing Eqs. (2.76) and (2.92), we see that the last two terms of Eq. (2.92) induce the electronic transitions via non-adiabatic coupling.

Taking the classical limit of the multi-configuration wavefunction, we arrive at surface hopping.[120] The nuclear wavefunction $\phi_j(\{\mathbf{R}\},t)$ is expressed as

$$\phi_j(\{\mathbf{R}\},t) = A_j(\{\mathbf{R}\},t)\exp\Big\{\frac{i}{\hbar}S_j(\{\mathbf{R}\},t)\Big\}, \tag{2.93}$$

with multiple $\phi_j(\{\mathbf{R}\},t)$ states contributing to the total wavefunction. Substituting Eq. (2.93) in Eq. (2.92) and separating the real and imaginary functions lead to two coupled sets of equations, as detailed in ref [120]. Taking the classical limit defined by $\hbar \to 0$, one of them reduces to

$$\frac{\partial S_j(\{\mathbf{R}\},t)}{\partial t} + \sum_{\alpha}\frac{1}{2M_\alpha}\left[\nabla_\alpha S_j(\{\mathbf{R}\},t)\right]^2 + E_j(\{\mathbf{R}\}) = 0, \tag{2.94}$$

which depends only on a single adiabatic surface and can be solved to find $S_j(\{\mathbf{R}\},t)$. The other equation (omitting the independent variables for clarity),

$$\begin{aligned}\frac{\partial A_j}{\partial t} &+ \sum_{\alpha}\frac{1}{M_\alpha}\nabla_\alpha A_j\cdot\nabla_\alpha S_j + \sum_{\alpha}\frac{1}{2M_\alpha}A_j\nabla^2_\alpha S_j \\ &+ \sum_{\alpha,i}\frac{1}{M_\alpha}A_i\mathbf{d}^{\alpha}_{j,i}\cdot\nabla_\alpha S_i\exp\Big\{\frac{i}{\hbar}\left(S_i - S_j\right)\Big\} = 0,\end{aligned} \tag{2.95}$$

describes the probability flux on each state. Due to the non-locality of the coupling terms, the flux on the adiabatic surfaces of one trajectory is affected by the other trajectories. This renders finding numerical solutions of Eq. (2.95) difficult. Surface hopping methods circumvent this difficulty by imposing the independent trajectory approximation, i.e, a trajectory evolves on a single adiabatic surface rather than on

an effective mean-field potential energy surface. The probability amplitudes of the nuclear wavefunctions,

$$c_j(t) = A_j \exp\Big\{-\frac{i}{\hbar}\int^t dt' E_j(t')\Big\}, \tag{2.96}$$

can be used to specify the electronic wavefunction at time t by expanding it in the adiabatic basis,

$$\psi(\{\mathbf{r}\},\{\mathbf{R}\},t) = \sum_j c_j(t)\psi_j(\{\mathbf{r}\},\{\mathbf{R}\}). \tag{2.97}$$

Substituting Eq. (2.97) into the TDSE for the electronic wavefunction, we arrive at the coupled equations of motion for the probability amplitudes,

$$i\hbar\dot{c}_j(t) = c_j(t)E_j(\{\mathbf{R}\}) - i\hbar\sum_{\alpha,i\neq j} c_i(t)E_j\dot{\mathbf{R}}_\alpha\cdot\mathbf{d}^\alpha_{j,i}(\{\mathbf{R}\}), \tag{2.98}$$

where $\dot{\mathbf{R}}_\alpha$ is the nuclear velocity vector. To derive an equation of motion for the probability flux of the adiabatic state j, A_j, Eq. (2.96) is substituted in Eq. (2.98). This gives

$$\frac{\partial A_j}{\partial t} + \sum_{\alpha,i}\frac{1}{M_\alpha}A_i\mathbf{d}^\alpha_{j,i}\cdot\dot{\mathbf{R}}_\alpha\exp\Big\{-\frac{i}{\hbar}\int^t dt'\left[E_i(t') - E_j(t')\right]\Big\} = 0. \tag{2.99}$$

$|A_j|^2$ is the probability that the system will be in adiabatic state j at time t. From Eq. (2.99) it follows that the probability of a transition between two adiabatic states is proportional to the product of nuclear velocities and first order derivative couplings between the states.

In practice, the variation of the amplitudes $c_j(t)$ with time is found by numerically integrating Eq. (2.98) along each trajectory. A trajectory can occupy different adiabatic states at different times t, and this leads to 'hopping' within adiabatic states. The hopping probabilities are determined by a stochastic algo-

rithm, and several surface hopping techniques with varied hopping algorithms have been suggested.[120–127] A famous choice for the hopping algorithm is Tully's fewest switches surface hopping (FSSH) technique,[122] which is designed to maintain the number of trajectories assigned to a given adiabatic surface j proportional to its relative population $|c_j(t)|^2$ within minimum number of hops. For a two-state system the FSSH switching probability from adiabatic state 1 to state 2 during a time Δt is given by

$$P_{1\to 2} = -\frac{d}{dt}\log|c_1(t)|^2. \tag{2.100}$$

After each successful hop, the nuclear velocities are changed in order to maintain conservation of energy.[122]

Readers are directed to ref [128] for a recent review of surface hopping techniques.

2.7.4 TEBD-Ehrenfest

Another approach to improve on the Ehrenfest method is to incorporate quantum effects to the nuclear degrees of freedom. Mannouch and Barford developed the TEBD-Ehrenfest method for dynamical simulations of the Frenkel-Holstein model.[129–131] In this formalism, nuclear motion is described by a mean-field displacement subjected to Ehrenfest dynamics, with quantum fluctuations around the mean-field value. The initial implementation of TEBD-Ehrenfest method for the Frenkel-Holstein Hamiltonian models the classical degrees of freedom as uncoupled Einstein oscillators.[130] Here we outline the generalisation of the TEBD-Ehrenfest method for coupled nuclei, which are described by Debye oscillators.

Following ref [93], the nuclear degrees of freedom of the H_{UVP} Hamiltonian given

by Eq. (2.59) can be quantised as,

$$H_{\mathrm{UVP}} = -\sum_{l} \left[t_0 + \hbar\omega_D A_D (B_{l+1} - B_l)\right] \hat{T}_{l,l+1} + \hbar\omega_D \sum_{l} \left[b_l^\dagger b_l + \frac{1}{2}\left(1 - B_{l+1} B_l\right)\right], \tag{2.101}$$

where $b_l^\dagger$ and b_l are the creation and destruction operators of the quantum harmonic oscillator at site l respectively, and

$$B_l = \frac{b_l^\dagger + b_l}{\sqrt{2}}, \tag{2.102}$$

is the dimensionless displacement of the lth oscillator. $\omega_D = \sqrt{2K/M}$ is the oscillator frequency of the (coupled) Debye phonons, and A_D is a dimensionless electron-phonon coupling constant given by

$$A_D = \alpha \sqrt{\frac{1}{2\hbar\omega_D K}}\ . \tag{2.103}$$

We seek a general solution to Eq. (2.101) that describes the nuclear motion as a summation of a mean-field classical component and a quantum fluctuation around the classical displacement, i.e.,

$$B_l = u_l^{\mathrm{eh}} + B_l', \tag{2.104}$$

where u_l^{eh} is the dimensionless classical displacement of the lth site described by Ehrenfest dynamics and B_l' is the *displaced* dimensionless displacement operator. B_l' can be expressed in terms of displaced simple harmonic ladder operators as

$$B_l' = \frac{b_l'^\dagger + b_l'}{\sqrt{2}}, \tag{2.105}$$

where

$$b_l'^{\dagger} = b_l{}^{\dagger} - \alpha_l^*(t). \tag{2.106}$$

$\alpha_l(t)$ parametrises the classical displacement of site l. It is related to u_l^{eh} by

$$\alpha_l = \frac{u_l^{\mathrm{eh}} + iP_l^{\mathrm{eh}}}{\sqrt{2}}, \tag{2.107}$$

where P_l^{eh} is the dimensionless momentum of the lth site.

A general solution of Eq. (2.101) is of the form

$$|\psi(t)\rangle = \sum_E \sum_{\{p\}} C_{E,\{p\}}(t)\, |E, \{p\}\rangle\,, \tag{2.108}$$

where $C_{E,\{p\}}(t)$ is a time-dependent coefficient determined by an effective Hamiltonian $\hat{H}_{\mathrm{eff}}$ yet to be defined. The product state $|E, \{p\}\rangle$ is of the form

$$|E, \{p\}\rangle = |\psi_E\rangle \otimes |p_1(t)\rangle \otimes |p_2(t)\rangle \otimes \cdots \otimes |p_N(t)\rangle\,, \tag{2.109}$$

where $|\psi_E\rangle$ is an eigenstate of the electronic Hamiltonian. $|p_l(t)\rangle$ is the pth displaced excitation of the coherent state on site l, $|\alpha_l\rangle$, i.e.,

$$|p_l(t)\rangle = \frac{(b_l'^{\dagger})^p}{\sqrt{p!}}\, |\alpha_l\rangle\,, \tag{2.110}$$

$|\alpha_l(t)\rangle$ is parametrised by $\alpha_l(t)$, i.e.,

$$|\alpha_l(t)\rangle = \exp\left(-\frac{|\alpha_l(t)|^2}{2}\right) \sum_q \frac{\alpha_l(t)^q}{\sqrt{q!}}\, |q_l\rangle\,, \tag{2.111}$$

with the quantum oscillator states $|q_l\rangle$ given by

$$|q_l\rangle = \frac{(b_l^\dagger)^q}{\sqrt{q!}}|0\rangle\,. \tag{2.112}$$

By substituting Eq. (2.108) in the TDSE, we get

$$i\hbar\frac{d}{dt}C_{E,\{p\}} = \sum_{E'}\sum_{\{p'\}} C_{E',\{p'\}}\,\langle E,\{p\}|H_{\text{eff}}|E',\{p'\}\rangle \tag{2.113}$$

where $H_{\text{eff}} = H_{\text{UVP}} + H'$ and H' satisfies

$$\frac{d}{dt}|E,\{p\}\rangle = |E,\{\dot{p}\}\rangle = \frac{i}{\hbar}H'\,|E,\{p\}\rangle\,. \tag{2.114}$$

Eq. (2.114) is an equation of motion to determine $C_{E,\{p\}}(t)$, and can be solved once H' is known. By differentiating $|E,\{p\}\rangle$ with respect to t, $|E,\{\dot{p}\}\rangle$ can be written as

$$|E,\{\dot{p}\}\rangle = \left[\sum_l O_l\right]|E,\{p\}\rangle\,, \tag{2.115}$$

where $O_l\,|p_l\rangle = |\dot{p}_l\rangle$. Then we can write

$$H' = -i\hbar\sum_l O_l. \tag{2.116}$$

Using Eqs. (2.106), (2.111), (2.110) and their time derivatives we arrive at an explicit expression for O_l, i.e.,

$$O_l = -\dot{\alpha}_l^* b_l' + \dot{\alpha}_l b_l'^\dagger + \frac{1}{2}(\dot{\alpha}_l\alpha_l^* - \alpha_l\dot{\alpha}_l^*) \tag{2.117}$$

Substituting for α_l in Eq. (2.117) from Eq. (2.107) and simplifying, we arrive at

the effective Hamiltonian

$$H_{\text{eff}} = -\sum_l \left[t_0 + \hbar\omega_D A_D \left(u_{l+1}^{\text{eh}} - u_l^{\text{eh}}\right)\right] \hat{T}_{l,l+1} - \hbar\omega_D A_D \sum_l \left(B'_{l+1} - B'_l\right) \left(\hat{T}_{l,l+1} - \left\langle \hat{T}_{l,l+1} \right\rangle\right)$$
$$+\hbar\omega_D \sum_l \left[b_l'^{\dagger} b'_l + \frac{1}{2}\right] + \frac{\hbar\omega_D A_D}{2} \sum_l \left(u_{l+1}^{\text{eh}} - u_l^{\text{eh}}\right) \left\langle \hat{T}_{l,l+1} \right\rangle - \frac{\hbar\omega_D}{2} \sum_l B'_{l+1} B'_l \tag{2.118}$$

The TEBD-Ehrenfest method works by propagating the nuclei degrees of freedom classically similar to Ehrenfest dynamics, and evolving the electronic wavefunction using TDSE under the effective Hamiltonian of Eq. (2.118).

Future work will focus on comparison of performance of FSSH and TEBD-Ehrenfest methods against the classical Ehrenfest simulations of Chapter 5.

Chapter 3

Computational Methods

This chapter describes the computational methods used to solve the models used in this thesis. Density Matrix Renormalisation Group (DMRG) is a powerful set of algorithms useful for modelling one-dimensional quantum systems. DMRG is extensively used for modelling the electronic degrees of freedom of the model Hamiltonians used in this thesis. This chapter introduces the key concepts of DMRG. This chapter also introduces the Ehrenfest method, a technique used to determine the motion of nuclei evolving under Newton's equations of motion by treating the electronic degrees of freedom as an effective potential. Finally, we describe the optimisation procedure to find the symmetry breaking Hamiltonians introduced in Chapter 2 via a projected gradient descent algorithm.

3.1 Density Matrix Renormalisation Group (DMRG)

The single-site basis for the π-electron models, $\{ \text{—}, \uparrow, \downarrow, \updownarrow \}$, has a dimensionality of 4. Therefore, exactly solving the Schrödinger equation for relevant carotenoid chain lengths like $N = 18$ would require solving a $S_z = 0$ Hilbert space of size $\approx 2.4 \times 10^9$, which is not feasible in realistic time scales. Density matrix renormalisation group (DMRG) methods are based on the premise that by an efficient

truncation of the exact Hilbert space to retain only the important many-particle states, the most important features of the system can be preserved at a significantly lower computational cost. We begin this section by introducing the numerical renormalisation group algorithm, the predecessor of DMRG, and its limitations. Then we introduce the static DMRG algorithm in the infinite and finite forms, and show how DMRG can easily be extended to model real time evolution via the adaptive time-dependent DMRG (tDMRG) algorithm, and to calculate dynamical correlation functions using the Lanczos-DMRG method. We discuss the accuracy of DMRG and why it works so well for one-dimensional quantum systems. Finally, we describe how DMRG can be formulated in terms of matrix product states.

Within the past 30 years, DMRG has evolved to be one of the premier numerical methods to study strongly correlated quantum systems. The initial DMRG formalism to model ground state equilibrium properties[132] has been generalised to study time-dependent phenomena[133,134] and dynamical correlations,[135] and has been adapted by the quantum chemistry community.[136–138] DMRG has been further developed under the Matrix Product State (MPS) formalism.[139,140] Two seminal reviews by Schollwöck, one from a traditional renormalisation perspective[141] and the other from the MPS perspective,[142] provide a good overview of DMRG methods. A major part of the work presented in this thesis is based on time-dependent DMRG, and readers are referred to ref [143] for a review of time-dependent density matrix renormalisation group methods.

3.1.1 Numerical Renormalisation Group (NRG)

Renormalisation group techniques attempt to solve the problem of exponentially growing Hilbert spaces by iteratively building up the system size and retaining only a certain number of relevant states at each step of the iterative procedure. Suppose a

system of size N is described accurately by D basis states. A new system of size $2N$ is constructed by augmenting two blocks A and B, each of size N. The augmented block AB is accurately described by a Hilbert space of size D^2, and any state $|\Psi\rangle$ of the new system can be expressed as

$$|\Psi\rangle = \sum_{i,j}^{D} \Psi_{i,j} |i\rangle_A |j\rangle_B . \tag{3.1}$$

NRG proceeds by diagonalising the augmented block Hamiltonian H_{AB} and retaining only the D lowest eigenstates of the system AB for the next iteration of the algorithm. As the system size grows exponentially with the number of iterations, NRG can very easily reach the thermodynamic limit, and was first used by Wilson to solve the Kondo problem.[144] While NRG has been later generalised to study quantum impurity problems,[145] it has not been able to properly describe the ground state properties of other many-body problems like the one-dimensional tight-binding or Heisenberg models. Using a single non-interacting particle in one-dimensional box model, White and Noack demonstrated that NRG fails due to its inability to account for boundary effects.[146] This is schematically illustrated in Fig. 3.1. The lowest eigenstate of the augmented block AB has its maximum amplitude at the boundary of the two constituent system blocks A and B. This boundary is not well described by the low energy states of the constituent system blocks A and B as these states have nodes at the boundary.

3.1.2 Static DMRG algorithm

3.1.2.1 Infinite Lattice DMRG

DMRG was first introduced in the form of infinite lattice DMRG, by White in 1992 to calculate ground state properties of antiferromagnetic Heisenberg spin chains.[132] We

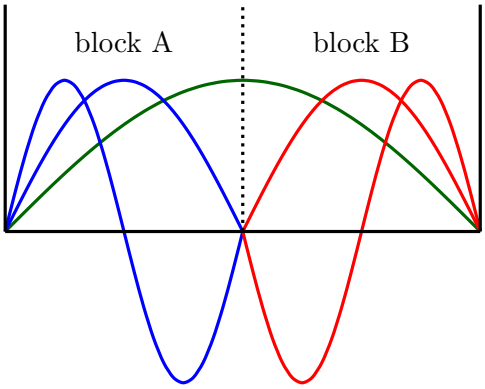

Figure 3.1: Diagram illustrating lowest lying eigenstates of block A (blue), block B (red), and the lowest eigenstate of the augmented block AB (green) of the single particle in a one-dimensional block model. States of blocks A and B have nodes at the boundary, and is unable to properly represent the lowest eigenstate of the augmented block AB, which has its highest amplitude at the boundary.

introduce a chain of sites consisting of two blocks, S (system) and E (environment), each containing one site at the beginning. The single site k is described by a d-dimensional basis $\{|\alpha_k\rangle\}$. (For the calculations presented in this thesis, we use the single-size basis of the p_z orbitals of a carbon atom, i.e., $\{|\alpha_k\rangle\} = \{$ —, ↑, ↓, ⇅ $\}$). Now we insert a pair of single sites between the blocks S and E. The resultant four primitive block four site chain is solved exactly by diagonalising the Hamiltonian, to achieve a new system block of size two. The algorithm proceeds, adding two sites at each step of the iteration. As the chain size grows linearly, its Hilbert space grows exponentially. Diagonalisation of the Hamiltonian is efficiently implemented via sparse-matrix diagonalisation (the conjugate gradient algorithm was used for the work presented in this thesis). Suppose that a system block of length $(k-1)$ is reached by exact diagonalisation. This block is described by a Hilbert space of size M_l, spanned by the basis states $\{|l_{k-1}\rangle\}$. Suppose exact diagonalisation beyond this chain size is not possible due to the exponentially growing Hilbert space, and a truncation procedure is required. The infinite lattice DMRG algorithm begins at this point.

Consider the process of the linear growth of this system block by adding a single site at index k (see Fig. 3.2). An augmented system block of length k is constructed

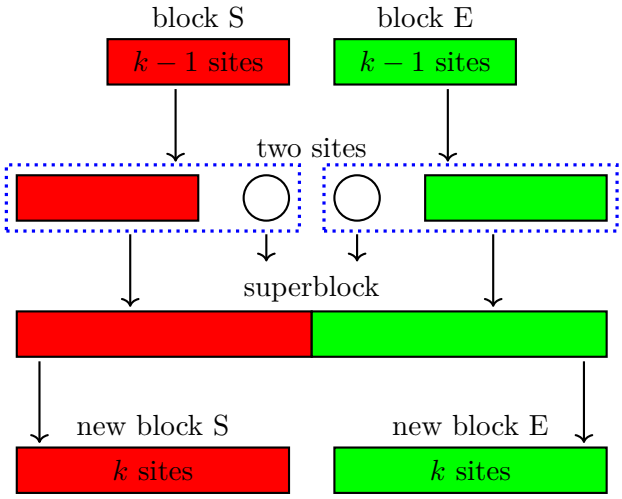

Figure 3.2: Schematic diagram illustrating one iteration of the infinite lattice DMRG algorithm.

in the product Hilbert space spanned by $\{|l_{k-1}\rangle \otimes |\alpha_k\rangle\}$, with dimensions $N_S = M_l \times d$. An analogous augmented environment is constructed in the product Hilbert space spanned by $\{|\alpha_{k+1}\rangle \otimes |r_{k-1}\rangle\}$, with dimensions $N_E = M_r \times d$. A superblock of length $2k$ is now formed in the product Hilbert space spanned by $\{|l_{k-1}\rangle \otimes |\alpha_k\rangle \otimes |\alpha_{k+1}\rangle \otimes |r_{k-1}\rangle\}$. The ground state,

$$|\Psi\rangle = \sum_{l_{k-1}=1}^{M_l} \sum_{\alpha_k=1}^{d} \sum_{\alpha_{k+1}=1}^{d} \sum_{r_{k-1}=1}^{M_r} \Psi_{l_{k-1},\alpha_k,\alpha_{k+1},r_{k-1}} |l_{k-1}\rangle \otimes |\alpha_k\rangle \otimes |\alpha_{k+1}\rangle \otimes |r_{k-1}\rangle\,, \quad (3.2)$$

is obtained by diagonalisation of the Hamiltonian in the superblock basis, using a sparse matrix diagonalisation routine.

Defining the augmented system block state $|i\rangle \in \{|l_{k-1}\rangle \otimes |\alpha_k\rangle\}$, and the augmented environment block state $|j\rangle \in \{|\alpha_{k+1}\rangle \otimes |r_{k-1}\rangle\}$, the ground state may also be expressed in the augmented block basis as,

$$|\Psi\rangle = \sum_{i=1}^{N_S} \sum_{j=1}^{N_E} \Psi_{i,j} |i\rangle \otimes |j\rangle\,. \quad (3.3)$$

From eq (3.3), we see that Ψ can be recast into a rectangular matrix of dimension

$N_S \times N_E$, which can then be decomposed using singular value decomposition (SVD) as

$$\Psi = UDV^\dagger, \tag{3.4}$$

where U is a unitary matrix of dimension $N_S \times N_E$, V is a unitary matrix of dimension $N_E \times N_E$, and D is a diagonal matrix of dimension $N_E \times N_E$ with elements $\{\lambda_\beta\}$. Assuming $N_E \leq N_S$, the coefficient $\Psi_{i,j}$ of the matrix Ψ can be written as

$$\Psi_{i,j} = \sum_{\beta=1}^{N_E} U_{i,\beta}\lambda_\beta (V^\dagger)_{\beta,j} = \sum_{\beta=1}^{N_E} U_{i,\beta}\lambda_\beta V^*_{\beta,j} \ . \tag{3.5}$$

Substituting eq (3.5) to eq (3.3) we get,

$$|\Psi\rangle = \sum_{i=1}^{N_S}\sum_{j=1}^{N_E}\left(\sum_{\beta}^{N_E} U_{i,\beta}\lambda_\beta V^*_{\beta,j}\right)|i\rangle \otimes |j\rangle = \sum_{\beta}^{N_E}\lambda_\beta\left(\sum_{i=1}^{N_S} U_{i,\beta}\,|i\rangle\right)\otimes\sum_{j=1}^{N_E}\left(\sum_{j=1}^{N_E} V^*_{\beta,j}\,|j\rangle\right). \tag{3.6}$$

Defining the transformation $|\beta\rangle_S = \sum_i U_{i,\beta}\,|i\rangle$ and $|\beta\rangle_E = \sum_j V^*_{\beta,j}\,|j\rangle$, we can express $|\Psi\rangle$ in a new orthogonal basis, i.e.,

$$|\Psi\rangle = \sum_{\beta=1}^{N_E}\lambda_\beta\,|\beta\rangle_S \otimes |\beta\rangle_E\,. \tag{3.7}$$

Eq (3.7) is known as the Schmidt decomposition of the state Ψ, and the bases $\{|\beta\rangle_S\}$ and $\{|\beta\rangle_E\}$ are called the Schmidt bases. In general, for $r = \min(N_S, N_E)$ we can write the Schmidt decomposition as[147]

$$|\Psi\rangle = \sum_{\beta=1}^{r}\lambda_\beta\,|\beta\rangle_S \otimes |\beta\rangle_E\,. \tag{3.8}$$

The reduced density operator of the system is defined by $\hat{\rho}_S = \mathrm{tr}_E\,|\Psi\rangle\langle\Psi|$. Since Schmidt bases are column vectors of the unitary matrices U and V, $\hat{\rho}_S$ can be

expressed in the Schmidt basis $\{|\beta\rangle_S\}$ as

$$\hat{\rho}_S = \sum_{\beta=1}^{N_S} \lambda_\beta^2 |\beta\rangle_S \ {}_S\langle\beta|. \tag{3.9}$$

It follows that $|\beta\rangle_S$ and $\lambda_\beta^2 = \omega_\beta$ are the eigenstates and eigenvalues, respectively, of $\hat{\rho}_S$. It can similarly be shown that the reduced density operator of the environment, $\hat{\rho}_E = \mathrm{tr}_S \, |\Psi\rangle \langle\Psi|$ is given by

$$\hat{\rho}_E = \sum_{\beta=1}^{N_E} \lambda_\beta^2 |\beta\rangle_E \ {}_E\langle\beta|. \tag{3.10}$$

Now a truncation procedure must be introduced to describe the system block of size k using a basis of dimension $M_S < N_S$. Suppose that the ground state of the system can be expressed by the approximate state $|\tilde{\Psi}\rangle$ in this truncated Hilbert space,

$$|\tilde{\Psi}\rangle = \sum_{p=1}^{M_S} \sum_{j=1}^{N_E} \tilde{\Psi}_{p,j} \, |p\rangle \otimes |j\rangle \, . \tag{3.11}$$

Finding the optimum $|\tilde{\Psi}\rangle$ is achieved by the minimisation of the quadratic norm S_2,

$$S_2 = | \, |\Psi\rangle - \, |\tilde{\Psi}\rangle \, |^2. \tag{3.12}$$

Using matrix notation for $|\tilde{\Psi}\rangle$ and $|\Psi\rangle$, and eq (3.5), S_2 can be evaluated as

$$S_2 = \sum_{i,j} \left(\sum_{\beta=1}^{N_S} U_{i,\beta} \lambda_\beta V^*_{\beta,j} - \sum_{\beta=1}^{M_S} U_{i,\beta} \lambda_\beta V^*_{\beta,j} \right)^2 = \sum_{\beta=M_S+1}^{N_S} \lambda_\beta^2 \, . \tag{3.13}$$

S_2 is therefore minimised by retaining the M_S eigenstates of $\hat{\rho}_S$ with the largest eigenvalues. This is the key result of DMRG. The sum of the discarded eigenvalues of $\hat{\rho}_S$ is referred to as the truncation error. DMRG proceeds by constructing the reduced density matrix $\hat{\rho}_S$ from $|\Psi\rangle$, and then diagonalising $\hat{\rho}_S$ using a dense matrix

diagonalisation procedure. The new truncated basis for the new system block of size k, $\{|l_k\rangle\}$, is now constructed by retaining the M_S eigenstates of $\hat{\rho}_S$ with the the highest eigenvalues. The truncated basis for the environment block $\{|r_k\rangle\}$ can be constructed similarly.

Once the truncated basis $\{|l_k\rangle\}$ is known, all operators, including the Hamiltonian, are rotated to the new Hilbert space via a similarity transformation. Suppose $\hat{O}_n$ is a generic operator, $n \in \{1, 2, \ldots, k\}$, and $|l_k\rangle$, $|\tilde{l}_k\rangle \in \{|l_k\rangle\}$, and $|\alpha_k\rangle$ and $|\tilde{\alpha}_k\rangle$ are single site basis states. Then $\hat{O}_k$ in the new truncated Hilbert space is given by

$$\langle l_k|\hat{O}_k|\tilde{l}_k\rangle = \sum_{l_{k-1}=1}^{M_l} \sum_{\alpha_k=1}^{d} \sum_{\tilde{\alpha}_k=1}^{d} [\langle l_k|l_{k-1}\rangle \otimes |\alpha_k\rangle] \langle \alpha_k|\hat{O}_k|\tilde{\alpha}_k\rangle [\langle l_{k-1}| \otimes \langle \tilde{\alpha}_k|\tilde{l}_k\rangle]. \quad (3.14)$$

$\hat{O}_n$ where $n < k$ is transformed to the truncated Hilbert space by

$$\langle l_k|\hat{O}_n|\tilde{l}_k\rangle = \sum_{l_{k-1}=1}^{M_l} \sum_{\tilde{l}_{k-1}=1}^{M_l} \sum_{\alpha_k=1}^{d} [\langle l_k|l_{k-1}\rangle \otimes |\alpha_k\rangle] \langle l_{k-1}|\hat{O}_n|\tilde{l}_{k-1}\rangle [\langle \tilde{l}_{k-1}| \otimes \langle \alpha_k|\tilde{l}_k\rangle]. \quad (3.15)$$

The operators and the reduced density matrices are stored to be used in the next iterations of the algorithm. This completes an iteration of infinite lattice DMRG. The procedure is repeated until the desired chain size N is reached.

3.1.2.2 Finite Lattice DMRG Sweeping

Suppose we have a system and environment block, each of length k during an intermediate step of the infinite lattice DMRG algorithm. The truncated basis $\{|l_k\rangle\}$ is optimised for a superblock of length $2k$, and not for a superblock of length N, which is the chain length we are interested in. Use of these intermediary bases which are not optimised for the final chain length introduces a systematic error to the calculations. Furthermore, if the system is considerably disordered such that the Hamiltonian will contain local minima, the states corresponding to the global min-

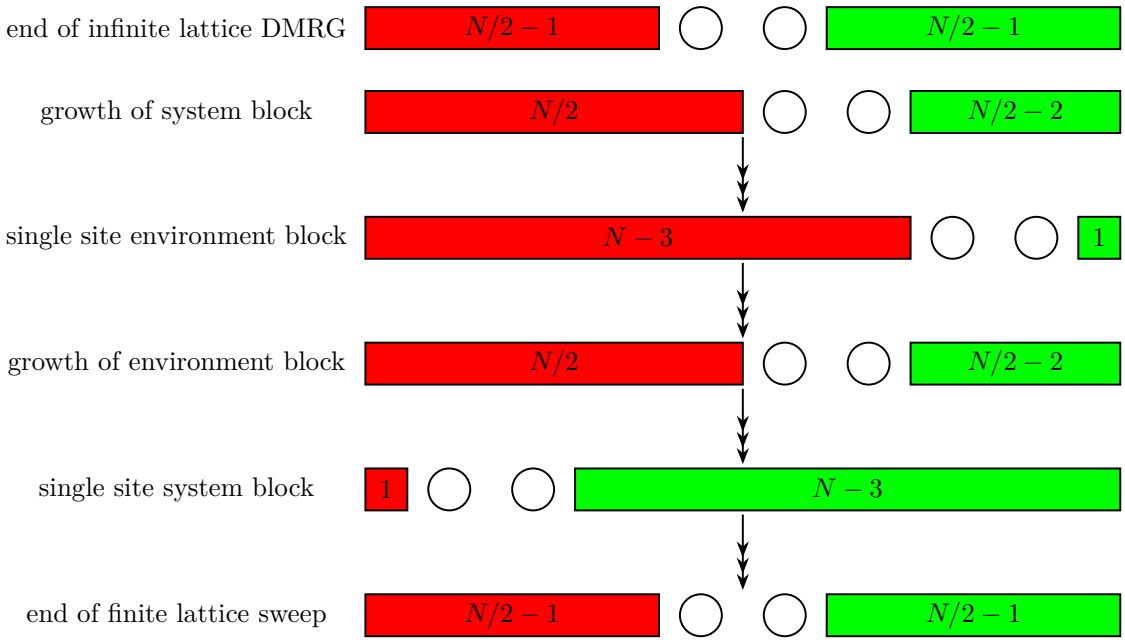

Figure 3.3: Schematic diagram for the finite lattice DMRG algorithm illustrating a single finite lattice sweep. The number of sites in each block is shown as text. An open circle represents a single site block.

ima might be discarded during the intermediate steps of the infinite lattice DMRG, as the algorithm has no knowledge on the final form of the Hamiltonian during the intermediary steps. These errors can not only effect the quantitative results, but also change qualitative behaviour of a system. For instance, Schollwöck et al. demonstrated using the $t-J$ ladder model that the long range correlation of the plaquette currents predicted by the infinite lattice DMRG calculations is erroneous, and the converged system shows an exponential decay of the plaquette currents.[148]

The finite size errors associated with infinite lattice DMRG can be resolved by performing finite 'sweeps' after the infinite lattice DMRG. The finite lattice DMRG algorithm is illustrated in Fig. 3.3. Once the desired system size N is reached, the steps of infinite lattice DMRG is continued, but with one block (system) growing at the expense of the other (environment). The superblock size remains fixed at N, and truncation of the basis is only performed for the growing block. Operators and the reduced density matrix corresponding to the shrinking block is retrieved from storage, as they have already been calculated during the infinite lattice DMRG or the

previous sweep of finite lattice DMRG. Determination of the superblock ground state is efficiently implemented using White's wavefunction mapping algorithm (discussed below),[149] where the ground state found during the previous step of the sweep is rotated into the new Hilbert space to be used as a trial state for the diagonalisation procedure. This procedure is continued until the shrinking block only contains a single site, and then the direction of the sweep is reversed. Several finite lattice DMRG sweeps are performed until the desired convergence is reached.

3.1.2.3 White's Wavefunction Mapping

At each step of the finite lattice DMRG algorithm, the target wavefunction in the superblock basis is found via a sparse matrix diagonalisation procedure. This constitutes the most computationally expensive part of the algorithm. The sparse matrix routines begin with a trial state, and make incremental improvements to it until convergence is achieved. Each iteration of the infinite lattice DMRG algorithm corresponds to a different physical chain length and therefore it is not possible to make an educated guess on the nature of the trial function, thus a random state is chosen as the trial state. However, the converged wavefunction at any step of the finite algorithm represents the same physical system, and in the absence of truncation, should be identical. Therefore, it is possible to use the converged wavefunction of a finite lattice DMRG step as the trial wavefunction for the sparse matrix diagonalisation at the next step, provided that it is rotated to the Hilbert space of the superblock. While this method was developed by White to reduce computational costs associated with finite lattice DMRG,[149] as discussed in Section 3.1.3 it forms an integral part of adaptive time-dependent DMRG.

Suppose the converged wavefunction of the finite lattice DMRG step where the system block is of length $k-1$ is known. Then the environment block is of length

$N-k-1$, and we can express the converged wavefunction as

$$|\Psi\rangle = \sum_{l_{k-1}} \sum_{\alpha_k} \sum_{\alpha_{k+1}} \sum_{r_{N-k-1}} \Psi_{l_{k-1},\alpha_k,\alpha_{k+1},r_{N-k-1}} |l_{k-1}\rangle \otimes |\alpha_k\rangle \otimes |\alpha_{k+1}\rangle \otimes |r_{N-k-1}\rangle \,. \quad (3.16)$$

Now we perform two incomplete basis transformations for the left (growing) and right (shrinking) blocks. That is, we approximate that $|\Psi\rangle$ can be accurately represented in the new truncated Hilbert space by

$$|\Psi\rangle = \sum_{l_k} \sum_{\alpha_{k+1}} \sum_{\alpha_{k+2}} \sum_{r_{N-k-2}} \Psi_{l_k,\alpha_{k+1},\alpha_{k+2},r_{N-k-2}} |l_k\rangle \otimes |\alpha_{k+1}\rangle \otimes |\alpha_{k+2}\rangle \otimes |r_{N-k-2}\rangle \,. \quad (3.17)$$

In order to construct the trial wavefunction $|\Psi\rangle$, we need to find an expression for $\Psi_{l_k,\alpha_{k+1},\alpha_{k+2},r_{N-k-2}}$. From Eq. (3.16) and Eq. (3.17), we get

$$\begin{aligned}
&\Psi_{l_k,\alpha_{k+1},\alpha_{k+2},r_{N-k-2}} \\
&= \langle l_k| \otimes \langle \alpha_{k+1}| \otimes \langle \alpha_{k+2}| \otimes \langle r_{N-k-2}|\Psi\rangle \\
&= \sum_{\substack{\tilde{l}_k,\tilde{\alpha}_{k+1},\\ \tilde{\alpha}_{k+2},\tilde{r}_{N-k-2}}} \Psi_{\tilde{l}_{k-1},\tilde{\alpha}_k,\tilde{\alpha}_{k+1},\tilde{r}_{N-k-1}} \Big[\langle l_k|\tilde{l}_{k-1}\rangle \otimes |\tilde{\alpha}_k\rangle \Big] \langle \alpha_{k+1}|\tilde{\alpha}_{k+1}\rangle \left[\langle \alpha_{k+2}| \otimes \langle r_{N-k-2}|\tilde{r}_{N-k-1}\rangle \right], \\
&= \sum_{\tilde{l}_k,\tilde{\alpha}_{k+2},\tilde{r}_{N-k-2}} \Psi_{\tilde{l}_{k-1},\tilde{\alpha}_k,\tilde{\alpha}_{k+1},\tilde{r}_{N-k-1}} \Big[\langle l_k|\tilde{l}_{k-1}\rangle \otimes |\tilde{\alpha}_k\rangle \Big] \left[\langle \alpha_{k+2}| \otimes \langle r_{N-k-2}|\tilde{r}_{N-k-1}\rangle \right], \qquad (3.18)
\end{aligned}$$

where $\langle l_k|\tilde{l}_{k-1}\rangle \otimes |\tilde{\alpha}_k\rangle = U^*_{i,l_k}$ with $|i\rangle = |\tilde{l}_{k-1}\rangle \otimes |\tilde{\alpha}_k\rangle$ and $\langle \alpha_{k+2}| \otimes \langle r_{N-k-2}|\tilde{r}_{N-k-1}\rangle = V_{j,r_{N-k-1}}$ with $|j\rangle = |\alpha_{k+2}\rangle \otimes |r_{N-k-2}\rangle$ are known from the reduced density operators of the left and right blocks, respectively.

3.1.2.4 Excited State Calculations

The static DMRG algorithm, first formulated for ground state calculations, can be readily generalised to target excited states. The excited states of a molecule are defined by the symmetries it possesses. Study of carotenoid photoexcited states is

a major objective of this thesis, and Section 2.5.1 discusses the symmetries relevant to carotenoid excited states in greater detail.

By exploiting the sparsity of the block symmetry operators (e.g., the particle-hole, spin-flip, and C_2 symmetries), excited states can be conveniently determined by constructing symmetry-adapted states.[150] We then find higher-lying states within a symmetry sector via a Gram-Schmidt projection. In order to accurately describe these excited states, it is necessary to retain the basis states that optimally represent them in the truncated Hilbert space. This is achieved by including them in the reduced density matrix,

$$\hat{\rho}_S = \mathrm{tr}_E \sum_i \kappa_i \left|\Psi_i\right\rangle \left\langle\Psi_i\right| , \tag{3.19}$$

where the summation includes all the targeted states. κ_i is usually chosen to be the same for all states such that $\sum_i \kappa_i = 1$. It is important to note that to accurately represent the ith eigenstate within a symmetry sector, $|\Psi_i\rangle$, in the truncated basis, it is necessary to include all states from the ground state up to $|\Psi_i\rangle$ in the reduced density operator $\hat{\rho}_S$.

3.1.3 Adaptive Time-Dependent DMRG (tDMRG)

The dynamics of the evolving system under the Hamiltonian $\hat{H}$ is fully determined by solving the time-dependent Schrödinger equation

$$i\hbar \frac{\partial}{\partial t} \left|\Psi(t)\right\rangle = \hat{H}(t) \left|\Psi(t)\right\rangle . \tag{3.20}$$

In the limit that $\delta t \to 0$, Eq. (3.20) has the formal solution

$$\left|\Psi(t+\delta t)\right\rangle = \exp\left(-i\hat{H}(t)\delta t/\hbar\right) \left|\Psi(t)\right\rangle . \tag{3.21}$$

For a time invariant Hamiltonian $\hat{H}(t) = \hat{H}$, if its eigenstates $\hat{H}\,|\psi_n\rangle = E_n\,|\psi_n\rangle$ are known, then $|\Psi(t=0)\rangle = \sum_n c_n\,|\psi_n\rangle$ and

$$|\Psi(t)\rangle = \sum_n c_n \exp\left(-iE_n t/\hbar\right)\,|\psi_n\rangle\,, \tag{3.22}$$

determines the evolving state $|\Psi(t)\rangle$ at any time t. However, as we have already seen in Section 2.4, the UVP Hamiltonian, the π-electron model used in this thesis for dynamical simulations, depends parametrically on the nuclear displacements $\{u_n\}$. As we will see in Section 3.2, under the Ehrenfest equations of motion, $\{u_n\}$ changes with time. In addition, while it is possible to completely determine the basis $\{|\psi_n\rangle\}$ for small systems, it is not possible to do so for strongly correlated systems in a truncated Hilbert space.

The first attempt to study time-dependent phenomena using DMRG by Cazalilla and Marston[151] employed the fixed Hilbert space optimised for the ground state of the corresponding time-independent problem found using infinite lattice DMRG. As the system evolves in time, this fixed Hilbert space is unable to accurately describe $|\Psi(t)\rangle$, and the method failed. Luo and co-workers[152] improved on their method by targeting multiple time-dependent states in the reduced density operator during dynamics. However, the requirement to keep track of several states in the reduced density operator meant their method was computationally too expensive.

The breakthrough came with Vidal's time-evolving block decimation (TEBD) algorithm, where it was proposed to use adaptive Hilbert spaces to simulate weakly entangled quantum systems.[139,140] The adaptive time-dependent density matrix renormalisation group (tDMRG) method, developed in 2004, generalised DMRG to study time-dependent phenomena using TEBD.[133,134] In this formalism, the evolving state $|\Psi(t)\rangle$ is determined in a truncated Hilbert space such that the loss of information about the system is minimised. The algorithm is efficiently implemented for

Hamiltonians containing only on-site and nearest neighbour interactions. Such a Hamiltonian can be written as a sum of bond Hamiltonians,

$$\hat{H} = \hat{H}_{1,2} + \hat{H}_{2,3} + \hat{H}_{3,4} + \cdots \hat{H}_{n,n+1} + \cdots + \hat{H}_{N-1,N}, \tag{3.23}$$

where

$$\hat{H}_{n,n+1} = \begin{cases} \hat{H}_1^{\text{intra}} + \frac{1}{2}\hat{H}_2^{\text{intra}} + \hat{H}_{1,2}^{\text{inter}} & , n = 1 \\ \frac{1}{2}\left(\hat{H}_n^{\text{intra}} + \hat{H}_{n+1}^{\text{intra}}\right) + \hat{H}_{n,n+1}^{\text{inter}} & , 1 < n < N-1 \\ \frac{1}{2}\hat{H}_{N-1}^{\text{intra}} + \hat{H}_N^{\text{intra}} + \hat{H}_{N-1,N}^{\text{inter}} & , n = N-1 \end{cases} \tag{3.24}$$

acts on the nth bond. In general, neighbouring bond Hamiltonians do not commute. Using the Baker-Campbell-Hausdorff theorem, we can write decompose the time evolution operator $\exp\left(-i\hat{H}(t)\delta t/\hbar\right)$ as

$$\mathrm{e}^{-i\hat{H}\delta t/\hbar} \approx \mathrm{e}^{-i\hat{H}_{1,2}\delta t/2\hbar}\mathrm{e}^{-i\hat{H}_{2,3}\delta t/2\hbar}\cdots\mathrm{e}^{-i\hat{H}_{N-1,N}\delta t/2\hbar}\mathrm{e}^{-i\hat{H}_{N-1,N}\delta t/2\hbar}\cdots\mathrm{e}^{-i\hat{H}_{2,3}\delta t/2\hbar}\mathrm{e}^{-i\hat{H}_{1,2}\delta t/2\hbar} + O(\delta t^3). \tag{3.25}$$

To propagate the evolving state for a time of t, this operator is applied $t/\delta t$ times, and therefore the overall error is in order $O(\delta t^2)$. This is known as a second order Suzuki-Trotter decomposition. A smaller 'Trotter error' can be achieved via higher order Suzuki-Trotter decompositions.[153]

The bond evolution operator, $\hat{U}_n = \mathrm{e}^{-i\hat{H}_{n,n+1}\delta t/2\hbar}$, lives in a Hilbert space of dimension $d \times d$, and therefore can be exactly applied on $|\Psi(t)\rangle$ at DMRG step $(n-1)$.[133] At this step the DMRG state is

$$|\Psi\rangle = \sum_{l,\alpha_n,\alpha_{n+1},r} \Psi_{l,\alpha_n,\alpha_{n+1},r} \, |l\rangle \otimes |\alpha_n\rangle \otimes |\alpha_{n+1}\rangle \otimes |r\rangle \,, \tag{3.26}$$

where the subscripts of the left and right primitive block states are dropped for clarity. The states $|\alpha_n\rangle$ and $|\alpha_{n+1}\rangle$ are the exact basis states for sites n and $n+1$.

To find $|\Phi\rangle = \hat{U}_n |\Psi\rangle$, the 2-site augmented block state $|m\rangle = |\alpha_n\rangle \otimes |\alpha_{n+1}\rangle$ is transformed to the basis spanned by the eigenstates of $\hat{H}_{n,n+1}$, i.e., $\hat{H}_{n,n+1} |m\rangle\rangle = \epsilon_m |m\rangle\rangle$, where

$$|m\rangle\rangle = \sum_{m'} \phi_{m',m} |m'\rangle . \tag{3.27}$$

With this transformation, $|\Phi\rangle = \hat{U}_n |\Psi\rangle$ can be written as,

$$|\Phi\rangle = \sum_{l,m'',r} \sum_{m,m'} \mathrm{e}^{-i\epsilon_{m'}\delta t/2\hbar} \phi_{m,m'} \phi_{m'',m'} \Psi_{l,m,r} |l\rangle \otimes |m''\rangle \otimes |r\rangle . \tag{3.28}$$

The algorithm now proceeds in precisely the same way as for the static finite lattice DMRG method, namely $|\Phi\rangle$ is truncated via a SVD and is then transformed to the basis for the next DMRG step via White's wavefunction mapping technique.[149] Usually, the initial state $|\Psi(t=0)\rangle$ is chosen to be either an excited state of the static DMRG Hamiltonian, or a state prepared by applying an operator, for instance the transition dipole moment operator $\hat{\mu}$, on the ground state. Dynamics is induced by changing parameters in the Hamiltonian or incorporating additional terms to the Hamiltonian. The choice of the initial states for the work presented in this thesis is described in Section 3.2.2. Fig. 3.4 illustrates the key steps of the adaptive tDMRG algorithm.

3.1.4 Lanczos-DMRG

This section describes the Lanczos-DMRG method, which provides a computationally inexpensive framework to calculate transient absorption spectra from a given evolving state $|\Psi(t)\rangle$. Transient (time-resolved) absorption experiments are among the most routinely utilised experimental techniques in the field of carotenoid photophysics.[154] A typical transient absorption measurement involves photopertur-

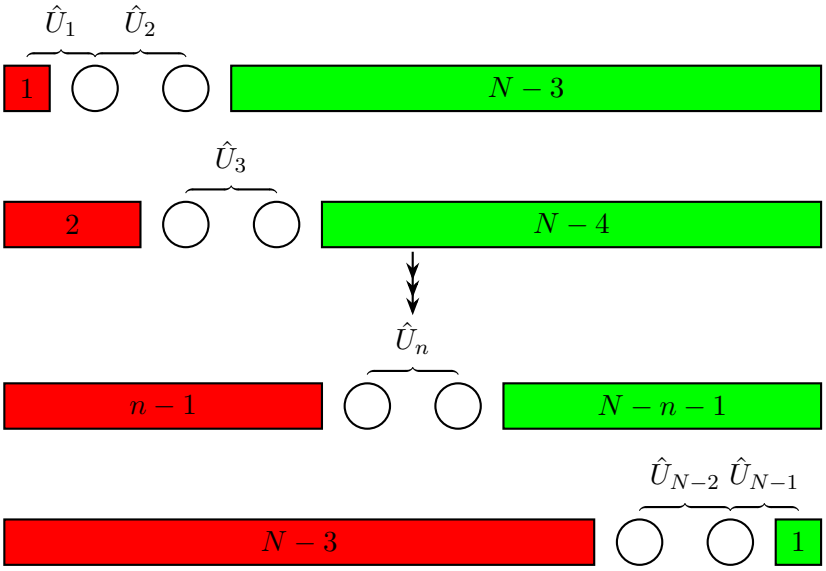

Figure 3.4: Schematic diagram for a single sweep of the adaptive tDMRG algorithm, illustrating the application of the time evolution operator for a time of $\Delta t/2$. The number of sites in each block is shown as text. An open circle represents a single site block. $\hat{U}_n = \mathrm{e}^{-i\hat{H}_{n,n+1}\delta t/2\hbar}$.

bation of the dynamical system at time t and measurement of the effect of the perturbation at time $t+\tau$. This corresponds to the dynamical correlation function $\tilde{G}_\mu(t,\tau)$ defined as

$$\tilde{G}_\mu(t,\tau) = \langle\Psi(t)|\hat{\mu}(t+\tau)\hat{\mu}(t)|\Psi(t)\rangle\,, \tag{3.29}$$

where $\hat{\mu}(t)$ is the Heisenberg representation of the dipole moment operator $\hat{\mu}$. Via a Fourier transform of ω with respect to τ, we obtain the dynamical correlation function in the frequency domain as[155]

$$G_\mu(t,\omega+i\hbar\eta) = -\frac{1}{\pi}\left\langle\Psi(t)\middle|\hat{\mu}\frac{1}{E_\Psi+\omega+i\hbar\eta-\hat{H}}\hat{\mu}\middle|\Psi(t)\right\rangle, \tag{3.30}$$

where E_Ψ is the energy of $|\Psi(t)\rangle$, and η is a small positive real number used to shift the poles of $G_\mu(t,\omega)$ into the complex plane. The imaginary part of $G_\mu(t,\omega+i\hbar\eta)$

is given by

$$I_\mu(t, \omega + i\hbar\eta) = \frac{1}{\pi} \left\langle \Psi(t) \middle| \hat{\mu} \frac{\eta}{(E_\Psi + \omega - \hat{H})^2 + \hbar^2\eta^2} \hat{\mu} \middle| \Psi(t) \right\rangle . \tag{3.31}$$

If a complete set of eigenstates $\{|n\rangle\}$ of $\hat{H}$, with eigenvalues $\{E_n\}$ is known, using $\hat{1} = \sum_n |n\rangle \langle n|$, we can write

$$I_\mu(t, \omega + i\hbar\eta) = \frac{1}{\pi} \sum_n |\langle n|\hat{\mu}|\Psi(t)\rangle|^2 \frac{\eta}{(E_\Psi + \omega - E_n)^2 + \hbar^2\eta^2}. \tag{3.32}$$

In the limit $\eta \to 0$, we obtain the transient absorption spectrum at time t via

$$I_\mu(t, \omega) = \frac{1}{\pi} \sum_n |\langle n|\hat{\mu}|\Psi(t)\rangle|^2 \delta(E_\Psi + \omega - E_n). \tag{3.33}$$

It is possible to calculate the transient absorption via a direct evaluation of $\{|n\rangle\}$ by targeting the n eigenstates in the DMRG density matrix.[156] However, for a fixed number of retained DMRG density matrix eigenstates, the truncation error grows rapidly with the number of targeted states in the density matrix and thus limits the use of this approach. Hallberg,[157] and Kühner and White[158] introduced the Lanczos-DMRG method which combines DMRG with the Lanczos algorithm.[159]

Lanczos method was developed as an efficient algorithm to diagonalise matrices by transforming a given matrix to a special basis where it is tridiagonal.[160] Tridiagonal matrices are sufficiently sparse to be efficiently diagonalised using standard matrix diagonalisation libraries. The special basis the Hamiltonian is transformed to is spanned by Lanczos vectors $\{|f_n\rangle\}$. If $n < D$, where D is the dimension of the original matrix, then the matrix is said to be projected on to the Krylov subspace spanned by the Lanczos vectors. Lanczos-DMRG is based on the observation that since only a few eigenstates of the Hamiltonian makes a finite contribution to the

spectrum (as shown by eq (3.33)), the original Hamiltonian can be projected on to a Krylov subspace of much smaller dimension which can accurately describe these excitations.

We calculate transient spectra from the state $|\Psi(t)\rangle = |S_i\rangle$ using the Lanczos-DMRG method, with normalised Lanczos vectors defined as in ref [158],

$$a_n = \langle f_n|\hat{H}|f_n\rangle\,, \tag{3.34}$$

$$|r_n\rangle = \left(\hat{H} - a_n\right)|f_n\rangle - b_{n-1}\,|f_{n-1}\rangle\,, \tag{3.35}$$

$$b_n = \||r_n\rangle\|_2, \tag{3.36}$$

and

$$|f_{n+1}\rangle = \frac{|r_n\rangle}{b_n}, \tag{3.37}$$

where $b_{-1} = 0$. $|S_i\rangle$ is the ith instantaneous eigenstate of the evolving Hamiltonian at time t. We require $|S_i\rangle$ to be the lowest energy eigenstate of the Hamiltonian in the projected Krylov subspace. This is achieved by projecting out the lower energy eigenstates via

$$|f_0\rangle = \left(\hat{1} - \sum_{j=0}^{i-1} |S_j\rangle\langle S_j|\right)|g_0\rangle\,, \tag{3.38}$$

where

$$|g_0\rangle = \frac{\hat{\mu}\,|S_i\rangle}{\|\hat{\mu}\,|S_i\rangle\|_2}. \tag{3.39}$$

Projecting out the eigenstates lower in energy than $|S_i\rangle$ is also motivated as we are only interested in the calculation of stimulated absorption spectra.

We now outline the implementation of Lanczos-DMRG within our adaptive tDMRG simulations. Once the dynamical simulation for time t is reached, we per-

form a static DMRG sweep to calculate observables, ending at the DMRG step where the system block is the same size as the environment block. We save the full Hilbert space, which is in the tDMRG basis. Then we perform a full static DMRG sweep, diagonalizing the Hamiltonian at each DMRG step to find $|S_i\rangle$, and the Lanczos vectors $\{|f_n\rangle\}$, as defined above. The first five Lanczos vectors are used as target states during the static DMRG sweep, weighted proportionately by their contribution to the spectrum as defined by eq (17) of ref [158],

$$w_n = \sum_m (\Phi_m^0)^2 (\Phi_m^n)^2, \tag{3.40}$$

where w_n is the weight of the Lanczos state n, $\Phi_m^n = \langle f_m | \Phi_n \rangle$, and $|\Phi_n\rangle$ is the nth eigenstate of the Hamiltonian in the Lanczos Hilbert space. Noting that we need an accurate representation of all eigenstates up to and including $|S_i\rangle$ during the static DMRG sweep, we assign 25% of the weight to $|\Psi(t)\rangle$, 25% of the weight to all eigenstates up to $|S_i\rangle$ (distributed equally), and the remaining 50% of the weight to the target Lanczos states. At the end of the static DMRG sweep, we calculate the transient absorption spectrum using eq (3.33). The dynamical simulation is then continued from the previously saved tDMRG Hilbert space.

Lanczos-DMRG is a simple and efficient method for the calculation of the low energy discrete absorption spectra, and is well suited for a tDMRG simulation where the transient absorption is calculated as a function of time during the dynamics. More accurate, but expensive, frequency-space DMRG methods, such as correction vector DMRG[158] and dynamical DMRG,[135] are required for the calculation of complex spectra with high energy absorptions, or continuous spectra.

3.1.5 DMRG and Entanglement Entropy

As discussed in Section 3.1.2, the DMRG algorithm finds the optimum $|\tilde{\Psi}\rangle$ by minimising the quadratic norm S_2 (see eq (3.12)). The truncation error, ϵ, associated with the DMRG algorithm can therefore be defined as the sum of the eigenvalues of $\hat{\rho}_S$ discarded during the DMRG truncation, i.e.,

$$\epsilon = \min(S_2) = 1 - \sum_{\beta=1}^{M_S} \omega_\beta, \tag{3.41}$$

and $\sum_{\beta=1}^{r} \omega_\beta = 1$. The reason for the remarkable success of DMRG in explaining the properties of one dimensional quantum systems is understood by the realisation that the DMRG truncation error is closely related to the amount of information that is required to accurately represent a quantum system.[139,140] This amount of information is dependent on the entanglement of the system, and is quantified via the von Neumann entanglement entropy,

$$S = -\sum_{\beta=1}^{r} \lambda_\beta^2 \log \lambda_\beta^2 = -\operatorname{Tr}_S(\hat{\rho}_S \log \hat{\rho}_S). \tag{3.42}$$

To illustrate this quantity, first consider a fully unentangled system. This state is described by a product state given by

$$|\Psi\rangle = \left(\sum_{i=1}^{N_S} \Psi_i |i\rangle\right) \otimes \left(\sum_{j=1}^{N_E} \Psi_i |j\rangle\right). \tag{3.43}$$

It follows that for this state, $\hat{\rho}_S = |\Phi_S\rangle \langle\Phi_S|$ where $|\Phi_S\rangle = \sum_{i=1}^{N_S} \Psi_i |i\rangle$, and thus $S = 0$. Therefore, the unentangled state has the minimum von Neumann entropy. To demonstrate the maximally entangled state, consider a two spin system described

by

$$|\Psi\rangle = \frac{1}{\sqrt{2}} \left(|\uparrow_S\rangle \, |\downarrow_E\rangle + |\downarrow_S\rangle \, |\uparrow_E\rangle \right). \tag{3.44}$$

For this state, $\hat{\rho}_S = \frac{1}{2} \left(|\uparrow_S\rangle \langle\uparrow_S| + |\downarrow_S\rangle \langle\downarrow_S| \right)$ and $S = \log 2$. In general, for the maximally entangled state, if the rank of the Schmidt decomposition is r, then $\omega_\beta = \lambda_\beta^2 = 1/r$, and $S = \log r$.

Recall from eq (3.7) that a general state $|\Psi\rangle$ can be written using a Schmidt basis, where the Schmidt coefficients λ_β are related to the eigenvalues of $\hat{\rho}_S$ by $\omega_\beta = \lambda_\beta^2$. Thus, if the eigenvalues $\{\omega_\beta\}$ decay rapidly, only a small error is introduced by retaining only a relatively small number of eigenstates. This is the fundamental idea of DMRG. While NRG minimises the loss of energy, DMRG minimises the loss of information.

The growth of entanglement with system size is related to the 'area law' which explains why DMRG works so well for one-dimensional systems, but fails in higher dimensions.[161] The area law states that the entanglement entropy of the ground state of a gapped, partitioned system is proportional to the size of the partition between the systems. For one-dimensional systems, the surface between two systems is a point, and as this does not change with system size the entanglement entropy is a constant with system size.[162] This further implies that the truncation error remains essentially constant for a fixed system basis size as a function of system size. DMRG is thus highly suitable for the study of the electronic states of insulating polyene systems.

3.1.6 DMRG and Matrix Product States (MPS)

As seen in Section 3.1.2, DMRG was first formulated as a real-space renormalisation group algorithm where degrees of freedom of a system are systematically integrated out to construct effective Hamiltonians in a truncated Hilbert space. It was later

realised that greater insights into the underlying structure of DMRG can be achieved by formulating DMRG in the language of matrix product states (MPS).

By defining the product state

$$|\alpha_1, \ldots, \alpha_N\rangle = |\alpha_1\rangle \otimes |\alpha_2\rangle \ldots |\alpha_{N-1}\rangle \otimes |\alpha_N\rangle \,, \tag{3.45}$$

a general pure quantum state on a lattice of length N in an untruncated Hilbert space is described by

$$|\Psi\rangle = \sum_{\alpha_1,\ldots,\alpha_N} c_{\alpha_1,\ldots,\alpha_N} |\alpha_1, \ldots, \alpha_N\rangle \,, \tag{3.46}$$

where the summation runs over exponentially many coefficients $c_{\alpha_1,\ldots,\alpha_N}$. For one-dimensional systems in consideration, $|\Psi\rangle$ is expected to have some local structure which is not reflected by the generic coefficients $c_{\alpha_1,\ldots,\alpha_N}$. We seek to establish this local notion of the state while preserving its quantum non-locality by expressing $c_{\alpha_1,\ldots,\alpha_N}$ using a set of matrices $\{A^{\alpha_k}; k \in 1, \ldots, N\}$.

We begin by noting $c_{\alpha_1,\ldots,\alpha_N}$, a vector of length d^N, can be recast to a matrix of dimension $(d \times d^{N-1})$ as

$$\Psi_{\alpha_1,(\alpha_2\ldots\alpha_N)} = c_{\alpha_1,\ldots,\alpha_N}. \tag{3.47}$$

Using a SVD on $\Psi_{\alpha_1,(\alpha_2\ldots\alpha_N)}$, we arrive at

$$\Psi_{\alpha_1,(\alpha_2\ldots\alpha_N)} = \sum_{\beta_1=1}^{r_1} U_{\alpha_1,\beta_1} \lambda_{\beta_1} (V^\dagger)_{\beta_1,(\alpha_2\ldots\alpha_N)}, \tag{3.48}$$

where $r_1 \leq d$, and U of dimension $(d \times d^{N-1})$ and V of dimension $(d^{N-1} \times d^{N-1})$ are unitary matrices. Multiplying the last two terms of the summation in eq (3.48)

and recasting the resultant term as a vector $c_{\beta_1,\alpha_2,\ldots,\alpha_N}$ of length $r_1 d^{N-1}$ we get

$$c_{\alpha_1,\ldots,\alpha_N} = \Psi_{\alpha_1,(\alpha_2\ldots\alpha_N)} = \sum_{\beta_1=1}^{r_1} U_{\alpha_1,\beta_1} c_{\beta_1,\alpha_2,\ldots,\alpha_N}. \tag{3.49}$$

We now denote the $\alpha_1{}^{\text{th}}$ row of the matrix U to be A^{α_1}, a vector of length r_1. Its entries are given by $A^{\alpha_1}_{\beta_1} = U_{\alpha_1,\beta_1}$. Then we get

$$c_{\alpha_1,\ldots,\alpha_N} = \sum_{\beta_1=1}^{r_1} A^{\alpha_1}_{\beta_1} c_{\beta_1,\alpha_2,\ldots,\alpha_N}. \tag{3.50}$$

Repeating this procedure to recast $c_{\beta_1,\alpha_2,\ldots,\alpha_N}$, we arrive at

$$c_{\beta_1,\alpha_2,\ldots,\alpha_N} = \Psi_{(\beta_1,\alpha_2),(\alpha_3\ldots\alpha_N)} = \sum_{\beta_2=1}^{r_2} U_{(\beta_1,\alpha_2),\beta_2} c_{\beta_2,\alpha_3\ldots\alpha_N}, \tag{3.51}$$

where $r_2 \leq r_1 d$. Now we decompose the matrix U of dimension $(r_1 d \times d^{N-2})$ by a set of d *matrices* A^{α_2} with entries $A^{\alpha_2}_{\beta_1,\beta_2} = U_{(\beta_1,\alpha_2),\beta_2}$. Thus, from eq (3.49) and eq (3.51) we get

$$c_{\alpha_1,\ldots,\alpha_N} = \sum_{\beta_1=1}^{r_1} U_{\alpha_1,\beta_1} c_{\beta_1,\alpha_2,\ldots,\alpha_N} = \sum_{\beta_1=1}^{r_1}\sum_{\beta_2=1}^{r_2} A^{\alpha_1}_{\beta_1} A^{\alpha_2}_{\beta_1,\beta_2} c_{\beta_2,\alpha_3\ldots\alpha_N}. \tag{3.52}$$

Performing further SVD's, we obtain

$$c_{\alpha_1,\ldots,\alpha_N} = \sum_{\beta_1=1}^{r_1}\sum_{\beta_2=1}^{r_2}\cdots\sum_{\beta_{N-1}=1}^{r_{N-1}} A^{\alpha_1}_{\beta_1} A^{\alpha_2}_{\beta_1,\beta_2}\ldots A^{\alpha_{N-1}}_{\beta_{N-2},\beta_{N-1}} A^{\alpha_N}_{\beta_{N-1}}, \tag{3.53}$$

which can compactly be written as the matrix product $c_{\alpha_1,\ldots,\alpha_N} = A^{\alpha_1}A^{\alpha_2}\ldots A^{\alpha_{N_1}}A^{\alpha_N}$. With this, we can write our original quantum state as a matrix product state, i.e.,

$$|\Psi\rangle = \sum_{\alpha_1,\ldots,\alpha_N} A^{\alpha_1}A^{\alpha_2}\ldots A^{\alpha_{N_1}}A^{\alpha_N}\,|\alpha_1,\ldots,\alpha_N\rangle\,. \tag{3.54}$$

Going from A^{α_1} to A^{α_N}, the matrices can have the maximum dimensions $(1\times d), (d\times d^2), \ldots, (d^{N/2-1}\times d^{N/2}), \ldots (d^2\times d), (d\times 1)$. The dimensions still grow exponentially, and similar to DMRG, a decimation procedure is employed to approximate them with matrices of lower dimensions. The approximation of matrix A^{α_k} by a matrix of dimension $(M\times M)$ corresponds to a DMRG truncation at physical site k retaining M augmented block states.[142] MPS truncation usually proceeds via a series of SVD's to successively truncate each bond of the MPS to find an approximate state $|\Psi'\rangle$. A subsequent variational optimisation of the overlap between $|\Psi\rangle$ and $|\Psi'\rangle$ ensures the global optimisation of $|\Psi'\rangle$.[163]

Ref [142] presents a comprehensive review of DMRG using MPS formalism, and time-evolution methods based on MPS is reviewed in ref [163].

3.2 Ehrenfest Dynamics

While the electronic wavefunction is determined by solving the TDSE using adaptive tDMRG, the dynamics of the nuclei are determined via the Ehrenfest equations of motion. The Ehrenfest method is based on two assumptions. The first assumption is that the nuclei evolve on a single effective potential energy surface corresponding to an average of the electronic states contributing to the electronic wavefunction. The second assumption is that the motion of nuclei follows Newton's equations of motion. As a consequence of constructing an averaged potential energy surface, the Ehrenfest method is able to describe transitions between different electronic states despite its mean-field nature.[113]

3.2.1 Hellmann-Feynman technique

For the work presented in thesis, the nuclear degrees of freedom are modelled by the UV-Peierls Hamiltonian introduced in Section 2.4.3. For a Hamiltonian $\hat{H}$, the

Hellmann-Feynman theorem states that the force on atom n, f_n is

$$f_{\mathrm{n}} = -\frac{\delta\langle\Psi|\hat{H}\,|\Psi\rangle}{\delta u_{\mathrm{n}}} = -\left\langle\frac{\delta\hat{H}}{\delta u_{\mathrm{n}}}\right\rangle. \tag{3.55}$$

Substituting for $\hat{H}$ from eq (2.59), this leads to

$$f_{\mathrm{n}} = 2\alpha\left(\langle\hat{T}_{\mathrm{n}}\rangle - \langle\hat{T}_{\mathrm{n-1}}\rangle\right) - K\left(2u_{\mathrm{n}} - u_{\mathrm{n+1}} - u_{\mathrm{n-1}}\right). \tag{3.56}$$

The nuclei obey Newton's equations of motion

$$\frac{du_{\mathrm{n}}(t)}{dt} = \frac{p_{\mathrm{n}}(t)}{m} \tag{3.57}$$

and

$$\frac{dp_{\mathrm{n}}(t)}{dt} = f_{\mathrm{n}}(t) - \gamma p_{\mathrm{n}}(t), \tag{3.58}$$

where p_n and m are the nuclear momentum and mass, respectively. A phenomenological linear damping term γp_{n} is introduced to encourage relaxation of the nuclei. The equations of motion are propagated using the damped Velocity Verlet scheme derived in appendix 5.A of reference [164],

$$u_n(t+\Delta t) = u_n(t) + \frac{p_n(t)}{m}\Delta t + \frac{1}{2}\frac{[f_n(t) - \gamma p_n(t)]}{m}\Delta t^2 \tag{3.59}$$

$$p_n(t+\Delta t) = \frac{1}{1+\Delta t\gamma/2}\left[p_n(t)[1-\Delta t\gamma/2] + \frac{\Delta t}{2}\left([f_n(t+\Delta t) + f_n(t)]\right]\right. . \tag{3.60}$$

The time-scales of our dynamical simulations is set by C-C bond stretching, which have typical oscillations of $\sim$ 20 fs. To replicate these oscillations, we set $\hbar\omega_D = 0.2$ eV where $\hbar$ is the reduced Planck constant and $\omega_D = \sqrt{2}\omega = \sqrt{(2K/m)}$ is the Debye phonon frequency. The linear damping term is set to $\gamma = \omega_D/2$.

The time step of the Velocity Verlet integrator is determined by the errors associ-

ated with the Trotter time step. After a convergence analysis (presented in appendix 5.B.2), and we find $\delta t = 3 \times 10^{-3}$ fs to be a suitable Trotter time step. We perform $n = 10$ tDMRG steps per each nuclear position update, and therefore $\Delta t = 10^{-2}$ fs.

3.2.2 Initial conditions

To model the electronic excitations at Franck-Condon point, we first determine the ground state of the system using the static DMRG method by solving eq (2.59) for fixed nuclear displacements, $\{u_n\}$. Starting from the undimerised geometry ($u_n = 0, \forall n$), ground and excited state energies and geometries are found by iterative application of eq (3.56) with the force per atom n, $f_{\mathrm{n}} = 0$.[104] The (classical) nuclei are initialised in their stationary state, $p_n(t = 0) = 0, \forall n$. The initial system, $\Psi(t = 0)$, is taken to be the adiabatic singlet state S_i with the largest projection onto the $1\,^1B_u^+$ diabat, determined via eq (2.74). This corresponds to a dipole-allowed vertical excitation from the ground state, S_0. The choice to define the initial system this way, instead of as $\hat{\mu}S_0$, is based on the observation that the Ehrenfest approximation (as discussed in Section 2.7.2) is most accurate for systems evolving on a single adiabatic potential energy surface.

3.2.3 tDMRG-Ehrenfest Algorithm

The full dynamical simulation scheme is now obtained by combining adaptive tDMRG with Ehrenfest equations of motion. Suppose we know at time t the nuclear coordinates $\mathbf{u}(t) = (u_1, u_2, \ldots, u_N)$, forces on each nuclei $\mathbf{f}(t) = (f_1, f_2, \ldots, f_N)$, momenta of each nuclei $\mathbf{p}(t) = (p_1, p_2, \ldots, p_N)$, Hamiltonian $\hat{H}$ which depends parametrically on $\mathbf{u}$, and the evolving state $|\Psi(t)\rangle$. Let $\Delta t = n\delta t$. The tDMRG-Ehrenfest algorithm proceeds as follows.

1. Evolve $|\Psi(t)\rangle$ for n time steps using the Trotter time δt via adaptive tDMRG

to find $|\Psi(t+\Delta t)\rangle$.

2. Calculate the bond order expectation values, and $\mathbf{f}(t+\Delta t)$ using $|\Psi(t+\Delta t)\rangle$ and eq (3.56).

3. Find $\mathbf{u}(t+\Delta t)$ and $\mathbf{p}(t+\Delta t)$ using eq (3.59) and eq (3.60).

4. Update $\hat{H}$ using the new nuclear positions $\mathbf{u}(t+\Delta t)$.

5. Repeat steps 1-4 until the required simulation time is reached.

3.3 Parametrising $\hat{H}_\epsilon$

Idealised carotenoids modelled using the UVP Hamiltonian are in uniform or dimerised geometries, and as described in Section 2.5 possess both C_2 and particle-hole symmetries. This section describes a numerical procedure to determine the symmetry breaking Hamiltonian (eq (2.67)). The symmetry breaking Hamiltonian alters the on-site potential energies, and therefore changes the Mulliken charge densities of the π-system from unity. Therefore we can use the ground state Mulliken charge densities of the π-system, found via density functional theory (DFT) calculations, to parametrise $\hat{H}_\epsilon$. The optimum Mulliken charge densities are calculated using the ORCA program package.[165,166] Geometry optimisations are performed using DFT with a B3LYP functional[167] and a def2-TZVP basis set,[168,169] followed by calculations of electron densities. To enforce charge neutrality in our model, the mean-shifted Mulliken charge densities are used as target densities in an optimisation algorithm to determine $\hat{H}_\epsilon$.

Allowing unconstrained optimisation of $\hat{H}_\epsilon$ leads to unphysical on-site potential energies and significant changes in the character of excited states. In order to avoid large perturbations, we use projected gradient descent algorithm to search for $\boldsymbol{\epsilon} = (\epsilon_1, \epsilon_2 \ldots \epsilon_N)$ such that $|\epsilon_i| < \epsilon_{\max}$, $\forall\ i \in \{1, 2, \ldots, N\}$.[170] For a given $\boldsymbol{\epsilon}$,

$\boldsymbol{d} = (d_1, d_2, \ldots, d_N)$ where $d_i(\boldsymbol{\epsilon}) = \langle\Psi|\hat{N}_i - 1|\Psi\rangle$ can be found via the static DMRG algorithm. We define the minimisation function as $E(\boldsymbol{\epsilon}) = \|\boldsymbol{d}_{\text{opt}} - \boldsymbol{d}(\boldsymbol{\epsilon})\|$ where $\boldsymbol{d}_{\text{opt}}$ is the target density vector found via DFT. The algorithm is as follows:

1. Choose initial $\boldsymbol{\epsilon}^0$ within the constraints,

2. Loop until the convergence condition is met. At the kth step:

   (a) Find the descent direction $-\nabla E(\boldsymbol{\epsilon}^k)$,

   (b) Find $\bar{\boldsymbol{\epsilon}}^{k+1} = \boldsymbol{\epsilon}^k - \nabla E(\boldsymbol{\epsilon}^k)$,

   (c) Projection: Find $\boldsymbol{\epsilon}^{k+1} = \left(\epsilon_1^{k+1}, \epsilon_2^{k+1} \ldots \epsilon_N^{k+1}\right)$ such that $\forall\, i \in \{1, 2, \ldots, N\}$,

$$\epsilon_i^{k+1} = \begin{cases} \bar{\epsilon}_i^{k+1} & , |\bar{\epsilon}_i^{k+1}| \leq \epsilon_{\max} \\ \epsilon_{\max} & , \bar{\epsilon}_i^{k+1} > \epsilon_{\max} \\ -\epsilon_{\max} & , \bar{\epsilon}_i^{k+1} < -\epsilon_{\max} \end{cases} \tag{3.61}$$

3. Convergence is evaluated via the coefficient of variation $r^2(\boldsymbol{\epsilon})$ defined as:

$$r^2(\boldsymbol{\epsilon}) = 1 - \frac{[E(\boldsymbol{\epsilon})]^2}{\|\boldsymbol{d}_{\text{opt}}\|^2}. \tag{3.62}$$

Chapter 4

Carotenoid Excited States

Having introduced the theoretical and computational methods used in this thesis, we begin the description of polyene excited states in this chapter. The first part of this chapter provides a summary of theoretical studies of polyene excited states, with an emphasis on DMRG methods. Then, a theoretical framework to study the nature of polyene excited states is described. The fundamental excitations of polyene systems (solitons, spinons, magnons, excitons) are introduced. Finally, we review our work from a published article on polyene excited states and show evidence for the existence of a family of dark excited states, called the '$2A_g$' family. These dark excited states are thought to be involved in carotenoid internal conversion pathways.

4.1 Theoretical Studies of Polyene Excited States

Theoretical studies of the exotic nature of polyene excited states were pioneered by a seminal paper from Schulten and Karplus, which described the experimentally observed low-lying dark excited state of polyenes.[34,35] They described the conjugated π-electron system using the semi-empirical Pariser-Parr-Pople (PPP) Hamiltonian (Section 2.4.2) and the configuration interaction (CI) method with double excitations. Their work was followed by several studies based on semi-empirical Hamil-

tonians, which helped formulate the theoretical understanding of polyene excited states.[40,171–176]

Early *ab initio* calculations of polyene excited states were based on self consistent field (SCF) and CI calculations.[177,178] Improvements to the ground and excited state geometries of polyenes were brought about by the use of multiconfiguration self consistent field (MCSCF) method.[179] Serrano-Andres and coworkers introduced the second order perturbation theory method CASPT2 with a complete active space SCF (CASSCF) wavefunction as the reference state to study electronic states of polyenes.[180] Their calculation provided first evidence from an *ab initio* study for the existence of a dark, low-lying polyene excited state.

Mike Robb and co-workers performed extensive studies on polyene systems using *ab initio* electronic structure calculations. They studied the radiationless $S_1 \rightarrow S_0$ decay of butadiene using MCSCF and hexatriene using CASSCF, and showed that the deactivation occurs via a conical intersection.[181,182] They developed the molecular mechanics-valence bond (MMVB) method to study the deactivation pathways of longer polyenes,[183,184] and demonstrated that the S_0 state immediately after the conical intersection is a transient biradical state, with a lifetime $\sim$ 40 fs.[185] Density functional theory (DFT) was applied to study the trans $\rightarrow$ cis isomerisation reaction of β-carotene.[186] Recently, by coupling CASCI electronic structure calculations to Ehrenfest dynamics, they modelled polyene charge migration and showed oscillatory charge migration lasting for several femtoseconds before subsequent dephasing.[187]

Time-dependent density functional theory (TD-DFT),[188,189] extended algebraic diagrammatic construction (extended-ADC(2)),[47] CASSCF with n-electron valence perturbation theory (NEVPT),[190] and density functional theory with multireference configuration interaction[191,192] have been utilised to study polyene excited states. However, application of complete active space methods to model long chain polyene

systems is challenging because of the exponential growth of the many-body Hilbert space with the size of the single particle basis.

The DMRG algorithm was first introduced to study strongly correlated quantum lattice systems in 1992.[132] DMRG was soon adapted to study π-conjugated polymers[101,193–195] and polyene photophysics,[93,102–105,147] as applied to one-dimensional systems it yields quasi-exact results for a finite-size Hilbert space. DMRG was first utilised to model *ab initio* Hamiltonians in 1999.[196] Ghosh *et al.* demonstrated that the CASSCF method could be incorporated into a DMRG algorithm, allowing the modelling of polyene systems of natural carotenoid lengths.[48] While the inherent multireference nature of DMRG accounts for static correlations, perturbative theory corrections are required to accurately describe the dynamic correlations present in the system.[197,198] More recent *ab initio* studies on polyene excited states using multireference perturbation theory (MRPT) NEVPT2/DMRG, which accounts for the dynamic correlations, have reignited the debate on carotenoid excited state energy ordering.[58,59]

The original DMRG formulation of White has been extended to form a family of time-dependent DMRG (TD-DMRG) algorithms, designed to model time dependent phenomena of molecular systems (Section 3.1.3). One of the widely used TD-DMRG algorithms is the adaptive time-dependent DMRG (tDMRG) algorithm, independently developed by Daley et al.,[134] and White and Feiguin[133] to study time evolution of weakly entangled systems. Examples of applications of adaptive tDMRG in molecular physics include modelling magnetisation transport in spin-$\frac{1}{2}$ chains,[199] demonstrating spin-charge separation in cold Fermi gases,[200] calculating zero temperature conductance of strongly correlated nanostructures,[201] elucidating transport properties of quantum-dot systems connected to metallic leads,[202] evaluating spectral functions of a spin-1 Heisenberg antiferromagnetic chain,[203] exciton

transport in one-dimensional Hubbard insulators,[204] and non-equilibrium transport in the single-impurity Anderson model.[205] Techniques based on tensor network models have recently been used to study dynamics of photophysical systems, for example, ultrafast relaxation and localisation of photoexcited states in light emitting polymers,[129,130,206] internal conversion in pyrazine,[207] and singlet fission in substituted pentacene dimers.[208] Readers are referred to a recent review by Ren and co-workers on applications of different TD-DMRG algorithms to model dynamics of quantum systems.[209]

While state-of-the-art *ab initio* methods have had great success in calculating static properties of polyene excited states, due to computational expediencies the use of semi-empirical Hamiltonians with a single electron basis is more attractive to model dynamical processes of photoexcited polyenes. With the correct parametrisation DMRG has been shown to work very well for semi-empirical Hamiltonians with a reduced single-particle basis.[95,210] For example, the DMRG algorithm with the PPP Hamiltonian has been widely used to study the electronic properties of conjugated polyenes.[101–106,150]

4.2 Polyene Excited States

4.2.1 Undimerised Polyenes with Noninteracting Electrons

We begin the description of the polyene excited states with the noninteracting Hückel π-electron model introduced in Section 2.4.1. By setting the on-site energy, $\epsilon_i = 0$, and the hybridisation integrals, $t_i = t_0$ in the Hückel Hamiltonian, we get

$$\hat{H} = -t_0 \sum_{i\sigma} \left(\hat{c}^{\dagger}_{i+1,\sigma} \hat{c}_{i,\sigma} + \hat{c}^{\dagger}_{i,\sigma} \hat{c}_{i+1,\sigma} \right). \tag{4.1}$$

Eq. (4.1) can be solved exactly using a Bloch transformation,[93]

$$\hat{c}^{\dagger}_{i,\sigma} = \sqrt{\frac{2}{N+1}} \sum_{\beta} \hat{c}^{\dagger}_{\beta,\sigma} \sin(\beta n a), \tag{4.2}$$

where β is the pseudo Block wavevector given by

$$\beta = \frac{\pi j}{(N+1)a}, \tag{4.3}$$

$1 \leq j \leq N$, and a is the lattice parameter. The energy of the single-particle molecular orbital state $|\beta\rangle$ is given by

$$E_{\beta} = -2t_0 \cos(\beta a). \tag{4.4}$$

The molecular orbital states will be of either A_u or B_g symmetry (2.5). For neutral polyenes with an even number of carbon atoms, the ground state at half filling is constructed by occupying the valence band,

$$|\mathrm{GS}\rangle = \prod_{\beta} \hat{c}^{v\dagger}_{\beta,\uparrow} \hat{c}^{v\dagger}_{\beta,\downarrow} |0\rangle \,. \tag{4.5}$$

The energy of the ground state is given by

$$E_0 = 2 \sum_{\beta} \epsilon^{v}_{\beta}. \tag{4.6}$$

An excited state from the ground state is created by exciting an electron to the conduction band, leaving behind a hole in the valence band. A singlet excitation is defined as

$$\left|{}^1 k_e, k_h\right\rangle = \frac{1}{\sqrt{2}} \left(\hat{c}^{c\dagger}_{k_e\uparrow} \hat{c}^{v}_{k_h\uparrow} + \hat{c}^{c\dagger}_{k_e\downarrow} \hat{c}^{v}_{k_h\downarrow} \right) |\mathrm{GS}\rangle \,, \tag{4.7}$$

and the $S_z = 1, 0, -1$ triplet excitations are

$$\left|{}^3k_e, k_h\right\rangle = \hat{c}^{c\dagger}_{k_e\uparrow}\hat{c}^{v}_{k_h\downarrow}\left|\mathrm{GS}\right\rangle, \tag{4.8}$$

$$\left|{}^3k_e, k_h\right\rangle = \frac{1}{\sqrt{2}}\left(\hat{c}^{c\dagger}_{k_e\uparrow}\hat{c}^{v}_{k_h\uparrow} - \hat{c}^{c\dagger}_{k_e\downarrow}\hat{c}^{v}_{k_h\downarrow}\right)\left|\mathrm{GS}\right\rangle, \tag{4.9}$$

and

$$\left|{}^3k_e, k_h\right\rangle = \hat{c}^{c\dagger}_{k_e\downarrow}\hat{c}^{v}_{k_h\uparrow}\left|\mathrm{GS}\right\rangle, \tag{4.10}$$

respectively. At the noninteracting limit, the created electron-hole pair is unbound (or *uncorrelated*) and the singlet and triplet excitations are degenerate. The excitation energy of the electron-hole state is

$$\epsilon(k_e, k_h) = E(k_e, k_h) - E_0 = \epsilon^c_{k_e} - \epsilon^v_{k_h}. \tag{4.11}$$

The noninteracting Hamiltonian of Eq. (4.1) commutes with the electron-hole operator defined in Section 2.5.2, and therefore its eigenstates can be symmetrised. We find that the ground state is the $1\,{}^1A_g^-$ state and the first singlet excitation is the $1\,{}^1B_u^+$ state.

The $1\,{}^1B_u^+$ state is connected to the $1\,{}^1A_g^-$ state by the dipole moment operator and therefore it corresponds to an optical excitation. The excitation energy of the $1\,{}^1B_u^+$ state is defined as the *optical gap*. The *band gap* is defined as the energy gap between the highest occupied molecular orbital (HOMO) and the lowest unoccupied molecular orbital (LUMO). At the noninteracting limit, this is precisely the $1\,{}^1B_u^+$ excitation and the optical and the band gaps are equivalent. The *spin gap* is defined as the excitation energy from the singlet ground state to the first triplet excited state. Since the singlet and the triplet states are degenerate at the noninteracting

limit, it follows that the spin gap is equivalent to the band gap. Finally, we define a *charge gap* as the energy of an uncorrelated electron-hole pair, given by

$$2\Delta = E_0(N+1) + E_0(N-1) - 2E_0(N), \tag{4.12}$$

where $E_0(M)$ is the energy of the ground state of an M-electron system. As the electron-hole excitations at the noninteracting limit are uncorrelated, the charge gap is equivalent to the band gap in the noninteracting limit.

We say that an excitation is *gapless* if the excitation energy approaches zero as the system size approaches infinity. The band gap scales as $\sim 1/N^2$ as $N \to \infty$.[93] Therefore, in the noninteracting limit, all excitations are gapless.

The second singlet excitation corresponds to an electronic transition from either HOMO to LUMO +1, or HOMO −1 to LUMO orbitals. This is the $2\,^1A_g^-$ excitation. Electronic transitions from the molecular orbitals that correspond to $1\,^1B_u^+$ and $2\,^1A_g^-$ excitations are shown in Fig. 4.1. At the noninteracting limit, the $2\,^1A_g^-$ state is always higher in energy than the $1\,^1B_u^+$ state, so polyenes at this limit are luminescent. However, as we will see in the following sections, electron-nuclear coupling and electron-electron interactions can lead to changes in the relative ordering of these excited states and for certain parameter regimes the $2\,^1A_g^-$ state becomes the lowest lying singlet excited state. The $2\,^1A_g^-$ state is not dipole connected to the ground state, so it cannot radiatively decay and it is non-luminescent. This reversal of energy levels is thought to be the origin of the non-luminescent characteristics of polyenes.

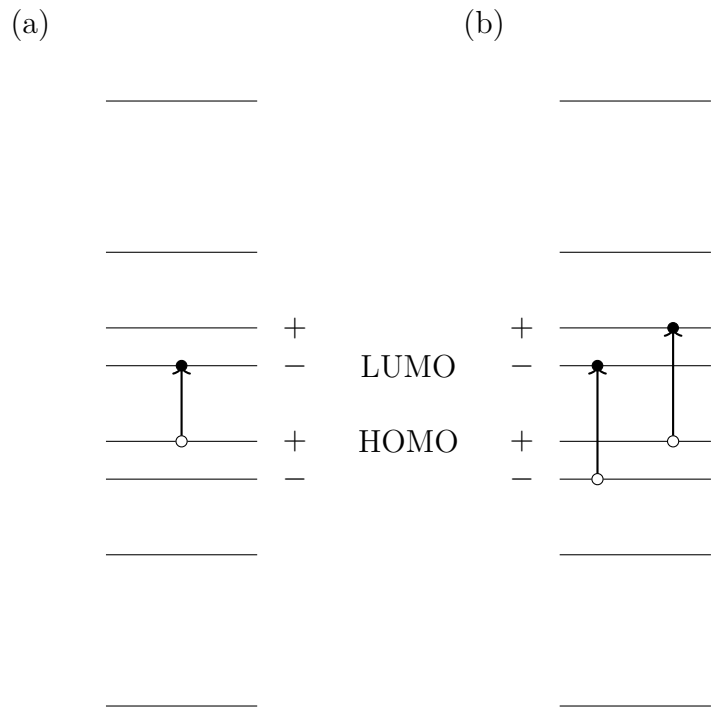

Figure 4.1: Energy level diagram illustrating (a) $1\,B_u$ and (b) $2\,A_g$ electron-hole excitations. The + and − symbols represent the rotational symmetries of the single-particle molecular orbital states.

4.2.2 Broken Symmetries

Prior to discussing the effect of electron-electron interactions and electron-nuclear coupling, it is useful to introduce the broken symmetries π-conjugated systems can exhibit. A state is said to be a broken symmetry state if it has a lower symmetry than the Hamiltonian that describes it. Broken symmetries in polyenes lead to long range order in some observables. In polyenes, there are three different kinds of broken symmetries corresponding to the observables,

$$\hat{S}_i^z \equiv \hat{N}_{i\uparrow} - \hat{N}_{i\downarrow}, \tag{4.13}$$

which creates a spin-density wave (SDW),

$$\hat{N}_i \equiv \hat{N}_{i\uparrow} + \hat{N}_{i\downarrow}, \tag{4.14}$$

which creates a charge density wave (CDW), and

$$\hat{T}_i \equiv \hat{c}^{\dagger}_{i+1,\sigma}\hat{c}_{i,\sigma} + \hat{c}^{\dagger}_{i,\sigma}\hat{c}_{i+1,\sigma}, \tag{4.15}$$

which creates a bond order wave (BOW). Electron-nuclear coupling leads to dimerisation of the polyene chains, which is an example of a BOW. In dimerised polyenes, BOWs and SDWs can coexist, and Mazumder and Campbell studied the transition of the ground state from a CDW to a SDW/BOW as a function of the electron-electron interaction.[211] Importantly, they showed that the parameters relevant for polyenes lead to a SDW/BOW ground state. As the electron-electron interactions increase and the strong coupling limit, defined by $U \gg 4t_0$, is reached, the high energy CDWs diverge from the low energy SDWs and the two types of excitations can be studied separately using simplified effective Hamiltonians.

4.2.3 Dimerised Chains with Noninteracting Electrons - Peierls Distortion and Solitons

The Peierls model, introduced in Section 2.3.3, describes the electron-nuclear interactions in π-electronic systems. A uniformly undistorted chain is defined by $\Delta_i = 0$ for all sites i. An important consequence of electron-nuclear coupling is the Peierls distortion. For non-zero electron-nuclear coupling, $\alpha > 0$, an undistorted chain undergoes spontaneous dimerisation,[212] leading to a dimerised chain with

$$\Delta_i = (-1)^i \Delta = (-1)^i \delta t_0, \tag{4.16}$$

where δ is the dimensionless dimerisation parameter. By calculating the energy of the ground state as a function of δ, it can be shown that the ground state energy surface contains two degenerate minima at $\delta = \delta_0$ and $\delta = -\delta_0$.[93,213] This

dimerisation breaks the translational symmetry of the Hamiltonian that describes the eigenstates, so the ground state is called a broken symmetry state. If the system can access both $\delta = \delta_0$ and $\delta = -\delta_0$ eigenstates, perhaps via tunnelling, then the ground state can be written as a linear combination of the two eigenstates and the translational symmetry is restored. But for realistic parameter regimes for polyene systems, this is not possible, and the broken symmetry ground states prevail. For polyenes with an even number of carbon atoms, the broken symmetry ground state will have alternating short-long-short bond lengths. An immediate consequence of the dimerisation is the opening of a band gap in the band structure. The band gap $2\Delta_0$ is related to the dimerisation by $2\Delta_0 = 4\delta t_0$ irrespective of the chain length.

Consider the process of instantaneous excitation of an even site carbon chain from the ground state across the band gap. This is a *vertical* transition as the instantaneous transition results in an excited electronic state in the ground state nuclear geometry. The excited states thus formed can be stabilised by larger distortions, which can sometimes lead to a reversal of bond-alternations. These changes in dimerisations are characterised by domain walls called solitons.

Isolated solitons are formed in linear open polyene chains with an odd number of carbon atoms. Two phases can be identified that correspond to the bond alternation pattern along the chain, labelled A and B in Fig 4.2. In such chains, to achieve the energetically stable short bonds at each end, the bonding phase changes at the middle of the chain, creating a radical soliton.

Solitons are characterised by the staggered bond dimerisation parameter, defined by

$$\delta_i = (-1)^i \frac{t_i - \bar{t}}{\bar{t}}, \tag{4.17}$$

where $\bar{t}$ is the average of t_i over all bonds. δ_i can be found for any state by first finding the force on bond i, f_i, using the Hellmann-Feynman theorem as described

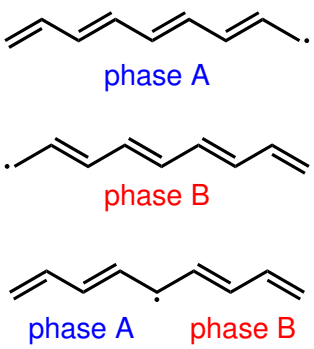

Figure 4.2: The two possible bond alternation phases A and B in a linear open ended chain. In the ground state structure, the bond alternation phase changes at the middle of the chain, creating a neutral radical soliton.

in Section 3.2.1,

$$f_i = -\frac{\delta\langle\Psi|\hat{H}_{\text{Peierls}}|\Psi\rangle}{\delta u_i} = -\left\langle\frac{\delta\hat{H}_{\text{Peierls}}}{\delta u_i}\right\rangle, \tag{4.18}$$

and then setting $f_i = 0$ and solving the resulting equations iteratively. Reversal of the sign of δ_i indicates a domain wall or a soliton. For example, the staggered bond dimerisation of the ground state of an odd numbered carbon chain fits the expression[214]

$$\delta_i = \delta_0 \tanh\left[\frac{(n_i - n_0)a}{\varepsilon}\right], \tag{4.19}$$

where ε is a coherence length which determines the width of the soliton centred at $n_i = n_0$, i.e., at $\delta_i = 0$. In the continuum limit, defined by $\varepsilon \gg a$, the single-particle wavefunction of the mid-gap state is given by[93]

$$\Psi_i = \left(\frac{a}{\varepsilon}\right)^{1/2} \text{sech}\left(\frac{(n_i - n_0)a}{\varepsilon}\right)\cos\left(\frac{n_i\pi}{2}\right). \tag{4.20}$$

Fig. 4.3 shows the variation of the staggered bond dimerisation, δ_i, and the single-particle wavefunction,Ψ_i, across an odd numbered carbon chain. The soliton defect leads to the localisation of the wavefunction.

The solitons are associated with mid-gap states.[215] In an open carbon chain with odd number of atoms N, there are $(N-1)/2$ energy states in the valence band, and $(N-1)/2$ energy states in the conduction band. The remaining single energy state

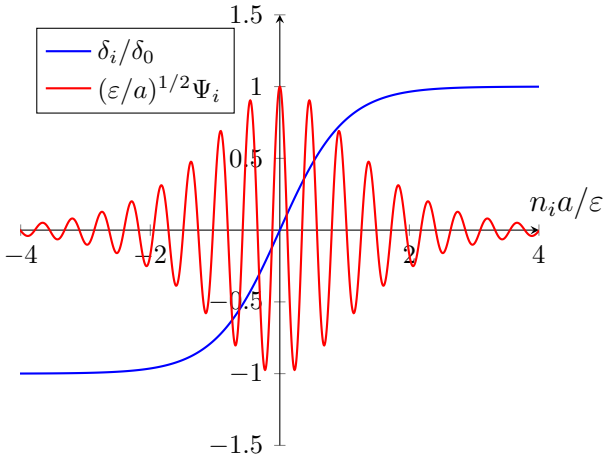

Figure 4.3: The normalised staggered bond dimerisation, δ_i, and the wavefunction of the mid-gap state in the continuum limit, Ψ_i, of an odd numbered carbon chain.

is a localised mid-gap state associated with the soliton. A singly occupied mid-gap state corresponds to a radical neutral soliton (or a spinon, see Section 4.2.4.1), a vacant mid-gap state corresponds to a positively charged ionic soliton, and a doubly occupied mid-gap state corresponds to a negatively charged ionic soliton, as shown in Fig. 4.4.

Analogous to an odd numbered chain, an even numbered carbon chain with two solitons is characterised by two mid-gap states. In the ground state, the two solitons form a soliton-antisoliton pair and they combine to restore the short-long-short bond dimerisation. As described above, excitations from the ground state can produce spatially separated soliton-antisoliton pairs. Excited states $1\,B_u$ and $2\,A_g$, which correspond to a single and a double excitation from the mid-gap ground state respectively, are shown in Fig. 4.5. The $1\,B_u$ state fits the functional form[216]

$$\delta_i = \delta_0 \left\{ 1 + \tanh\left(\frac{2n_0 a}{\varepsilon}\right) \left[\tanh\left(\frac{(n_i - n_0)a}{\varepsilon}\right) - \tanh\left(\frac{(n_i + n_0)a}{\varepsilon}\right) \right] \right\}, \quad (4.21)$$

and is a two soliton state with solitons centred at $n_i = -n_0$ and $n_i = n_0$, whereas

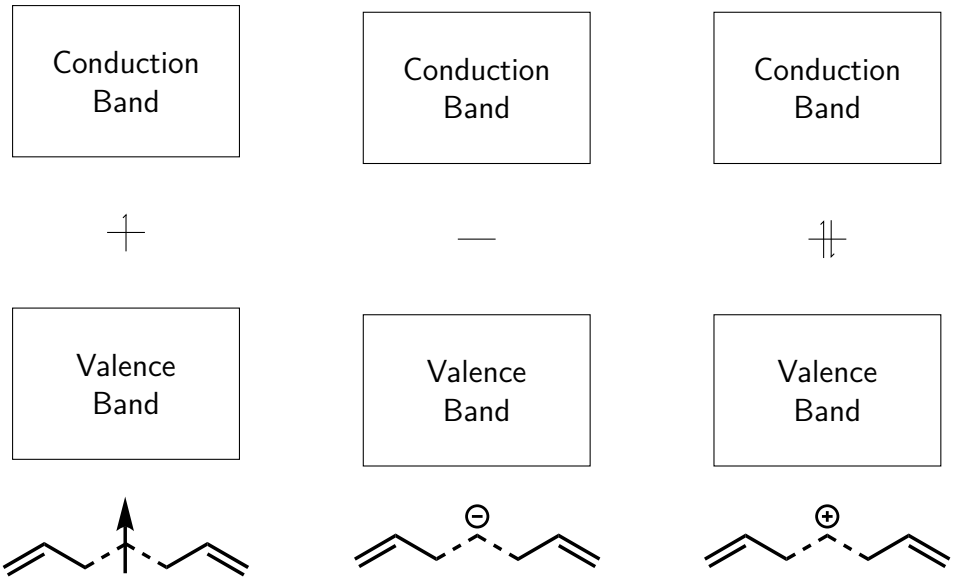

(a) Neutral radical soliton $(S = 1/2, Q = 0)$ **(b)** Charged anionic soliton $(S = 0, Q = -e)$ **(c)** Charged cationic soliton $(S = 0, Q = e)$

Figure 4.4: Mid-gap soliton states in an open ended, odd chain length carbon chain. S and Q quantum numbers are the spin and charge of each state, respectively.

the $2\,A_g$ state fits the functional form[2,217]

$$\delta_i = \delta_0 \left\{ 1 + \tanh\left(\frac{2n_0 a}{\varepsilon}\right) \left[\tanh\left(\frac{2(n_i - n_d - n_0)a}{\varepsilon}\right) - \tanh\left(\frac{2(n_i - n_d + n_0)a}{\varepsilon}\right) + \tanh\left(\frac{2(n_i + n_d - n_0)a}{\varepsilon}\right) - \tanh\left(\frac{2(n_i + n_d + n_0)a}{\varepsilon}\right) \right] \right\}, \tag{4.22}$$

and is a four soliton state with solitons centred at $n_i = -n_d - n_0$, $n_i = -n_d + n_0$, $n_i = n_d - n_0$, and $n_i = n_d + n_0$.

At the nuclear geometry of the vertical excitation, the soliton-antisoliton separation is zero. The $1\,B_u$ state is a single excitation across the band gap and will have an energy $2\Delta_0$. The $2\,A_g$ state is a double excitation and will have an energy of $4\Delta_0$. However, as shown by Eqs. (4.21) and (4.22), the excited states are stabilised by spatially separated soliton-antisoliton pairs, and within a time $\sim 2\pi/\omega_0$ the soliton pairs are separated by a distance $\sim \varepsilon$. Energies of both the states are stabilised by nuclear relaxation, and the excited states move to the band gap. As the soliton-antisoliton separation increases, energies of the two excited states $1\,B_u$

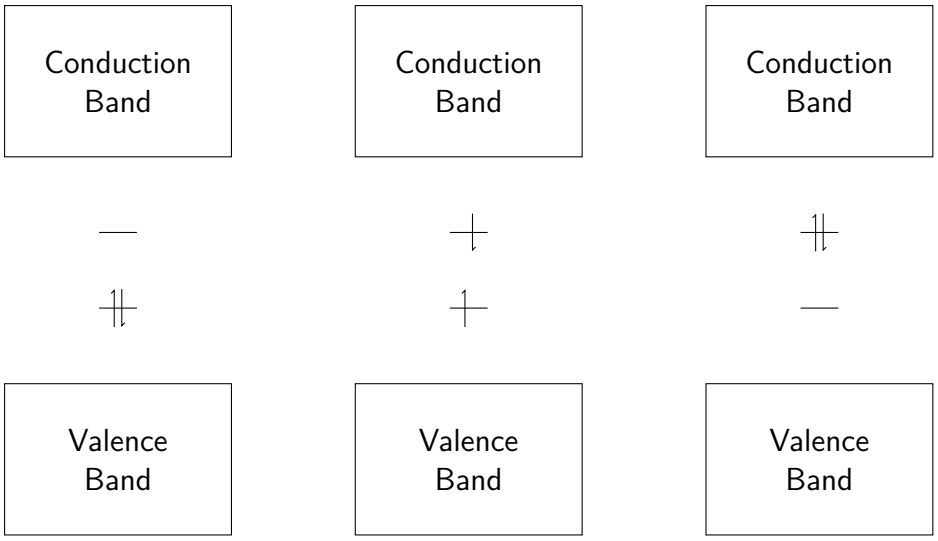

(a) $1\,^1A_g$ **(b)** $1\,^1B_u$ **(c)** $2\,^1A_g$

Figure 4.5: Mid-gap soliton states in an open ended, even chain length carbon chain. $1\,A_g$ is the ground state. $1\,B_u$ and $2\,A_g$ correspond to singly and doubly excited soliton states respectively.

and $2\,A_g$ decrease, and the energy of the ground state $1\,A_g$ increases as the solitons destabilise the ground state. As the separation is increased further, all three energies reach the asymptotic energy of $4\Delta_0/\pi$. The adiabatic energy profiles of the three states are shown in Fig. 4.6.

Following ref [93], it can be shown that the singlet $1\,^1B_u$ state produces a pair of charged solitons, the triplet $1\,^3B_u$ state produces a pair of neutral solitons, and the singlet $2\,^1A_g$ state produces an equal number of charged and neutral pairs of solitons.

Including electron-nuclear coupling in the noninteracting Hamiltonian leads to a dimerised ground state and gapped spin and charge excitations. However, the $1\,^1B_u^+$ state is still the lowest lying excited state at this limit, and inclusion of electron-electron interactions is necessary for a realistic representation of the polyene excited states. In the following section, we describe the effect of electron interactions on the excited states of polyenes.

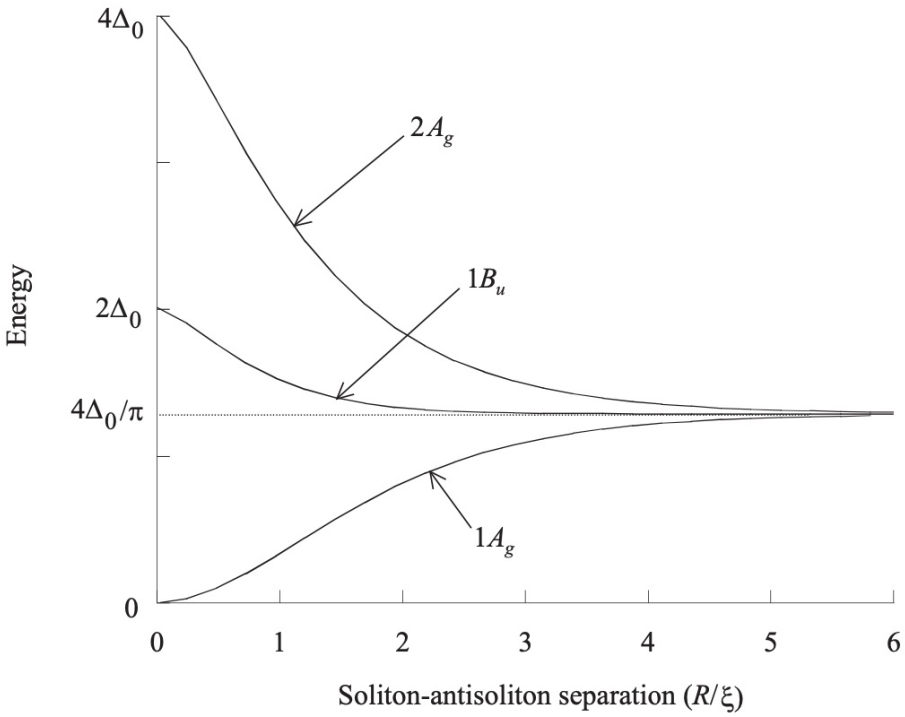

Figure 4.6: Adiabatic energies of the $1\,A_g$, $1\,B_u$, and $2\,A_g$ states as a function of soliton-antisoliton separation. Reproduced with permission from Barford, W., *Electronic and Optical Properties of Conjugated Polymers*; Oxford University Press: 2013.

4.2.4 Interacting Electrons

Both the spin and charge degrees of freedom show gapless excitations at the non-interacting limit in undimerised chains. Inclusion of electronic interactions in the Hamiltonian opens a charge gap, as the Coulomb repulsions impose an energy barrier for charge separations. The spin excitations are unaffected however, and this leads to a natural separation of spin and charge degrees of freedom. Using the PPP Hamiltonian, we first describe the electronic interactions in the strong-coupling limit, defined by $U \gg 4t_0$. In this limit the charge and spin degrees of freedom are entirely separable. We introduce the fundamental spin excitations, spinons and magnons, to describe the spin degrees of freedom. Then we consider the weak-coupling limit, and describe the formation of bound electron-hole excitations called excitons. Finally, we describe how the nature of the different low-lying excited states change as a function of Coulomb interaction parameter U.

4.2.4.1 Strong-Coupling Limit - Spinons and Magnons

In the strong coupling limit of the PPP Hamiltonian, defined by $U \gg t_0$, the energies of the charge-transfer states diverge from the energies of the spin-density waves, and thus the former can be integrated out of the Hamiltonian. This limit therefore serves as a convenient domain to study the fundamental excitations of spin-density waves, which are spinons and magnons. In this limit, the PPP Hamiltonian reduces to the dimerised Heisenberg antiferromagnet,

$$\hat{H} = \sum_i J_i \mathbf{S}_i . \mathbf{S}_{i+1}, \tag{4.23}$$

where

$$\mathbf{S}_i = \sum_{\rho\rho'} c^\dagger_{i\rho} \sigma_{\rho\rho'} c_{i\rho'}. \tag{4.24}$$

σ are the Pauli spin matrices, and

$$J_i = \frac{4t_0^2(1 - 2\delta_i + \delta_i^2)}{U - V_1}, \tag{4.25}$$

where U and V_1 are the on-site and the nearest-neighbour Coulomb interaction parameters of the PPP Hamiltonian respectively.

We can define a *dimer limit* where the polyene chain is composed of alternating short and long bonds by $0 \ll \delta \lesssim 1$, where $\delta_i = (-1)^i \delta$. Fig. 4.7 illustrates the ground state and the first singlet and triplet excited states of the dimerised Heisenberg antiferromagnet. The ground state is described by a singlet state localised on each strong/short/double bond. A triplet ($S = 1$) excitation, which corresponds to a spin-flip of a singlet on a dimer unit, requires an energy of $J = 4t_0^2/(U - V_1)$. The neutral radical spin-1/2 object is called a spinon. The triplet excitation is made of two strongly bound (i.e., localised on the same dimer) spinons, and is called a

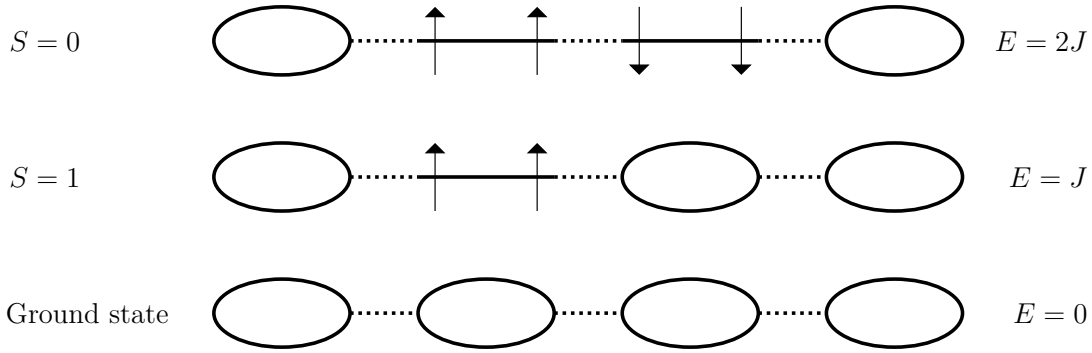

Figure 4.7: A schematic representation of the singlet ground state and the lowest singlet and triplet excited states of the dimerised Heisenberg antiferromagnet.

magnon. In polyenes, at the strong coupling limit, this state is the $1\,^3B_u^-$ state. The first singlet ($S = 0$) excitation at the dimer limit requires two spin-flips and has an excitation energy of $E(S = 0) = 2J$. This is a bimagnon state, and in polyenes it is the $2\,^1A_g^-$ state. The $2\,^1A_g^-$ state is a bimagnon state for all δ values with $E(S = 0) = 2E(S = 1)$ unless $\delta \to 0$. An opposite *weakly dimerised limit* is defined where $0 \lesssim \delta \ll 1$. At this limit, $E(S = 0) \to \sqrt{3}E(S = 1) < 2E(S = 1)$,[218] so at this limit the $2\,^1A_g^-$ state is a bound bimagnon.

The charge-transfer states at the strong coupling limit are described by a spinless fermion model.[93] The single-particle valence and conduction band structure developed in Section 4.2.1 is no longer valid at this limit, and the charge gap separates many-particle states from which electrons can be removed (known as the lower Hubbard band) and many-particle states to which electrons can be added (known as the upper Hubbard band). A charge-transfer excitation creates an electron-hole pair across the charge gap, and the attractive Coulomb interaction binds the created electron-hole pair, forming a Mott-Hubbard exciton. The $1\,^1B_u^+$ state at this limit is the lowest energy Mott-Hubbard singlet exciton.

By considering the $U = 0$ Peierls model and the PPP model with $\alpha = 0$, Barford and coworkers performed numerical simulations using DMRG to study separately the effects of electron-nuclear coupling and electronic interactions on undimerised polyenes.[104] Fig. 4.8 shows their results on the variation of the excitation energies

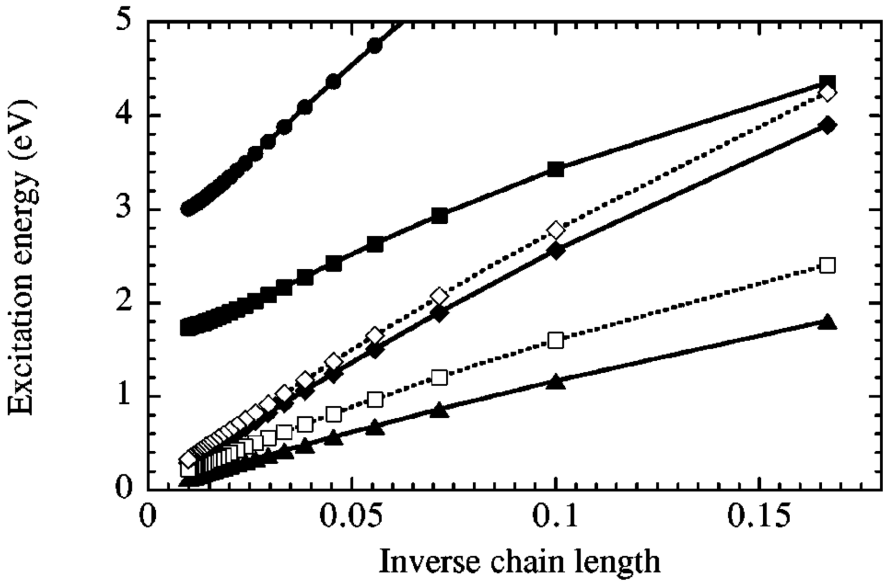

Figure 4.8: Excitation energies for the $1\,^1B_u^+$ (squares), $2\,^1A_g^-$ (diamonds), and $1\,^3B_u^-$ (triangles) states, and the charge gap (circles) as a function of inversion chain length. Dashed lines and solid symbols show results for $U = 0$ Peierls model, and solid lines and filled symbols show the results for $\alpha = 0$ PPP model. For the Peierls model the $1\,^1B_u^+$ and $1\,^3B_u^-$ states are degenerate. Parameters : $t_0 = 2.539$ eV; for the Peierls model, $\alpha = 4.593$ eV Å^{-1}; for the PPP model, $U = 10.06$ eV. Note that the electron-hole sign convention is opposite to the convention used in this text. Reproduced with permission from Barford, W.; Bursill, R. J.; Lavrentiev, M. Y. Density-matrix renormalization-group calculations of excited states of linear polyenes. *Phys. Rev. B* **2001**, *63*, 195108.

of the low-lying singlet and triplet states as a function of inverse chain length. For the $U = 0$ Peierls model, the lowest lying singlet ($1\,^1B_u^+$) and triplet ($1\,^3B_u^-$) excitations are degenerate and the $2\,^1A_g^-$ state is always above the $1\,^1B_u^+$ state. At the long chain limit, the soliton-antisoliton pair of the singlet excited states are well separated, and both energies reach the asymptotic energy of $4\Delta_0/\pi \sim 0.1$ eV. The $\alpha = 0$ PPP model is in the strong coupling limit, and the SDW excited states $2\,^1A_g^-$ and $1\,^3B_u^-$ are the lowest singlet and triplet excitations respectively. Both excitations are gapless, confirming the bimagnon nature of the $2\,^1A_g^-$ state at this limit. The $1\,^1B_u^+$ state is the lowest energy singlet CDW excitation. Its excitation energy is about ~ 1 eV lower than the charge gap, owing to its exciton (bound) nature.

4.2.4.2 Weak-Coupling Limit - Excitons

At the noninteracting limit, a dimerised chain is a band insulator with a non-zero energy gap between the valence and the conduction bands. Electronic excitations from the valence band to the conduction band create electron-hole pairs. While these electron-hole pairs are unbound in the noninteracting limit, as electronic interactions are introduced the electron-hole pair is stabilised via the Coulomb interactions. This gives rise to a bound electron-hole pair, or an exciton.

Following Section 4.2.1, we can define $S_z = 0$ exciton basis states $\{\,|k_e, k_h\rangle\}$ as

$$\left|{}^{1/3}k_e, k_h\right\rangle = \frac{1}{\sqrt{2}}\left(\hat{c}^{c\dagger}_{k_e\uparrow}\hat{c}^{v}_{k_h\uparrow} \pm \hat{c}^{c\dagger}_{k_e\downarrow}\hat{c}^{v}_{k_h\downarrow}\right)|\mathrm{GS}\rangle\,. \tag{4.26}$$

By defining the centre-of-mass (COM) wavevector,

$$K = k_e - k_h, \tag{4.27}$$

and the relative wavevector,

$$k' = \frac{k_e + k_h}{2}, \tag{4.28}$$

a general excitation can be expressed in the exciton basis as

$$\left|\Phi_K^{\mathrm{MW}}\right\rangle = \sum_{k'} \Phi(k', K) \left|k' + K/2, k' - K/2\right\rangle . \tag{4.29}$$

An expression for $\Phi(k', K)$ is necessary to make further progress. As the Coulomb interaction is not diagonal in the momentum space, a more intuitive approach is to use a real space representation. This is achieved by mapping the momentum space representation to the real space representation via the Fourier transform,[93]

$$c_{R\sigma}^{v/c\dagger} = \frac{1}{\sqrt{N_u}} \sum_k c_{k\sigma}^{c/v\dagger} \exp(i2kRa), \tag{4.30}$$

where $N_u = N/2$ is the number of repeat units in the polyene. $c_{R\sigma}^{v/c\dagger}$ creates an electron in the valence/conduction band Wannier orbital at the Rth repeat unit. The electron-hole (exciton) creation operator is defined as,

$${}^{1/3}S_{rR}^{\dagger} = \frac{1}{\sqrt{2}} \left(c_{R+r/2,\uparrow}^{c\dagger} c_{R-r/2,\uparrow}^{v} \pm c_{R+r/2,\downarrow}^{c\dagger} c_{R-r/2,\downarrow}^{v} \right) . \tag{4.31}$$

$S_{rR}^{\dagger}$ creates a hole in the valence band Wannier orbital at the $(R - r/2)^{\mathrm{th}}$ repeat unit and an electron in the conduction band Wannier orbital at the $(R + r/2)^{\mathrm{th}}$ repeat unit. These excitons are called Mott-Wannier excitons. Exciton basis states in the real space representation is given by,

$$\left|R + r/2, R - r/2\right\rangle = S_{rR}^{\dagger} \left|\mathrm{GS}\right\rangle , \tag{4.32}$$

where $|\mathrm{GS}\rangle$ is the ground state,

$$|\mathrm{GS}\rangle = \prod_R c^{v\dagger}_{R\uparrow} c^{v\dagger}_{R\downarrow}. \tag{4.33}$$

A general excitation in the real space representation is defined as,

$$\left|\Phi^{\mathrm{MW}}\right\rangle = \sum_{r,R} \Phi(r,R) \left|R + r/2, R - r/2\right\rangle, \tag{4.34}$$

where $\Phi(r,R)$ is the exciton wavefunction given by

$$\Phi(r,R) = \left\langle \mathrm{GS}\middle| S_{rR} \middle|\Phi^{\mathrm{MW}}\right\rangle. \tag{4.35}$$

$\Phi(r,R)$ is the real space projection of a two-particle bound state and it has solutions analogous to the hydrogen atom. We can introduce an effective particle model by separating the centre-of-mass (COM) and the relative degrees of freedom. Then we arrive at the product wavefunction,

$$\Phi_{n,j}(r,R) = \psi_n(r)\Psi_j(R), \tag{4.36}$$

where $\Psi_j(R)$ is the COM wavefunction whose energy depends on the quantum number j, and $\psi_n(r)$ is the effective particle wavefunction describing the relative motion of the electron-hole pair whose energy depends on the quantum number n.

In Section 4.3.3, we present our numerical results of the exciton wavefunction calculations on low energy singlet excitations in polyenes using the PPP Hamiltonian. We show that the $1\,^1B_u^+$ and $1\,^1A_g^+$ states are the $n = 1, j = 1$ and $n = 1, j = 2$ excitons. They belong to the same family of states. Importantly, we show that the $2\,^1A_g^-$, $1\,^1B_u^-$, and $3\,^1A_g^-$states have exciton components belonging to the $n = 2$ family of odd-parity excitons. They are fundamentally the same excitation with different

COM energies, and their energies converge to the same value in the long-chain limit, where the COM energies disappear.

4.2.4.3 Variation of the Character of Excited States with Electron Interactions

Here we summarise the previous discussions on electronic interactions and describe how the character of low energy singlet and triplet excited states on a dimerised chain changes as a function of electronic interactions.

At the noninteracting limit, the singlet and triplet excitations are degenerate. $2\,^1A_g^-$ is the second excitation in the singlet manifold. As the long-chain limit is reached, large soliton-antisoliton pair separation causes the $2\,^1A_g^-$ state to be degenerate with the $1\,^1B_u^+$ and $1\,^3B_u^-$ states.

As electronic interactions are introduced, a charge gap opens and the $1\,^1B_u^+$ and $1\,^3B_u^-$ states become $n = 1, j = 1$ bound Mott-Wannier excitons. $2\,^1A_g^-$ is the $n = 2, j = 1$ Mott-Wannier exciton. At first, as U increases, energies of all exciton states increase. Energies of the $n = 2$ states grow more rapidly than the $n = 1$ states.

However, the $1\,^3B_u^-$ and the $2\,^1A_g^-$ states are radical soliton states, and as U increase further they evolve to be SDWs and their energies begin to decrease. The $1\,^1B_u^+$ state is a charged soliton state, and its energy continues to rise with U and the state evolves to a Mott-Hubbard exciton. Therefore, as U increases, first the degeneracy between the $1\,^1B_u^+$ and the $1\,^3B_u^-$ state is lifted, and then the energy of the $2\,^1A_g^-$ state drops below the energy of the $1\,^1B_u^+$ state. This reversal of energy levels give rise to the non luminescent properties of certain polyenes, including carotenoids. These results are shown in Fig. 4.9.

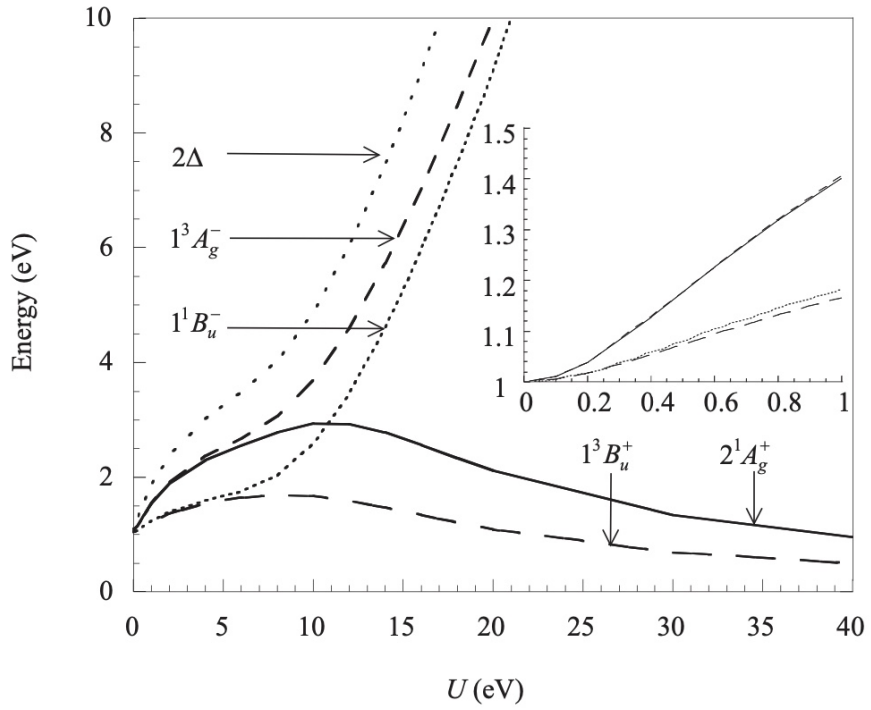

Figure 4.9: Excitation energies for the $1\,^3B_u^-$, $1\,^1B_u^+$, $2\,^1A_g^-$, $3\,^1A_g^-$, and 2Δ (charge gap) on a dimerised chain as a function of the Coulomb interaction U of the PPP Hamiltonian. The inset shows the energies for small U. Parameters : $\delta = 0.1$, $t_0 = 2.5$ eV. Note that the electron-hole sign convention is opposite to the convention used in this text. Reproduced with permission from Barford, W., *Electronic and Optical Properties of Conjugated Polymers*; Oxford University Press: 2013.

4.3 Triplet-Pair States in Polyenes

In this section we review results of our DMRG study of polyene excited states using the PPPP Hamiltonian.[2] As we have seen in Chapter 1, the triplet-pair states play an important role in polyene internal conversion and singlet fission processes. The PPPP Hamiltonian, introduced in Section 2.4.2, explicitly accounts for the electronic interactions and electron-nuclear coupling of the π-electron system. Here we describe our analysis of the triplet-pair nature of polyene excited states using excitation energies, soliton structures, and exciton wavefunctions. Long-range Coulomb interactions are modelled by the Ohno potential. We use the parametrisation of Chandross and Mazumdar for screened polyacetylene,[95] namely $U = 8$ eV, $\epsilon_r = 2$, and $t_0 = 2.4$ eV, and the electron-nuclear coupling parameter of Barford *et al.*,[104] namely $\alpha = 4.593$ eV Å^{-1}.

4.3.1 Excitation Energies

Following Section 3.2.2, we can find the dimerised ground state geometry of a polyene chain. A vertical or an instantaneous excitation is defined as an excitation from the ground state geometry. Fig. 4.10 shows the calculated vertical excitation energies for several low-lying excited states. The $2\,^1A_g^-$ state is below the $1\,^1B_u^+$ state for all chain lengths. For shorter chain lengths, the conventional energy ordering of $2\,^1A_g^- < 1\,^1B_u^+ < 1\,^1B_u^- < 3\,^1A_g^-$ is observed. However, as the chain length (N) increases, states with SDW character are more stabilised compared to the charge-transfer $1\,^1B_u^+$ state, so the $1\,^1B_u^-$ and $3\,^1A_g^-$ states fall below the $1\,^1B_u^+$ state for $N > 26$ and $N > 46$ respectively. The inset of Fig. 4.10 (a) shows that the energies of $2\,^1A_g^-$, $1\,^1B_u^-$, and $3\,^1A_g^-$ converge to the same value at the long chain limit. This indicates that the three excitations belong to the same excitation family

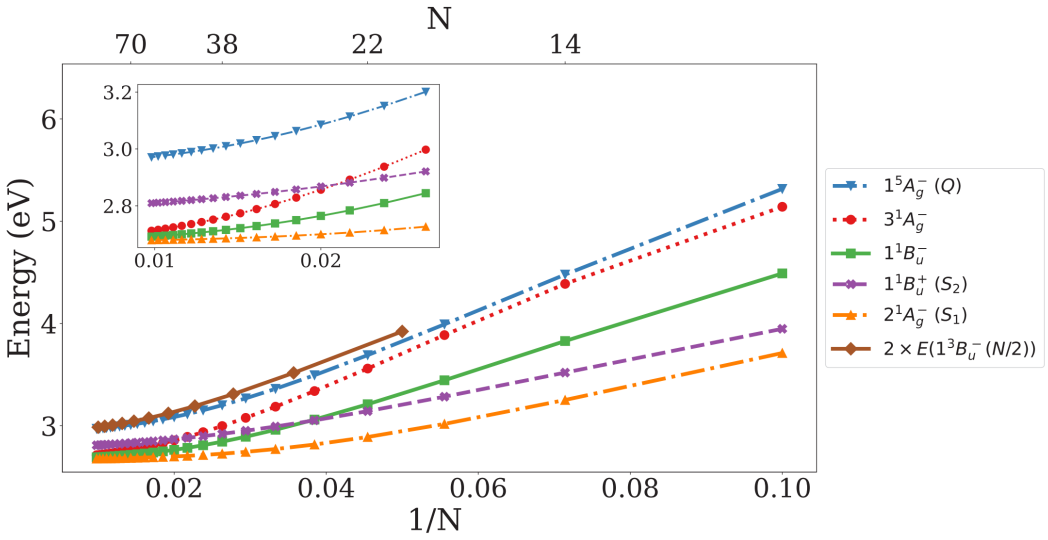

Figure 4.10: Vertical excitation energies of the low-lying singlet and quintet states, calculated using the PPPP model. N is the number of conjugated carbon atoms of the system. Also shown is twice the vertical energy of the lowest triplet excitation for a chain length of $N/2$. Inset shows the energies as $N \to \infty$. Reproduced with permission from Valentine, D. J.; Manawadu, D.; Barford, W. Higher energy triplet-pair states in polyenes and their role in intramolecular singlet fission. *Phys. Rev. B* **2020**, *102*, 125107.

with different pseudomomentum quantum numbers. This is described further in Section 4.3.3 using exciton wavefunctions. We call this family of excitations the '$2A_g$' family. Further, we see that the energy of the $1\,^5A_g^-$ state converges to the energy of two independent triplets ($1\,^3B_u^-$) on the same chain. We can therefore consider that the $1\,^5A_g^-$ state is an unbound triplet-pair state. This energy is ~ 0.3 eV higher than the energy of the $2A_g$ family of states, and can be thought of as the triplet-pair binding energy.

The relaxed energy of an excited state can be defined as the energy of that state in its equilibrium geometry. Fig. 4.11 shows the calculated relaxed energies. As the triplet-pair states couple to the nuclei strongly than the charge-transfer states, they have larger reorganisation energies than the $1\,^1B_u^+$ state. We see that $2\,^1A_g^-$ is always below the $1\,^1B_u^+$ state, and the energy of the $1\,^1B_u^-$ and $3\,^1A_g^-$ states fall below the energy of the $1\,^1B_u^+$ state for $N > 10$ and $N > 20$ respectively. The energy of the $1\,^5A_g^-$ state too falls below the energy of the $1\,^1B_u^+$ state for $N > 16$.

Comparing the vertical and relaxed excitation energies, we see that for $10 <$

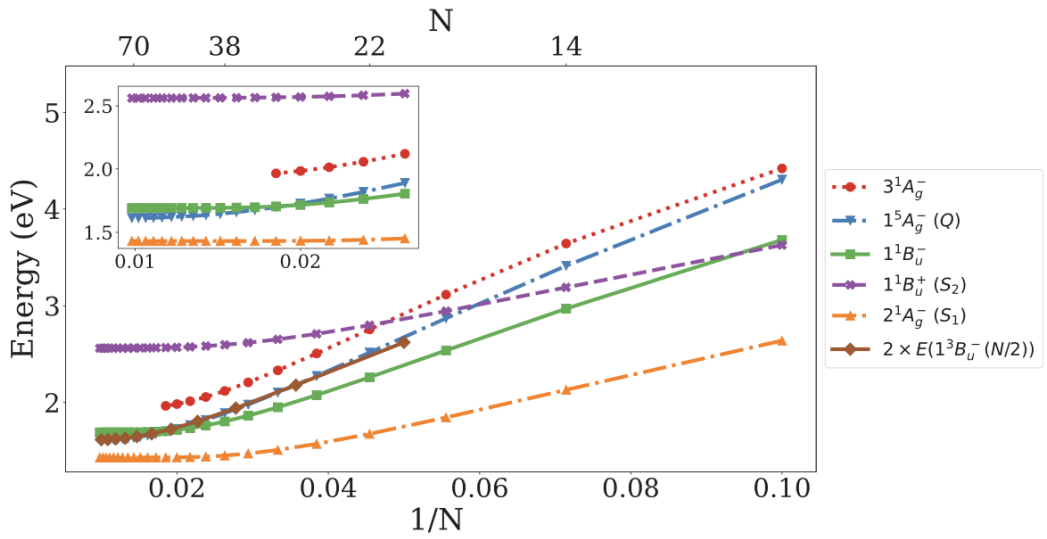

Figure 4.11: Relaxed energies of the low-lying singlet and quintet states, calculated using the PPPP model. N is the number of conjugated carbon atoms of the system. Also shown is twice the relaxed energy of the lowest triplet excitation for a chain length of $N/2$. Inset shows the energies as $N \to \infty$. Reproduced with permission from Valentine, D. J.; Manawadu, D.; Barford, W. Higher energy triplet-pair states in polyenes and their role in intramolecular singlet fission. *Phys. Rev. B* **2020**, *102*, 125107.

$N < 26$, the vertical $1\,^1B_u^-$ state is above the vertical $1\,^1B_u^+$ state, and the relaxed $1\,^1B_u^-$ state is below the relaxed $1\,^1B_u^+$ state. Therefore, energetically we might expect internal conversion from the $1\,^1B_u^+$ state to the $1\,^1B_u^-$ state for $10 < N < 26$. These chain lengths are the naturally occurring carotenoid conjugation lengths, and therefore we can expect to see $1\,^1B_u^+ \to 1\,^1B_u^-$ internal conversion in carotenoids. This process is investigated via dynamical simulations using the tDMRG-Ehrenfest method in Chapter 5.

4.3.2 Soliton Structures

The soliton structure of the excited states is investigated by calculating the staggered bond dimerisation (Eq. (4.17)) for a chain of length $N = 54$. The results are shown in Fig. 4.12. The dimerisation pattern of two half-chain ($N = 26$) triplets at either end of the chain matches the dimerisation of the $1\,^5A_g^-$ state, providing further evidence that the $1\,^5A_g^-$ state is an unbound triplet-pair. From the calculated dimerisation, we see that the triplet-pair in the $2\,^1A_g^-$ state is less spatially separated

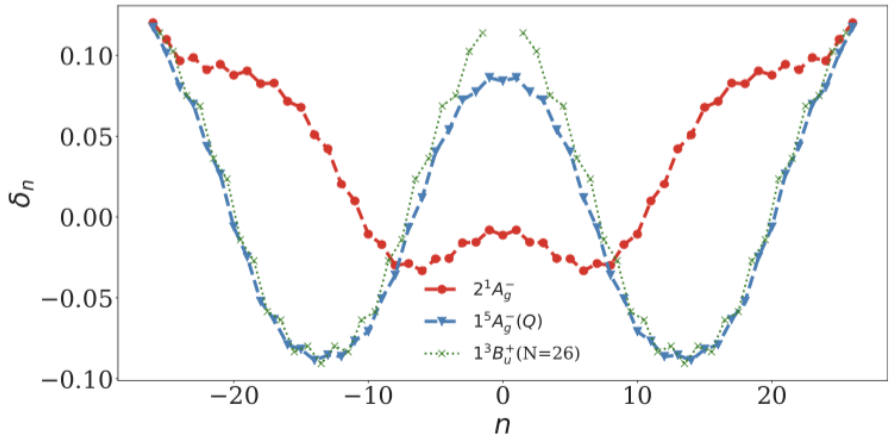

Figure 4.12: Staggered bond dimerisations for a chain of length $N = 54$ of $2\,^1A_g^-$, $1\,^5A_g^-$, and $1\,^3B_u^-$ (for $N = 26$) states, calculated from Eq. (4.17). n is the site index. Reproduced with permission from Valentine, D. J.; Manawadu, D.; Barford, W. Higher energy triplet-pair states in polyenes and their role in intramolecular singlet fission. *Phys. Rev. B* **2020**, *102*, 125107.

(more bound). Similar calculations showed that the $1\,^1B_u^-$ state is a four soliton state, and the $3\,^1A_g^-$ has a complicated soliton structure as it is formed of multiple triplet-pair states.[2,164]

(The calculation of the excitation energies and staggered bond dimerisations was performed by Barford group member Darren Valentine. See Valentine, D. Singlet fission in linear π-conjugated systems, Ph.D. Thesis, Universirty of Oxford, 2020.)

4.3.3 Exciton Wavefunctions

Further evidence for the existence of the '$2A_g$' family is provided by the calculation of exciton wavefunctions for the low-lying singlet excitations. The exciton wavefunctions calculated for a polyene with $N = 102$ using Eq. (4.35) are shown in Fig. 4.13. The nodes across the relative coordinate r corresponds to the effective particle pseudomomentum quantum number n, and the nodes across the COM coordinate R corresponds to the COM quantum number j. The $1\,^1B_u^+$ and $1\,^1A_g^+$ states belong to the $n = 1$ family of excitons, and the $2\,^1A_g^-$, $1\,^1B_u^-$, and $3\,^1A_g^-$ states belong to the $n = 2$ or '$2A_g$' family.

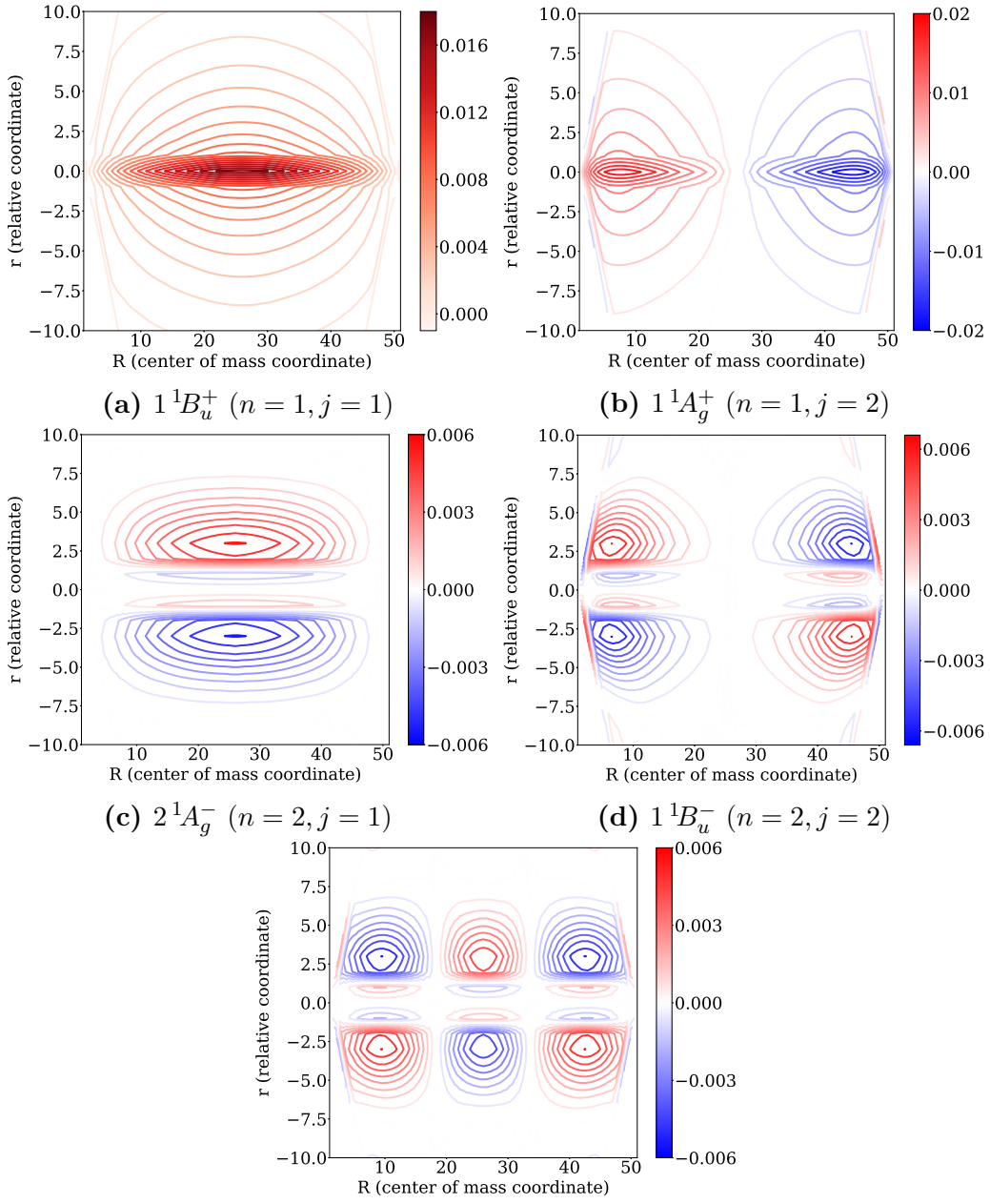

(a) $1\,^1B_u^+$ $(n = 1, j = 1)$

(b) $1\,^1A_g^+$ $(n = 1, j = 2)$

(c) $2\,^1A_g^-$ $(n = 2, j = 1)$

(d) $1\,^1B_u^-$ $(n = 2, j = 2)$

(e) $3\,^1A_g^-$ $(n = 2, j = 3)$

Figure 4.13: Exciton wavefunctions of low-lying singlet excitations of a polyene with $N = 102$, calculated using Eq. (4.35). Reproduced with permission from Valentine, D. J.; Manawadu, D.; Barford, W. Higher energy triplet-pair states in polyenes and their role in intramolecular singlet fission. *Phys. Rev. B* **2020**, *102*, 125107.

4.4 Conclusions

In this chapter we reviewed results of our work on polyene excited states by first introducing a theoretical framework to study fundamental excitations in polyenes, and then using that framework to study the low-lying excited states of polyenes using the PPPP Hamiltonian. By calculating the vertical and relaxed energies of low-lying singlet states, it was found that for experimentally relevant chain lengths the energies of the $1\,^1B_u^-$ and $3\,^1A_g^-$ lie below the bright $1\,^1B_u^+$ state. This indicates these states could be involved in dynamical relaxation pathways of the photoexcited state, and we investigate these relaxation processes in Chapter 5. Further, the energy of the $1\,^5A_g^-$ state, which is twice the energy of the lowest lying triplet state $1\,^3B_u^-$ occupying half of the chain, is ~ 0.3 eV higher than the $2\,^1A_g^-$ state. Further, the calculated dimerisation pattern of the $1\,^5A_g^-$ state fits that of two unbound triplets. Considering these factors, the $1\,^5A_g^-$ state can be assigned to be an unbound triplet-pair state, and the $2\,^1A_g^-$ is a bound triplet-pair state with a binding energy of ~ 0.3 eV.

Furthermore, we presented evidence for the existence of a family of 'dark' triplet-pair states called the '$2A_g$' family. In this chapter, we reviewed evidence based on the vertical excitation energies, dimerisation patterns, and exciton wavefunctions of these states. First, at the long chain limit, energies of the $2\,^1A_g^-$, $1\,^1B_u^-$, and $3\,^1A_g^-$ states reach the same asymptotic limit. Second, an analysis of the soliton structures indicate that both $2\,^1A_g^-$ and $1\,^1B_u^-$ are four soliton states. Finally, by calculating the exciton wavefunctions of the $2\,^1A_g^-$, $1\,^1B_u^-$, and $3\,^1A_g^-$ states we demonstrated that they are fundamentally the same excitation with different centre-of-mass quantum numbers. For further evidence for the existence of '$2A_g$' family based on calculation of spin-spin correlation and triplet-pair overlap, readers are referred to ref [2].

Chapter 5

Singlet Triplet-Pair Production via Internal Conversion

We describe our simulations of the excited state dynamics of carotenoids in this chapter. After photoexcitation, the 'bright' $1\,^1B_u^+$ state can undergo internal conversion to a 'dark' triplet-pair state. The internal conversion pathways depend on the symmetries of the carotenoid molecule and the relative ordering of its low-lying singlet excited states. In order to study these pathways, we investigate the internal conversion process in two carotenoids, zeaxanthin and neurosporene, and in two parameter regimes. For one parameter set, internal conversion from the $1\,^1B_u^+$ state to $2\,^1A_g^-$ state can occur via the 'dark' intermediate $1\,^1B_u^-$ state. For the other parameter set, direct internal conversion from the $1\,^1B_u^+$ state to the $2\,^1A_g^-$ state is possible. After describing the parametrisation of the UV Hamiltonian, we present our results for the dynamical simulations, including the calculations of the singlet triplet-pair yields. These simulations are performed using the adaptive tDMRG method on the UV Hamiltonian, and a single trajectory is used to evaluate observables. The Ehrenfest equations of motion are used to simulate the coupled nuclei dynamics. We then describe results from our theoretical transient spectra calculations performed using Lanczos-DMRG.

5.1 Parametrisation of the UV-Peierls Hamiltonian

As described in Section 3.1.3, the adaptive tDMRG method used to simulate dynamical systems in this work requires a Hamiltonian which only contains up to nearest neighbour interactions. A suitable Hamiltonian is the UVP Hamiltonian, introduced in Section 2.4.3,

$$\begin{aligned}\hat{H}_{\mathrm{UVP}} = &-\sum_{i\sigma} t_0 \left(\hat{c}^{\dagger}_{i+1,\sigma}\hat{c}_{i,\sigma} + \hat{c}^{\dagger}_{i,\sigma}\hat{c}_{i+1,\sigma}\right) + U\sum_{i}\left(\hat{N}_{i\uparrow} - \frac{1}{2}\right)\left(\hat{N}_{i\downarrow} - \frac{1}{2}\right) \\ &+ \frac{V}{2}\sum_{i}\left(\hat{N}_i - 1\right)\left(\hat{N}_{i+1} - 1\right) + 2\alpha\sum_{i\sigma}\left(u_{i+1} - u_i\right)\left(\hat{c}^{\dagger}_{i+1,\sigma}\hat{c}_{i,\sigma} + \hat{c}^{\dagger}_{i,\sigma}\hat{c}_{i+1,\sigma}\right) \\ &+ \frac{K}{2}\sum_{i}\left(u_{i+1} - u_i\right)^2 . \end{aligned} \tag{5.1}$$

We seek to parametrise the U and V Coulomb interaction terms of the UVP model, while retaining the Chandross-Mazumdar parametrisation of $t_0 = 2.4$ eV,[95] $K = 46$ eV Å^{-2} and $\alpha = 4.593$ eV Å^{-1} from Barford and co-workers.[104] We find two parameter sets corresponding to two potential internal conversion pathways as described below.

5.1.1 Internal Conversion via the $1\,^1B_u^-$ State

In Section 4.3 we described our results of a study of polyene excited states using the PPPP Hamiltonian. By comparing the vertical and relaxed energies of the PPP model, we showed that internal conversion from the $1\,^1B_u^+$ state to the $1\,^1B_u^-$ state is energetically possible for polyenes with $10 < N < 26$ carbon atoms. These are the conjugation lengths of naturally occurring carotenoids, and therefore we parametrise our model to simulate internal conversion via the $1\,^1B_u^-$ state by choosing U and V

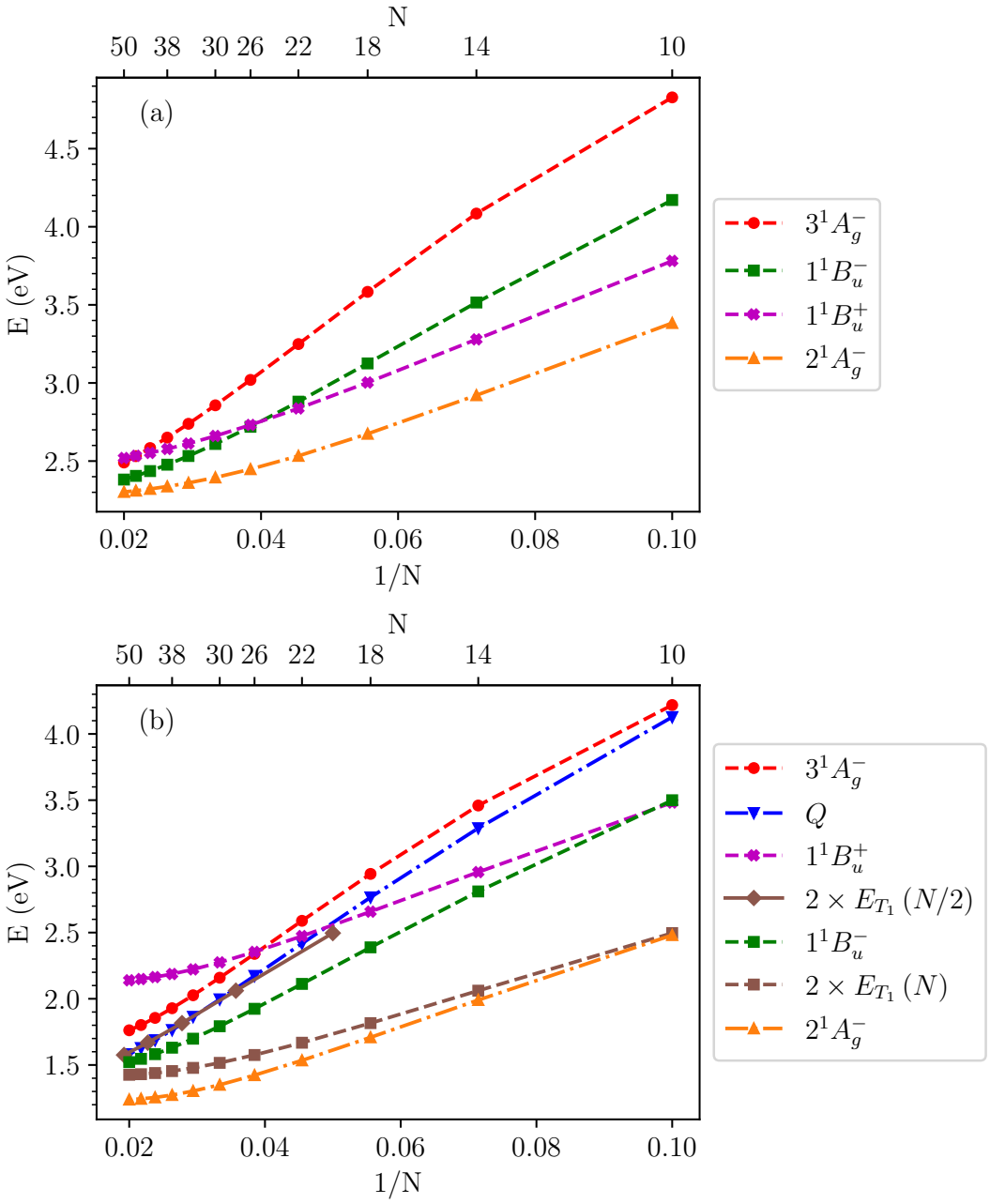

Figure 5.1: Vertical (a) and relaxed (b) singlet excitation energies of the UV-Peierls model with $U = 7.25$ eV and $V = 2.75$ eV. N is the number of conjugated carbon atoms of the system. U and V are parametrised to reproduce the vertical and relaxed excited state energies of the PPP model, shown in Figs. 4.10 and 4.11.

to replicate the excited state energies of the PPPP model. We find that $U = 7.25$ eV and $V = 2.75$ eV reproduces the ordering of the low-lying vertical and relaxed energies of Figs. 4.10 and 4.11. The calculated vertical and relaxed energies for the parameters $U = 7.25$ eV and $V = 2.75$ eV using the UVP model are shown in Fig. 5.1.

5.1.2 Direct $1\,^1B_u^+ \rightarrow 2\,^1A_g^-$ Internal Conversion

Taffet et al. recently reported a study of carotenoid excited states using highly accurate *ab initio* calculations.[58] They used DFT, TDDFT, and CASSCF(4,4) to determine the geometric minima of the $1\,^1A_g^-$,$1\,^1B_u^+$, and $2\,^1A_g^-$ states, respectively. Then they performed DMRG self-consistent-field (DMRG-CASSCF) calculations to determine the excitation energies, with N-electron valence-state perturbation theory (NEVPT2) correction to account for dynamic correlations. They showed that for $N \leq 26$, the lowest lying singlet excited state at the vertical geometry is not the $2\,^1A_g^-$ state, but the bright $1\,^1B_u^+$ state. As the nuclei relax, the $2\,^1A_g^-$ falls below the $1\,^1B_u^+$ state owing to its larger nuclear reorganisation energy. This suggests it is possible for the $1\,^1B_u^+$ state to directly undergo internal conversion to the $2\,^1A_g^-$ state, without the need of an intermediary state like $1\,^1B_u^-$.

In order to study this internal conversion pathway, we parametrise the UVP model to reproduce the vertical excitation energies of ref [58] (shown in Fig. 5.2). For a given U, increasing V decreases $(E_{1\,^1B_u^+} - E_{2\,^1A_g^-})$. Keeping all other parameters the same (i.e., $U = 7.25$ eV, $t_0 = 2.4$ eV, $K = 46$ eV Å^{-2}, and $\alpha = 4.593$ eV Å^{-1}), we find $V = 3.25$ eV such that $E_{1\,^1B_u^+}$(vertical) $- E_{2\,^1A_g^-}$(vertical) replicates the lowest-lying carotenoid dark and bright state vertical excitation energies reported in ref [58]. The vertical and relaxed energies for the UVP model with these parameters are illustrated in Fig. 5.3. In this parameter regime, for all carotenoid chain lengths

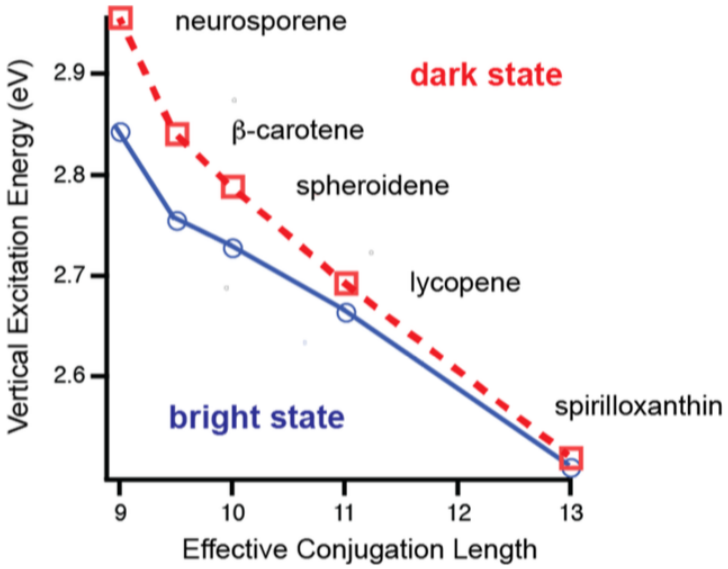

Figure 5.2: Dependence of vertical excited energies of a series of naturally occurring carotenoids as a function of their conjugation length. The bright state ($1B_u$), determined as the singlet excited state with the highest transition dipole moment to the ground state is shown with a solid blue line. The dashed red line corresponds to the formally dark $2A_g$ state. Adapted with permission from Taffet, E. J.; Lee, B. G.; Toa, Z. S. D.; Pace, N., et al. Carotenoid Nuclear Reorganization and Interplay of Bright and Dark Excited States. *J. Phys. Chem. B* **2019**, *123*, 8628–8643.

under consideration, $1\,^1B_u^+$ vertical energies lie below $2\,^1A_g^-$ vertical energies, while $1\,^1B_u^+$ relaxed energies are above $2\,^1A_g^-$ relaxed energies. Therefore it is possible to observe direct internal conversion from the $1\,^1B_u^+$ to the $2\,^1A_g^-$ state via a diabatic energy level crossing.

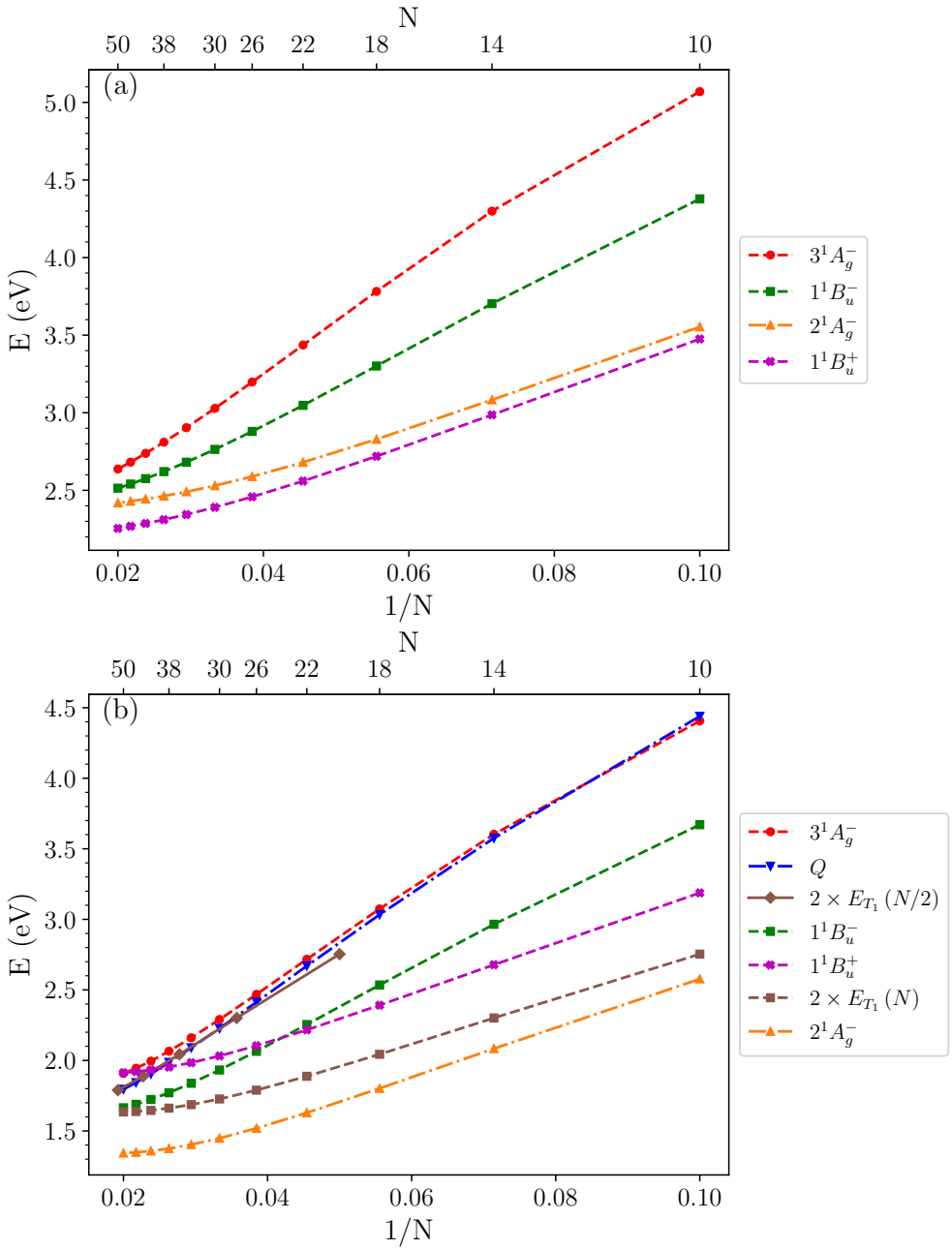

Figure 5.3: Vertical (a) and relaxed (b) singlet excitation energies of the UV-Peierls model with $U = 7.25$ eV and $V = 3.25$ eV. N is the number of conjugated carbon atoms of the system. The vertical energy gaps of ~ 0.1 eV between $1\,^1B_u^+$ (magenta) and $2\,^1A_g^-$ (orange) for $18 \leq N \leq 26$ agree with the corresponding excitation energies reported in ref[58] (and shown in Fig. 5.2).

5.2 Internal Conversion via the $1\,^1B_u^-$ State

In this section we describe the results of our simulations of internal conversion for zeaxanthin and neurosporene *via* the first pathway. Following Section 3.2.2, the initial state at $t = 0$, $\Psi(t = 0)$ is prepared in the S_2 state, the adiabatic state exhibiting the highest overlap with the $1\,^1B_u^+$ state at the Franck-Condon point for $V = 2.75$ eV. The initial state is determined numerically using the static DMRG algorithm outlined in Section 3.1.2. At the Franck-Condon point, the nuclei are in their ground state geometries, and experience resultant forces exerted by the electrons. This causes the $\hat{H}_{\text{el-ph}}$ term of the UVP Hamiltonian to change, and initiates the evolution of the electronic and nuclear degrees of freedom. The electronic evolution follows the time-dependent Schrödinger equation, and is numerically simulated using tDMRG as described in Section 3.1.3. Nuclear motion is treated classically using Ehrenfest dynamics introduced in Section 3.2. We keep track on the nature of the evolving state $\Psi(t)$ by calculating the instantaneous diabatic and adiabatic eigenstates of the evolving Hamiltonian, defined in Section 2.6. The symmetry breaking Hamiltonians, $\hat{H}_\epsilon$, for neurosporene are found following Section 3.3. (The calculated $\hat{H}_\epsilon$ are given in Appendix 5.A.)

5.2.1 Numerical Results for Zeaxanthin

Zeaxanthin is a carotenoid with 18 fully conjugated carbon atoms. Zeaxanthin plays a key role in biological photophysical systems[11,61] and is thought to exhibit singlet fission.[31] Its structural formula is shown in Fig. 5.4. Because of its twisted end groups, zeaxanthin possesses C_2 symmetry, but its photophysics can be modelled using a π-electron model with $C_{2\text{h}}$ symmetry. The symmetry breaking Hamiltonian, $\hat{H}_\epsilon$ for zeaxanthin is even under two-fold rotation, and $\left\langle n\,^1B_u^\pm \middle| \hat{H}_\epsilon \middle| m\,^1A_g^\pm \right\rangle = 0$.

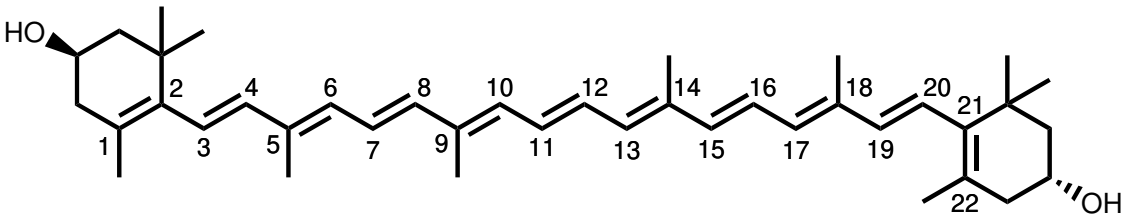

Figure 5.4: Structural formula of zeaxanthin. The end groups formed of six-membered carbon rings are twisted by 75° out of the plan of the molecule, thus reducing its effective conjugation length to 18 carbon atoms. Zeaxanthin possesses C_2 symmetry due to its twisted end groups, but its π-electron system can be modelled under C_{2h} symmetry.

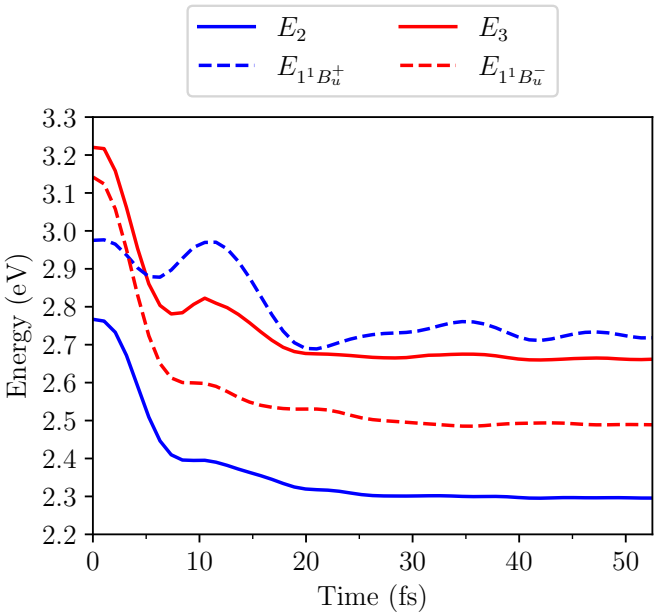

Figure 5.5: Excited energies of the diabatic states $1\,^1B_u^+$ and $1\,^1B_u^-$, and adiabatic states S_2 and S_3, as a function of time. Diabatic states are the eigenstates of $\hat{H}_{\mathrm{UVP}} + \hat{H}_\lambda$ as defined by Eq. (2.71). Adiabatic states are the eigenstates of $\hat{H}_{\mathrm{UVP}} + \hat{H}_\lambda + \hat{H}_\epsilon$ as defined by Eq. (2.70). The results are for zeaxanthin, calculated using the UVP model with $U = 7.25$ eV and $V = 2.75$ eV. The initial condition is $\Psi(t = 0) = S_2$.

We can model the twist of the end groups of zeaxanthin by altering the electron transfer integrals, t_i, for the 2nd and the 20th bonds (i.e., $\mathrm{C}_2 - \mathrm{C}_3$ and $\mathrm{C}_{20} - \mathrm{C}_{21}$, as shown in Fig. 5.4) according to $t_i = t_0 \cos\phi_i$, where $\phi_i = 75°$ is the dihedral angle for these bonds.[219]

The calculated diabatic energies of the $1\,^1B_u^+$ and $1\,^1B_u^-$ states, and the adiabatic energies of the S_2 and S_3 states, as a function of time are shown in Fig. 5.5. As the system evolves the energies of the diabatic states $1\,^1B_u^+$ and $1\,^1B_u^-$ exhibit a crossover at ~ 3 fs. The corresponding adiabatic energies, S_2 and S_3, how-

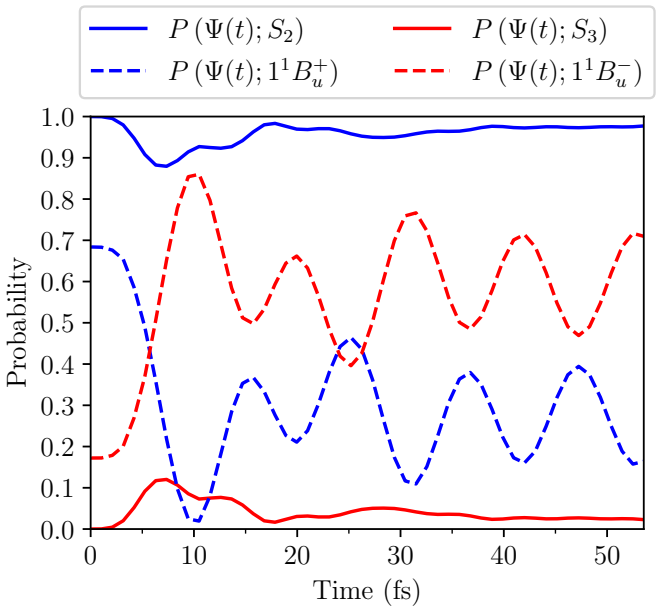

Figure 5.6: Probabilities that the system described by $\Psi(t)$ occupies the adiabatic states S_2 and S_3, and the diabatic states $1\,^1B_u^+$ and $1\,^1B_u^-$. Adiabatic and diabatic probabilities are calculated using Eqs. (2.72) and (2.73) respectively. Note that $\Psi(t)$ predominately evolves adiabatically on the surface of S_2. The oscillations in the occupations of $1\,^1B_u^+$ and $1\,^1B_u^-$, with a period of 11 fs, are the nonstationary state oscillations described in Section 6.1.

ever exhibit an avoided crossing, because the coupling between the diabatic states, $\langle 1\,^1B_u^+|\hat{H}_\epsilon|1\,^1B_u^-\rangle \neq 0$.

Insights into the nature of the evolving state $\Psi(t)$ can be obtained by calculating its projection on to the diabatic and adiabatic singlet states. Fig. 5.6 illustrates the probability that the evolving system described by $\Psi(t)$ occupies the diabatic states $1\,^1B_u^+$ and $1\,^1B_u^-$, and adiabatic states S_2 and S_3, as a function of time. The initial condition is that $\Psi(t)$ entirely occupies the lower adiabatic state S_2, but around the avoided crossing at ~ 5 fs this probability drops to $\sim 88\%$ while the probability of occupying S_3 rises to $\sim 12\%$. After ~ 30 fs the probability that the system occupies S2 increases to over $\sim 95\%$ and then remains essentially constant. Similarly, the probability that the system occupies S_3 reduces to less than $\sim 5\%$. As the evolving system described by $\Psi(t)$ remains on a single adiabatic surface S_2, this process can be described as an adiabatic transition.

Fig. 5.7 shows the probabilities that the adiabatic states, S_2 and S_3, occupy the

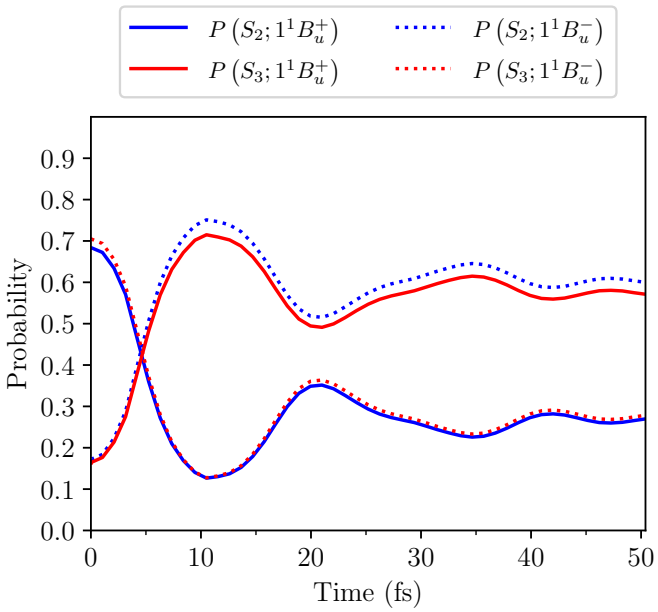

Figure 5.7: Probabilities that the adiabatic states S_2 and S_3 occupy the diabatic states $1\,^1B_u^+$ and $1\,^1B_u^-$ as a function of time, calculated using Eq. (2.74). At time $t = 0$, S_2 is the primary photoexcited state, which is predominantly occupied by the exciton state $1\,^1B_u^+$. Within 50 fs, S_2 predominately occupies the triplet-pair state $1\,^1B_u^-$ while retaining some exciton component. The oscillations in the probabilities with a period $\sim$ 20 fs coincide with the period of C-C bond stretching vibrations.

diabatic states, $1\,^1B_u^+$ and $1\,^1B_u^-$. Reflecting the crossover in the diabatic energies, at $t = 0$ the lower adiabatic state, S_2, predominately occupies $1\,^1B_u^+$, while the upper adiabatic state, S_3, predominately occupies $1\,^1B_u^-$. At the avoided crossing the adiabatic states are equal admixtures of both diabatic states. These probabilities then oscillate, before becoming damped after $\sim$ 40 fs (or two C-C bond oscillations). At this time S_2 predominately occupies $1\,^1B_u^-$. Due to the spatial symmetry of zeaxanthin, further internal conversion to the $2\,^1A_g^-$ state is not observed. A scheme illustrating the internal conversion between the excited states of zeaxanthin is shown in Fig. 5.8.

Extensive calculations on polyenes using the PPP model have demonstrated that $1\,^1B_u^-$ is the second member of the '$2A_g$' family of states described in Chapter 4.[2,164] By calculating the staggered bond dimerisation for zeaxanthin, we confirm that $1\,^1B_u^-$ is indeed a triplet-pair state. Fig. 5.9 shows the staggered bond dimerisations of the $2\,^1A_g^-$, $1\,^1B_u^+$, and $1\,^1B_u^-$ states of zeaxanthin calculated using the UVP model

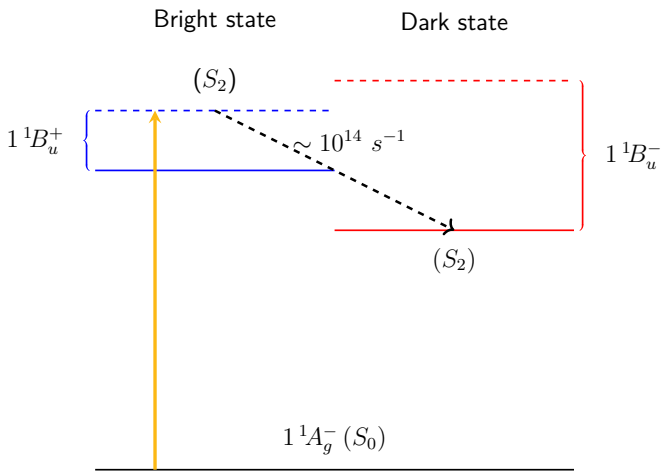

Figure 5.8: A schematic diagram illustrating internal conversion between the excited states of zeaxanthin (using $V = 2.75$ eV) in the diabatic representation. The dashed (solid) horizontal lines represent the vertical (relaxed) energies of the states. The approximate rate constant is also indicated. $1\,^1B_u^+$ (blue) and $1\,^1B_u^-$ (red). The yellow arrow illustrates the vertical excitation. The black dashed arrow indicates internal conversion.

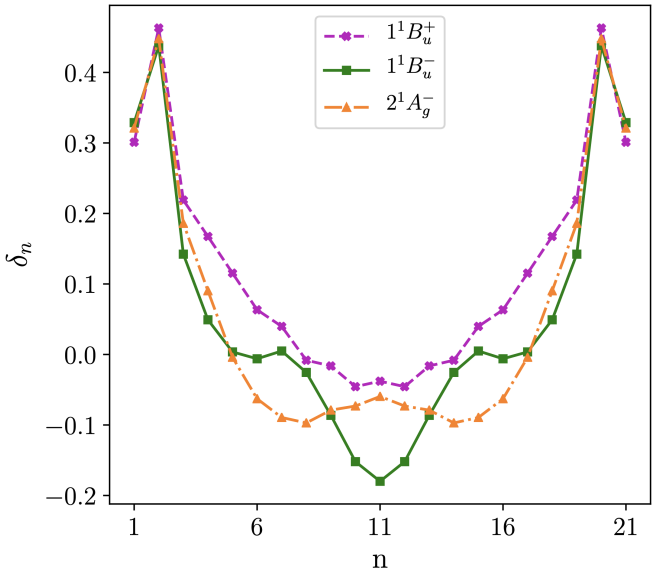

Figure 5.9: The staggered bond dimerization, δ_n, versus bond index, n, for zeaxanthin of the $2\,^1A_g^-$, $1\,^1B_u^-$, and $1\,^1B_u^+$ states, indicating the four-soliton structure of the $2\,^1A_g^-$ and $1\,^1B_u^-$ triplet-pair states. Solitons in polyene excited states are described in Section 4.2.3.

with $U = 7.25$ eV and $V = 2.75$ eV. Both $2\,^1A_g^-$ and $1\,^1B_u^-$ states demonstrate the characteristic four soliton structure of triplet-pair states.

The diabatic state probabilities of Fig. 5.6 show oscillations after the system evolves adiabatically to the $1\,^1B_u^-$ state. These oscillations, described in more detail in Section 6.1, can be interpreted as nonstationary state oscillations of a two-level quantum system. In realistic systems, however, these oscillations are damped by the interactions of the carotenoids with its surroundings. This is an effect not captured by the Ehrenfest approximation. We can estimate a 'classical' probability for the triplet-pair yield as,

$$P_{\text{classical}}(\Psi; 1\,^1B_u^-) = P(\Psi; S_2) \times P(S_2; 1\,^1B_u^-) + P(\Psi; S_3) \times P(S_3; 1\,^1B_u^-). \quad (5.2)$$

The derivation of Eq. (5.2) is described in Section 6.1. We find that for zeaxanthin, $P_{\text{classical}}(\Psi; 1\,^1B_u^-) \sim 60\%$ after ~ 50 fs.

5.2.2 Numerical Results for Neurosporene

In the previous section we described the internal conversion process of zeaxanthin. Due to the spatial symmetry, internal conversion from the diabatic states of B_u symmetry to the diabatic states of A_g symmetry is forbidden in zeaxanthin. In this section, we describe results of our dynamical simulations of photoexcited neurosporene, a molecule which does not possess C_2 symmetry. As a result, transitions from B_u to A_g states are not symmetry forbidden, and this gives rise to a complex dynamical relaxation process involving the $1\,^1B_u^+$, $1\,^1B_u^-$, and $2\,^1A_g^-$ diabatic states. The structural formula of neurosporene is shown in Fig. 5.10.

We first describe the results of our dynamical simulations using the UVP model with $U = 7.25$ eV and $V = 2.75$ eV. The initial photoexcited system $\Psi(t)$ is prepared

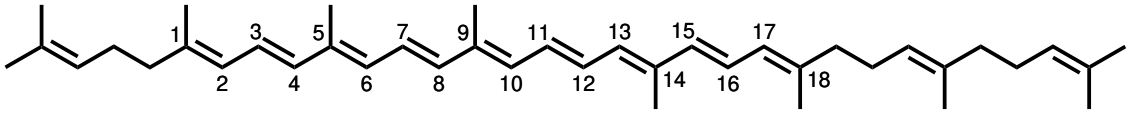

Figure 5.10: Structural formula of neurosporene, illustrating the 18 carbon atom π-conjugated system.

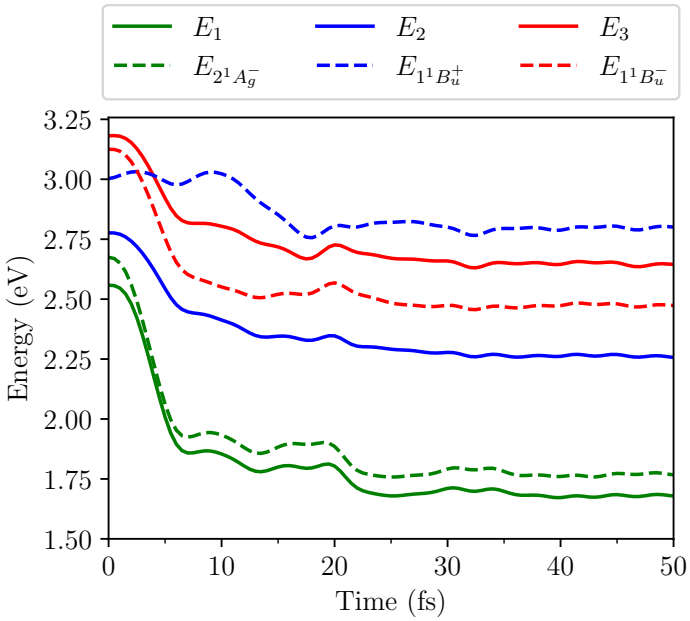

Figure 5.11: Excitation energies as a function of time of the diabatic $2\,^1A_g^-$, $1\,^1B_u^+$, and $1\,^1B_u^-$ states, and the adiabatic S_1, S_2, and S_3 states. These energies are found for neurosporene with $V = 2.75$ eV. The $1\,^1B_u^+$ and $1\,^1B_u^-$ energies exhibit a crossover at ~ 5 fs, while the S_2 and S_3 energies (i.e., E_2 and E_3, respectively) exhibit an avoided crossing.

in the adiabatic state S_2 as this has the largest overlap with the diabatic $1\,^1B_u^+$ state at the Franck-Condon point. Fig. 5.11 shows the calculated adiabatic and diabatic excited energies as a function of time. A crossover of the diabatic $1\,^1B_u^-\$$ and $1\,^1B_u^+$ energies occurs at ~ 5 fs, while the adiabatic S_2 and S_3 energies exhibit an avoided crossing.

The triplet-pair nature of the system at time t is determined by calculating the probabilities that the system described by $\Psi(t)$ occupies the triplet-pair states, $1\,^1B_u^-$ and $2\,^1A_g^-$. Fig. 5.12 shows the probabilities that $\Psi(t)$ occupies the diabatic states $2\,^1A_g^-$, $1\,^1B_u^+$ and $1\,^1B_u^-$, and the adiabatic states S_1, S_2 and S_3. At the avoided crossing $\Psi(t)$ exhibits an adiabatic transition from the $1\,^1B_u^+$ state to the $1\,^1B_u^-$ state. Within 10 fs, $\Psi(t)$ predominantly occupies the $1\,^1B_u^-$ diabatic state. After the

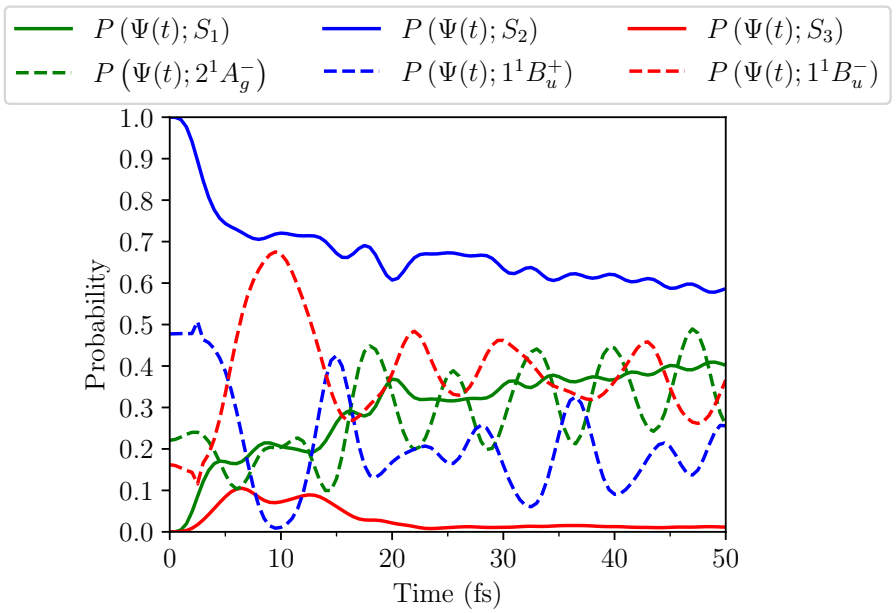

Figure 5.12: Probabilities as a function of time that the system described by $\Psi(t)$ occupies the adiabatic states, S_1, S_2 and S_3, and the diabatic states, $2\,^1A_g^-$, $1\,^1B_u^+$ and $1\,^1B_u^-$. The results are for neurosporene with $V = 2.75$ eV.

ultrafast adiabatic transition to the $1\,^1B_u^-$ state, the system continues to undergo a slow non-adiabatic transition to the $2\,^1A_g^-$ state. This is a consequence of the nonzero coupling between the $1\,^1B_u^-$ and $2\,^1A_g^-$ states, i.e., $\left\langle 1\,^1B_u^- \middle| \hat{H}_\epsilon \middle| 2\,^1A_g^- \right\rangle \neq 0$. This slow non-adiabatic transition is seen in neurosporene, but not in zeaxanthin as zeaxanthin conserves C_2 symmetry and therefore $\left\langle 1\,^1B_u^- \middle| \hat{H}_\epsilon \middle| 2\,^1A_g^- \right\rangle = 0$.

As both $2\,^1A_g^-$ and $1\,^1B_u^-$ are triplet-pair states, and noting that $P(S_3;\Psi(t)) \sim 0$ in the long-time limit, we can extend the singlet triplet-pair yield calculation for a two level system introduced in the previous section to calculate the total triplet-pair state probability, $P_{\text{classical}}$, as

$$\begin{aligned} P_{\text{classical}} =& P(\Psi(t);S_1) \times P(S_1;2\,^1A_g^-) + P(\Psi(t);S_2) \times P(S_2;2\,^1A_g^-) \\ &+ P(\Psi(t);S_1) \times P(S_1;1\,^1B_u^-) + P(\Psi(t);S_2) \times P(S_2;1\,^1B_u^-). \end{aligned} \tag{5.3}$$

After ~ 50 fs this yield is $\sim 70\%$. The probabilities, $P(S_i,\phi_j)$, that the adiabatic state, S_i occupies the diabatic state ϕ_j, are shown in Fig. 5.13.

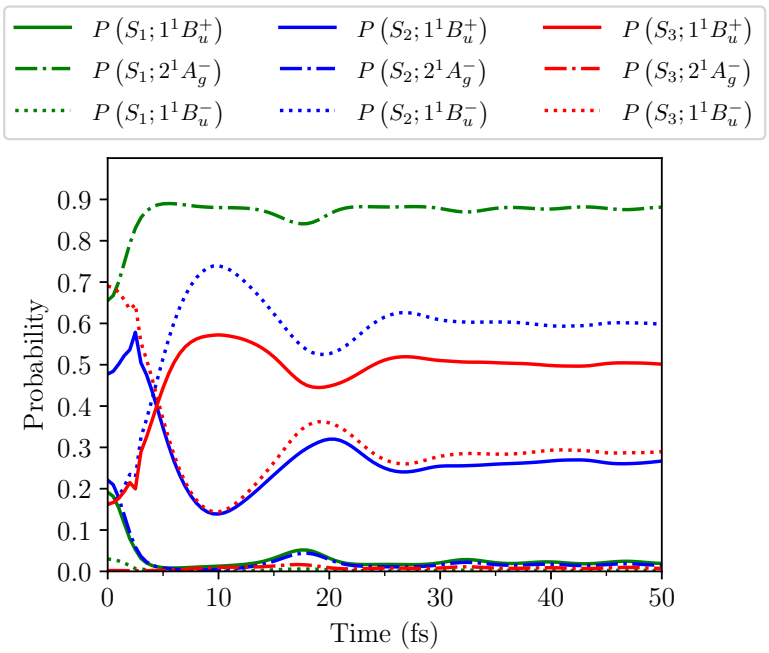

Figure 5.13: Probabilities that the adiabatic states S_1, S_2, and S_3 occupy the diabatic states $2\,^1A_g^-$, $1\,^1B_u^+$, and $1\,^1B_u^-$as a function of time. The results are for neurosporene with $V = 2.75$ eV.

A scheme illustrating the internal conversion between the excited states of neurosporene with $V = 2.75$ eV is shown in Fig. 5.14.

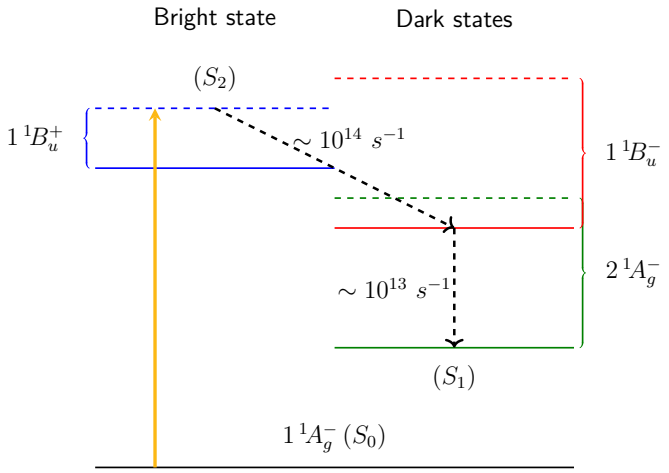

Figure 5.14: A schematic diagram illustrating internal conversion between the excited states of neurosporene (using $V = 2.75$ eV) in the diabatic representation. The dashed (solid) horizontal lines represent the vertical (relaxed) energies of the states. The approximate rate constant is also indicated. $1\,^1B_u^+$ (blue), $1\,^1B_u^-$ (red) and $2\,^1A_g^-$(green). The yellow arrow illustrates the vertical excitation. The black dashed arrows indicate internal conversion.

5.3 Direct $1\,^1B_u^+ \rightarrow 2\,^1A_g^-$ Internal Conversion

We investigate the direct $1\,^1B_u^+ \rightarrow 2\,^1A_g^-$ internal conversion pathway in carotenoids using neurosporene as our model system and the UVP model with $U = 7.25$ eV and $V = 3.25$ eV. For these parameters, the primary photoexcited state is S_1, which is predominately $1\,^1B_u^+$ in character. The singlet adiabatic and diabatic energies as a function of time are illustrated in Fig. 5.15. The $2\,^1A_g^-$and $1\,^1B_u^+$ energies crossover within ~ 3 fs. In contrast, as a consequence of the diabatic coupling of the $2\,^1A_g^-$ and $1\,^1B_u^+$ states, the S_1 and S_2 energies display an avoided crossing.

The probabilities that $\Psi(t)$ occupies the adiabatic and diabatic states, illustrated in Fig. 5.16, show that the avoided crossing is accompanied by a transition of $\Psi(t)$ from the $1\,^1B_u^+$ state to the $2\,^1A_g^-$ state, while predominantly remaining in the S_1 state. The oscillations of the diabatic populations, also observed for zeaxanthin, can be understood by a quasistationary two-state approximation, as discussed in Section 6.1.

Further evidence for the adiabatic transition is provided by the calculated prob-

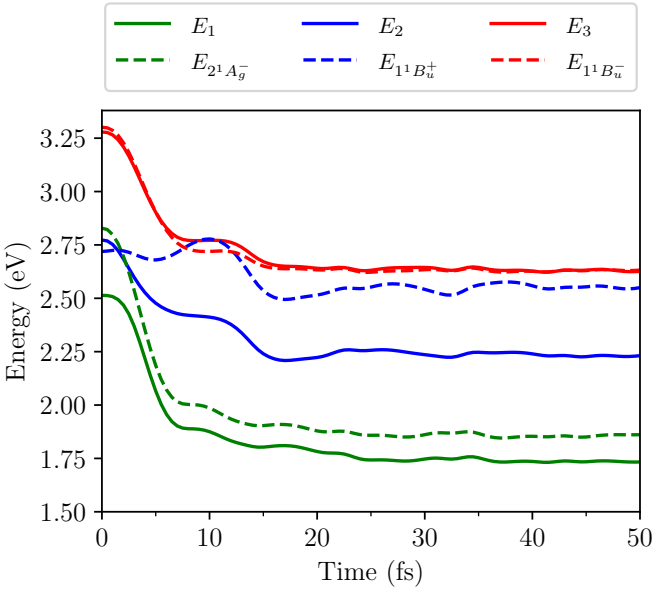

Figure 5.15: Excitation energies as a function of time of the diabatic $1\,^1B_u^+$, $2\,^1A_g^-$ and $1\,^1B_u^-$ states, and the adiabatic S_1, S_2 and S_3 states. These energies are found for neurosporene with $V = 3.25$ eV. The $1\,^1B_u^+$ and $2\,^1A_g^-$ energies exhibit a crossover at ~ 3 fs, while the S_1 and S_2 energies exhibit an avoided crossing.

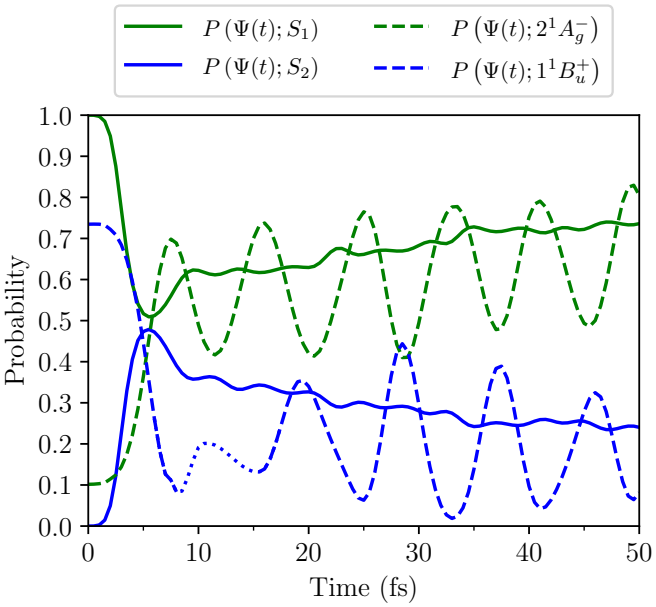

Figure 5.16: Probabilities as a function of time that the system described by $\Psi(t)$ occupies the adiabatic states, S_1 and S_2, and the diabatic states, $2\,^1A_g^-$ and $1\,^1B_u^+$. These results are for neurosporene with $V = 3.25$ eV. Note that $\Psi(t = 0) = S_1$. (The dotted curve for the $1\,^1B_u^+$ occupation is an interpolation of the computed data from 8 to 15 fs, as during this time the $1\,^1B_u^+$ and $1\,^1B_u^-$ energies are quasidegenerate, making it difficult to numerically resolve these wavefunctions.)

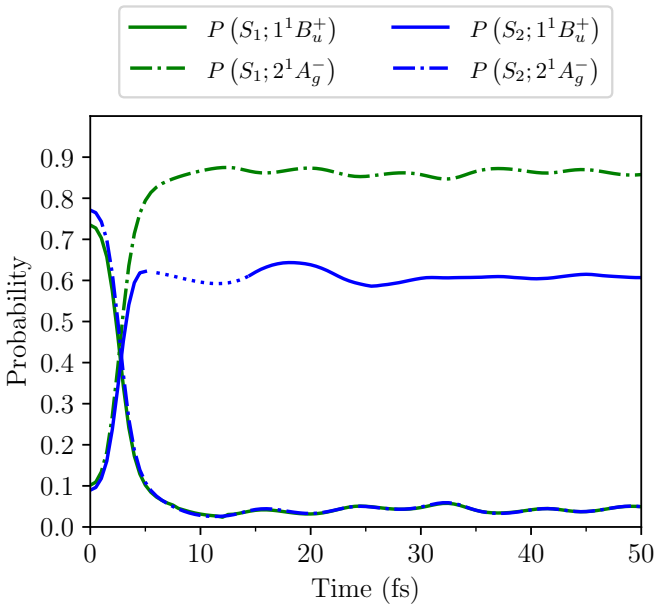

Figure 5.17: Probabilities as a function of time that the adiabatic states, S_1 and S_2, occupy the diabatic states, $2\,^1A_g^-$ and $1\,^1B_u^+$. These results are for neurosporene with $V = 3.25$ eV. (The dotted curve for the $1\,^1B_u^+$ occupation is an interpolation of the computed data from 8 to 15 fs, as during this time the $1\,^1B_u^+$ and $1\,^1B_u^-$ energies are quasidegenerate, making it difficult to numerically resolve these wavefunctions.)

abilities that the adiabatic states occupy the diabatic states, shown in Fig. 5.17. At $t = 0$, the photoexcited state, S_1, primarily occupies the exciton state, $1\,^1B_u^+$, while S_2 primarily occupies the triplet-pair state, $2\,^1A_g^-$. After the avoided crossing, at which the diabatic states contribute equally to the adiabatic states, the S_1 state predominantly occupies the $2\,^1A_g^-$ state, while the S_2 state predominantly occupies the $1\,^1B_u^+$ state. A 'classical' $2\,^1A_g^-$ yield can be calculated similar to the zeaxanthin by

$$P_{\text{classical}}(\Psi; 2\,^1A_g^-) = P(\Psi; S_1) \times P(S_1; 2\,^1A_g^-) + P(\Psi; S_2) \times P(S_2; 2\,^1A_g^-). \quad (5.4)$$

After ~ 50 fs, this yield is $\sim 60\%$.

A scheme illustrating the internal conversion between the excited states for direct internal conversion is shown in Fig. 5.18.

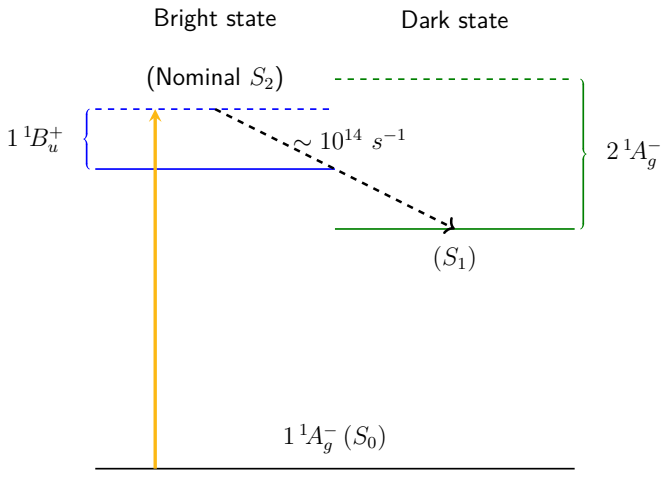

Figure 5.18: Schematic diagrams illustrating internal conversion between the excited states of neurosporene (using $V = 3.25$ eV) in the diabatic representation. The dashed (solid) horizontal lines represent the vertical (relaxed) energies of the states. The approximate rate constant is also indicated. $1\,^1B_u^+$ (blue) and $2\,^1A_g^-$ (green). The yellow arrow illustrates the vertical excitation. The black dashed arrow indicates internal conversion.

5.4 Transient Spectra Calculations

Transient (i.e., time-resolved) spectroscopy is an important experimental technique used in the study of carotenoid photophysics.[154] Seminal work which utilised transient spectroscopy experiments include the measurement of the S_1 lifetime of carotenoids,[220] direct observation of the S_1 dark state,[221] and the detection of dark intermediate states between the S_1 and S_2 states.[50,222]

The theoretical transient absorption spectrum from state S_i at time t is given by Eq. (3.33),

$$I_\mu(t,\omega) = \frac{1}{\pi}\sum_n |\langle n|\hat{\mu}|S_i(t)\rangle|^2 \,\delta(E_i+\omega-E_n), \tag{5.5}$$

where E_i is the energy of state S_i. In this section, we present our results for transient excited state absorption calculations using the Lanczos-DMRG method.[157,158]

We present results for $V = 3.25$ eV, when there is direct $1\,^1B_u^+$ to $2\,^1A_g^-$ state conversion. First, we consider an ideal system with both particle-hole and C_2 symmetries (i.e., we set $\hat{H}_\epsilon = 0$). Thus, at the Franck-Condon point (i.e., at $t = 0$ fs) $S_1 \equiv 1\,^1B_u^+$ and $S_2 \equiv 2\,^1A_g^-$. The calculated initial absorption spectra from S_1 and S_2, and the triplet ground state, T_1, is shown in Fig. 5.19. The three peaks arising from the S_1 state at 0.1 eV, 1.3 eV and 1.4 eV are attributed to transitions from the $1\,^1B_u^+$ state to the $2\,^1A_g^-$, $4\,^1A_g^-$ and $5\,^1A_g^-$ states, respectively.

For the parameter regime relevant to carotenoids, the $2\,^1A_g^-$ state is comprised of a singlet triplet-pair component and an odd-parity charge-transfer exciton component (see refs [2] and [223]). If the absorption signal from the $2\,^1A_g^-$ state arose from a transition from its bound triplet-pair component to $T_1T_1^*$, we would expect this to be higher in energy than the T_1 to T_1^* transition.[224] We note, however, that this absorption peak is significantly lower in energy compared to the lowest absorption

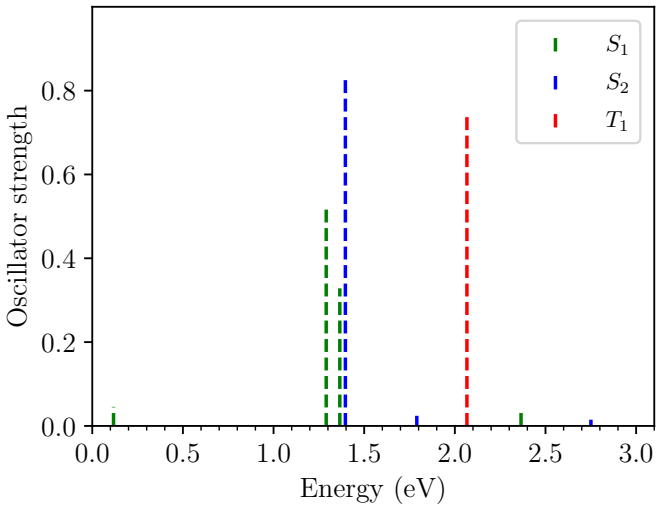

Figure 5.19: Calculated transient absorption spectra at $t = 0$ from the $S_1 \equiv 1\,^1B_u^+$, $S_2 \equiv 2\,^1A_g^-$ and T_1 states. Results are for a system with no broken-symmetry, i.e., $\hat{H}_\epsilon = 0$.

from the T_1 state. In contrast, if the absorption signal from the $2\,^1A_g^-$ state arose from a transition from its charge-transfer exciton component, the resulting $n\,^1B_u^+$ state would be an even-parity exciton. We verify this latter hypothesis by calculating the exciton wave function of the $n\,^1B_u^+$ state; this is shown in Fig. 5.20.

Fig. 4.13 (a) shows the exciton wavefunction of the $1\,^1B_u^+$ state. This has no nodes along the electron-hole coordinate. The exciton wavefunction of $2\,^1A_g^-$ state, dipole connected to the $1\,^1B_u^+$ state has one node along this coordinate (shown in Fig. 4.13 (c)). Fig. 5.20 is the exciton wavefunction of the $n\,^1B_u^+$ state, a high energy state dipole connected to the $2\,^1A_g^-$ state. It has two nodes along the electron-hole coordinate. Therefore we can conclude that the $2\,^1A_g^-$ to $n\,^1B_u^+$ transition does indeed arise from the charge-transfer exciton component of the $2\,^1A_g^-$ state to a Mott-Wannier exciton.

Next, we consider the realistic Hamiltonian with the inclusion of the symmetry breaking term, $\hat{H}_\epsilon$. For this set of parameters the $1\,^1B_u^+$ and $2\,^1A_g^-$ energies exhibit a crossover, while the S_1 and S_2 energies exhibit an avoided crossing (as shown in Fig. 5.15).

The calculated absorption spectra at the Franck-Condon point from the S_1 and

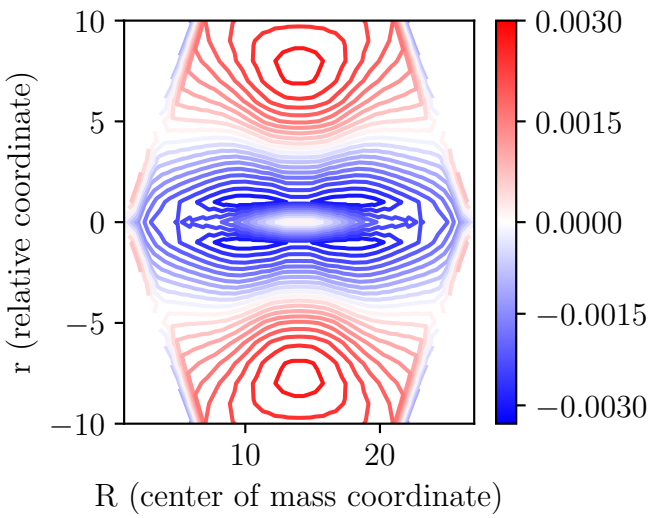

Figure 5.20: The $n\,^1B_u^+$ exciton wave function calculated using Eq. (4.35), using the PPP model with $N = 54$. This has two nodal surfaces along the relative (i.e., electron-hole) coordinate and is thus dipole-connected to the charge-transfer exciton component of the $2\,^1A_g^-$ state, which has one nodal surface along the relative coordinate. See Section 4.3 for the full parametrisation.

S_2 states, and the triplet ground state, T_1, is shown in Fig. 5.21(a). At $t = 0$ fs, S_1 predominantly occupies the $1\,^1B_u^+$ state, while S_2 predominantly occupies the $2\,^1A_g^-$ state. The absorption at ~ 0.3 eV corresponds to the S_1 to S_2 transition, while the absorption maxima observed around 1.4 eV is the transition from the $1\,^1B_u^+$ state to a high energy $^1A_g^-$ state.

Due to the inclusion of the symmetry breaking term, the adiabatic state T_1 will have some diabatic triplet excited state character, and therefore two absorption peaks are observed from T_1. As for Fig. 5.19, the transition from the charge-transfer exciton component of the $2\,^1A_g^-$ state to the $n\,^1B_u^+$ state at ~ 1.4 eV is lower in energy than the triplet absorption peaks.

As the evolving photoexcited system, $\Psi(t)$, reaches equilibrium it occupies both the S_1 and S_2 states. Fig. 5.21(b) shows the weighted absorption spectra at $t = 20$ fs of these states, as well as the absorption spectra of the T_1 state. After passing through the avoided crossing at ~ 3 fs the S_1 state now predominantly occupies the $2\,^1A_g^-$ state, while the S_2 state predominantly occupies the $1\,^1B_u^+$ state. This change

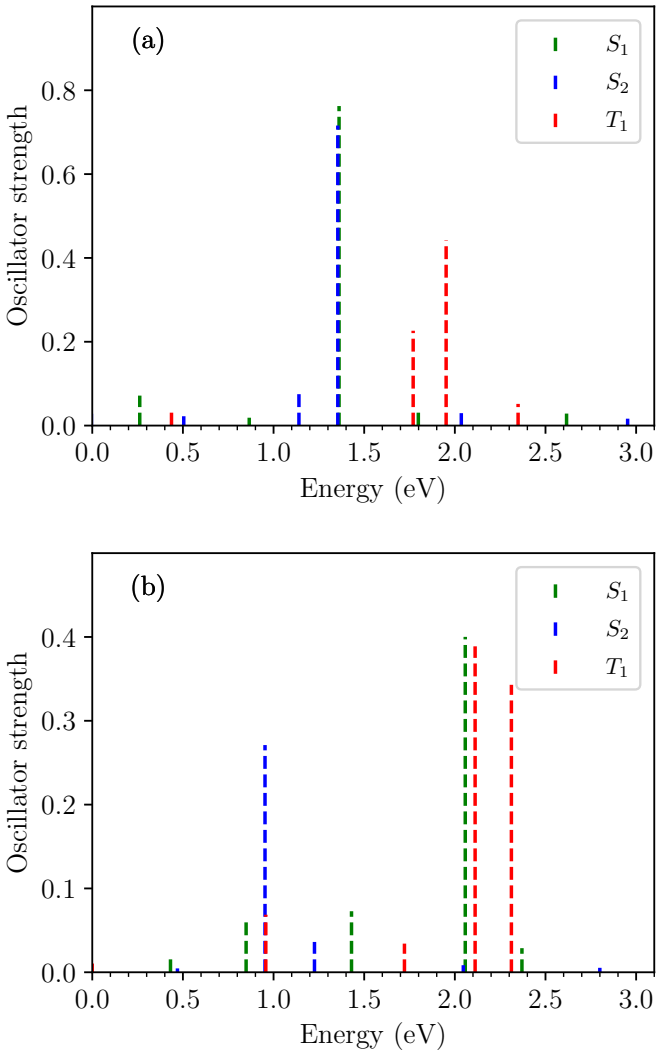

Figure 5.21: Calculated transient absorption spectra from the S_1, S_2 and T_1 states of neurosporene. (a) At $t = 0$, where $S_1 \approx 1\,^1B_u^+$ and $S_2 \approx 2\,^1A_g^-$. Note the overlapping S_1 and S_2 absorption at ~ 1.4 eV. (b) At $t = 20$ fs, where $S_1 \approx 2\,^1A_g^-$ and $S_2 \approx 1\,^1B_u^+$. Here, the singlet state absorption spectra are weighted by $P(\Psi(t); S_i)$.

of occupations is reflected in the calculated transient spectra, as the major signals originating from the S_1 state are now higher in energy compared to those originating from the S_2 state. At the relaxed geometry, the triplet peaks are blue shifted to 2.1 eV and 2.3 eV, which are close to the relaxed excited state values previously calculated for polyenes.[2]

As the S_1 state at 20 fs now predominantly occupies the $2\,^1A_g^-$ state, we attribute the absorption peak of the S_1 state at $\sim$ 2.1 eV to a transition from the charge-transfer exciton component of the $2\,^1A_g^-$ state. This energy is blue-shifted from the corresponding transition from the $2\,^1A_g^-$ component of the S_2 state at $t = 0$, because of the large reorganisation energy of the $2\,^1A_g^-$ state. This energy is close to the experimentally observed $2\,^1A_g^-$ to $n\,^1B_u^+$ transition of carotenoids.[55,220,224] We also note that the energy of the major absorption from S_2 around 0.9 eV agrees with the experimentally observed $1\,^1B_u^+$ to $m\,^1A_g^-$ transition.[225]

5.5 Conclusions

In this chapter we described our simulations of the excited state dynamics of the carotenoids zeaxanthin and neurosporene following its photoexcitation into the 'bright' (nominally $1\,^1B_u^+$) state. We employed the adaptive tDMRG method on the UV model of π-conjugated electrons and used the Ehrenfest equations of motion to simulate the coupled nuclei dynamics. To account for the experimental and theoretical uncertainty in the relative energetic ordering of the nominal $1\,^1B_u^+$ and $2\,^1A_g^-$ states at the Franck−Condon point, we considered two sets of parameters, which can give rise to two internal conversion pathways. We found that for both internal conversion pathways ultrafast (within $\sim$ 5 fs) internal conversion of the photoexcited $1\,^1B_u^+$ state to a 'dark' triplet-pair state, i.e., to one member of the '$2A_g$' family of states. The ultrafast internal conversion from the $1\,^1B_u^+$ state to the triplet-pair state is as-

sociated with an avoided crossing of the corresponding adiabatic states. In the case where the internal conversion occurs via the $1\,^1B_u^-$ state, we find subsequent slower (within $\sim$ 50 fs) internal conversion from the high energy triplet-pair state $1\,^1B_u^-$ to the lowest triplet-pair state $2\,^1A_g^-$. In the case of zeaxanthin where $B_u \rightarrow A_g$ is symmetry forbidden, the system remains in the $1\,^1B_u^-$ state. For both internal conversion pathways and both molecules under consideration, we find that within 50 fs the photoexcited state is converted to a triplet-pair state with a yield $\sim 65\%$.

We make a direct connection from our predictions to experimental observables by calculating transient excited state absorption spectra. For the case of direct $1\,^1B_u^+$ to $2\,^1A_g^-$internal conversion, we showed that at the Franck-Condon point there will be a photoexcited absorption at ca. 1.4 eV resulting from the $1\,^1B_u^+$ to $n\,^1A_g^-$ transition (and a weak transition at ca. 0.3 eV resulting from the $1\,^1B_u^+$ to $2\,^1A_g^-$ transition). Within 20 fs, however, the adiabatic evolution of S_1 from $1\,^1B_u^+$ to $2\,^1A_g^-$ character results in a new dominant excited-state transition at ca. 2 eV, being close to but lower in energy than the T to T^* transition. This can be attributed to the $2\,^1A_g^-$component of S_1 state. Moreover, we show that it is the charge-transfer exciton component of the $2\,^1A_g^-$ state that is responsible for this transition (to a higher-lying exciton state), and not its triplet-pair component. This transition is blue-shifted from the Franck−Condon point, because of the large reorganisation energy of the $2\,^1A_g^-$ state.

Appendices

5.A Symmetry Breaking Hamiltonians

5.A.1 Zeaxanthin

The parametrisation of the symmetry breaking Hamiltonian, $\hat{H}_\epsilon$, used for the simulations of zeaxanthin (Fig. 5.A.1) described in this chapter is given in Table 5.A.1.

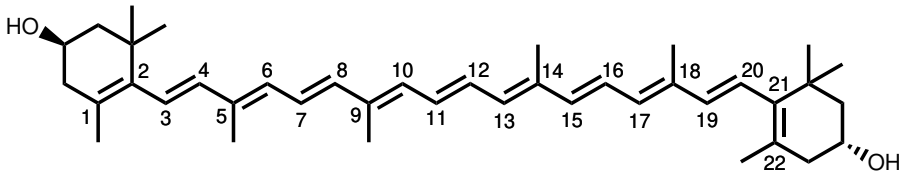

Figure 5.A.1: Structural formula of zeaxanthin. The end groups formed of six-membered carbon rings are twisted by 75° out of the plan of the molecule. Zeaxanthin possesses C_2 symmetry due to its twisted end groups, but its π-electron system can be modelled under $C_{2\mathrm{h}}$ symmetry.

Carbon site, n	Mulliken charges (q)	ϵ_n (eV)
1	0.34	-3.6
2	-0.06	-1.0
3	0.04	0.0
4	-0.03	0.0
5	0.22	-1.6
6	-0.02	-0.6
7	0.05	0.0
8	-0.02	0.0
9	0.22	-1.6
10	-0.02	-0.6
11	-0.03	0.0

Table 5.A.1: The π-electron Mulliken charges from the *ab initio* DFT calculation and the parameters for the symmetry-breaking term, $\hat{H}_\epsilon$. In order to maintain π-electron charge neutrality, each *ab initio* charge was increased by $0.07q$. $\epsilon_n = +\epsilon_{N+1-n}$. The structural formula of zeaxanthin is shown in Fig. 5.A.1.

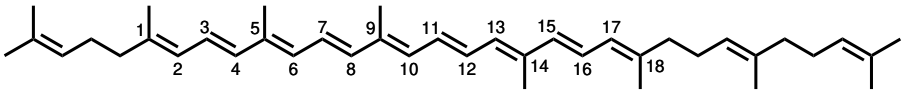

Figure 5.A.2: Structural formula of neurosporene.

		$V = 2.75$ eV		$V = 3.25$ eV	
Carbon site, n	Mulliken charges (q)	ϵ_n (eV)	$\left\langle \hat{N}_n - 1 \right\rangle$	ϵ_n (eV)	$\left\langle \hat{N}_n - 1 \right\rangle$
1	0.14	-1.00	0.17	-1.00	0.17
2	-0.18	0.81	-0.14	0.56	-0.14
3	-0.05	1.00	0.05	1.00	0.06
4	-0.18	1.00	-0.10	0.82	-0.10
5	0.15	-1.00	0.15	-1.00	0.15
6	-0.14	0.27	-0.10	0.02	-0.10
7	-0.07	1.00	0.03	1.00	0.03
8	-0.16	1.00	-0.09	0.84	-0.09
9	0.13	-1.00	0.12	-1.00	0.12
10	-0.09	0.14	-0.07	-0.01	-0.07
11	-0.11	1.00	-0.03	1.00	-0.04
12	-0.10	1.00	-0.02	1.00	-0.03
13	-0.11	0.32	-0.09	0.09	-0.09
14	0.14	-1.00	0.13	-1.00	0.13
15	-0.18	1.00	-0.09	0.92	-0.10
16	-0.05	1.00	0.05	1.00	0.06
17	-0.19	0.90	-0.14	0.61	-0.14
18	0.14	-1.00	0.18	-1.00	0.17

Table 5.A.2: The π-electron Mulliken charges from the *ab initio* DFT calculation, parameters for the symmetry-breaking term, $\hat{H}_\epsilon$, and the expectation values of number densities calculated from the parametrised $\hat{H}_\epsilon$. In order to maintain π-electron charge neutrality, each *ab initio* charge was increased by $0.05q$. The structural formula of neurosporene is shown in Fig. 5.10.

5.A.2 Neurosporene

The symmetry breaking Hamiltonians for neurosporene (Fig. 5.A.2) are found via the numerical minimisation scheme outlined in Section 3.3. We perform the minimisation for $\epsilon_{\max} = 1.0$ eV. This upper bound is imposed to prevent the formation of an unphysical potential energy gradients across the conjugated carbon atoms which causes an unphysical mixing of the ionic and covalent states. (However, the effect of an arbitrary symmetry-breaking potential is described in Section 6.3.) The optimised $\hat{H}_\epsilon$ found for neurosporene with $V = 3.25$ eV and $r^2(\boldsymbol{\epsilon}) = 0.92$ is shown in Table 5.A.2.

5.B Accuracy and Convergence Analysis

The adaptive tDMRG algorithm utilised in the calculations presented in this chapter suffers from two sources of error. First, the accuracy of the DMRG algorithm is dictated by the truncation error, defined by eq (3.41). This error is minimised by retaining more states during the truncation. Second, the Suzuki-Trotter decomposition introduces the Trotter error which is reduced by reducing the Trotter time step, δt. Minimising the Trotter time step also minimises the error associated with the use of Velocity Verlet integrator for the nuclear dynamics.

5.B.1 Truncation Error and Entanglement Entropy

Due to the variational nature of the DMRG algorithm, its accuracy can be systematically improved by increasing the number of states retained during the DMRG truncation step. Convergence of the closely related PPPP model has been extensively studied.[103,105,106,150]

The convergence of the DMRG truncation error can be determined by evaluating the convergence of an observable as a function of the truncation error. As an illustrative example, Fig. 5.B.1 shows the variation of energy of the evolving wavefunction $\Psi(t)$ with the DMRG truncation error for neurosporene ($N = 18$), with $V = 3.25$ eV. The energy is converged for a truncation error of $\sim 10^{-8}$ to an accuracy of 0.1 eV.

In general, the number of states required to be retained in a DMRG scheme is given by[147]

$$m \approx \exp(S), \tag{5.6}$$

where S is the von Neumann entanglement entropy (defined in eq (3.42)). For our simulations, the maximum von Neumann entanglement entropy reached, $S_{\max} < 4.0$, and thus from eq (5.6) the number of states required to retain $m \approx 55$. The truncation cutoff of $\sim 10^{-8}$ is reached by typically retaining ~ 400 augmented block states during the DMRG truncation, which is much larger than the number

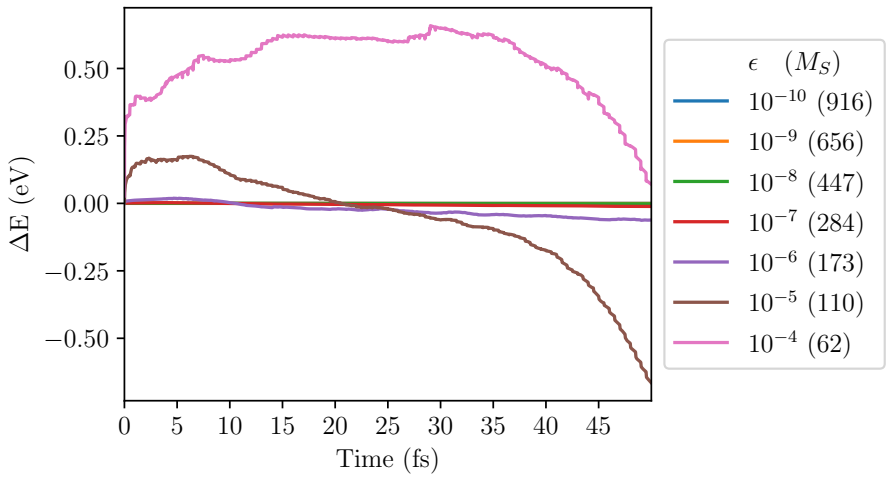

Figure 5.B.1: The calculated difference of the energy as a function of time of the system described by the evolving state vector $\Psi(t)$ for different DMRG truncation errors, ϵ, with respect to the energy calculated with a DMRG truncation error of 10^{-11}. The maximum number of augmented block states, M_S, retained to reach the specified DMRG accuracy is indicated within parenthesis. The evolving state energy is converged for a DMRG truncation error $\epsilon = 10^{-8}$.

of states required by eq (5.6).

5.B.2 Trotter Error

For an accurate representation of nuclear dynamics, the Velocity Verlet time step Δt (see Section 3.2.1) should be smaller than the timescale of nuclear motion, set by carbon-carbon bond oscillations. Typical carbon-carbon bond oscillation frequencies are $\sim$ 20 fs, and thus we require $\Delta t < 20 \times 10^{-3}$ fs. Fig. 5.B.2 illustrates the calculated expectation value of energy of the evolving wavefunction $\Psi(t)$ as a function of the Trotter time-step δt, for neurosporene ($N = 18$), with $V = 3.25$ eV. We notice that the energy is well converged for $\delta t = 10^{-3}$ fs, and we use this value as the Trotter time step. We perform 10 tDMRG steps per each nuclear position update, therefore $\Delta t = 10^{-2}$ fs.

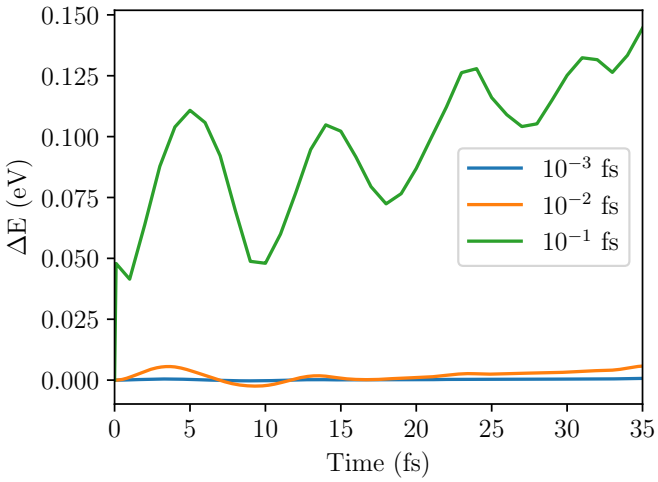

Figure 5.B.2: The calculated difference of the energy as a function of time of the system described by the evolving state vector $\Psi(t)$ for different Trotter time steps, δt, with respect to the energy calculated with a Trotter time step of 10^{-4} fs. Convergence is reached with a Trotter time step of 10^{-3} fs.

5.C Comparison with Static DMRG Calculations Based on the Hellmann-Feynman Theorem

Convergence of our programme is also evaluated by comparing our dynamical results to static DMRG results obtained via the Hellmann-Feynman theorem. In the absence of the symmetry breaking term, a system prepared in $\Psi(t=0) = 1^1B_u^+$ at the Franck-Condon point will evolve under linear damping on the $1\,^1B_u^+$ potential energy surface, reaching its equilibrium geometry in the long time limit. As the force on atom n, $f_n = 0$ once equilibrium is reached, the relaxed $1\,^1B_u^+$ state can also be found via static DMRG by setting $f_n = 0$ in eq (3.56) and solving the resultant equation iteratively. By comparing observables, we find that the results of our dynamic simulations converge to the same results we obtain via the self iterative Hellmann-Feynman procedure. We illustrate this convergence for the two observables of energy and staggered bond dimerizations. Fig. 5.C.1 shows the staggered bond dimerizations, defined for the nth bond by $\delta_n = (-1)^n(\delta u_n - \bar{\delta u_n})/\bar{\delta u_n}$ (where $\delta u_n = u_{n+1} - u_n$ and $\bar{\delta u_n}$ is the average of δu_n over all bonds), are converged. The

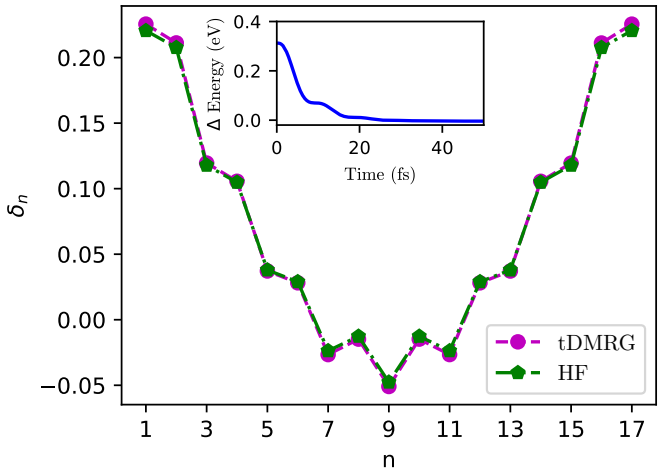

Figure 5.C.1: Staggered bond dimerizations of the relaxed $1\,^1B_u^+$ state calculated via tDMRG (magenta) and Hellmann-Feynman procedure (green). The inset shows the difference between the energy of the $1\,^1B_u^+$ state calculated via the adaptive tDMRG and the energy of the $1\,^1B_u^+$ state at the relaxed geometry calculated via the Hellmann-Feynman procedure, showing that the two energies converge to the same value.

inset shows that the energy of the $1\,^1B_u^+$ state as it evolves reaches the relaxed energy calculated via the Hellmann-Feynman procedure.

5.D Accuracy of Lanczos-DMRG Calculations

The $1\,^1B_u^+$ state is connected to the excited states in the A_g^- sector by the dipole moment operator. Therefore, the accuracy of the Lanczos-DMRG can be evaluated by comparing the calculated transient spectra to the energies and transition dipole moments of the excited states in the A_g^- sector, calculated using static DMRG in the absence of symmetry breaking and at the vertical geometry. The results are shown in Fig. 5.D.1, and demonstrate a good agreement between the two methods.

Although targeting several Lanczos states during the static DMRG sweep of the Lanczos-DMRG procedure increases the accuracy of the calculation, it leads to a large computational expense. In our simulations, we target five Lanczos vectors, which maintains the DMRG truncation error at around $\epsilon \sim 10^{-8}$ while keeping $M_S \sim 1000$ augmented block states.

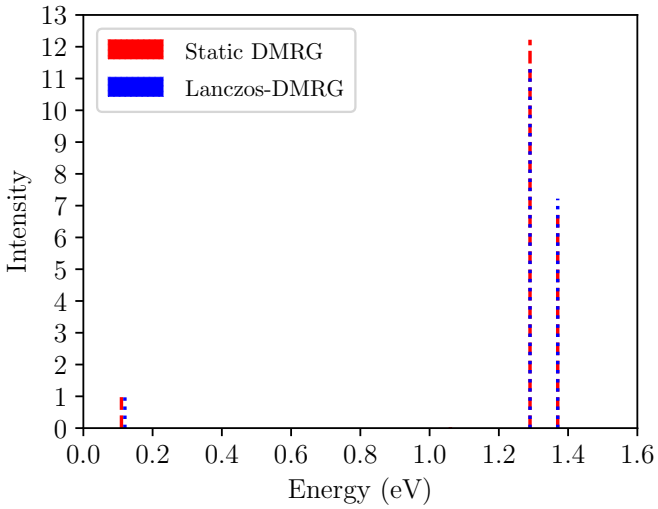

Figure 5.D.1: The transient absorption spectra calculated from the $1\,^1B_u^+$ state using static DMRG (red) and Lanczos-DMRG (blue). The three signals correspond to transitions to the $2\,^1A_g^-$, $4\,^1A_g^-$, and $5\,^1A_g^-$ states in order of increasing energy. The intensity (I) is normalized with respect to the $2\,^1A_g^-$ signal, i.e., $I(n\,^1A_g^-) = \left|\left\langle n\,^1A_g^-\middle|\hat{\mu}\middle|1\,^1B_u^+\right\rangle\right|^2 / \left|\left\langle 2\,^1A_g^-\middle|\hat{\mu}\middle|1\,^1B_u^+\right\rangle\right|^2$.

Chapter 6

Approximate Two Level Dynamics

The internal conversion processes between two diabatic states can be modelled as a simple two-level quantum system. In this chapter, we develop this framework using direct $1\,^1B_u^+ \rightarrow 2\,^1A_g^-$ internal conversion as an illustrative example. Landau-Zener theory provides a theoretical description of electronic transitions of a two-level system at an avoided crossing. We introduce the Landau-Zener theory and use it to describe the electronic transitions of carotenoid photoexcited states described in Chapter 5.

6.1 Two-Level Quantum System

To illustrate that the internal conversion processes described in Chapter 5 may be described as transitions between a two-level quantum system, we revisit the adiabatic internal conversion from the $1\,^1B_u^+$ state to the $2\,^1A_g^-$ state of neurosporene described in Section 5.3. The probabilities that the evolving state state $\Psi(t)$ is occupied by the adiabatic states S_1 and S_2, and diabatic states $1\,^1B_u^+$ and $2\,^1A_g^-$, is illustrated in Fig. 5.16. We include a reproduction of Fig. 5.16 here (Fig. 6.1) for convenience as it relates to the discussion in this chapter.

As evident from Fig. 6.1, the optically prepared state $\Psi(t)$ is almost entirely composed of two adiabatic states, S_1 and S_2, during the entirety of the time evolu-

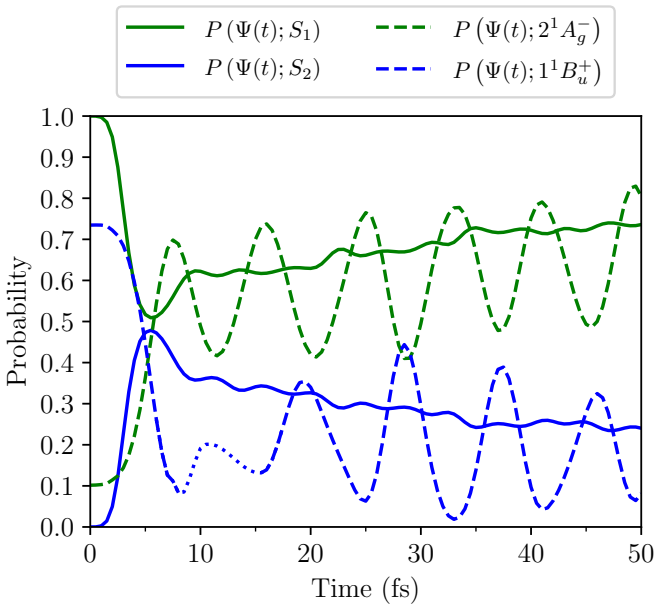

Figure 6.1: Probabilities as a function of time that the system described by $\Psi(t)$ occupies the adiabatic states, S_1 and S_2, and the diabatic states, $2\,^1A_g^-$ and $1\,^1B_u^+$. These results are for neurosporene for the direct $1\,^1B_u^+ \rightarrow 2\,^1A_g^-$ internal conversion pathway. $\Psi(t=0) = S_1$. The figure is a reproduction of Fig. 5.16.

tion. Thus, to a good approximation, we can adopt a two-level system and express $\Psi(t)$ as the non-stationary state,

$$|\Psi(t)\rangle \approx \psi_1 |S_1\rangle \exp(-\mathrm{i}E_1 t/\hbar) + \psi_2 |S_2\rangle \exp(-\mathrm{i}E_2 t/\hbar), \tag{6.1}$$

where S_1 and S_2 are the two contributing adiabatic states, and the probability amplitudes ψ_1 and ψ_2 are assumed to be constant.

We can express the adiabatic states in the diabatic basis $\{|1\,^1B_u^+\rangle, |2\,^1A_g^-\rangle\}$ as,

$$|S_1\rangle \approx a(t) \left|1\,^1B_u^+\right\rangle + b(t) \left|2\,^1A_g^-\right\rangle, \tag{6.2}$$

and

$$|S_2\rangle \approx c(t) \left|1\,^1B_u^+\right\rangle + d(t) \left|2\,^1A_g^-\right\rangle. \tag{6.3}$$

In an exact two-level system, $|a|^2 = |d|^2$ and $|c|^2 = |b|^2$. Thus, the probability that

the system occupies the diabatic state $2\,^1A_g^-$, $P(\Psi(t); 2\,^1A_g^-) = \left| \langle 2\,^1A_g^- | \Psi(t) \rangle \right|^2$, is

$$P(\Psi(t); 2\,^1A_g^-) = |\psi_1 b|^2 + |\psi_2 d|^2 + (\psi_1 b)^*(\psi_2 d)\cos(E_1 - E_2)t/\hbar. \tag{6.4}$$

Eqn. (6.4) describes the observed oscillatory behaviour of the diabatic probabilities of the two-level system (as shown in Fig. 6.1). Once the transition is complete ($t > 25$ fs), the adiabatic energy gap $E_2 - E_1$ of Fig. 5.15 is ~ 0.5 eV, corresponding to a period of oscillation $T = h/(E_2 - E_1) \sim 8$ fs. This matches the period of oscillations in Fig. 6.1, which indicates that the two-state assumption is largely valid.

These oscillations are the results of the quantum coherences, and in realistic systems they decay rapidly via interactions with the environment. To calculate the $2\,^1A_g^-$ triplet-pair yields, we can omit the oscillatory term and calculate the 'classical' probability of the $2\,^1A_g^-$ state as

$$P_{\text{classical}}(2\,^1A_g^-) = |\psi_1 b|^2 + |\psi_2 d|^2. \tag{6.5}$$

i.e.,

$$P_{\text{classical}}(\Psi; 2\,^1A_g^-) = P(\Psi; S_1) \times P(S_1; 2\,^1A_g^-) + P(\Psi; S_2) \times P(S_2; 2\,^1A_g^-). \tag{6.6}$$

6.2 Landau-Zener Theory of Electronic Transitions

In this section we describe the Landau-Zener theory of electronic transitions, a theory describing the electronic transitions in a system comprised of two potential energy surfaces that exhibit an avoided crossing.[226,227]

Consider a two-level system described by the adiabatic (Born-Oppenheimer) Hamiltonian $\hat{H}\left|\psi_i\right\rangle = E_i\left|\psi_i\right\rangle, i \in \{1,2\}$ (the nuclear coordinates are omitted for brevity). At an avoided crossing, the non-adiabatic coupling terms (defined by Eqs. (2.11) and (2.12)) are non-negligible and it is convenient to partition the full adiabatic Hamiltonian to a diabatic Hamiltonian $\hat{H}_D$ and a coupling term $\hat{V}$ as

$$\hat{H} = \hat{H}_D + \hat{V}, \tag{6.7}$$

with eigenfunctions of $\hat{H}_D$ given by $\hat{H}_D\left|\phi_j\right\rangle = E_j\left|\phi_j\right\rangle, j \in \{A,B\}$. As described below, $\hat{H}_D$ is constructed such that its eigenfunctions exhibit an actual crossing at the nuclear coordinate $Q = Q_C$, where the adiabatic eigenstates exhibit an avoided crossing. $\hat{V}$ captures the coupling of the diabatic surfaces at the avoided crossing and in the diabatic basis $\{\phi_A, \phi_B\}$, it is represented by the matrix

$$\boldsymbol{V} = \begin{pmatrix} 0 & -V \\ -V & 0 \end{pmatrix}, \tag{6.8}$$

where $V = -\left\langle\phi_A|\hat{V}|\phi_B\right\rangle > 0$. Around the avoided crossing, the diabatic energies E_A and E_B change linearly with the nuclear coordinate Q. Setting $E_A(Q_C) = E_B(Q_C) = 0$, around $Q = Q_C$ we can write $E_A(Q) = -E_B(Q) = \Delta(Q)$. Therefore, in the diabatic basis, $\hat{H}$ can be written in the matrix form as

$$\boldsymbol{H} = \begin{pmatrix} \Delta & -V \\ -V & -\Delta \end{pmatrix}. \tag{6.9}$$

Diagonalising $\boldsymbol{H}$, we obtain the adiabatic eigenvalues as

$$E_{1/2} = \mp\left(\Delta^2 + V^2\right)^{1/2}, \tag{6.10}$$

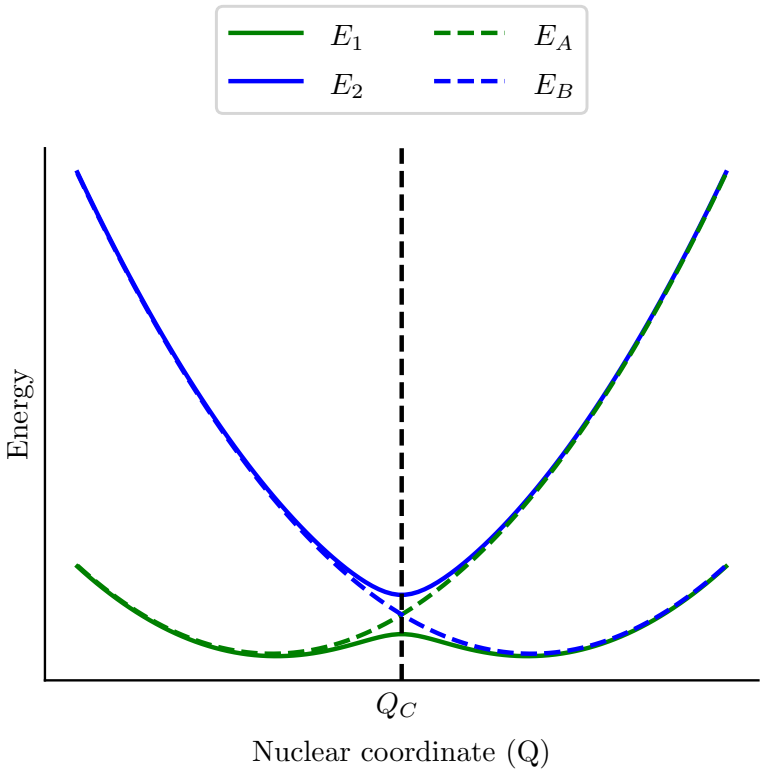

Figure 6.2: A schematic diagram showing the potential adiabatic energy surfaces, E_1 and E_2, and diabatic potential energy surfaces, E_A and E_B, in a two-level system exhibiting an avoided crossing at the nuclear coordinate ($Q = Q_C$).

and the adiabatic eigenfunctions,

$$|\psi_1\rangle = c_A\,|\phi_A\rangle + c_B\,|\phi_B\rangle\,, \tag{6.11}$$

$$|\psi_2\rangle = c_B\,|\phi_A\rangle - c_A\,|\phi_B\rangle\,, \tag{6.12}$$

where

$$c_A = \left(\frac{E-\Delta}{2E}\right)^{1/2}, \tag{6.13}$$

$$c_B = \left(\frac{E+\Delta}{2E}\right)^{1/2}. \tag{6.14}$$

It follows that when $Q \ll Q_C$ and $Q \gg Q_C$, the adiabatic and diabatic surfaces coincide while at $Q = Q_C$, the diabatic surfaces smoothly interpolates between the adiabatic surfaces, as shown in Fig. 6.2.

To derive the Landau-Zener theory of electron transfer, we now consider $Q = Q(t)$ to be a dynamical variable varying linearly in time,

$$\Delta(Q) = \frac{F}{2}(Q - Q_C) = \alpha t, \tag{6.15}$$

where F can be thought of as a 'force' between the potential energy surfaces. Then,

$$\nu = \frac{dQ}{dt} = \frac{2}{F}\frac{d\Delta(Q)}{dt} = \frac{2\alpha}{F} \tag{6.16}$$

is the speed at which the surfaces approach each other. The adiabatic Hamiltonian is now time-dependent,

$$\boldsymbol{H}(t) = \begin{pmatrix} \alpha t & -V \\ -V & -\alpha t \end{pmatrix}, \tag{6.17}$$

and satisfies the time-dependent Schrödinger equation,

$$i\hbar\frac{d}{dt}\left|\psi\right\rangle = \hat{H}(t)\left|\psi\right\rangle, \tag{6.18}$$

with the initial condition that as $t \to -\infty$, the system is in the diabatic state $|\phi_A\rangle$,

$$\left|\psi(t \to -\infty)\right\rangle = \left|\phi_A\right\rangle. \tag{6.19}$$

$|\psi\rangle$ can be written in the diabatic basis as

$$\left|\psi\right\rangle = c_A(t)\left|\phi_A\right\rangle + c_B(t)\left|\phi_B\right\rangle, \tag{6.20}$$

where the coefficients $c_A(t)$ and $c_B(t)$ are now time-dependent. Given the definition of the initial condition, $|c_B(t)|^2 = P_{A\to B}$ is the probability of a transition from diabatic state $|\phi_A\rangle$ to $|\phi_B\rangle$ in time t. Substituting Eq. (6.20) into Eq. (6.18) and

using the matrix expansion in the diabatic basis, we arrive at the coupled differential equations,

$$i\hbar\dot{c}_A = \alpha t c_A - V c_B, \tag{6.21}$$

$$i\hbar\dot{c}_B = -V c_A - \alpha t c_B, \tag{6.22}$$

from which we can derive the equation of motion for $c_A(t)$,

$$\ddot{c}_A = \left[-\frac{i\alpha}{\hbar} - \frac{1}{\hbar^2}\left(V^2 + \alpha^2 t^2\right)\right] c_A. \tag{6.23}$$

Eq. (6.23) is known as the Weber equation whose solutions are cylindrical functions.[226] We are interested at the asymptotic limit $t \to \infty$, at which

$$P_A = |c_A|^2 = \exp\Big(-\pi V^2/\alpha\hbar\Big), \tag{6.24}$$

$$P_B = 1 - |c_A|^2 = 1 - \exp\Big(-\pi V^2/\alpha\hbar\Big). \tag{6.25}$$

Surfaces approaching each other slowly are characterised by a small α value (Eq. (6.16)). As α decreases, the probability that the system stays at the diabatic state $|\phi_A\rangle$, P_A, decreases. We define the adiabatic limit as the limit at which $\alpha \to 0$. Then $P_A \to 0$ and $P_B \to 1$. This process follows the adiabatic theorem, which states that a system initially in the nth (adiabatic) eigenstate of an initial Hamiltonian $\hat{H}_i$ will remain in the nth eigenstate of the final Hamiltonian $\hat{H}_f$ if the transition from $\hat{H}_i$ to $\hat{H}_f$ is gradual.

In contrast, at large α we reach the non-adiabatic limit, characterised by $V/\alpha \ll 1$. Then $P_A \sim 1 - \pi V^2/\alpha\hbar \sim 1$ and $P_B \sim \pi V^2/\alpha\hbar \ll 1$. In this limit, the system jumps from the adiabatic state $|\psi_1\rangle$ to the adiabatic state $|\psi_2\rangle$ while remaining on the diabatic state $|\phi_A\rangle$. The variation of P_A and P_B as a function of $V^2/\alpha\hbar$ is shown

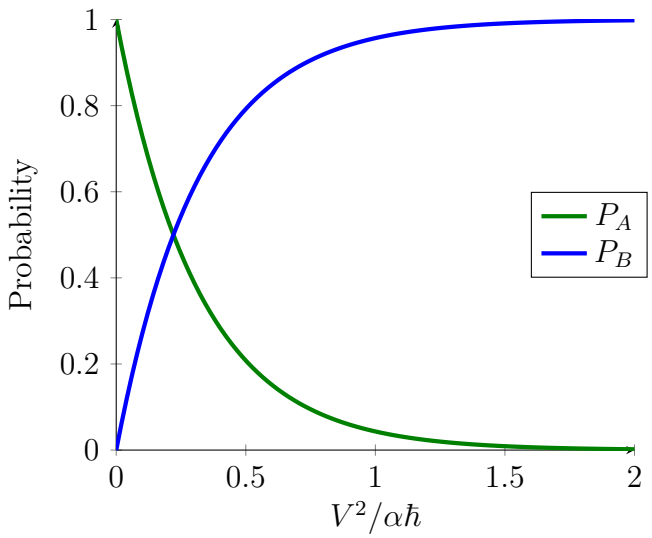

Figure 6.3: Diagram illustrating the probability that a system prepared in $|\phi_A\rangle$ at $t \to -\infty$ occupies the diabatic states $|\phi_A\rangle$ and $|\phi_B\rangle$ as $t \to \infty$. The transition from a slow adiabatic process as $\alpha \to 0$ to a fast non-adiabatic process as $\alpha \gg V$ corresponds to a Landau-Zener transition.

in Fig. 6.3.

In the next section, we look at the internal conversion process of carotenoids as a dynamical process within an approximate two-level system, and describe the effect of the change of the symmetry breaking term introduced in Eq. (2.67) on the dynamics as a Landau-Zener type transition. For a recent review on Landau-Zener transitions, see ref [228].

6.3 Landau-Zener-Like Transition

In Section 6.1, we developed a two-state model and used it to explain the observed oscillatory behaviour of the diabatic state probabilities following the internal conversion. In this section, we use this model to investigate the dynamics at the quantum transition itself, and describe the effect of the particle-hole symmetry breaking term $\hat{H}_\epsilon$ on this transition using the Landau-Zener theory introduced in Section 6.2.

The full adiabatic Hamiltonian given by Eq. (2.69),

$$\hat{H} = \hat{H}_{\mathrm{UVP}} + \hat{H}_\lambda + \hat{H}_\epsilon, \tag{6.26}$$

can be partitioned as

$$\hat{H} = \hat{H}_D + \hat{V}, \tag{6.27}$$

where $\hat{H}_D = \hat{H}_{\mathrm{UVP}} + \hat{H}_\lambda$ is the two-level diabatic Hamiltonian with the two eigenstates $1\,^1B_u^+$ and $2\,^1A_g^-$, and $\hat{V} = \hat{H}_\epsilon$ couples the diabatic states (cf. Eq. (6.7)). The diabatic coupling term V of the two-level system is given by $V = -\left\langle 1\,^1B_u^+ \middle| \hat{H}_\epsilon \middle| 2\,^1A_g^- \right\rangle$.

In the limit of a vanishing electron-hole symmetry breaking term, defined by $\hat{H}_\epsilon \to 0$, the coupling term $V \to 0$. From Eqs. (6.24) and (6.24), it follows that at this limit $P_A = P(\Psi; 1\,^1B_u^+) \to 1$ and $P_B = P(\Psi; 2\,^1A_g^-) \to 0$. This is the non-adiabatic limit of Landau-Zener theory. At this limit, a system prepared in the $1\,^1B_u^+$ state will remain on the same diabatic surface throughout the dynamical evolution. Further, at this limit the diabatic and adiabatic states are equivalent. Since the diabatic surfaces cross during the dynamical process, this implies that $\Psi(t)$ will undergo a non-adiabatic transition from S_1 to S_2 while remaining in the $1\,^1B_u^+$ diabatic state such that at the crossing the adiabatic states swap their ordering.

As evident from dynamical simulations of Chapter 5, the inclusion of a non-zero $\hat{H}_\epsilon$ term causes an avoided crossing of the adiabatic states and an adiabatic transition where the evolving system $\Psi(t)$ predominately occupies a single adiabatic surface. We study this Landau-Zener-like transition from a 'fast' non-adiabatic process to a 'slow' adiabatic process in more detail by linearly scaling the potential energies in the symmetry breaking Hamiltonian (presented in Table 5.A.2 with $V = 3.25$ eV) by a scaling factor ζ. Fig. 6.4 illustrates the calculated probabilities of the contributing adiabatic and diabatic states for a linear scaling factor of $\zeta = 0.2$. The system undergoes a non-adiabatic transition from S_1 to S_2 adiabatic states, while remaining on the $1\,^1B_u^+$ diabatic state.

Conversely, for a large symmetry-breaking term, Landau-Zener thery predicts an adiabatic transition with $P_A = P(\Psi; 1\,^1B_u^+) \to 0$ and $P_B = P(\Psi; 2\,^1A_g^-) \to 1$. At this

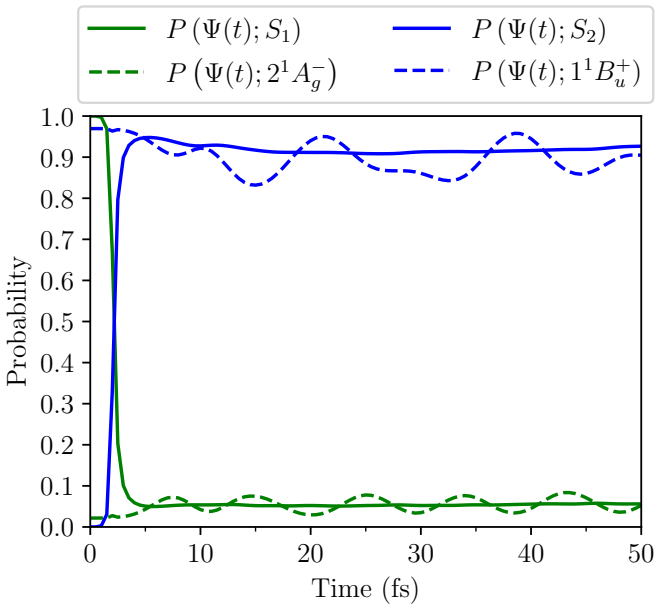

Figure 6.4: The probabilities as a function of time that the system described by $\Psi(t)$ occupies the adiabatic states, S_1 and S_2 (calculated using eq (2.72)), and the diabatic states, $2\,^1A_g^-$ and $1\,^1B_u^+$ (calculated using eq (2.73)). The initial condition is that $\Psi(0) = S_1$. Results are for $N = 18$ and $V = 3.25$ eV, and for the symmetry breaking Hamiltonian presented in Table 5.A.2 with $V = 3.25$ eV scaled by a linear scaling factor of $\zeta = 0.2$.

limit, the evolving system will remain in the S_1 adiabatic state while undergoing an adiabatic transition from the $1\,^1B_u^+$ state to the $2\,^1A_g^-$ state. The results presented for realistic symmetry-breaking Hamiltonians in Chapter 5 are close to this regime. Fig. 6.5 further illustrates this limit using a linear scaling parameter of $\zeta = 1.2$. For large symmetry-breaking Hamiltonian, there is an adiabatic transition: $\Psi(t)$ predominately occupies S_1, while there is a transition from the $1\,^1B_u^+$ to the $2\,^1A_g^-$ diabatic states. Comparing Fig. 6.1 and Fig. 6.5, we note that as ζ increases, the probability that the evolving system occupies S_1 around the avoided crossing increases. The adiabaticity of the transition increases as ζ increases.

To further illustrate that this transition can be described by Landau-Zener theory, we calculate the probabilities that the system described by $\Psi(t)$ occupies the adiabatic excited states S_1 and S_2 at $t = 50$ fs as a function of ζ, given the initial condition that $\Psi(t = 0) = S_1$. This is illustrated in Fig. 6.6. The probabilities $P(\Psi; S_1)$ and $P(\Psi; S_2)$ as a function of ζ illustrate the crossover from the non-adiabatic to

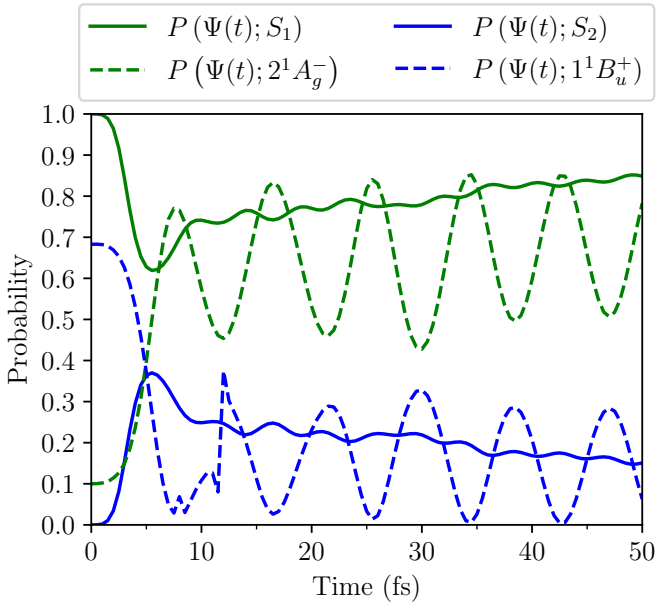

Figure 6.5: The probabilities as a function of time that the system described by $\Psi(t)$ occupies the adiabatic states, S_1 and S_2 (calculated using eq (2.72)), and the diabatic states, $2\,^1A_g^-$ and $1\,^1B_u^+$ (calculated using eq (2.73)). The initial condition is that $\Psi(0) = S_1$. Results are for $N = 18$ and $V = 3.25$ eV, and for the symmetry breaking Hamiltonian presented in Table 5.A.2 with $V = 3.25$ eV scaled by a linear scaling factor of $\zeta = 1.2$.

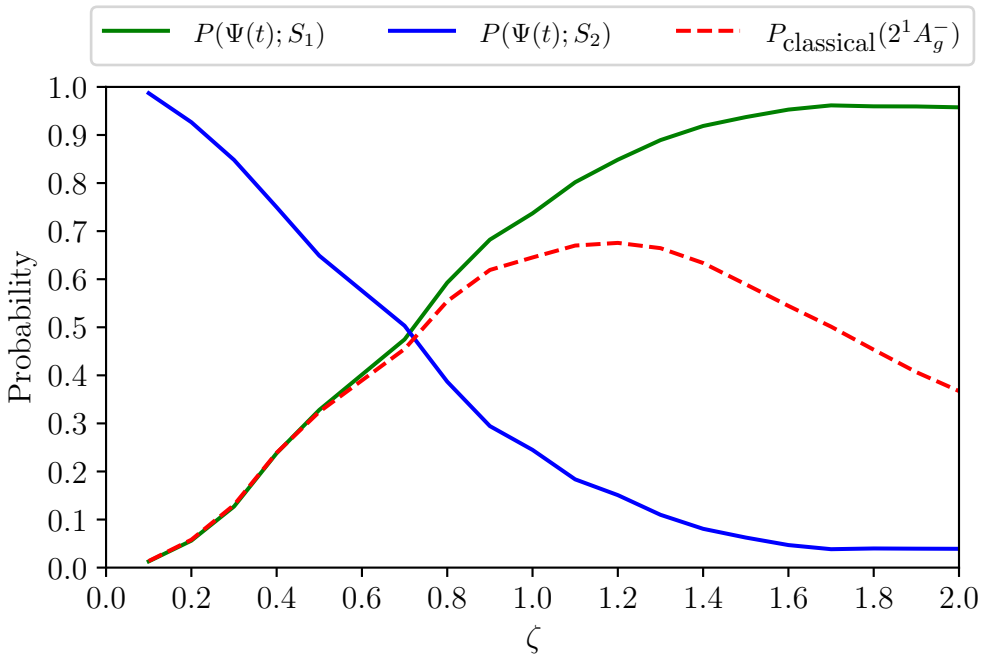

Figure 6.6: The probabilities at $t = 50$ fs as a function of increasing the strength of the particle-hole symmetry term (ζ) that the system described by $\Psi(t)$ occupies the adiabatic states, S_1 and S_2. Also shown is the classical $2\,^1A_g^-$ yield. The initial condition is that $\Psi(0) = S_1$. Results are for $N = 18$ and $V = 3.25$ eV.

adiabatic limits described above.

Due to the nonstationary state oscillations, we use the 'classical' probability of the $2\,^1A_g^-$ state defined by eq (6.6) as a proxy for the probability that the the evolving system occupies the diabatic state $2\,^1A_g^-$ as $t \to 0$. This probability gradually rises with ζ until $\zeta \sim 1.0$, and closely matches the behaviour of diabatic state probabilities for an ideal two-level Landau-Zener transition illustrated in Fig. 6.3.

As the electron-hole symmetry breaking term, ζ, increases further, $P_{\text{classical}}$ gradually increases and reaches a maximum $\sim 65\%$ around $\zeta = 1.2$. As ζ further increases however, $P_{\text{classical}}$ begin to decrease. At this region, the two-level approximation fails. As a result of the S_1 adiabatic state gaining contributions from higher energy diabatic states, $P(\Psi(t); 1\,^1B_u^+) + P(\Psi(t); 2\,^1A_g^-) < 1$. Consequently, the process can no longer be modelled as a two-level system.

6.4 Conclusions

In this chapter, we demonstrated that the internal conversion processes described in Chapter 5 can be modelled using a simple two-level system. First, we showed that the oscillations of the diabatic state probabilities observed for the numerical simulations are quasistationary state oscillations of a two-level quantum system, with the calculated diabatic oscillation frequencies corresponding to the energy gap of the adiabatic states. Then, by linearly scaling the symmetry-breaking Hamiltonian $\hat{H}_\epsilon$, we showed that the quantum transition at the avoided crossing evolves from a non-adiabatic process to an adiabatic process, akin to a Landau-Zener-like transition. For the relevant carotenoid parameters considered in this thesis, the internal conversion from the 'bright' state to the 'dark' state is essentially an adiabatic process.

Chapter 7

Conclusions and Future Work

7.1 Conclusions

Over the past 50 years, the exotic properties of polyene excited states have fascinated the experimental and theoretical photophysics community.[34,35,40,61,93] In this work, we investigated the ultrafast internal conversion processes of an important class of linear polyenes, carotenoids, upon photoexcitation.

A carotenoid photoexcited state undergoing internal conversion results in a triplet-pair state at ultrafast timescales. In order to investigate the triplet-pair nature of the low energy excited states of polyenes, we performed a density matrix renormalisation group (DMRG) study of these states using the Pariser-Parr-Pople-Peierls (PPPP) Hamiltonian. The calculated vertical and relaxed excitation energies indicated that for the parameters relevant for carotenoids, the photoexcited $1\,^1B_u^+$ state can undergo internal conversion to the $1\,^1B_u^-$ triplet-pair state. Further, by calculating bond dimerisations and exciton wavefunctions, it was established that both $1\,^1B_u^-$ and $3\,^1A_g^-$ are high energy members of the same family of triplet-pair states, termed the '$2A_g$' family.

Having established energetically that internal conversion of the $1\,^1B_u^+$ state to a triplet-pair state is possible for carotenoids, we proceeded to investigate the dynamics of the internal conversion process using the carotenoids zeaxanthin and neurosporene as model systems. While our study of the PPPP model suggested an internal conversion pathway *via* a high-energy triplet-pair state, a different direct

internal conversion pathway to the $2\,^1A_g^-$ has been proposed by recent *ab initio* calculations.[58] Indeed, there is a significant experimental and theoretical debate around the relative ordering of polyene excited states which can lead to multiple relaxation pathways.[55] To account for this uncertainty, we considered two parameter sets which gives rise to the two internal conversion pathways. After parametrising the UV-Peierls (UVP) Hamiltonian, a Hamiltonian suitable to study time evolving systems, we performed dynamical studies using the adaptive time-dependent DMRG (tDMRG) method and Ehrenfest dynamics. Ultrafast internal conversion (within ~ 5 fs) of the photoexcited $1\,^1B_u^+$ state to a member of the $2A_g$ family was observed for both pathways, with an associated avoided crossing of the adiabatic excited states. When internal conversion occurs through the $1\,^1B_u^-$ state, a subsequent slower internal conversion (around ~ 50 fs) from the $1\,^1B_u^-$ state to the $2\,^1A_g^-$ state is observed for neurosporene. For both internal conversion pathways and both molecules under consideration, a triplet-pair yield of $\sim 65\%$ was achieved within 50 fs. To our knowledge, this work reports the first instance of a dynamical simulation of the internal conversion process in carotenoids.

To relate our simulations to the wider experimental spectroscopy research, we calculated transient excited state absorption spectra along the direct internal conversion pathway using the Lanczos-DMRG method. We find a dominant absorption signal ca. 1.4 eV at the Franck-Condon point resulting from the $1\,^1B_u^+ \rightarrow n\,^1A_g^-$ transition. After the avoided crossing, the adiabatic evolution of the $1\,^1B_u^+$ state to the $2\,^1A_g^-$ state results in a new dominant excited state transition at ca. 2 eV. This excitation is close to, but lower than the excitation from the lowest energy triplet state. By calculating the exciton wavefunctions of the excited state dipole connected to the $2\,^1A_g^-$ state, we confirmed that this transition arises from the charge-transfer component of the $2\,^1A_g^-$ state.

Carotenoid internal conversion can be described by a simple two-level toy model constituting the adiabatic and diabatic states that contribute to the process. Using this model, we described the oscillatory behaviour of the diabatic state probabil-

ities observed after the avoided crossing, and defined a classical triplet-pair yield to quantify the extent of internal conversion. Finally, we used the two-level model to describe the dynamics at the avoided crossing. By varying the strength of the electron-hole symmetry breaking term, we showed that the electronic transition at the avoided crossing can be interpreted as a Landau-Zener-like transition. For the parameter regime relevant for carotenoids, this transition approaches the adiabatic limit and we can conclude that the internal conversion from the 'bright' $1\,^1B_u^+$ state to a 'dark' triplet-pair state is essentially an adiabatic process.

7.2 Future Work

Results for the ultrafast internal conversion processes described in this work indicate that the evolving state described by $\Psi(t)$ remains on a single adiabatic potential energy surface as it passes the avoided crossing, hence the Ehrenfest approximation used to model nuclear dynamics is largely valid. However, it would be instructive to evaluate the performance of Ehrenfest dynamics against other non-adiabatic methods like surface hopping (Section 2.7.3). In particular, the validity of Ehrenfest approximation for the slow non-adiabatic transition from the S_2 state to the S_1 state of neurosporene described in Section 5.2.1 requires further study. In our model, the Ehrenfest approximation treats the nuclear dynamics classically and does not capture vibronic coupling. It has been suggested that pentacene and related singlet fission systems possess vibronic coherence features which can serve as a pathway for internal conversion of the photoexcited state to a triplet-pair state.[229,230] Duan *et al.* demonstrated that, for pentacene dimers, internal conversion is facilitated by vibronic coherence rather than by electronic coherence.[231] By identifying vibrational normal modes with the largest non-adiabatic couplings, they concluded that internal conversion proceeds via a conical intersection, with the wave-packet oscillating with a period of ~ 32 fs (see Fig. 5.B of ref [231]). In our simulations, the adiabatic states approach each other within about ~ 3 fs, and the energy gap between the adiabatic surfaces remain non-vanishing during the dynamics. These suggest that the internal

conversion of the photoexcited state in carotenoids considered in this thesis proceeds via an avoided crossing. However, experimental evidence suggests that the $S_2 \rightarrow S_1$ internal conversion in β-carotene proceeds via a conical intersection.[232] It is possible that the effective Hamiltonian model we use overestimates the electronic coherence, and quantised nuclear degrees of freedom should be incorporated into dynamics for a more accurate description of the system. To this end, future work will investigate vibronic couplings by supplementing our model with quantised phonons using the TEBD-Ehrenfest method introduced in Section 2.7.4.

This thesis primarily considered the internal conversion process of carotenoid photoexcited states, which is the first step of the singlet fission process in carotenoids. Future work will aim at developing a full kinetic model to study the entire singlet fission process for carotenoid dimers, which can exhibit intermolecular singlet fission.[233] Inspection of Fig. 5.1 and Fig. 5.3 reveal that for both parameter regimes for which dynamical simulations are performed, the energy of the $2\,^1A_g^-$ state is about 0.3 eV below the energy of the $1\,^3B_u^-$ state for conjugation lengths relevant to carotenoids. Therefore our model predicts that the intermolecular singlet fission from the $2\,^1A_g^-$ state is endothermic. In our recent work,[4] by supplementing the PPP Hamiltonian with torsional degrees of freedom we showed that exothermic intermolecular singlet fission is energetically feasible for carotenoids in twisted ground state geometries. Therefore, incorporating torsional degrees of freedom to the UVP Hamiltonian is necessary to simulate the singlet fission process. Additionally, to model the spin decoherence processes by which the bound triplet-pair state of overall singlet character evolves into an unbound triplet-pair, spin symmetries of the model must be lifted. The polyene excited state study report in Chapter 4 reveals that the $1\,^5A_g^-$ is an unbound triplet-pair state and this offers an alternative pathway for singlet fission. Indeed, signatures of an intermediate $1\,^5A_g^-$ state has been detected in pentacene dimers.[234] A complete model allowing for spin mixing could investigate singlet fission pathways via the $1\,^5A_g^-$ state. This work would follow the spin decoherence model of Marcus and Barford.[235]

Various ultrafast time-resolved spectral studies have provided evidence for the existence of a long lived dark state labelled S^*. Similar to the intermediary dark state within the $S_2 - S_1$ gap, the nature of the S^* state has attracted significant debate.[55] A series of studies by Frank *et al.*[236–238] attributed the S^* state to a S_1 state in a twisted conformation. By calculating transient absorption spectra with a Hamiltonian that includes torsional degrees of freedom, it would be possible to comment on the nature of this S^* state using our model. A further improvement to our transient spectra calculations may be achieved by including ground state bleach in our spectral calculations, which experimentally arises due to the absorptions from the molecules in the ground state.

With the correctly parametrised model Hamiltonians, DMRG methods are highly-suited to study the photodynamics of low-dimensional π-conjugated systems. The theoretical and computational techniques developed in this work can easily be generalised to study other systems, such as such as retinals,[85–91] light-emitting polymers[106,150] and acenes.[239] Diphenylhexatrienes (DPH) are a particularly important class of molecules to study in the context of photovoltaic devices. Due to their shorter conjugation lengths, they exhibit a large spin gap ($\sim$ 1.5 eV) compatible with the band gap of silicon ($\sim$ 1.1 eV) and their use as an efficient singlet fission chromophore is well established.[240–242] Recently, Millington *et al.* reported a series of DPH derivative dimers that exhibit intramolecular singlet fission in solution.[243] DMRG techniques developed in this work could be useful to investigate the relaxation pathways of these molecules upon photoexcitation.

Bibliography

(1) Manawadu, D.; Valentine, D. J.; Barford, W. Dynamical Simulations of Carotenoid Photoexcited States Using Density Matrix Renormalization Group Techniques. *J. Phys. Chem. A* **2023**, *127*, 3714–3727.

(2) Valentine, D. J.; Manawadu, D.; Barford, W. Higher energy triplet-pair states in polyenes and their role in intramolecular singlet fission. *Phys. Rev. B* **2020**, *102*, 125107.

(3) Manawadu, D.; Valentine, D. J.; Marcus, M.; Barford, W. Singlet Triplet-Pair Production and Possible Singlet-Fission in Carotenoids. *J. Phys. Chem. Lett.* **2022**, *13*, 1344–1349.

(4) Manawadu, D.; Georges, T. N.; Barford, W. Photoexcited State Dynamics and Singlet Fission in Carotenoids. *J. Phys. Chem. A* **2023**, *127*, 1342–1352.

(5) Yabuzaki, J. Carotenoids Database: structures, chemical fingerprints and distribution among organisms. *Database* **2017**, *2017*, DOI: `10.1093/database/bax004`.

(6) Rodriguez-Concepcion, M.; Avalos, J.; Bonet, M. L.; Boronat, A., et al. A global perspective on carotenoids: Metabolism, biotechnology, and benefits for nutrition and health. *Prog. Lipid Res.* **2018**, *70*, 62–93.

(7) Schalch, W. Carotenoids in the retina—a review of their possible role in preventing or limiting damage caused by light and oxygen. *Free radicals aging* **1992**, 280–298.

(8) Miller, N. J.; Sampson, J.; Candeias, L. P.; Bramley, P. M., et al. Antioxidant activities of carotenes and xanthophylls. *FEBS Lett.* **1996**, *384*, 240–242.

(9) Navara, K. J.; Hill, G. E. Dietary carotenoid pigments and immune function in a songbird with extensive carotenoid-based plumage coloration. *Behav. Ecol.* **2003**, *14*, 909–916.

(10) Peto, R.; Doll, R.; Buckley, J. D.; Sporn, M. B. Can dietary beta-carotene materially reduce human cancer rates? *Nature* **1981**, *290*, 201–208.

(11) Hashimoto, H.; Uragami, C.; Yukihira, N.; Gardiner, A. T., et al. Understanding/unravelling carotenoid excited singlet states. *J. R. Soc. Interface* **2018**, *15*, 20180026.

(12) Fraser, N. J.; Hashimoto, H.; Cogdell, R. J. Carotenoids and bacterial photosynthesis: The story so far... *Photosynth. Res.* **2001**, *70*, 249–256.

(13) Hashimoto, H.; Uragami, C.; Cogdell, R. J. Carotenoids and Photosynthesis. *Subcell. Biochem.* **2016**, *79*, 111–139.

(14) Uragami, C.; Sato, H.; Yukihira, N.; Fujiwara, M., et al. Photoprotective mechanisms in the core LH1 antenna pigment-protein complex from the purple photosynthetic bacterium, Rhodospirillum rubrum. *J. Photochem. Photobiol. A Chem.* **2020**, *400*, 112628.

(15) Smith, M. B.; Michl, J. Singlet Fission. *Chem. Rev.* **2010**, *110*, 6891–6936.

(16) Shockley, W.; Queisser, H. J. Detailed Balance Limit of Efficiency of p-n Junction Solar Cells. *J. Appl. Phys.* **1961**, *32*, 510–519.

(17) Ehrler, B.; Hutter, E. M.; Berry, J. J. The Complicated Morality of Named Inventions. *ACS Energy Lett.* **2021**, *6*, 565–567.

(18) Archer, M. D.; Bolton, J. R. Requirements for ideal performance of photochemical and photovoltaic solar energy converters. *J. Phys. Chem.* **1990**, *94*, 8028–8036.

(19) Hanna, M. C.; Nozik, A. J. Solar conversion efficiency of photovoltaic and photoelectrolysis cells with carrier multiplication absorbers. *J. Appl. Phys.* **2006**, *100*, 74510.

(20) Polman, A.; Atwater, H. A. Photonic design principles for ultrahigh-efficiency photovoltaics. *Nat. Mater.* **2012**, *11*, 174–177.

(21) Lewis, N. S. Research opportunities to advance solar energy utilization. *Science (80-.).* **2016**, *351*, aad1920.

(22) Andreani, L. C.; Bozzola, A.; Kowalczewski, P.; Liscidini, M., et al. Silicon solar cells: toward the efficiency limits. *Adv. Phys. X* **2019**, *4*, 1548305.

(23) Rao, A.; Friend, R. H. Harnessing singlet exciton fission to break the Shockley–Queisser limit. *Nat. Rev. Mater.* **2017**, *2*, 17063.

(24) Lee, J.; Jadhav, P.; Reusswig, P. D.; Yost, S. R., et al. Singlet Exciton Fission Photovoltaics. *Acc. Chem. Res.* **2013**, *46*, 1300–1311.

(25) Rademaker, H.; Hoff, A. J.; Van Grondelle, R.; Duysens, L. N. M. Carotenoid triplet yields in normal and deuterated Rhodospirillum rubrum. *Biochim. Biophys. Acta - Bioenerg.* **1980**, *592*, 240–257.

(26) Johnson, R. C.; Merrifield, R. E. Effects of Magnetic Fields on the Mutual Annihilation of Triplet Excitons in Anthracene Crystals. *Phys. Rev. B* **1970**, *1*, 896–902.

(27) Musser, A. J.; Clark, J. Triplet-Pair States in Organic Semiconductors. *Annu. Rev. Phys. Chem.* **2019**, *70*, 323–351.

(28) Miyata, K.; Conrad-Burton, F. S.; Geyer, F. L.; Zhu, X.-Y. Triplet Pair States in Singlet Fission. *Chem. Rev.* **2019**, *119*, 4261–4292.

(29) Wang, C.; Tauber, M. J. High-yield singlet fission in a zeaxanthin aggregate observed by picosecond resonance Raman spectroscopy. *J. Am. Chem. Soc.* **2010**, *132*, 13988–13991.

(30) Wang, C.; Schlamadinger, D. E.; Desai, V.; Tauber, M. J. Triplet excitons of carotenoids formed by singlet fission in a membrane. *ChemPhysChem* **2011**, *12*, 2891–2894.

(31) Musser, A. J.; Maiuri, M.; Brida, D.; Cerullo, G., et al. The Nature of Singlet Exciton Fission in Carotenoid Aggregates. *J. Am. Chem. Soc.* **2015**, *137*, 5130–5139.

(32) Smith, M. B.; Michl, J. Recent advances in singlet fission. *Annu. Rev. Phys. Chem* **2013**, *64*, 361–386.

(33) Casanova, D. Theoretical Modeling of Singlet Fission. *Chem. Rev.* **2018**, *118*, 7164–7207.

(34) Hudson, B. S.; Kohler, B. E. A low-lying weak transition in the polyene α,ω-diphenyloctatetraene. *Chem. Phys. Lett.* **1972**, *14*, 299–304.

(35) Schulten, K.; Karplus, M. On the origin of a low-lying forbidden transition in polyenes and related molecules. *Chem. Phys. Lett.* **1972**, *14*, 305–309.

(36) Wasielewski, M. R.; Kispert, L. D. Direct measurement of the lowest excited singlet state lifetime of all-trans-β-carotene and related carotenoids. *Chem. Phys. Lett.* **1986**, *128*, 238–243.

(37) Anderson, N. A.; Durfee, C. G.; Murnane, M. M.; Kapteyn, H. C., et al. The internal conversions of trans- and cis-1,3,5-hexatriene in cyclohexane solution studied with sub-50 fs UV pulses. *Chem. Phys. Lett.* **2000**, *323*, 365–371.

(38) Ohta, K.; Naitoh, Y.; Tominaga, K.; Yoshihara, K. Excited-State Dynamics of all-trans-1,3,5,7-Octatetraene in Solution. Direct Observation of Internal Conversion from the S_2 to S_1 State and Relaxation Processes in the S_1 State. *J. Phys. Chem. A* **2001**, *105*, 3973–3980.

(39) Boguslavskiy, A. E.; Schalk, O.; Gador, N.; Glover, W. J., et al. Excited state non-adiabatic dynamics of the smallest polyene, trans 1,3-butadiene. I. Time-resolved photoelectron-photoion coincidence spectroscopy. *J. Chem. Phys.* **2018**, *148*, 164302.

(40) Tavan, P.; Schulten, K. Electronic excitations in finite and infinite polyenes. *Phys. Rev. B* **1987**, *36*, 4337.

(41) Cerullo, G.; Polli, D.; Lanzani, G.; Silvestri, S. D., et al. Photosynthetic Light Harvesting by Carotenoids: Detection of an Intermediate Excited State. *Science (80-.).* **2002**, *298*, 2395–2398.

(42) Frank, H. A.; Desamero, R. Z. B.; Chynwat, V.; Gebhard, R., et al. Spectroscopic Properties of Spheroidene Analogs Having Different Extents of π-Electron Conjugation. *J. Phys. Chem. A* **1997**, *101*, 149–157.

(43) Englman, R.; Jortner, J. The energy gap law for radiationless transitions in large molecules. *Mol. Phys.* **1970**, *18*, 145–164.

(44) Akimoto, S.; Yamazaki, I.; Takaichi, S.; Mimuro, M. Excitation relaxation dynamics of linear carotenoids. *J. Lumin.* **2000**, *87-89*, 797–799.

(45) Polli, D.; Cerullo, G.; Lanzani, G.; De Silvestri, S., et al. Conjugation Length Dependence of Internal Conversion in Carotenoids: Role of the Intermediate State. *Phys. Rev. Lett.* **2004**, *93*, 163002.

(46) Kosumi, D.; Yanagi, K.; Fujii, R.; Hashimoto, H., et al. Conjugation length dependence of relaxation kinetics in β-carotene homologs probed by femtosecond Kerr-gate fluorescence spectroscopy. *Chem. Phys. Lett.* **2006**, *425*, 66–70.

(47) Starcke, J. H.; Wormit, M.; Schirmer, J.; Dreuw, A. How much double excitation character do the lowest excited states of linear polyenes have? *Chem. Phys.* **2006**, *329*, 39–49.

(48) Ghosh, D.; Hachmann, J.; Yanai, T.; Chan, G. K. L. Orbital optimization in the density matrix renormalization group, with applications to polyenes and ß -carotene. *J. Chem. Phys.* **2008**, *128*, 144117.

(49) Koyama, Y.; Rondonuwu, F. S.; Fujii, R.; Watanabe, Y. Light-harvesting function of carotenoids in photo-synthesis: The roles of the newly found $1^1B_u^-$ state. *Biopolymers* **2004**, *74*, 2–18.

(50) Fujii, R.; Inaba, T.; Watanabe, Y.; Koyama, Y., et al. Two different pathways of internal conversion in carotenoids depending on the length of the conjugated chain. *Chem. Phys. Lett.* **2003**, *369*, 165–172.

(51) Rondonuwu, F. S.; Watanabe, Y.; Fujii, R.; Koyama, Y. A first detection of singlet to triplet conversion from the $1^1B_u^-$ to the $1^3A_g^-$ state and triplet internal conversion from the $1^3A_g^-$ to the $1^1B_u^-$ state in carotenoids: dependence on the conjugation length. *Chem. Phys. Lett.* **2003**, *376*, 292–301.

(52) Nishimura, K.; Rondonuwu, F. S.; Fujii, R.; Akahane, J., et al. Sequential singlet internal conversion of $1^1B_u^+ \rightarrow 3^1A_g^- \rightarrow 1^1B_u^- \rightarrow 2^1A_g^- \rightarrow$ ($1^1A_g^-$ ground) in all-trans-spirilloxanthin revealed by two-dimensional sub-5-fs spectroscopy. *Chem. Phys. Lett.* **2004**, *392*, 68–73.

(53) Ikuta, M.; Yabushita, A.; Rondonuwu, F. S.; Akahane, J., et al. The $1^1B_u^+ \rightarrow 3^1A_g^- \rightarrow 1^1B_u^- \rightarrow 2^1A_g^-$ internal conversion in carotenoids following the energy-gap law identified by 5fs spectroscopy. *Chem. Phys. Lett.* **2006**, *422*, 95–99.

(54) Hashimoto, H.; Yanagi, K.; Yoshizawa, M.; Polli, D., et al. The very early events following photoexcitation of carotenoids. *Arch. Biochem. Biophys.* **2004**, *430*, 61–69.

(55) Polívka, T.; Sundström, V. Dark excited states of carotenoids: Consensus and controversy. *Chem. Phys. Lett.* **2009**, *477*, 1–11.

(56) Hauer, J.; Buckup, T.; Motzkus, M. Pump-Degenerate Four Wave Mixing as a Technique for Analyzing Structural and Electronic Evolution: Multidimensional Time-Resolved Dynamics near a Conical Intersection. *J. Phys. Chem. A* **2007**, *111*, 10517–10529.

(57) Christensson, N.; Polivka, T.; Yartsev, A.; Pullerits, T. Photon echo spectroscopy reveals structure-dynamics relationships in carotenoids. *Phys. Rev. B* **2009**, *79*, 245118.

(58) Taffet, E. J.; Lee, B. G.; Toa, Z. S. D.; Pace, N., et al. Carotenoid Nuclear Reorganization and Interplay of Bright and Dark Excited States. *J. Phys. Chem. B* **2019**, *123*, 8628–8643.

(59) Khokhlov, D.; Belov, A. Ab Initio Study of Low-Lying Excited States of Carotenoid-Derived Polyenes. *J. Phys. Chem. A* **2020**, *124*, 5790–5803.

(60) Bachilo, S. M.; Spangler, C. W.; Gillbro, T. Excited state energies and internal conversion in diphenylpolyenes: from diphenylbutadiene to diphenyltetradecaheptaene. *Chem. Phys. Lett.* **1998**, *283*, 235–242.

(61) Polívka, T.; Sundström, V. Ultrafast dynamics of carotenoid excited states-from solution to natural and artificial systems. *Chem. Rev.* **2004**, *104*, 2021–2071.

(62) Tavan, P.; Schulten, K. The low-lying electronic excitations in long polyenes: A PPP-MRD-CI study. *J. Chem. Phys.* **1986**, *85*, 6602–6609.

(63) DeCoster, B.; Christensen, R. L.; Gebhard, R.; Lugtenburg, J., et al. Low-lying electronic states of carotenoids. *Biochim. Biophys. Acta - Bioenerg.* **1992**, *1102*, 107–114.

(64) Ehlers, F.; Scholz, M.; Lenzer, T.; Oum, K. Excited State Dynamics of Selected All-trans $C_4$0 Xanthophyll Carotenoids. *Zeitschrift für Phys. Chemie* **2015**, *229*, 1815–1830.

(65) Kasha, M. Characterization of electronic transitions in complex molecules. *Discuss. Faraday Soc.* **1950**, *9*, 14–19.

(66) Itoh, T. Evidence for the coexistence of two different mechanisms for the occurrence of anti-Kasha S_2 (1^1B_u) fluorescence from α,ω-diphenylpolyenes. *J. Chem. Phys.* **2004**, *121*, 6956–6960.

(67) Andersson, P. O.; Gillbro, T.; Asato, A. E.; Liu, R. S. H. Dual singlet state emission in a series of mini-carotenes. *J. Lumin.* **1992**, *51*, 11–20.

(68) Andersson, P. O.; Bachilo, S. M.; Chen, R.-L.; Gillbro, T. Solvent and temperature effects on dual fluorescence in a series of carotenes. Energy gap dependence of the internal conversion rate. *J. Phys. Chem.* **1995**, *99*, 16199–16209.

(69) Christensen, R. L.; Goyette, M.; Gallagher, L.; Duncan, J., et al. S_1 and S_2 States of Apo- and Diapocarotenes. *J. Phys. Chem. A* **1999**, *103*, 2399–2407.

(70) Frank, H. A.; Josue, J. S.; Bautista, J. A.; van der Hoef, I., et al. Spectroscopic and Photochemical Properties of Open-Chain Carotenoids. *J. Phys. Chem. B* **2002**, *106*, 2083–2092.

(71) Catalán, J.; Hopf, H.; Mlynek, C.; Klein, D., et al. Electronic Energy Levels in all-trans Long Linear Polyenes: The Case of the 3,20-Di(tert-butyl)-2,2,21,21-tetramethyl-all-trans-3,5,7,9,11,13,15,17,19-docosanonaen (ttbp9) Conforming to Kasha's Rule. *Chem. – A Eur. J.* **2005**, *11*, 3915–3920.

(72) Catalán, J.; Hopf, H.; Klein, D.; Kilickiran, P. Absorption to and emission from the excited electronic state 11Bu in long linear all-trans-polyenes: The case of ttbP9 and ttbP11. *J. Phys. Org. Chem.* **2022**, *35*, e4292.

(73) D'Amico, K. L.; Manos, C.; Christensen, R. L. Electronic energy levels in a homologous series of unsubstituted linear polyenes. *J. Am. Chem. Soc.* **1980**, *102*, 1777–1782.

(74) Bautista, J. A.; Connors, R. E.; Raju, B. B.; Hiller, R. G., et al. Excited State Properties of Peridinin: Observation of a Solvent Dependence of the Lowest Excited Singlet State Lifetime and Spectral Behavior Unique among Carotenoids. *J. Phys. Chem. B* **1999**, *103*, 8751–8758.

(75) Frank, H. A.; Bautista, J. A.; Josue, J.; Pendon, Z., et al. Effect of the Solvent Environment on the Spectroscopic Properties and Dynamics of the Lowest Excited States of Carotenoids. *J. Phys. Chem. B* **2000**, *104*, 4569–4577.

(76) Wild, D. A.; Winkler, K.; Stalke, S.; Oum, K., et al. Extremely strong solvent dependence of the $S_1 \rightarrow S_0$ internal conversion lifetime of 12′-apo-β-caroten-12′-al. *Phys. Chem. Chem. Phys.* **2006**, *8*, 2499–2505.

(77) Ehlers, F.; Wild, D. A.; Lenzer, T.; Oum, K. Investigation of the $S_1/ICT \rightarrow S_0$ Internal Conversion Lifetime of 4‘-apo-β-caroten-4‘-al and 8‘-apo-β-caroten-8‘-al: Dependence on Conjugation Length and Solvent Polarity. *J. Phys. Chem. A* **2007**, *111*, 2257–2265.

(78) Kosumi, D.; Kajikawa, T.; Sakaguchi, K.; Katsumura, S., et al. Excited state properties of β-carotene analogs incorporating a lactone ring. *Phys. Chem. Chem. Phys.* **2017**, *19*, 3000–3009.

(79) Hudson, B. S.; Kohler, B. E. Polyene spectroscopy: The lowest energy excited singlet state of diphenyloctatetraene and other linear polyenes. *J. Chem. Phys.* **1973**, *59*, 4984–5002.

(80) Gavin, R. M.; Weisman, C.; McVey, J. K.; Rice, S. A. Spectroscopic properties of polyenes. III. 1,3,5,7-Octatetraene. *J. Chem. Phys.* **1978**, *68*, 522–529.

(81) Heimbrook, L. A.; Kenny, J. E.; Kohler, B. E.; Scott, G. W. Free-jet fluorescence excitation spectrum of trans, trans-1,3,5,7-octatetraene. *J. Chem. Phys.* **1981**, *75*, 4338–4342.

(82) Leopold, D. G.; Vaida, V.; Granville, M. F. Direct absorption spectroscopy of jet-cooled polyenes. I. The 1 1B+u←1 1A−g transition of trans, trans-1,3,5,7-octatetraene. *J. Chem. Phys.* **1984**, *81*, 4210–4217.

(83) Bouwman, W. G.; Jones, A. C.; Phillips, D.; Thibodeau, P., et al. Fluorescence of gaseous tetraenes and pentaenes. *J. Phys. Chem.* **1990**, *94*, 7429–7434.

(84) Matthews, G. G., *Neurobiology: molecules, cells and systems*; Wiley-Blackwell: 2000.

(85) Kropf, A.; Hubbard, R. The photoisomerization of retinal*. *Photochem. Photobiol.* **1970**, *12*, 249–260.

(86) Rosenfeld, T.; Alchalel, A.; Ottolenghi, M. Role of the triplet state in the photoisomerization of retinal isomers. *J. Phys. Chem.* **1974**, *78*, 336–341.

(87) Waddell, W. H.; Hopkins, D. L.; Uemura, M.; West, J. L. Influence of alkyl substitution on the trans → cis photoisomerization of all-trans-retinal and related polyenes. *J. Am. Chem. Soc.* **1978**, *100*, 1970–1972.

(88) Waddell, W. H.; West, J. L. Photochemistry of linear polyenes related to vitamin A. 13-Demethylretinal and 14-methylretinal. *J. Phys. Chem.* **1980**, *84*, 134–139.

(89) Becker, R. S.; Freedman, K. A comprehensive investigation of the mechanism and photophysics of isomerization of a protonated and unprotonated Schiff base of 11-cis-retinal. *J. Am. Chem. Soc.* **1985**, *107*, 1477–1485.

(90) Zgrablić, G.; Voïtchovsky, K.; Kindermann, M.; Haacke, S., et al. Ultrafast Excited State Dynamics of the Protonated Schiff Base of All-trans Retinal in Solvents. *Biophys. J.* **2005**, *88*, 2779–2788.

(91) Bassolino, G.; Sovdat, T.; Liebel, M.; Schnedermann, C., et al. Synthetic Control of Retinal Photochemistry and Photophysics in Solution. *J. Am. Chem. Soc.* **2014**, *136*, 2650–2658.

(92) Landau, L. D.; Lifshitz, E. M., *Quantum mechanics: non-relativistic theory*; Pergamon Press: 1977; Vol. 3.

(93) Barford, W., *Electronic and Optical Properties of Conjugated Polymers*; Oxford University Press: 2013.

(94) Rohlfing, M.; Louie, S. G. Optical excitations in conjugated polymers. *Phys. Rev. Lett.* **1999**, *82*, 1959–1962.

(95) Chandross, M.; Mazumdar, S. Coulomb interactions and linear, nonlinear, and triplet absorption in poly(para-phenylenevinylene). *Phys. Rev. B - Condens. Matter Mater. Phys.* **1997**, *55*, 1497–1504.

(96) Hückel, E. Quantentheoretische Beiträge zum Benzolproblem. *Zeitschrift für Phys.* **1931**, *70*, 204–286.

(97) Pariser, R.; Parr, R. G. A semi-empirical theory of the electronic spectra and electronic structure of complex unsaturated molecules. I. *J. Chem. Phys.* **1953**, *21*, 466–471.

(98) Pariser, R.; Parr, R. G. A semi-empirical theory of the electronic spectra and electronic structure of complex unsaturated molecules. II. *J. Chem. Phys.* **1953**, *21*, 767–776.

(99) Pople, J. A. Electron interaction in unsaturated hydrocarbons. *Trans. Faraday Soc.* **1953**, *49*, 1375–1385.

(100) Pople, J. A. The electronic spectra of aromatic molecules II: A theoretical treatment of excited states of alternant hydrocarbon molecules based on self-consistent molecular orbitals. *Proc. Phys. Soc. Sect. A* **1955**, *68*, 81.

(101) Yaron, D.; Moore, E. E.; Shuai, Z.; Brédas, J. L. Comparison of density matrix renormalization group calculations with electron-hole models of exciton binding in conjugated polymers. *J. Chem. Phys.* **1998**, *108*, 7451–7458.

(102) Fano, G.; Ortolani, F.; Ziosi, L. The density matrix renormalization group method: Application to the PPP model of a cyclic polyene chain. *J. Chem. Phys.* **1998**, *108*, 9246–9252.

(103) Bursill, R. J.; Barford, W. Electron-Lattice Relaxation, and Soliton Structures and Their Interactions in Polyenes. *Phys. Rev. Lett.* **1999**, *82*, 1514–1517.

(104) Barford, W.; Bursill, R. J.; Lavrentiev, M. Y. Density-matrix renormalization-group calculations of excited states of linear polyenes. *Phys. Rev. B* **2001**, *63*, 195108.

(105) Barford, W.; Bursill, R. J.; Lavrentiev, M. Y. Breakdown of the adiabatic approximation in trans-polyacetylene. *Phys. Rev. B - Condens. Matter Mater. Phys.* **2002**, *65*, 075107.

(106) Bursill, R. J.; Barford, W. Large-scale numerical investigation of excited states in poly(para-phenylene). *Phys. Rev. B* **2002**, *66*, 205112.

(107) Bursill, R. J.; Barford, W. Symmetry-adapted density matrix renormalization group calculations of the primary excited states of poly(para-phenylene vinylene). *J. Chem. Phys.* **2009**, *130*, DOI: 10.1063/1.3149536.

(108) Porter, R. N.; Raff, L. M. In *Dyn. Mol. Collisions Part B*, Miller, W. H., Ed.; Springer US: Boston, MA, 1976, pp 1–52.

(109) Allen, M. P.; Tildesley, D. J., *Computer simulation of liquids*; Oxford University Press: 2017.

(110) Karplus, M.; Petsko, G. A. Molecular dynamics simulations in biology. *Nature* **1990**, *347*, 631–639.

(111) Kollman, P. A.; Massova, I.; Reyes, C.; Kuhn, B., et al. Calculating Structures and Free Energies of Complex Molecules: Combining Molecular Mechanics and Continuum Models. *Acc. Chem. Res.* **2000**, *33*, 889–897.

(112) Genheden, S.; Ryde, U. The MM/PBSA and MM/GBSA methods to estimate ligand-binding affinities. *Expert Opin. Drug Discov.* **2015**, *10*, 449–461.

(113) Tully, J. C. In *Mod. Methods Multidimens. Dyn. Comput. Chem.* World Scientific: 1998, pp 34–72.

(114) Gerber, R. B.; Buch, V.; Ratner, M. A. Time-dependent self-consistent field approximation for intramolecular energy transfer. I. Formulation and application to dissociation of van der Waals molecules. *J. Chem. Phys.* **1982**, *77*, 3022–3030.

(115) Micha, D. A. A self-consistent eikonal treatment of electronic transitions in molecular collisions. *J. Chem. Phys.* **1983**, *78*, 7138–7145.

(116) Sawada, S.-I. I.; Nitzan, A.; Metiu, H. Mean-trajectory approximation for charge- and energy-transfer processes at surfaces. *Phys. Rev. B* **1985**, *32*, 851–867.

(117) Head-Gordon, M.; Tully, J. C. Molecular dynamics with electronic frictions. *J. Chem. Phys.* **1995**, *103*, 10137–10145.

(118) Bała, P.; Grochowski, P.; Lesyng, B.; McCammon, J. A. Quantum-Classical Molecular Dynamics Simulations of Proton Transfer Processes in Molecular Complexes and in Enzymes. *J. Phys. Chem.* **1996**, *100*, 2535–2545.

(119) Andrade, X.; Castro, A.; Zueco, D.; Alonso, J. L., et al. Modified Ehrenfest Formalism for Efficient Large-Scale ab initio Molecular Dynamics. *J. Chem. Theory Comput.* **2009**, *5*, 728–742.

(120) Tully, J. C.; Preston, R. K. Trajectory surface hopping approach to nonadiabatic molecular collisions: The reaction of H^+ with D_2. *J. Chem. Phys.* **1971**, *55*, 562–572.

(121) Preston, R. K.; Cohen, J. S. Chemi-ionization in atom–diatom collisions. *J. Chem. Phys.* **1976**, *65*, 1589–1590.

(122) Tully, J. C. Molecular dynamics with electronic transitions. *J. Chem. Phys.* **1990**, *93*, 1061–1071.

(123) Kuntz, P. J. Classical path surface-hopping dynamics. I. General theory and illustrative trajectories. *J. Chem. Phys.* **1991**, *95*, 141–155.

(124) Shenvi, N.; Roy, S.; Tully, J. C. Dynamical Steering and Electronic Excitation in NO Scattering from a Gold Surface. *Science (80-.).* **2009**, *326*, 829–832.

(125) Subotnik, J. E.; Shenvi, N. A new approach to decoherence and momentum rescaling in the surface hopping algorithm. *J. Chem. Phys.* **2011**, *134*, 24105.

(126) Wang, L.; Beljonne, D. Flexible Surface Hopping Approach to Model the Crossover from Hopping to Band-like Transport in Organic Crystals. *J. Phys. Chem. Lett.* **2013**, *4*, 1888–1894.

(127) Dou, W.; Nitzan, A.; Subotnik, J. E. Surface hopping with a manifold of electronic states. II. Application to the many-body Anderson-Holstein model. *J. Chem. Phys.* **2015**, *142*, 84110.

(128) Wang, L.; Qiu, J.; Bai, X.; Xu, J. Surface hopping methods for nonadiabatic dynamics in extended systems. *WIREs Comput. Mol. Sci.* **2020**, *10*, e1435.

(129) Mannouch, J. R.; Barford, W.; Al-Assam, S. Ultra-fast relaxation, decoherence, and localization of photoexcited states in π-conjugated polymers. *J. Chem. Phys.* **2018**, *148*, 034901.

(130) Barford, W.; Mannouch, J. R. Torsionally induced exciton localization and decoherence in π -conjugated polymers. *J. Chem. Phys.* **2018**, *149*, 214107.

(131) Mannouch, J. Exciton Dynamics in π-Conjugated Polymer Systems, Ph.D. Thesis, Universirty of Oxford, 2019.

(132) White, S. R. Density matrix formulation for quantum renormalization groups. *Phys. Rev. Lett.* **1992**, *69*, 2863–2866.

(133) White, S. R.; Feiguin, A. E. Real-Time Evolution Using the Density Matrix Renormalization Group. *Phys. Rev. Lett.* **2004**, *93*, 76401.

(134) A. J. Daley; C. Kollath; U. Schollwöck; G. Vidal Time-dependent density-matrix renormalization-group using adaptive effective Hilbert spaces. *J. Stat. Mech. Theory Exp.* **2004**, *2004*, P04005.

(135) Jeckelmann, E. Dynamical density-matrix renormalization-group method. *Phys. Rev. B* **2002**, *66*, 45114.

(136) Baiardi, A.; Reiher, M. The density matrix renormalization group in chemistry and molecular physics: Recent developments and new challenges. *J. Chem. Phys.* **2020**, *152*, 40903.

(137) Ma, H.; Schollwöck, U.; Shuai, Z. In *Density Matrix Renorm. Gr. (DMRG)-based Approaches Comput. Chem.* Elsevier: 2022, pp 57–90.

(138) Ma, H.; Schollwöck, U.; Shuai, Z. In *Density Matrix Renorm. Gr. (DMRG)-based Approaches Comput. Chem.* Elsevier: 2022, pp 91–147.

(139) Vidal, G. Efficient Classical Simulation of Slightly Entangled Quantum Computations. *Phys. Rev. Lett.* **2003**, *91*, 147902.

(140) Vidal, G. Efficient Simulation of One-Dimensional Quantum Many-Body Systems. *Phys. Rev. Lett.* **2004**, *93*, 40502.

(141) Schollwöck, U. The density-matrix renormalization group. *Rev. Mod. Phys.* **2005**, *77*, 259–315.

(142) Schollwöck, U. The density-matrix renormalization group in the age of matrix product states. *Ann. Phys. (N. Y).* **2011**, *326*, 96–192.

(143) Schollwöck, U. Time-dependent Density-Matrix Renormalization-Group Methods. *J. Phys. Soc. Japan* **2005**, *74*, 246–255.

(144) Wilson, K. G. The renormalization group: Critical phenomena and the Kondo problem. *Rev. Mod. Phys.* **1975**, *47*, 773–840.

(145) Bulla, R.; Costi, T. A.; Pruschke, T. Numerical renormalization group method for quantum impurity systems. *Rev. Mod. Phys.* **2008**, *80*, 395–450.

(146) White, S. R.; Noack, R. M. Real-space quantum renormalization groups. *Phys. Rev. Lett.* **1992**, *68*, 3487–3490.

(147) Feiguin, A. E. In *Strongly Correl. Syst. Numer. Methods*, Avella, A., Mancini, F., Eds.; Springer Berlin Heidelberg: Berlin, Heidelberg, 2013, pp 31–65.

(148) Schollwöck, U.; Chakravarty, S.; Fjærestad, J. O.; Marston, J. B., et al. Broken Time-Reversal Symmetry in Strongly Correlated Ladder Structures. *Phys. Rev. Lett.* **2003**, *90*, 186401.

(149) White, S. R. Spin Gaps in a Frustrated Heisenberg Model for CaV_4O_9. *Phys. Rev. Lett.* **1996**, *77*, 3633–3636.

(150) Bursill, R. J.; Barford, W. Symmetry-adapted density matrix renormalization group calculations of the primary excited states of poly(para-phenylene vinylene). *J. Chem. Phys.* **2009**, *130*, 234302.

(151) Cazalilla, M. A.; Marston, J. B. Time-Dependent Density-Matrix Renormalization Group: A Systematic Method for the Study of Quantum Many-Body Out-of-Equilibrium Systems. *Phys. Rev. Lett.* **2002**, *88*, 256403.

(152) Luo, H. G.; Xiang, T.; Wang, X. Q. Comment on "Time-Dependent Density-Matrix Renormalization Group: A Systematic Method for the Study of Quantum Many-Body Out-of-Equilibrium Systems". *Phys. Rev. Lett.* **2003**, *91*, 49701.

(153) Feiguin, A. E. In *Strongly Correl. Syst. Numer. Methods*, Avella, A., Mancini, F., Eds.; Springer Berlin Heidelberg: Berlin, Heidelberg, 2013, pp 131–152.

(154) Berera, R.; van Grondelle, R.; Kennis, J. T. M. Ultrafast transient absorption spectroscopy: principles and application to photosynthetic systems. *Photosynth. Res.* **2009**, *101*, 105–118.

(155) Jeckelmann, E.; Benthien, H. In *Comput. Many-Particle Phys.* Springer: 2008, pp 621–635.

(156) Jeckelmann, E.; Fehske, H. Exact numerical methods for electron-phonon problems. *La Riv. del Nuovo Cim.* **2007**, *30*, 259–292.

(157) Hallberg, K. A. Density-matrix algorithm for the calculation of dynamical properties of low-dimensional systems. *Phys. Rev. B* **1995**, *52*, R9827–R9830.

(158) Kühner, T. D.; White, S. R. Dynamical correlation functions using the density matrix renormalization group. *Phys. Rev. B* **1999**, *60*, 335–343.

(159) Gagliano, E. R.; Balseiro, C. A. Dynamical Properties of Quantum Many-Body Systems at Zero Temperature. *Phys. Rev. Lett.* **1987**, *59*, 2999–3002.

(160) Lanczos, C. An iteration method for the solution of the eigenvalue problem of linear differential and integral operators. *J. Res. Natl. Bur. Stand. B* **1950**, *45*, 255–282.

(161) Eisert, J.; Cramer, M.; Plenio, M. B. Colloquium: Area laws for the entanglement entropy. *Rev. Mod. Phys.* **2010**, *82*, 277.

(162) Hastings, M. B. An area law for one-dimensional quantum systems. *J. Stat. Mech. theory Exp.* **2007**, *2007*, P08024.

(163) Paeckel, S.; Köhler, T.; Swoboda, A.; Manmana, S. R., et al. Time-evolution methods for matrix-product states. *Ann. Phys. (N. Y).* **2019**, *411*, 167998.

(164) Valentine, D. Singlet fission in linear π-conjugated systems, Ph.D. Thesis, Universirty of Oxford, 2020.

(165) Neese, F. The ORCA program system. *Wiley Interdiscip. Rev. Comput. Mol. Sci.* **2012**, *2*, 73–78.

(166) Neese, F. Software update: the ORCA program system, version 4.0. *Wiley Interdiscip. Rev. Comput. Mol. Sci.* **2017**, *8*, 73–78.

(167) Stephens, P. J.; Devlin F. J.; Chabalowski, C. F.; Frisch, M. J. Ab Initio Calculation of Vibrational Absorption and Circular Dichroism Spectra Using Density Functional Force Fields. *J. Phys. Chem.* **1994**, *98*, 11623.

(168) Weigend, F.; Ahlrichs, R. Balanced basis sets of split valence, triple zeta valence and quadruple zeta valence quality for H to Rn: Design and assessment of accuracy. *Phys. Chem. Chem. Phys.* **2005**, *7*, 3297.

(169) Weigend, F.; Ahlrichs, R. Accurate Coulomb-fitting basis sets for H to Rn. *Phys. Chem. Chem. Phys.* **2006**, *8*, 1057.

(170) Levitin, E. S.; Polyak, B. T. Constrained minimization methods. *USSR Comput. Math. Math. Phys.* **1966**, *6*, 1–50.

(171) Čížek, J.; Paldus, J.; Hubač, I. Correlation effects in the low–lying excited states of the PPP models of alternant hydrocarbons. I. Qualitative rules for the effect of limited configuration interaction. *Int. J. Quantum Chem.* **1974**, *8*, 951–970.

(172) Szabo, A.; Langlet, J.; Malrieu, J.-P. Length dependence of excitation energies in linear polyenes: Localized and delocalized descriptions. *Chem. Phys.* **1976**, *13*, 173–179.

(173) Schulten, K.; Ohmine, I.; Karplus, M. Correlation effects in the spectra of polyenes. *J. Chem. Phys.* **1976**, *64*, 4422–4441.

(174) Ohmine, I.; Karplus, M.; Schulten, K. Renormalized configuration interaction method for electron correlation in the excited states of polyenes. *J. Chem. Phys.* **1978**, *68*, 2298–2318.

(175) Tavan, P.; Schulten, K. The 2^1A_g - 1^1B_u energy gap in the polyenes: An extended configuration interaction study. *J. Chem. Phys.* **1979**, *70*, 5407–5413.

(176) Lasaga, A. C.; Aerni, R. J.; Karplus, M. Photodynamics of polyenes: The effect of electron correlation on potential surfaces. *J. Chem. Phys.* **1980**, *73*, 5230–5243.

(177) Buenker, R. J.; Whitten, J. L. Ab Initio SCF MO and CI Studies of the Electronic States of Butadiene. *J. Chem. Phys.* **1968**, *49*, 5381–5387.

(178) Hosteny, R. P.; Dunning Jr, T. H.; Gilman, R. R.; Pipano, A., et al. A binitio study of the π-electron states of trans-butadiene. *J. Chem. Phys.* **1975**, *62*, 4764–4779.

(179) Aoyagi, M.; Osamura, Y.; Iwata, S. An MCSCF study of the low-lying states of trans-butadiene. *J. Chem. Phys.* **1985**, *83*, 1140–1148.

(180) Serrano-Andrés, L.; Lindh, R.; Roos, B. O.; Merchán, M. Theoretical study of the electronic spectrum of all-trans-1,3,5,7-octatetraene. *J. Phys. Chem.* **1993**, *97*, 9360–9368.

(181) Olivucci, M.; Ragazos, I. N.; Bernardi, F.; Robb, M. A. A conical intersection mechanism for the photochemistry of butadiene. A MC-SCF study. *J. Am. Chem. Soc.* **1993**, *115*, 3710–3721.

(182) Olivucci, M.; Bernardi, F.; Celani, P.; Ragazos, I., et al. Excited-state cis-trans isomerization of cis-hexatriene. A CAS-SCF computational study. *J. Am. Chem. Soc.* **1994**, *116*, 1077–1085.

(183) Bemardi, F.; Olivucci, M.; Robb, M. A. Simulation of MC-SCF Results on Covalent Organic Multi-Bond Reactions: Molecular Mechanics with Valence Bond (MM-VB). *J. Am. Chem. Soc.* **1992**, *114*, 1606–1616.

(184) Bearpark, M. J.; Boggio-Pasqua, M.; Robb, M. A.; Ogliaro, F. Excited States of Conjugated Hydrocarbons Using the Molecular Mechanics - Valence Bond (MMVB) Method: Conical Intersections and Dynamics. *Theor. Chem. Acc.* **2006**, *116*, 670–682.

(185) Garavelli, M.; Smith, B. R.; Bearpark, M. J.; Bernardi, F., et al. Relaxation paths and dynamics of photoexcited polyene chains: Evidence for creation and annihilation of neutral soliton pairs. *J. Am. Chem. Soc.* **2000**, *122*, 5568–5581.

(186) Bernardi, F.; Garavelli, M.; Olucci, M. Trans cis isomerization in long linear polyenes as beta-carotene models: A comparative CAS-PT2 and DFT study. *Mol. Phys.* **1997**, *92*, 359–364.

(187) Polyak, I.; Jenkins, A. J.; Vacher, M.; Bouduban, M. E., et al. Charge migration engineered by localisation: electron-nuclear dynamics in polyenes and glycine. *Mol. Phys.* **2018**, *116*, 2474–2489.

(188) Hsu, C.-P.; Hirata, S.; Head-Gordon, M. Excitation Energies from Time-Dependent Density Functional Theory for Linear Polyene Oligomers: Butadiene to Decapentaene. *J. Phys. Chem. A* **2001**, *105*, 451–458.

(189) Silva-Junior, M. R.; Schreiber, M.; Sauer, S. P. A.; Thiel, W. Benchmarks for electronically excited states: Time-dependent density functional theory and density functional theory based multireference configuration interaction. *J. Chem. Phys.* **2008**, *129*, 104103.

(190) Angeli, C.; Pastore, M. The lowest singlet states of octatetraene revisited. *J. Chem. Phys.* **2011**, *134*, 184302.

(191) Marian, C. M.; Gilka, N. Performance of the density functional theory/ multireference configuration interaction method on electronic excitation of extended π-systems. *J. Chem. Theory Comput.* **2008**, *4*, 1501–1515.

(192) Kleinschmidt, M.; Marian, C. M.; Waletzke, M.; Grimme, S. Parallel multireference configuration interaction calculations on mini-β-carotenes and β-carotene. *J. Chem. Phys.* **2009**, *130*, 044708.

(193) Barford, W.; Bursill, R. J. Theory of molecular excitons in the phenyl-based organic semiconductors. *Chem. Phys. Lett.* **1997**, *268*, 535.

(194) Barford, W.; Bursill, R. J.; Lavrentiev, M. Y. Density matrix renormalization group calculations of the low-lying excitations and non-linear optical properties of poly(para-phenylene). *J. Physics-Condensed Matter* **1998**, *10*, 6429–6446.

(195) Lavrentiev, M. Y.; Barford, W.; Martin, S. J.; Daly, H., et al. Theoretical investigation of the low-lying electronic structure of poly(p-phenylene vinylene). *Phys. Rev. B* **1999**, *59*, 9987–9994.

(196) White, S. R.; Martin, R. L. Ab initio quantum chemistry using the density matrix renormalization group. *J. Chem. Phys.* **1999**, *110*, 4127–4130.

(197) Helgaker, T.; Jørgensen, P.; Olsen, J., *Molecular electronic-structure theory*; John Wiley & Sons: 2014.

(198) Wouters, S.; Van Neck, D. The density matrix renormalization group for ab initio quantum chemistry. *Eur. Phys. J. D* **2014**, *68*, 272.

(199) Gobert, D.; Kollath, C.; Schollwöck, U.; Schütz, G. Real-time dynamics in spin-1/2 chains with adaptive time-dependent density matrix renormalization group. *Phys. Rev. E - Stat. Nonlinear, Soft Matter Phys.* **2005**, *71*, 036102.

(200) Kollath, C.; Schollwöck, U.; Zwerger, W. Spin-charge separation in cold fermi gases: A real time analysis. *Phys. Rev. Lett.* **2005**, *95*, 176401.

(201) Al-Hassanieh, K. A.; Feiguin, A. E.; Riera, J. A.; Büsser, C. A., et al. Adaptive time-dependent density-matrix renormalization-group technique for calculating the conductance of strongly correlated nanostructures. *Phys. Rev. B - Condens. Matter Mater. Phys.* **2006**, *73*, 195304.

(202) Dias Da Silva, L. G.; Heidrich-Meisner, F.; Feiguin, A. E.; Büsser, C. A., et al. Transport properties and Kondo correlations in nanostructures: Time-dependent DMRG method applied to quantum dots coupled to Wilson chains. *Phys. Rev. B - Condens. Matter Mater. Phys.* **2008**, *78*, 195317.

(203) White, S. R.; Affleck, I. Spectral function for the S=1 Heisenberg antiferromagetic chain. *Phys. Rev. B - Condens. Matter Mater. Phys.* **2008**, *77*, 134437.

(204) Al-Hassanieh, K. A.; Reboredo, F. A.; Feiguin, A. E.; González, I., et al. Excitons in the one-dimensional Hubbard model: A real-time study. *Phys. Rev. Lett.* **2008**, *100*, 166403.

(205) Heidrich-Meisner, F.; Feiguin, A. E.; Dagotto, E. Real-time simulations of nonequilibrium transport in the single-impurity Anderson model. *Phys. Rev. B* **2009**, *79*, 235336.

(206) Perez, I. G.; Barford, W. Ultrafast Fluorescence Depolarization in Conjugated Polymers. *J. Phys. Chem. Lett.* **2021**, *12*, 5344–5348.

(207) Xie, X.; Liu, Y.; Yao, Y.; Schollwöck, U., et al. Time-dependent density matrix renormalization group quantum dynamics for realistic chemical systems. *J. Chem. Phys.* **2019**, *151*, 224101.

(208) Schröder, F. A.; Turban, D. H.; Musser, A. J.; Hine, N. D., et al. Tensor network simulation of multi-environmental open quantum dynamics via machine learning and entanglement renormalisation. *Nat. Commun.* **2019**, *10*, 1–10.

(209) Ren, J.; Li, W.; Jiang, T.; Wang, Y., et al. Time-dependent density matrix renormalization group method for quantum dynamics in complex systems. *Wiley Interdiscip. Rev. Comput. Mol. Sci.* **2022**, e1614.

(210) Castleton, C. W.; Barford, W. Screening and the quantitative π-model description of the optical spectra and polarizations of phenyl based oligomers. *J. Chem. Phys.* **2002**, *117*, 3570–3582.

(211) Mazumdar, S.; Campbell, D. K. Broken Symmetries in a One-Dimensional Half-Filled Band with Arbitrarily Long-Range Coulomb Interactions. *Phys. Rev. Lett.* **1985**, *55*, 2067–2070.

(212) Peierls, R.; Peierls, R. E., *Quantum theory of solids*; Oxford University Press: 1955.

(213) Longuet-Higgins, H. C.; Salem, L. The alternation of bond lengths in long conjugated chain molecules. *Proc. R. Soc. London. Ser. A. Math. Phys. Sci.* **1959**, *251*, 172–185.

(214) Su, W. P.; Schrieffer, J. R.; Heeger, A. J. Solitons in Polyacetylene. *Phys. Rev. Lett.* **1979**, *42*, 1698–1701.

(215) Pople, J. A.; Walmsley, S. H. Bond alternation defects in long polyene molecules. *Mol. Phys.* **1962**, *5*, 15–20.

(216) Bishop, A. R.; Campbell, D. K.; Fesser, K. Polyacetylene and Relativistic Field Theory Models. *Mol. Cryst. Liq. Cryst.* **1981**, *77*, 253–264.

(217) Su, W. P. Lattice Relaxation of Even-Parity Singlet Excited States in Polyacetylene and Four-Soliton Bound State. *Phys. Rev. Lett.* **1995**, *74*, 1167–1170.

(218) Zheng, W.; Hamer, C. J.; Singh, R. R. P.; Trebst, S., et al. Deconfinement transition and bound states in frustrated Heisenberg chains: Regimes of forced and spontaneous dimerization. *Phys. Rev. B* **2001**, *63*, 144411.

(219) Bartalucci, G.; Coppin, J.; Fisher, S.; Hall, G., et al. Unravelling the chemical basis of the bathochromic shift in the lobster carapace; new crystal structures of unbound astaxanthin, canthaxanthin and zeaxanthin. *Acta Crystallogr. Sect. B* **2007**, *63*, 328–337.

(220) Wasielewski, M. R.; Johnson, D. G.; Bradford, E. G.; Kispert, L. D. Temperature dependence of the lowest excited singlet-state lifetime of all-trans-β-carotene and fully deuterated all-trans-β-carotene. *J. Chem. Phys.* **1989**, *91*, 6691–6697.

(221) Polívka, T.; Herek, J. L.; Zigmantas, D.; Åkerlund, H. E., et al. Direct observation of the (forbidden) S_1 state in carotenoids. *Proc. Natl. Acad. Sci. U. S. A.* **1999**, *96*, 4914–4917.

(222) Gradinaru, C. C.; Kennis, J. T.; Papagiannakis, E.; Van Stokkum, I. H., et al. An unusual pathway of excitation energy deactivation in carotenoids: Singlet-to-triplet conversion on an ultrafast timescale in a photosynthetic antenna. *Proc. Natl. Acad. Sci. U. S. A.* **2001**, *98*, 2364–2369.

(223) Barford, W. Theory of the dark state of polyenes and carotenoids. *Phys. Rev. B* **2022**, *106*, 35201.

(224) Polak, D. W.; Musser, A. J.; Sutherland, G. A.; Auty, A., et al. Band-edge Excitation of Carotenoids Removes S^* Revealing Triplet-pair Contributions to the S_1 Absorption Spectrum. *arXiv:1901.04900.*

(225) Zhang, J.-P.; Skibsted, L. H.; Fujii, R.; Koyama, Y. Transient Absorption from the $1B_u^+$ State of All-trans-β-carotene Newly Identified in the Near-infrared Region. *Photochem. Photobiol.* **2001**, *73*, 219.

(226) Zener, C. Non-adiabatic crossing of energy levels. *Proc. R. Soc. London. Ser. A, Contain. Pap. a Math. Phys. Character* **1932**, *137*, 696–702.

(227) Nitzan, A., *Chemical Dynamics in Condensed Phases: Relaxation, Transfer and Reactions in Condensed Molecular Systems*; Oxford University Press: 2006; Chapter 16.

(228) Ivakhnenko, O. V.; Shevchenko, S. N.; Nori, F. Nonadiabatic Landau–Zener–Stückelberg– Majorana transitions, dynamics, and interference. *Phys. Rep.* **2023**, *995*, 1–89.

(229) Musser, A. J.; Liebel, M.; Schnedermann, C.; Wende, T., et al. Evidence for conical intersection dynamics mediating ultrafast singlet exciton fission. *Nat. Phys.* **2015**, *11*, 352–357.

(230) Miyata, K.; Kurashige, Y.; Watanabe, K.; Sugimoto, T., et al. Coherent singlet fission activated by symmetry breaking. *Nat. Chem.* **2017**, *9*, 983–989.

(231) Duan, H. G.; Jha, A.; Li, X.; Tiwari, V., et al. Intermolecular vibrations mediate ultrafast singlet fission. *Sci. Adv.* **2020**, *6*.

(232) Liebel, M.; Schnedermann, C.; Kukura, P. Vibrationally coherent crossing and coupling of electronic states during internal conversion in β-carotene. *Phys. Rev. Lett.* **2014**, *112*, 1–5.

(233) Barford, W.; Chambers, C. A. Theory of Singlet Fission in Carotenoid Dimers. *arXiv Prepr. arXiv2304.10404* **2023**.

(234) Tayebjee, M. J. Y.; Sanders, S. N.; Kumarasamy, E.; Campos, L. M., et al. Quintet multiexciton dynamics in singlet fission. *Nat. Phys.* **2017**, *13*, 182–188.

(235) Marcus, M.; Barford, W. Triplet-triplet decoherence in singlet fission. *Phys. Rev. B* **2020**, *102*, 35134.

(236) Niedzwiedzki, D. M.; Sullivan, J. O.; Polívka, T.; Birge, R. R., et al. Femtosecond Time-Resolved Transient Absorption Spectroscopy of Xanthophylls. *J. Phys. Chem. B* **2006**, *110*, 22872–22885.

(237) Niedzwiedzki, D.; Koscielecki, J. F.; Cong, H.; Sullivan, J. O., et al. Ultrafast Dynamics and Excited State Spectra of Open-Chain Carotenoids at Room and Low Temperatures. *J. Phys. Chem. B* **2007**, *111*, 5984–5998.

(238) Cong, H.; Niedzwiedzki, D. M.; Gibson, G. N.; Frank, H. A. Ultrafast Time-Resolved Spectroscopy of Xanthophylls at Low Temperature. *J. Phys. Chem. B* **2008**, *112*, 3558–3567.

(239) Pati, Y. A.; Ramasesha, S. Exact Solution of the PPP Model for Correlated Electronic States of Tetracene and Substituted Tetracene. *J. Phys. Chem. A* **2014**, *118*, 4048–4055.

(240) Evans, D. F.; Tucker, J. N. Magnetic perturbation of singlet-triplet transitions. Part 7.—Simultaneous electronic transitions. *J. Chem. Soc. Faraday Trans. 2 Mol. Chem. Phys.* **1972**, *68*, 174–176.

(241) Ramamurthy, V.; Caspar, J. V.; Corbin, D. R.; Schlyer, B. D., et al. Triplet-state photophysics of naphthalene and. alpha.,. omega.-diphenylpolyenes included in heavy-cation-exchanged zeolites. *J. Phys. Chem.* **1990**, *94*, 3391–3393.

(242) Dillon, R. J.; Piland, G. B.; Bardeen, C. J. Different Rates of Singlet Fission in Monoclinic versus Orthorhombic Crystal Forms of Diphenylhexatriene. *J. Am. Chem. Soc.* **2013**, *135*, 17278–17281.

(243) Millington, O.; Montanaro, S.; Leventis, A.; Sharma, A., et al. Soluble Diphenylhexatriene Dimers for Intramolecular Singlet Fission with High Triplet Energy. *J. Am. Chem. Soc.* **2023**, *145*, 2499–2510.